Flinders University

Australian Uranium and NORM: Ecological Transfer to Native Vegetation Within the Arid Zone and UOC Phase Analysis Using Variable Temperature Synchrotron-XRD

By

Samantha Brooke Pandelus

B.Sc. (Hons)

Thesis
Submitted to Flinders University
for the degree of

Doctor of Philosophy
College of Science and Engineering
28th November 2022

Declaration

I certify that the thesis entitled 'Australian Uranium and NORM: Ecological Transfer to Native Vegetation Within the Arid Zone and UOC Phase Analysis Using Variable Temperature Synchrotron-XRD' does not incorporate without acknowledgement any material previously submitted for a degree or diploma in any university and the research within will not be submitted for any other future degree or diploma without the permission of Flinders University; and to the best of my knowledge and belief, does not contain any material previously published or written by another person except where due reference is made in the text.

Samantha Brooke Pandelus

28th November 2022

Acknowledgements

Presentations and publications

Publications

Samantha B. Pandelus, Brendan J. Kennedy, Gabriel Murphy, Helen Brand, Elizabeth Keegan, Allan Pring, Rachel S. Popelka-Filcoff. (2021). Phase analysis of Australian uranium ore concentrates determined by variable temperature synchrotron powder X-Ray diffraction. *Inorganic Chemistry*. 60(15), 11569-11578. DOI: 10.1021/acs.inorgchem.1c01562.

Maria Angelica D. Rea, Mathew P. Johansen, Timothy E. Payne, Samantha Pandelus, Jim Hondros, William Tucker, Attila Stopic, Liesel Green, Gillian Hirth, Allan Pring, Claire E. Lenehan, Rachel S. Popelka-Filcoff, (2021). Radionuclides and Stable elements in vegetation in Australian arid environments: concentration ratios and seasonal variation, *Journal of Environmental Radioactivity,* 234, 106627. DOI: https://doi.org/10.1016/j.jenvrad.2021.106627

Presentations

Royal Australian Chemical Institute (RACI) R&D Flinders University, Adelaide, December 1st-4th 2019 (Poster Presentation).

International Commission on Radiological Protection (ICRP) conference in Adelaide November 19th-21st 2019 (Poster Presentation).

AINSE Online symposium 23rd July 2019 (10-minute online oral presentation).

Radioanalytical and Nuclear Chemistry (RANC) conference in Budapest Hungary, May 5th-10th 2019, invited Presentation (30-minute oral presentation).

South Pacific Environmental Radioactivity Association (SPERA) November 6th-9th 2018 (20-minute oral presentation).

Presentation at the American Chemical Society (ACS) National Meeting, Nuclear division, Boston, MA, 19th-23rd August 2018 (15-minute oral Presentation).

Presentation at the Synchrotron Workshop, Flinders University, April 17th 2018 (Poster Presentation).

Presentation at RACI R&D Topics Conference, University of Tasmania, December 3rd-6th 2017 (Poster Presentation).

Abstract

Understanding uranium and naturally occurring radioactive materials (NORM) in a radioecology and nuclear forensic context is critical for protecting the environment and nuclear security.

Environmental risk assessments for radiological contamination follow internationally accepted methods including the 'Environmental Risk from Ionising Contaminants: Assessment and Management' (ERICA) tool. However, these assessment tools lack the necessary reference data for Australian native species, within an arid environment. The understanding of radionuclide uptake in biota is also an area of increasing interest due to the ICRP recommendations to demonstrate protection of the environment. This research provides activity concentrations of ^{238}U, ^{235}U and ^{232}Th chain radionuclides in soil and native vegetation from the arid Australian environment from two distinct locations, Olympic Dam and the Flinders Ranges Region. Both sites offer vastly different conditions when considering the natural geology, background radiation and surface operations. This research provides site specific concentration ratio (CR) datasets for shrubs and grasses for use within the ERICA tool to increase the confidence of Australian environmental impact assessments. The CRs calculated for the Olympic Dam region vary significantly from the CRs in the wildlife transfer database (WTD), however, the CRs from the Flinders Ranges region are in good agreement with the WTD.

In order to increase Australia's nuclear security, extensive characterisation of nuclear materials must be performed. Uranium ore concentrate (UOC) is the final stage of Australian involvement within the nuclear fuel cycle. Therefore, UOCs are a focus for nuclear forensics regarding Australian uranium. The chemical speciation of uranium oxides is sensitive to the provenance of the samples and their storage conditions. Here, we use diffraction methods to characterize the phases found in three aged (>10 years) uranium ore concentrates of different origins as well as in situ analysis of the thermally induced structural transitions of these materials. The structures of the crystalline phases found in the three samples have been refined, using high-resolution synchrotron X-ray diffraction data. Rietveld analysis of the samples from the Olympic Dam and Ranger uranium mines has revealed the presence of

crystalline α-UO$_2$(OH)$_2$, together with metaschoepite (UO$_2$)$_4$O(OH)$_6$ 5H$_2$O, in the aged U$_3$O$_8$ samples, and it is speculated that this forms as a consequence of the corrosion of U$_3$O$_8$ in the presence of metaschoepite. The third sample, from the Beverley uranium mine, contains the peroxide [UO$_2$(η^2-O$_2$)(H$_2$O)$_2$] (metastudtite) together with α-UO$_2$(OH)$_2$ and metaschoepite. A core–shell model is proposed to account for the broadening of the diffraction peaks of the U$_3$O$_8$ evident in the samples. This thesis will also establish the profile of Australian UOC phase analysis to increase the confidence for nuclear security relating to Australian produced uranium.

Table of Contents

List of abbreviations

Abbreviation	Meaning
ANSTO	Australian Nuclear Science and Technology Organisation
ARPANSA	Australian Radiation Protection and Nuclear Safety Agency
CR	Concentration Ratios
DCCs	Dose Conversion Coefficients
Eh	Redox potential
EIS	Environmental Impact Statement
EMCLs	Environmental Media Concentration Limits
EMP	Environmental Management Program
EPA	Environment Protection Authority
ERICA	Environmental Risk from Ionising Contaminants: Assessment and Management
ERISS	Environmental Research Institute of the Supervising Scientist
FREDERICA	FASSET Radiation Effects Database Environmental Risks from Ionising Contaminants
FASSET	Framework for Assessment of Environmental Impact
GUI	Graphical User Interface
HPGe	High Purity Germanium
HREE	Heavy Rare Earth Element
IAEA	International Atomic Energy Agency
ICP-MS	Inductively Coupled Plasma Mass Spectrometry
ICRP	International Commission on Radiological Protection
IOCG	Iron Oxide Copper Gold
ISO	International Standard Organisation
ISOCS	In-Situ Object Counting Systems
ISR	In-Situ Recovery
LA-ICP-MS	Laser Ablation Inductively Coupled Plasma Mass Spectrometry
LabSOCS	Laboratory Source less Calibration Software
LREE	Light Rare Earth Element
LOD	Limit of Detection

MDA	Minimum Detectable Activity
NAA	Neutron Activation Analysis
NIST	National Institute of Standards and Technology
NORM	Naturally Occurring Radioactive Material
OPAL	Open-pool Australian light water research reactor
PBS	Phosphate Buffered Saline
PD	Powder Diffraction
pH	Potential Hydrogen
PVC	Polyvinyl Chloride
RBS	Rutherford Backscattering
REE	Rare Earth Element
RQ	Risk Quotient
SA	South Australia
SEM/EDS	Scanning Electron Microscopy Energy Dispersive Spectroscopy
TRS	Tailings Retention System
UOC	Uranium Ore Concentrate
WO	Whole Organism
WTD	Wildlife Transfer Database
XRD	X-Ray Diffraction
XRF	X-Ray Fluorescence

Safety considerations

A license through the South Australian Environment Protection Authority to 'Use or Handle a Radioactive Substance' has been held by Samantha Pandelus for the duration of her PhD. Personal dosimetry through ARPANSA has been worn whenever in the laboratory and potentially in contact with radioactive materials.

Chapter 1. Introduction to NORM and Australian uranium mining

1.1. Thesis directions: Australia's uranium, expanding environmental protection and strengthening nuclear security

This thesis aims to provide data to increase the confidence in the Australian uranium industry by exploring two major themes that currently contribute towards potential uncertainty: the environmental impact and nuclear security (IAEA, 2013). This thesis addresses two issues: 1. To develop the understanding of the effect of NORM on the environment within the Australian arid climate towards environmental protection. This will be used to increase the validity of the environmental risk assessment for arid regions and hence, reduce the uncertainty towards environmental radiation. Overall, this thesis contributes to the radionuclide transfer data available for Australian native vegetation within an arid environment. 2. This thesis also determines the phase analysis of Australian UOCs to increase the data available to characterise UOCs for nuclear security.

Chapters three to six of the thesis will explore the environmental radioactivity of vegetation within the Australian arid zone. Radionuclide concentration ratios of NORM are employed in environmental impact assessments. This research will increase the data available for Australian specific species therefore, increasing the confidence in understanding the impact of NORM and ionizing radiation on vegetation. This research will increase the understanding of how radionuclides behave within the arid Australian environment in terms of uptake within vegetation and permeation throughout surface soil from deposition. The statistical analysis of very low activity NORM materials will also be considered, as the concentration ratios may be skewed due to very low activity concentrations due to measurements close to the LOD.

In order to address and ease the uncertainty towards environmental radiation within Australia, increasing the understanding of the behaviour of radionuclides within the arid environment is vital (Hirth et al., 2017). The impact of ionizing radiation on the environment and vegetation is an area that is still highly debated within the literature (Beresford et al., 2020). Procedures are currently implemented globally to predict the radiation dose to vegetation (Brown et al., 2008). However, there are few studies on the impact of ionising radiation on Australia's vegetation in the arid zone (Hirth et al., 2017). The arid climate is important to consider within Australia, as Olympic Dam, Beverley, Carrapatena and Maralinga

are all sites of significant interest to radioactive environmental monitoring and all of these sites are found within arid Australia. This study focused on two locations within the arid Australian environment, at the Olympic Dam and Flinders Ranges Region. Both of these regions are of potential increased risk to radionuclide exposure from naturally occurring radioactive materials (NORM). Researching both locations may provide information on radionuclide uptake by vegetation in the arid Australian environment.

Chapter seven details the uranium ore concentrate and uranium oxide phase analysis to expand the knowledge on these samples to increase the confidence in Australia's nuclear security. Australia is a major contributor to the world's supply of uranium, nuclear material outside of regulatory control is a risk to national security. Nuclear forensics is required to determine the origin of ceased nuclear material. There is still more information that can be gathered regarding signatures for nuclear material for investigations. The UOC phase analysis has been previously shown to have potential use for the distinguishing between geographical locations or UOC processing characteristics. This study aims to determine the difference in UOC phase composition from Olympic Dam, Ranger and Beverley mines. This thesis also endeavours to determine the phase transition temperature of U_3O_8 from orthorhombic to hexagonal and to collect a high-resolution neutron diffraction pattern of U_3O_8 at a high temperature. Australia is a major contributor to the world's supply of uranium, producing approximately 7000 tonnes of uranium ore concentrate (UOC) annually (Dolchinkov, 2019; Keith et al., 2015). In 2013 Australia produced 9% of the worlds uranium supply behind Kazakhstan (39%) and Canada (22%) (Wang et al., 2017). UOC production is the final stage of the nuclear fuel cycle that is currently undertaken in Australia (Ditcham et al., 2016).

1.2. NORM

NORM consists of the naturally occurring U and Th isotopes ^{238}U, ^{235}U and ^{232}Th and daughters. In a theoretical sealed environment, with no chance of radionuclide escape or contribution, each member of the ^{238}U, ^{235}U, and ^{232}Th decay series will be in radioactive equilibrium. There are two types of radioactive equilibrium: secular and transient. The transient equilibrium occurs when the half-life of the parent is longer than the half-life of the

daughter. The decay of the parent is the rate-determining step. Secular equilibrium occurs when the half-life of the parent is much greater than the half-life of the daughter, there is a build-up of the daughter radionuclide until the number of atoms of the daughter being produced is the same as the number of the atoms of the daughter decaying, this leads to the parent and daughter having the same activity (Al-Shboul et al., 2017; Prince, 1979). Equation 1.1 shows the connection between the half-life and the rate of decay, considering radioactive decay follows first order kinetics.

$$\lambda = \frac{ln2}{t_{1/2}}$$

Equation 1.1. First order radioactive decay equation where t = time, and λ = the decay constant (Scholz & Scholz, 2015).

As radioactive decay follows first order kinetics, when the activity of radionuclides that belong within a decay series are known, the activity of the other radionuclides within the decay series can be calculated based on the parent. The Bateman equation (Equation 1.2.) is used for this purpose (Cetnar, 2006; R. Lozano, San Miguel, & Bolívar, 2011; Thibes & de Oliveira, 2014).

$$N_n(t) = \sum_{i=1}^{n}\left[N_i(0) * \left(\prod_{j=i}^{n-1} \lambda_j \right) * \left(\sum_{k=i}^{n} \left(\frac{e^{-\lambda_k t}}{\prod_{p=1,p\neq k}^{n}(\lambda_p - \lambda_k)} \right) \right) \right]$$

Equation 1.2. The general formula of the Bateman equation.

Equation 1.2. expands at each radioactive decay step within the decay series, to model the ingrowth and decay of each radionuclide within the chain. It can be broken down into the following steps to calculate the activity of the consecutive radionuclides within a single decay chain, assuming equilibrium. For example, the first radionuclide in the series follows the formula shown in Equation 1.3, the second radionuclide in chain is shown in Equation 1.4 and the third radionuclide in a chain is shown in Equation 1.5.

$$N_{1(t)} = N_{1(0)} * 1 * \frac{e^{-\lambda_1 t}}{1} = N_{1(0)}e^{-\lambda_1 t}$$

Equation 1.3. The Bateman equation for the first radionuclide in a decay series (where $N_{1(t)}$ = Number of nuclei at a time, $N_{1(0)}$ = number of nuclei at time 0, λ = Rate equation, t =time (seconds).

$$N_{2(t)} = N_{1(0)} * \lambda_1 * \left(\frac{e^{-\lambda_1 t}}{(\lambda_2 - \lambda_1)}\right) + \left(\frac{e^{-\lambda_2 t}}{(\lambda_1 - \lambda_2)}\right) + N_{2(0)} * 1 * \left(\frac{e^{-\lambda_2 t}}{1}\right)$$

Equation 1.4. The Bateman equation for the second radionuclides in a decay series (where i=1 to 2, j=1 to 2 and k=1 to 2).

$$N_{3(t)} = N_{1(0)} * \lambda_1 \lambda_2$$

$$* \left(\left(\frac{e^{-\lambda_1 t}}{(\lambda_2 - \lambda_1)(\lambda_3 - \lambda_1)}\right) + \left(\frac{e^{-\lambda_2 t}}{(\lambda_1 - \lambda_2)(\lambda_3 - \lambda_2)}\right) + \left(\frac{e^{-\lambda_3 t}}{(\lambda_1 - \lambda_3)(\lambda_2 - \lambda_3)}\right)\right)$$

$$+ N_{2(0)} * \lambda_2 \left(\left(\frac{e^{-\lambda_2 t}}{(\lambda_3 - \lambda_2)}\right) + \left(\frac{e^{-\lambda_3 t}}{(\lambda_2 - \lambda_3)}\right)\right) + N_{3(0)} * 1 * \left(\frac{e^{-\lambda_3 t}}{1}\right)$$

Equation 1.5. The Bateman equation for the third radionuclide in a decay series (where i=1 to 3, j=1 to 3 and k=1 to 3).

Equations 1.3 to 1.5 show how the rate of decay from each radionuclide and the ingrowth from the parents is modelled. For daughter radionuclides in the lower radionuclide down the decay series the equation builds using the rate equations (λ) for each radionuclide. The decay schemes of ^{238}U, ^{235}U and ^{232}Th are shown below in Figures 1.1, 1.2 and 1.3, respectively below.
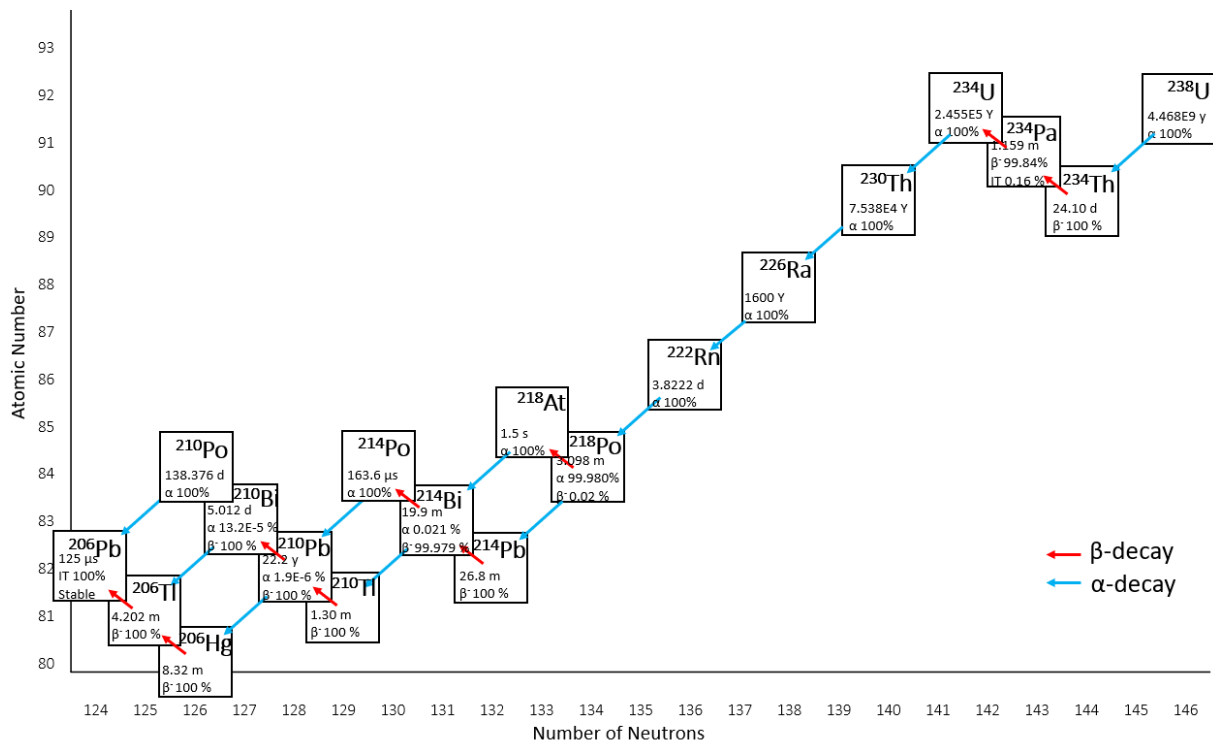
Figure 1.1. ^{238}U decay series, the number of neutrons is plotted along the x-axis and the number of protons is plotted along the y axis (Brookhaven).

Figure 1.1 shows all the daughters of ^{238}U with the half-life and decay modes. The ^{238}U decay series has radionuclides which decay via α, β$^-$, and internal transition (IT). While some radionuclides such as ^{238}U decay 100% via alpha decay, others such as ^{214}Bi decay via both α and β$^-$, and ^{206}Pb is stable (Gilmore, 2008). The half-lives range over multiple orders of magnitude, from ^{238}U at 4.468 X 10^{+9} years to ^{214}Po at 163.6 µs. The ^{238}U daughter nuclides from this decay scheme include highly radiotoxic nuclides including ^{226}Ra, ^{210}Pb and ^{210}Po (Tuovinen et al., 2015).

As a closed system is often not the case when dealing with environmental samples, disequilibrium needs to be considered. Disequilibrium of the ^{238}U chain may occur due to the following factors: differences in solubility, surface affinity, the degree of weathering, diffusion of ^{222}Rn gas, alpha recoil effects, redox processes, groundwater movement and human interference (Gilmore, 2008; Yanase et al., 1995). Equilibrium between ^{238}U and its ^{234}Th and ^{234m}Pa daughters is re-established relatively quickly. This is due to the relatively short half-lives of ^{234}Th and ^{234m}Pa are 24.1 days and 1.17 minutes respectively. The activity of the daughters becomes equal to the ^{238}U activity within 6 to 8 months after chemical separation (Murphy, 2005). The half-life of ^{210}Pb is 22.7 years, natural events such as groundwater flow can remove ^{210}Pb from rock, producing a deficit in the rock, and an increase of ^{210}Pb in the water. For this reason ^{210}Pb is not an ideal choice for the estimation of ^{238}U activity (Gilmore, 2008). As radon is a gas, it can escape from the system, therefore, creating disequilibrium within the decay series, this is the main cause of disequilibrium in natural materials (Mudd, 2008). When radon is removed from the decay chain the majority of the daughters will also be lost due to relatively short half-lives. When ^{220}Rn in the ^{232}Th series is lost, equilibrium is established relatively quickly, within minutes. However when ^{222}Rn from the ^{238}U decay series is lost, due to the half-life of ^{222}Rn being 3.825 days, 10 half-lives need to be re-established before equilibrium is obtained (Gilmore, 2008). Therefore, it takes approximately 38.25 days for equilibrium to re-establish between ^{222}Rn and its daughters (Gilmore, 2008). The ^{238}U and ^{234}U radionuclides are both found in the ^{238}U decay series, the other U isotope ^{235}U is in a separate decay series, it is detailed below in Figure 1.2.

6
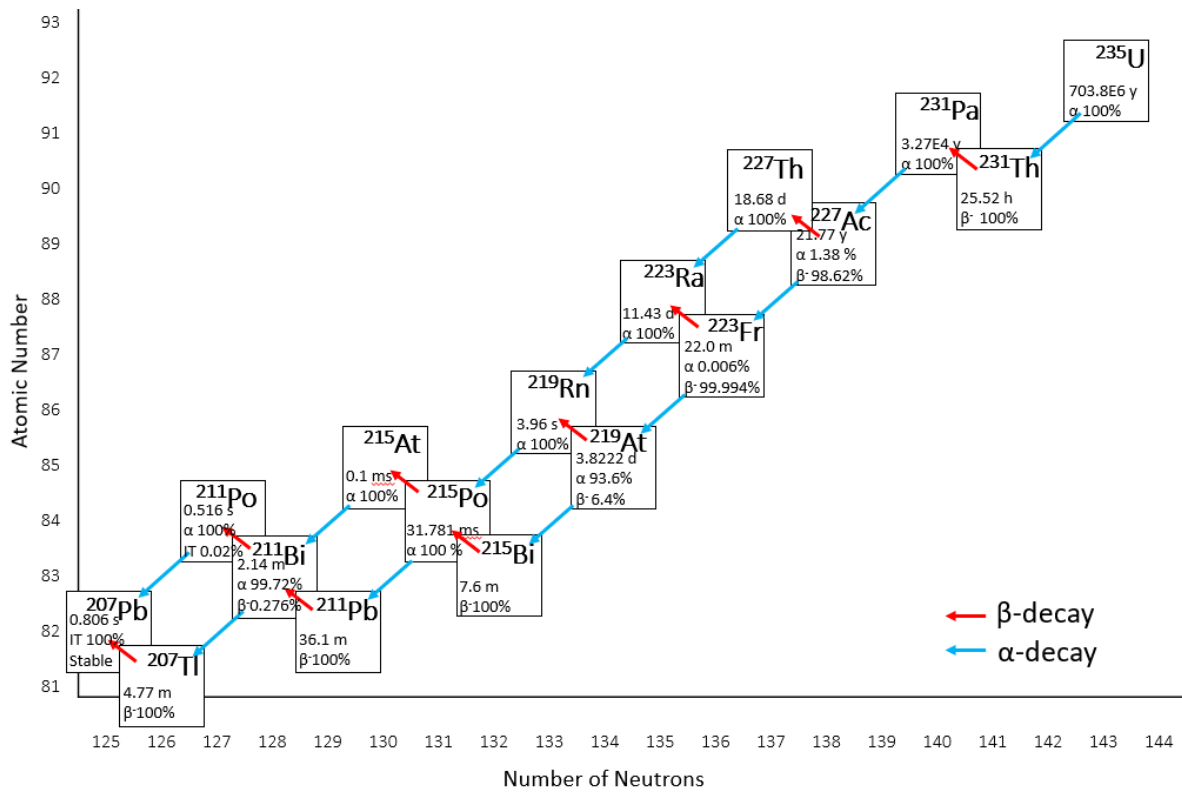
Figure 1.2. ^{235}U decay series, the number of neutrons is plotted along the x-axis and the number of protons is plotted along the y axis (Brookhaven)

Figure 1.2 shows the ^{235}U decay series, the radionuclides within this series decay via α, β-, γ and internal transition (IT). The half-lives range from ^{235}U at 703.8 X 10^6 years and ^{215}At at 0.1 milliseconds. ^{207}Pb is the isotope of Pb that is the final and stable element from the ^{235}U chain, ^{207}Pb is only active via IT. The gas ^{219}Rn is the major source of disequilibrium within this decay series. The ^{232}Th decay series is shown below in Figure 1.3.
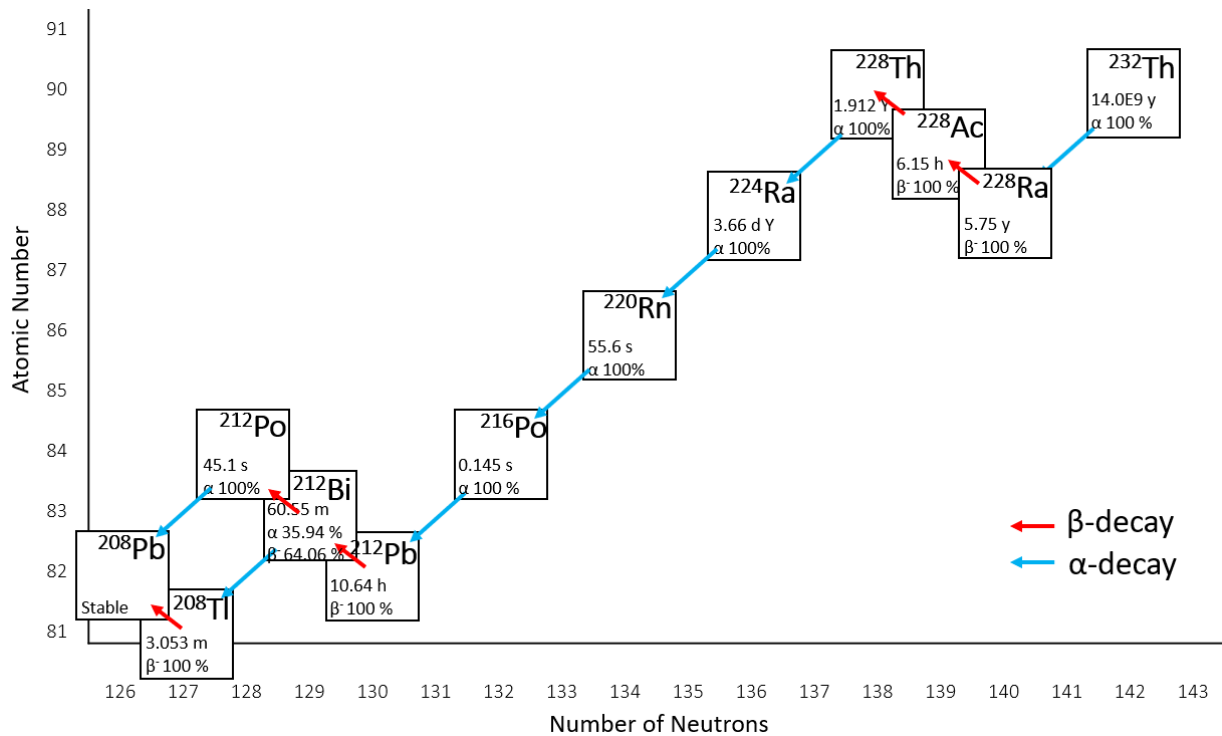
Figure 1.3. ^{232}Th decay scheme, the number of neutrons is plotted along the x-axis and the number of protons is plotted along the y axis (Brookhaven).

Figure 1.3 show the ^{232}Th decay series, the radionuclide with the longest half-life is ^{232}Th at 14.0 X 10^9 years and the shortest is ^{216}Po at 0.145 seconds. Radionuclides within this decay series decay via α, β$^-$ and γ. The main source of disequilibrium within this series is the loss of ^{220}Rn gas.

The different elements from the three different decay series outlined above have different chemical properties and will behave differently within a natural system. The different chemical properties must be carefully considered when studying the NORM series as the different reactions, solubility and mobility affects equilibrium. The chemical properties of the different elements are detailed below.

1.2.1. Chemistry of NORM elements

U is the parent in both the ^{238}U and ^{235}U decay chains while, ^{234}U forms as progeny from the ^{238}U decay series. All U radionuclides decay via alpha emission. The mobility of ^{234}U can be higher than the others due to alpha recoil processes occurring within the system allowing for migration (Yanase et al., 1995). U is found in the environment, in soil, air and water and is found in the earth's crust in approximately 2-4 ppm (Keith et al., 2015). The natural

8

abundance ratio of ^{234}U, ^{235}U and ^{238}U is approximately 0.000055:0.00725:1 respectively (Richter et al., 1999). However, their abundance ratio can vary slightly depending on the geographical locations of the originating sample. These slight variations can occur through natural isotope fractionation, nuclear reactions, or contamination from anthropogenic uranium. Variations from the n(^{234}U)/n(^{238}U) ratio may result from disturbances of secular equilibrium. The main application of isotope ratio analysis has been for nuclear forensics, and the identification of the geographical origin (Crean et al., 2015; Keegan et al., 2014; Richter et al., 1999; Varga et al., 2011). The mechanism of disequilibrium between ^{238}U and ^{234}U have been proposed to include lattice damage from radioactive decay, daughter bound weakly in interstitial sites and oxidation state changes from +4 to +6 leading to an increase in solubility and α-recoil processes (Yanase et al., 1995). As U is present in the environment at background levels, human exposure is unavoidable with an estimated daily intake of 0.9-1.5 µg/day. In the environment oxidation-reduction reactions convert U from soluble U^{6+} to insoluble U^{4+}. This can occur due to microbial action under anaerobic soil or sediment, which can affect the mobility of U in soil (Van Nostrand et al., 2011). The U oxidation state is dependent on the pH, the speciation of U dictates the sorption to surfaces (Harris et al., 2000)

Pa is an actinide element, it has a valence of +5 (Pa(V)), this differs from U with valences of +4 or +6, therefore, different chemical processes in the environment can cause chemical fractionation between Pa and U. Due to the disequilibrium of U and Pa, they can be used for dating applications. ^{231}Pa can be measured using alpha spectroscopy with the assumption of equilibrium with ^{227}Th (Pickett et al., 1994).

Th is an actinide element, that is most commonly found in the +4 oxidation state (Th(IV)) in the environment, however, Th(III) species also exist (Arnold et al., 2014; Ortu et al., 2016). Th is very insoluble in natural geological environments (Yanase et al., 1995) and Th concentration is soils ranges from 2-12 mg/kg; however, concentration increases with clay contents. At low pH Th is present as Th^{4+}, above a pH of 4 the main Th species is $Th(OH)_2^{2+}$ and at high pH ThO_2 (Harmsen & De Haan, 1980). Th bioavailability from soil to vegetation will determine the level of harm received by the organism from Th. However the soil to plant transfer of radionuclides is also influenced by the plants, soil conditions, such as bacteria, and the growth stage of the plant (Guo et al., 2010).

Ra has four different radionuclides within the three NORM series detailed above, ^{226}Ra, ^{223}Ra and ^{224}Ra all decay via α emission while ^{228}Ra decays via β$^-$. The half-lives range from 1600 years to 3.66 days. All of the Ra nuclides decay via a strong alpha emission, ^{226}Ra, ^{223}Ra and ^{224}Ra having a major α emission at 4784.34 keV, 5685.37 keV and 5716.23 keV, respectively (Brookhaven). Ra is an alkaline earth element, therefore has similar chemical properties to barium. Ra exists in the Ra^{2+} form, Ra compounds are often insoluble and some common forms are carbonates, silicates, phosphates and sulphates (Mitchell et al., 2013). Ra is more bioavailable in comparison to U. Ra is absorbed strongly to soils, where approximately half of Ra is fixed to soil surfaces. Higher salt concentrations e.g., KCl, NaCl, CaCl$_2$ increases the mobility of Ra in the environment, this therefore increases the bioavailability to biota. As Ra and Ca are in the same group of elements, they share similar chemical properties, therefore, uptake of Ca and Ra can be competitive. Where soils contain high concentrations of Ca and Mg, lower Ra will be leached from soils due to similarities in chemical properties. The preference of Ca uptake in comparison to Ra in some cases can be attributed to ionic radii, where Ca = 0.99Å and Ra = 1.43Å. Ra availability to plants is lower than strontium and calcium (MacDonell, 1986).

Rn is a gas; it is the only gas found within all three decay schemes discussed in section 1.2. All three forms of Rn discussed, ^{222}Rn, ^{220}Rn and ^{219}Rn, have short half-lives and therefore equilibrium with Ra can be re-established reasonable quickly. As Rn is a gas, radioactive equilibrium may be disturbed where an unsealed system occurs. Rn escapes from minerals by a number of mechanisms, ejection from the surface of the material during alpha decay, or diffusion through fractures, joints or pores in minerals (Telahigue et al., 2018). A study by Müllerová et al. 2018, determined the level of Rn exhalation from soil to be higher during dry periods. (Müllerová et al., 2018). Rn is a noble gas and therefore, has very low to no chemical reactivity, the release of Rn is called 'emanation'. Rn emanation from soil is primarily from α recoil processes from the decay of Ra. Following this decay, the Rn atoms have kinetic energies of 86 keV and 123 keV for ^{222}Rn and ^{220}Rn respectively. The distance Rn can travel through material ranges from 4 X 10^{-02} μm to 6 X 10^{-02} μm within a granular media such as soil, and 6 X 10^{01} μm within air. Following Rn emanation into the atmosphere, the diffusion within the atmosphere depends on wind speed, atmospheric stability, moisture and wet and dry removal. The deposition of Rn from the atmosphere to surfaces can be determined when

considering the deposition rate deposited onto a surface and the concentration in the air (Gurau et al., 2014; Zahorowski et al., 2004).

The activity of ^{210}Po in soils ranges significantly, however a range of 20 to 240 Bq/kg is common. The major source of atmospheric ^{210}Po is from the decay of ^{222}Rn gas (Matthews et al., 2007; Thakur & Ward, 2020). Due to the surface deposition, surface soil often has higher activity concentrations within the first 0-3 cm. The ^{210}Po concentration in soil depends on the natural geological setting, depth, biological processes, pH and sedimentation. Depending on geographical location and altitude the ^{210}Po concentration in the atmosphere ranges from 0.03 and 0.3 Bq/m^3 and in the stratosphere is 1.9 MBq/m^3 (Thakur & Ward, 2020). The major source of atmospheric ^{210}Po is from the decay of ^{222}Rn. (Matthews et al., 2007; Thakur & Ward, 2020). ^{210}Po is a very active radionuclide, a comparison of alpha emissions of 1 μg of ^{210}Po, emits the same number of alpha particles per second as 4.5 mg of ^{226}Ra, 262 mg of ^{238}Pu and 446 kg of ^{238}U (Thakur & Ward, 2020). Therefore, ^{210}Po is a major dose contributor to organisms and must be considered when calculating dose rates. Po can naturally exist in many different oxidation states, -2, +2, +4 and +6, where Po^{4+} is most stable in aqueous solutions. Po^{4+} readily hydrolyses, the hydrolysed species readily absorbs to surfaces, however, when in acidic conditions of <2 pH, Po will remain in solution. Po in different environmental conditions exists in a variety of different states, in groundwater is may be found as PoO(OH)$^+$, PoO(OH)$_2$ or PoO$_2$, in acidic conditions and PoO$_3^{2-}$ is found in alkaline conditions. Po can also form salts with chlorides, nitrates and other anions.

Bi in the environment is often found as Bi$_2$O$_3$ or as Bi[0], the main Bi species found in freshwater is Bi^{3+}, BiOH$^-$ or BiO$^+$, depending on pH (Feldmann et al., 1999).

Pb has both radioactive and stable forms present within the ^{238}U, ^{235}U and ^{232}Th decay series. Pb is also found in the atmosphere, typical ^{210}Pb concentrations in the atmosphere air ranged from 0.2-1.5 Bq/m^3 however, concentrations tend to increase with altitude (Thakur & Ward, 2020).

1.3. Australian uranium mines, their geological setting and current environmental monitoring

The first step in the nuclear fuel cycle is U mining and extraction of U from ore, this is the first and only step Australia is currently involved with (Liu et al., 2017). There are many U deposits in Australia, the focus of this present research is based around the UOC produced from Olympic Dam, Beverley and Ranger. The environmental focus of this research is on environmental samples from the Olympic Dam region, near the Olympic Dam mine and Flinders Rangers Region, which was located near the Flinders Ranges (Figure 1.4).

This adapted image has been removed due to copyright restriction. The original image is available online from [Hirth, G. (2014). *A review of existing Australian radoinuclide activity concentration data in non-human biota inhabliting uiranium mining environments*. (Technical Report Series No. 167)]

Figure 1.4. U mines in Australia, Olympic Dam, Ranger and Beverly are the focus of this present study (Hirth, 2014).

1.3.1. Ranger mine

The Ranger mine is located within the Northern Territory, Australia, approximately 250 km east of Darwin, it is in a tropical climate, in the Alligator River region and is on the boundary of the Kakadu National Park and the Arnhem Land Aboriginal Reserve (Hein, 2002). At the Ranger site there are multiple ore deposits, the Ranger 1 deposit contained 140,000 t of U. The Jabiluka deposit contains 141,640 t or U_3O_8 at 0.48% U_3O_8 and the Ranger 3 deposit contained 34,867 t U_3O_8 at 0.28 % U_3O_8 (Skirrow et al., 2016).

Ranger mineralogy and geology

The Ranger deposit is found within the Alligator River Uranium Field (ARUF). The ARUF is hosted by Archean-Proterozoic basement of the Pine Creek Orogen (PCO). U-Pb dating of uraninite from the ARUF spot analysis have been dated at 1685 Ma from the Jabiluka deposit. However, there has also been a range of younger dating to ~500 Ma from other deposits in the ARUF. The deposits Ranger, Jabiluka and Koongarra are hosted within the Cahill formation, which is comprised by variably altered pelitic to psammitic and locally carbonaceous schists (e.g. quartz-biotite-feldspar-muscovite ± garnet ± amphibole ± graphite) (Skirrow et al., 2016). The ore deposit is shown in Figure 1.5 below (Skirrow et al., 2016).

Figure 1.5. Ranger ore deposit lithography of cross sections from the Ranger 1 Number 3 orebody (Skirrow et al., 2016).

Mining and processing

The Ranger mine was operated by an open pit mining method. The Ranger mining process involved crushing, grinding and milling of ore, leaching using sulfuric acid and pyrolusite, U recovery using Alamine 336 and kerosene, extraction using ammonia to precipitate U following by calcination to remove ammonia. The waste material from this process is sent to the tailings dams for storage (Noller, 1991).

Environmental monitoring of radionuclides at Ranger mine and the Alligator Rivers Region

ANSTO and Environmental Research Institute of the Supervising Scientist (ERISS) have previously provided Australian CR data to the WTD (Johansen, M & Twining, J, 2010; Martin, P. et al. 1998). ERISS data included whole organism CRs, ANSTO data was a mixture of WO and tissue CRs. Limited data has also been collected from other sources (Hirth, 2014). There

have been studies that have looked into developing CRs$_{(WO-Media)}$ for Australian species, this includes tropical climate in the vicinity of the Ranger mine in the Northern Territory and within the Alligator Rivers Region. A study by Doering et al. (2018), collected whole organism concentration ratios from near the Ranger mine in the Northern Territory. The Ranger mine is in a tropical climate; determined 410 CR$_{WO-media}$ values to assist with the remediation of the mine site and focused on tissue specific data from a variety of fauna however some freshwater vascular plants were also analysed. The species analysed was 'Blue Lilly' (*Nymphaea violacea*), the foliage included vegetation collected from above the sediment, including stems and leaves, the CRs are in Table 1.1 (Doering et al., 2018).

Table 1.1. CRs from Doering et al. (2018) paper (CR = Concentration ratio, SD = standard deviation).

Element	Foliage CR	Rhizome CR	Roots CR
Po	1.7E+0 AM 6.0E-1 SD	8.1E-1 AM, 4.1E-1 SD	6.3E-1 AM, 2.9E-1 SD
Ra	1.1E+0 AM, 3.6E-1 SD	1.1E+0 AM, 8.1E-1 SD	1.2E+0 AM, 8.2E-1 SD
Th	1.7E+0 AM, 8.3E-1 SD	7.2E-1 AM, 6.6E-1 SD	1.0E+0 AM, 1.5E+0 SD
U	1.7E+0 AM, 7.2E-1 SD	1.3E+0 AM, 1.1E+0 SD	6.2E-1 AM, 3.2E-1 SD

A short communication by Doering and Bollhofer, 2016, presented a database of radionuclide activity specifically for the Alligator Rivers region in the Australian wet-dry tropics. This database contains radionuclide activity values on fauna, vegetation, soil, sediment and water collected by the Environmental Research Institute of the Supervising Scientist (ERISS). Eleven radionuclides are of interest in this database, they include [227]Ac, [40]K, ^{210}Pb, [210]Po, [226]Ra, [228]Th, [230]Th, [232]Th, [234]U and [238]U. There are 57,473 concentration values in the database, which also includes elemental information (Doering & Bollhöfer, 2016). A study by Doering et al. 2017, estimated doses from Aboriginal bushfoods from the site of the remediated Ranger U mine and the Alligator Rivers region. Concentration ratios were calculated for the different types of bush foods including crocodile, snake, fruit and yam. Concentration ratio data for fruit flesh is in Table 1.2 (Doering et al., 2018).

Table 1.2. Concentration Ratio data for fruit flesh (AM = Arithmetic mean, AMSD = Arithmetic mean standard deviation) (Doering et al., 2018).

Element	CR
Pb	2.2E-2 AM, 4.2E-2 AMSD
Po	3.2E-2 AM, 3.7E-2 AMSD
Ra	2.7E-2 AM, 3.0E-2 AMSD
Th	1.3E-2 AM, 3.8E-2 AMSD
U	2.3E-3 AM, 3.1E-3 AMSD

1.3.2. Olympic Dam mine

Olympic Dam is located within South Australia, approximately 600 kilometres north of Adelaide and is located near the Roxby Downs township. Olympic Dam is Australia's largest known accumulation of U, containing more than two million tons. The ore deposit was discovered in 1975 and mining began in 1988, the deposit is shown in Figure 1.5 (Government of South Australia; Kirchenbaur et al., 2016). The U element is found in the ore primarily in the form of uraninite (UO_2), which can be found in many different textural forms. The structure of uraninite is often defective due to the decay through the series to Pb, where Pb has a different size and shape that does not fit into the lattice of uraninite (Marshall et al., 2014). U is also present as coffinite (U^{4+},Th)$(SiO_4)_{1-x}(OH)_{4x}$) and brannerite (U^{4+},REE,Th,Ca)(Ti,Fe^{3+},Nb)$_2$(O,OH)$_6$, hematite (Fe_2O_3), quartz (SiO_2), sericite ($KAl_2(AlSi_3O_{10})(OH)_2$), feldspars ($AT_4O_8$ (where A = K, Na, Ca or T = Si or Al), barite ($BaSO_4$), fluorite (CaF_2), siderite ($FeCO_3$), Chlorite $(X,Y)_{4-6}(Si,Al)_4O_{10}(OH,O)_8$ Where X and Y could represent Fe^{2+}. Fe^{3+}, Mg^{2+}, Mn^{2+}, Ni^{2+}. $Zn^{2+,}$ Al^{3+}, Li^{+1} or Ti^{4+}, pyrite (FeS_2), chalcopyrite ($CuFeS_2$), bornite (Cu_5FeS_4) and chalcocite (Cu_2S) (Schmandt et al., 2017).

Olympic Dam mineralogy and geology

The Olympic Dam ore deposit is the largest known U source in the form of an IOCG-U-Ag deposit (Macmillan et al., 2016). The IOCG-U-Ag deposit is an Fe oxide, Cu, Au, U and Ag deposit. The ore deposit is 7 by 5 km in size, funnel shape (Figure 1.6) (Corriveau, 2006). The Olympic Dam region is approximately 550 km NNW of Adelaide, the ore deposit is located in the eastern margin of the Gawler Craton. There is low levels of rainfall with no seasonal

patterns (Rea et al., 2021). The soil type at Olympic Dam is mostly Calcarosol or Sodosol. Calcarosol soil is majority carbonate and Sodosols is alkaline soils with an increase in soil texture with depth (Metcalfe & Biu, 2016). The soil at the Olympic Dam region is deep in pigmentation of orange and has swale and dunes. The soil from the dunes is sandy, this is where the majority of the vegetation is present.

This adapted image has been removed due to copyright restriction. The original image is available online from [https://www.google.com/maps/search/olympic+dam/@-30.4415645,136.814652,11934m/data=!3m1!1e3?entry=ttu]
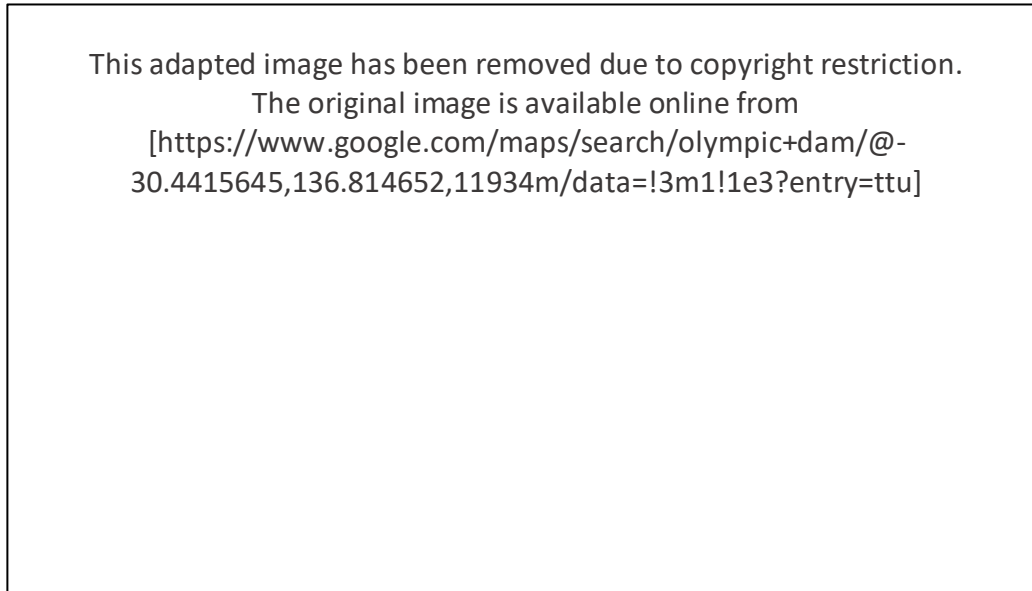
Figure 1.6. Olympic Dam ore deposit over layered over Olympic dam map (courtesy of Olympic Dam Operations).

Impurity elements of uraninite include Ca, Th, Fe, Si, P, Al, Mg, Mn, K and other trace elements have been identified in the deposit at Olympic Dam, these include Th, Bi, As, W, Cu, Mo, V, Si, P, Al, Fe, Mg, Na and K (Macmillan et al., 2016; Macmillan et al., 2016). A study by Janeczek *et al.* 1992, identified than the natural UO_2 structure is a highly defective fluorite structure (Janeczek & Ewing, 1996). The defects come from the decay of U, oxidation of U and cationic substitution (Ewing, 1992; Macmillanet al., 2016). The main U containing minerals found at the Olympic Dam deposit are uraninite (UO_2), brannerite (UTi_2O_6) and coffinite ($U(SiO_4)_{1-x}(OH)_{4x}$) (Macmillan et al., 2016). A Schematic of a cross section of the Olympic Dam Breccia Complex is shown below in Figure 1.7.

Figure 1.7. Olympic Dam ore deposit, cross section of the Breccia Complex (Esdale et al., 2003).

The ore deposit at Olympic Dam Is found within the Mesoproterozoic rocks of the eastern Gawler Craton. The Gawler Craton comprise the basement to the Neoproterozoic succession deposited on Stuart Shelf. The shelf sediments above the Olympic Dam ore deposit include the Cambrian Andamooka Limestone and the Neoproterozoic Arcoona Quartzite, Corraberra Sandstone and Tregolana Shale. The depth of the ore deposit is 260 meters minimum below surface level, the thickness of the ore deposit is greater than 500 meters at the thickets point (Esdale et al. 2003).

Olympic Dam mining and processing

The ability to extract and or leach U from ore and minerals depends on U speciation, deportment, mineral structure, presence of trace elements and availability of U within the deposit. Different considerations when processing U containing ore material include ore hardness, leach and flotation kinetics and the presence of impurities or penalty elements,

crush and grinding size, inflow sheet design, equipment size, oxidation conditions, acid or alkaline media, temperature and pressure (Bowell et al., 2011). When an ore deposit has multiple elements that are economically viable to extract such as Olympic Dam, the recovery and extraction of the ore will be dependent on the characteristics of the ore and elements of interest. The Cu, U, Au and Ag in the ore at Olympic Dam requires processing streams to separate. Cu is extracted via flotation and smelting, U is recovered by acid leaching of the Cu tailings, Ag and Au in the Cu concentrate and are extracted separately during electrorefining of the cured Cu matte, these processes are detailed below (Boisvert et al., 2013). The source terms of environmental emissions from Olympic Dam according to the EIS from 1975 include the underground mine, mine ventilation, ore transfer, ore processing and the tailings retention system (Roger, 1982).

The ore at Olympic Dam, containing Cu, U, Au and Ag is mined by the underground stope mining method. After the ore is removed from the stopes, the ore is generally brought to the surface via winding shafts. The ore is then milled to a fine powder (Brooker et al., 2005). Following milling, chemical processing begins, the form of chemical processing is depending on the elements contained within the ore and the desired extraction, and the mineralogy of the ore. U extraction is often performed using an acid leaching process with H_2SO_4 to form $[UO_2(SO_4)_3]^{4-}$ (Equation 1.6) or leaching with $Na_2CO_3/NaHCO_3$ mixture, which produces $[UO_2(CO_3)_3]^{4-}$. CU extraction in an acidic environment (Equation 1.7).

$$2(R_3NH_+)_2SO_4^{2-} + UO_2(SO_4)_3^{4-} \rightarrow (R_3NH_+)_4[UO_2(SO_4)_3^{4-}] + 2SO_4^{2-}$$
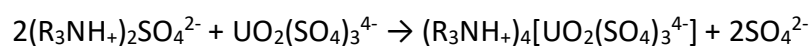
Equation 1.6. U extraction via H_2SO_4 leaching.

$$2R\text{-}H^{2+} + Cu \rightleftharpoons R - Cu + 2H^+$$
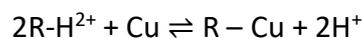
Equation 1.7. CU extraction in an acidic environment

An oxidizing agent is often added to convert the oxidation state of U from the U(IV) to U(VI). Leachates are then often extracted from this slurry by a liquid-liquid extraction or ion exchange process. The U is then commonly isolated using acidic aqueous $(NH_4)_2SO_4$, then precipitation occurs as $(NH_4)_2U_2O_7$ using ammonia gas, then dried using heat. Another pathway is the sodium diurinate is precipitated by NaOH and then re-dissolved and converted to ammonium diurinate. This process produces a crude oxide, this is then separated and precipitated. Reagents that can be used for this include H_2O_2, NaOH, NH_4OH and MgO (Murphy, 2005). A study by Zhu et al. 2016 developed a U extraction process that includes the

use of MgO (Figure 1.8). The U extraction process in Figure 1.8 works efficiently as strongly acidic conditions are favourable for U stripping as it is simpler and more efficient. The precipitation of U requires more neutral conditions. Which the Cyanex 923 has shown to be effective in assisting with the transfer of U from strongly acidic conditions to weaker acidic conditions without the need to neutralize (Zhu et al., 2016).

This image has been removed due to copyright restriction. Available online from [Zhu, Z., Pranolo, Y., & Cheng, C. Y. (2016). Uranium recovery from strong acidic solutions by solvent extraction with Cyanex 923 and a modifier. *Minerals Engineering,* 89, 77-83]
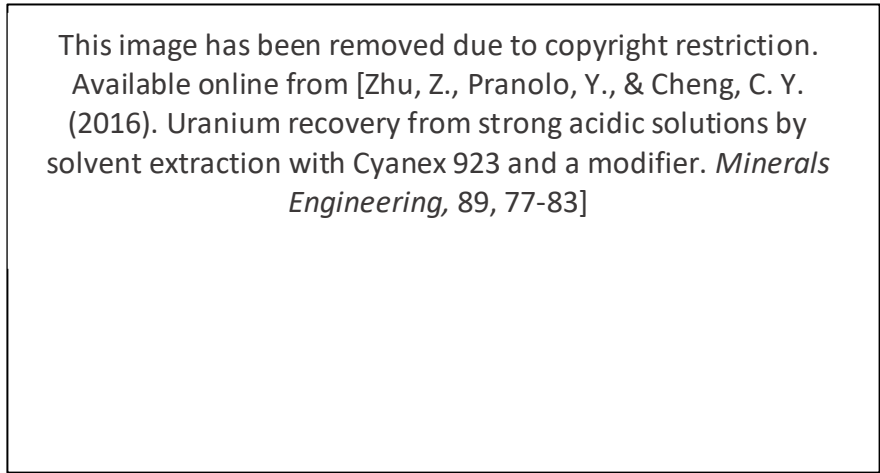
Figure 1.8. U recovery using acidic conditions and Cyanex 923 (Zhu et al., 2016).

In U ore processing, after either solvent extraction using ammonia or ion exchange, the U precipitate is then calcined to form U_3O_8. Calcination process material using a thermal treatment at high temperatures (~600 °C), in the absence of air or oxygen. This process removes the water from the U compounds (Crean et al., 2015).

After solvent extraction and flotation, Cu is recovered and fed into the smelters where it undergoes smelting, electro refining and anode casting. During the ore processing in the smelter, radionuclides including Po, Bi and Pb report to slag in the direct to blister process. Some Po and Pb is caught in the off-gas handling system, dust is recycled and requires a bleed to limit build-up of Po and Pb. Slag is the by-product of the smelting process; flue dust and off gas are also by-products. Radionuclides have the ability to become enriched within a particular stream due to feedback loops in the processing. Flue dust has been shown to contain ^{210}Pb and ^{210}Po at relatively higher concentrations compared to the initial ore, indicating that they are concentrating. Build-up occurs when the dusts are recycled into the process to recover excess Cu. The disposal of the radionuclide contaminated flue dust is a complex and expensive process (Lane et al., 2016).The waste from a mine and the ore processing circuit is called the tailings. As of 2011, the extraction of U has created about a

billion tons of tailings material from 4000 U mine sites worldwide. The storage of tailings material is performed by collection in surface dams. This however has been considered a risk to the environment, due to the presence of leachable and mobile toxic metals in the tailings material in weathering environments (Liu et al., 2017). U release into the environment is influenced greatly by ground and surface water (Hu et al., 2016; Liu et al., 2017).

1.3.3. Beverley mine

The Beverley mine is located in the Lake Frome Basin in the North Flinders Ranges. The deposit is a sandstone-hosted U deposit. The grade of U in the deposit is about 0.25wt% U_3O_8 (Wülser et al., 2011) The Beverley U mines, operated by Heathgate Pty Ltd, use In-Situ Recovery (ISR) methods (Wang et al., 2012). The Lake Frome Basin and the Flinders Ranges area is naturally elevated in background radiation. The Paralana hot springs are located near the Flinders Ranges and the Beverley region, the hot springs are naturally rich in Ra (Brugger et al., 2005).

Beverley mineralogy and geology

The U deposit Is located at the Lake Frome Basin in at the Flinders Ranges Region in South Australia, the ore deposit is hosted within a permeable unreactive sandstone sediment. Most of the U containing mineralogy in the deposit is coffinite ($U(SiO_4)_{1-x}(OH)_{4x}$) and uraninite (UO_2). Small amounts of carnotite ($K_2(UO_2)_2(VO_4)_3 \cdot 3H_2O$) is also present within the ore deposit. Due to the nature of the sandstone sediment, which is highly permeable and has low reactivity makes this deposit ideal for mining via the *In-Situ* Recovery (ISR) method (Wülser et al., 2011). A schematic of a cross section of the Beverley ore deposits is shown in Figure 1.9 below.

This image has been removed due to copyright restriction. Available online from [Hou, B., Keeling, J., & Li, Z. (2017) Paleovalley-related uranium deposits in Australia and China: A review of geological and exploration models and methods. *Ore Geology Reviews*, 88, 201-234. http://dx.doi.org/10.1016/j.oregeorev.217.05.005]

Figure 1.9. Beverley Ore Deposit geology (Hou et al., 2017).

The ore deposit Beverley, Four Mile East, Four Mile West, Pepegoona and Pannikin are all found within the northern Callabonna sub basin. The Four Mile East, Pannikin and Pepegoona deposits are hosted in alluvial fans and amalgamated fluvial sands, these are of Eocene age. The Beverley deposits are found in the Miocene fluvial sediments of Namba Formation and Four Mile West is hosted in sandy sediments of Mesozoic Frome Embayment of the Eromanga Basin (Hou et al., 201). The Flinders Ranges Region is located around 600 km north of Adelaide, it is found in the Flinders and Olary subregions on the North Olary Plains (Rea et al., 2021). The soil type at the Beverly mine is mostly Calcarosol with pockets of Sodosol. Calcarosol soil is majority carbonate and Sodosols is alkaline soils with an increase in soil texture with depth (Metcalfe & Biu, 2016). The soil at the Beverley regions is hard and paler in colour in comparison to the deep orange of the Olympic Dam region.

Beverley mining and processing

U can be mined by In-Situ Recovery (ISR) otherwise known as in-situ leaching. ISR methods are used at the Beverley U mine in South Australia. When considering environmental impacts, the ISR process is favourable, compared to open pit mining as ISR has minimal surface disturbance. There is no ore brought to the surface and no waste rocks or tailings are produced using the ISR method. However, ISR mining is only feasible when the geology and hydrology of the orebody have appropriate characteristics. The mineral zone must be easily permeable, contain natural groundwater and the U must be easily mobilized. The geology around the orebody must include impermeable strata above and below the orebody (Woods, 2011).

Figure 1.10. Beverly mine, schematic of in-situ recovery mining process (Märten, 2006).

ISR can be used for mining directly or recovering U from U rich tailings material (Wang et al., 2012). The ISR process (Figure 1.10) involves the addition of oxidizing and complexing reagents.

At the Beverley mines an acid leach of dilute H_2SO_4 is used with H_2O_2, this is known as the lixiviant. The lixiviant is injected into the orebody using injection wells which mobilizes the U. The U leached as the soluble $UO_2(SO_4)_2^{2-}$ species, the U containing solution is pumped to the surface where anion exchange resins are used to extract the U (Märten, 2006; Woods, 2011). NaCl and H_2SO_4 is used to elute the U from the anion exchange resins. The U is precipitated with the addition of H_2O_2 to form UO_4. This product is then washed, thickened, dried and packaged (Märten, 2006). The lixiviant is recycled between 50-100 times (Woods, 2011). Beverley currently does not calcine their product and the final product is shipped as the U peroxide (UO_4).

1.4. Literature environmental monitoring of radionuclides within arid Australian and the arid environment internationally

Previous radionuclide analysis of soil and at Olympic Dam had been completed by Read and Pickering (1997). They measured the radionuclide concentrations of soil samples from a control site and at a site near a tailings dam. The control site chosen for sampling was at least 5 km from the tailings dam. The mean control soil results were (n=3) ^{238}U = 2.3±0.5 Bq/kg, ^{230}Th = 7.9±1.7 Bq/kg, ^{226}Ra = <17 Bq/kg, ^{210}Pb = 7.2±2.3 Bq/kg and ^{210}Po = 5.9±1.7 Bq/kg. The

soil results from the tailings site were (n=3) ^{238}U = 3.5±0.04 Bq/kg, ^{230}Th 17±5 Bq/kg, ^{226}Ra <17 Bq/kg, ^{210}Pb 7.2±2.3 Bq/kg and ^{210}Po 5.9±1.7 Bq/kg (Read & Pickering, 1999). These data provide a baseline data set of Olympic Dam as a comparison for this present research.

The Maralinga test site is located within the arid zone of Australia, there has been considerable prior research around radionuclides within this location. However, the focus has been on anthropogenic radionuclides from the weapons testing and less focus on NORM. The focus on studies at the Maralinga test site is on Pu radionuclides and not NORM (Ikeda-Ohno et al., 2016)

The Nevada Test Site is located in the arid desert region of Nevada, United States, this was a nuclear weapons test site (Caffrey E. et al., 2015). This site has been extensively studied within the scientific literature. The major focus of the radionuclides within these studies are anthropogenic radionuclides from weapons testing. Koranda et al, (1978) has previously discussed the radionuclide uptake into vegetation at the Nevada test site, the focus of this study was on ^{137}Cs and ^{90}Sr. This study also discussed the intake of radionuclides through foliar intake (Koranda et al., 1978). The main issue with implementing the data produced from international sites is the inference that different native species will behave the same, therefore, highlighting the importance to provide a dataset for the Australian specific context.

1.4.1. South Australian site comparison and natural background radiation
The Olympic Dam and the Flinders Ranges Region are both located within the arid region of South Australia, however, the geology of the two sites is vastly different. The differences in geology and mineral abundance dictates the natural background radiation. The soil types between Olympic Dam and Beverley are different, where Olympic Dam has dunes and swale, where the Flinders Ranges region soil is majority swale. The geology of the Olympic Dam region is discussed in section 1.3.2 and the Flinders Ranges Region Beverley deposit is discussed in section 1.3.3.

Background radiation concentrations have been previously reported as 20 Bq/kg by Long 2012 in the ARPANSA report 'A survey of Naturally Occurring Radioactive Material Associated

with Mining' (Long, 2012). Other literature background ranges include the UNCEAR worldwide background values of ^{238}U is on average 0.035 Bq/g (35 Bq/kg) and ranges from 0.016 Bq/g to 0.110 Bq/g, ^{232}Th on average is 0.030 (30 Bq/kg) with a range of 0.011 Bq/g to 0.064 Bq/g (UNSCEAR, 2000). The IAEA worldwide background activities are reported, ^{238}U at an average of 0.025 Bq/g (25 Bq/kg) with a range of 0.010 Bq/g to 0.050 Bq/g and ^{232}Th with an average of 0.025 Bq/g (25 Bq/kg) and range of 0.007 Bq/g to 0.050 Bq/g (IAEA, 2000).

1.5. NORM radionuclide uptake in Australian native vegetation within arid Australia

This thesis will focus on increasing the understanding of the effect of NORM on the arid Australian climate zone. NORM and elemental uptake into native Australian vegetation from both the Olympic Dam and Flinders Ranges regions is the focus of this study. The Olympic Dam region may have a potential increase in NORM materials through deposition of dust from mechanical disturbance from >30 years on surface activities and mining in the area. The Flinders Ranges region has higher natural background radiation compared to Olympic Dam due to the nature of the geology. Therefore, composite soil samples of the Flinders Ranges region were the focus for this region. A combination of radioanalytical and elemental analysis was performed on bulk samples. For the stratified soil samples and vegetation from Olympic Dam, imaging and radiography techniques were implemented. As the radionuclides present within the samples are estimated to be of low activity based on the background radiation from both sites, different analytical methodologies were implemented as well as a consideration for the statistical validity of very low activity quantitative measurements for environmental radiation. The usefulness of concentration ratio values will be discussed in relation to very low activity concentrations for environmental analysis. There is a potential for CRs to skew towards larger numbers because the concentrations is close to the LOD. CRs will also be discussed as to their relevance when depositional radionuclides are in the environment.

1.4.1. Current environmental monitoring standards

Environments of increased risk to radiation contamination must be monitored and controlled. Environmental impact assessments to determine the radiological risk to non-human biota

(NHB) is required around mining sites involving NORM (Hirth et al., 2017). Current environmental monitoring methods for radiological impact involve the use of modelling tools such as the Environmental Risk from Ionising Contaminants: Assessment and Management (ERICA) tool from the Norwegian Radiation Protection Authority. Environmental monitoring for radiation protection is of great importance as the effects of low dose on biota are not well understood. NORM (section 1.2) are the main radionuclides of interest for environmental radionuclide monitoring for Australia.

1.4.2. Concentration ratios (CRs)

Concentration ratios are a key component for the method of the analysis of the radiological impact on environments (Copplestone et al., 2013). CRs (equation 2.1) are a measure of the transfer of radionuclides between the media in which an organism grows or lives, and the concentration within the whole organism (WO) itself. The media that relates to the organism can include soil for land biota and water for aquatic life, air for flying animals and combinations of medias for multimedia dwelling organisms (Hirth et al., 2017). Concentration ratios are the value that used to describes the transfer of radionuclides from environmental media to an organism, CRs are calculated using (Equation 1.8) (Copplestone et al., 2013).

$$CR_{wo-soil}$$
$$= \frac{Activity\ concentration\ in\ organism\ whole-body\ (Bq/kg)(fresh\ mass)}{Activity\ concentration\ in\ soil\ (dry\ mass(Bq\ per\ unit\ media\ mass\ or\ volume))}$$
$$CR_{WO} = \frac{Plant\ Mass_{Dry}}{Plant\ Mass_{Fresh}} * \frac{Plant\ Activity_{Dry}}{Soil\ Activity}$$

Equation 1.8. CR determination WO-Media (Copplestone et al., 2013; Johansen et al., 2014).

The study by Beresford et al. 2008, shows tables of concentration ratio data that is the default for elements within different species types (Beresford et al., 2008). Derivation of CR$_{WO-Media}$ values, the weighted arithmetic mean (AM) (Equation 1.9) is the mean for an individual study is given weight based on the number of observations in the study (Howard et al., 2013).

$$AM = \frac{\Sigma_i n_i CR_i}{N}$$

Equation 1.9. Concentration ratio weighted arithmetic mean, Where: AM = weighted arithmetic mean, ni = the number of observations in the study, CRi = the mean CRWO-Media for the study, N = The total number of observations in all studies (Howard et al., 2013).

Radionuclide uptake by wildlife is commonly represented as concentration ratios, which are calculated from the activity of radionuclides in the whole organism and the activity of the

radionuclide in the surrounding environmental medium e.g., soil or water (Beresford, 2010; Brown et al., 2008; Johansen et al., 2014). Concentration ratios are a measure of the transfer of radionuclides between the media in which an organism grows and the concentration within the whole organism (WO) itself. Concentration ratios are a key method for the quantification of the radiological impact on environments (Copplestone et al., 2013).

1.4.3. Environmental risk from ionising contaminants: assessment and management (ERICA) assessment tool

The ERICA assessment tool is based on a tiered approach to assessing the radiological risk to terrestrial, freshwater, and marine biota. The ERICA tool uses an integrated approach which seeks to characterise and manage risk from exposure/dose/effect assessment ("Environmental Risk From Ionising Contaminants: Assessment and Management (ERICA) ", 2015; ERICA, 2015). The ERICA tool is used to assess the risk to terrestrial, marine and freshwater biota (Brown et al., 2008; ERICA, 2015). ERICA uses a three-tiered assessment method (Figure 1.11), tier one of ERICA assessments involves a screening method of the environmental media only. The environmental media is set as soil if a terrestrial species is selected, or the surrounding media is set to seawater if a marine species is selected. Tier one assessments consider the activity of the media and compares to the literature 'environmental media concentration limits' (EMCLs) to determine a risk quotient based on an estimated dose. The parameters in a tier 1 assessment are simple and minimal input by the user is required as the media concentration is the only needed input. Tier 2 assessments require more data input by the user and provide a more accurate assessment. Tier two assessments involve a dose rate calculation and involves concentration ratios (CRs) for the biota of interest, as shown in Equation 3 (ERICA, 2015). Tier 2 assessment use concentration ratios, distribution coefficients, percentage dry weight soil or sediment, dose conversion coefficients, radiation weighting factors, uncertainty factors and occupancy factors. These factors can all be seen and edited by the user (Brown et al., 2016). Tier three uses the same input parameters as tier two assessments, however, the tier-three assessments are fully probabilistic and provide the option to run the assessment probabilistically if the underlying parameter probability distribution functions are defined (ERICA, 2015). Tier 3 assessments involve evaluation of possible effects caused from ionising radiation, the effects that relate to reproduction,

mortality and morbidity. Tier 3 assessments do not involve a numerical screening value (Garnier-Laplace et al., 2008).
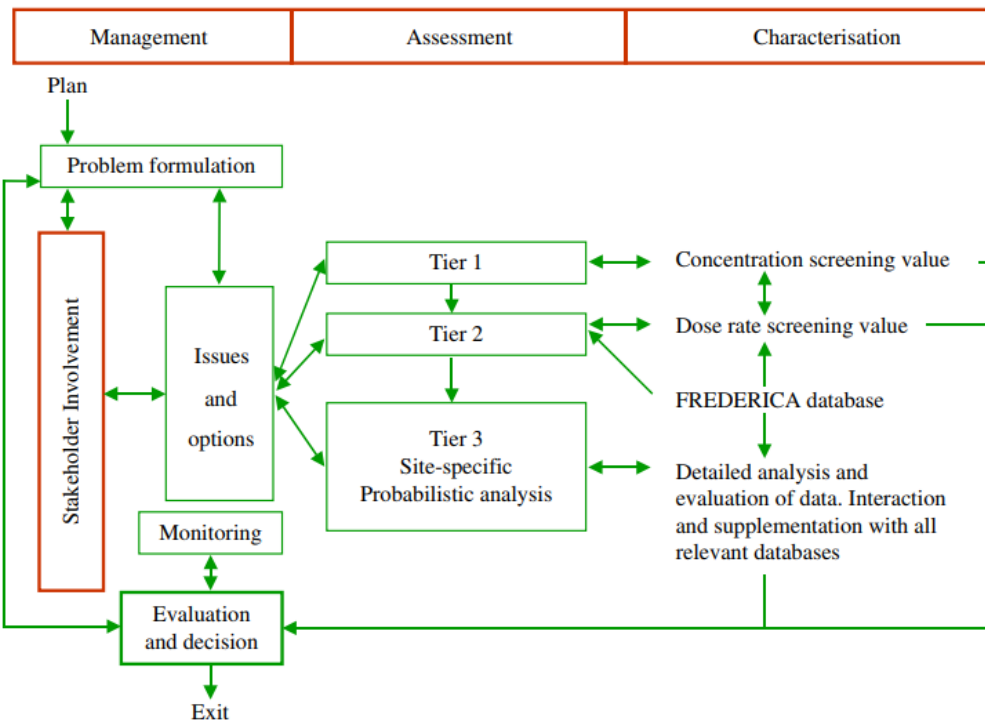
Figure 1.11. Schematic of the ERICA framework (Nick Beresford et al., 2007; Zinger, Copplestone, & Howard, 2008).

Overall the ERICA tool uses simple transport models which provide conservative estimates of media activity concentrations from discharge data if measurements are not available; the transport models are taken from IAEA (2001) models for use in assessing the impact of discharges of radioactive substances to the environment (ERICA, 2015). The dose rate screening values that ERICA implements are either 10 μGy h^{-1}, 40 μGy h^{-1} for terrestrial animals, birds, amphibians, and reptiles, and 400 μGy h^{-1} for plants and other aquatic organisms, where this is the value of chronic exposure and below this no measurable population effects would occur (ERICA, 2015).

A comparison of the ERICA tool to other radiological environmental risk assessment models has been previously performed. A study by Wood et al. (2009), compared the three radiological environmental risk assessment models ERICA, R&D128/SP1a and RESRAD/BIOTA. R&D128/SP1a and RESRAD-BIOTA generally provided more conservative estimates. The ERICA tool overall provided the closest predictions to the measured data for animals (Wood et al., 2009).

1.4.4. Dose responses

The effect of ionizing radiation on vegetation is poorly understood in terms of relating dose and effect. The dose of ionizing radiation may cause effects to an organism such as death, reduced health or ability to reproduce. However, this is dependent on the type and activity of radiation exposure, duration of exposure and individual species sensitivity. The effect of different dose levels on basic biological function is not well known. Determining the actual dose received by a plant is also somewhat difficult to determine when considering the height of the plant, thickness of the trunk, thickness of branches and the amount of the plant above and below the ground. Seasonal factors can also interfere with the effect to the plant (ICRP, 2008).

A paper by Andersson et al. (2009), outlined the need for regulatory benchmarks for μGy h^{-1} does of environmental radiation. This paper has outlined the 10 μGy h^{-1} screening level for dose response to species. This was determined from background radiation dose rates and the observed effects data. The 10 μGy h^{-1} screening value has been developed to protect 95% of all species, therefore may over or under protect in some cases. This study recommended further work to providing more robust organism group values so that they may be specific screening values for these individual groups (Andersson et al., 2009).

1.4.5. The wildlife transfer database (WTD)

The WTD is the concentration ratio database that is used as the CR input data for ERICA (Radioecologists). The ERICA tool draws upon default concentration ratios from the WTD for the different reference organisms. Within vegetation there are different default values for each of the categories of 'grasses and herbs', 'shrubs' and 'trees' (Beresford et al., 2008; Brown et al., 2008). The wildlife transfer database is a collection of NHB whole body concentration ratios. A study by Copplestone et al. (2013), strongly recommends that the primary source for CR$_{WO-media}$ values be the IAEA wildlife handbook and the Wildlife transfer database (Copplestone et al., 2013). The WTD was specifically developed for use for radiological environmental impact assessments. The WTD is based on the ICRP MAPs and relates each MAP to the three ecosystems used in the FREDERICA database, freshwater, marine or terrestrial (Strans, 2009).

1.4.6. The FREDERICA radiation effects database

The FREDERICA database which ERICA refers to, contains data on dose effect relationships. A study by Copplestone et al. (2008), explains the development and purpose of the FREDERICA database. FREDERICA is a radiation effects database for non-human biota (NHB), the data is collected from the scientific literature and categorizing NHB within biological groups. These groups are amphibians, aquatic invertebrates, aquatic plants, bacteria, birds, crustaceans, fish, fungi, insects, mammals, molluscs, mosses/lichens, reptiles, soil fauna, terrestrial plants and zooplankton. Each group is then allocated to an ecosystem type, either freshwater, marine or terrestrial. The database relates literature doses to observed biological effects for each of these groups (Copplestone et al., 2008). The dose-effect relationship for non-human biota is the input data to ERICA when assessing the dose effect to the organism in tier two and tier three assessments (FREDERICA, 2010). The FREDERICA database contains data from 1509 references from the scientific literature from the period 1945 to 2004 with 29,400 data entries. The FREDERICA database is used to assess the dose to risk impacts of ionizing radiation on NHB. The data in the FREDERICA database is grouped within seven groups, mutation, morbidity, reproductive capacity, mortality, stimulation, adaption and ecological (Copplestone, 2005; Copplestone et al., 2008; FREDERICA, 2010).

1.4.9. How appropriate is the current environmental impact assessment models for the arid Australian climate and Australian specific species?

The ERICA tool draws upon concentration ratio (CR) data from the Wildlife Transfer Database (WTD) (Copplestone, 2005; Copplestone et al., 2008; FREDERICA, 2010). A study by Hirth et al. (2017), highlighted the variation between Australian arid environment concentration ratios and the CR values of other species in other climates shown in Figure 1.12. and Figure 1.13. (Hirth et al., 2017).

Figure 1.12. Whole organism concentration ratios from Australian terrestrial vs non Australian terrestrial values (Hirth et al., 2017).

Figure 1.12 shows a visual comparison of different species and a comparison between Australian CRs compared to the mean CRs from the WTD and Australian CRs from a U mine tailings area. The study by Hirth et al. (2017) highlighted the inconsistency between trends of CRs for Australian native vegetation species CRs compared to the CRs found within the WTD as >90% of all currently available CRs available originate from Europe and North

This image has been removed due to copyright restriction. Available online from [Hirth, G. A., Johansen, M. P., Carpenter, J. G., Bollhöfer, A., & Beresford, N. A. (2017). Whole-organism concentration ratios in wildlife inhabiting Australian uranium mining environments. *Journal of environmental radioactivity, 178*, 385-393]

Figure 1.13. Australian CRs compared to international mean CRs from the WTD (Hirth et al., 2017).

America (Hirth et al., 2017). The 'Australian U CRs (mine tailings)' data in Figure 1.13 are the data available from near mine tailings. The need for site specific arid Australian concentration ratios (CRs) is essential for accurate environmental impact assessments of Australian species within the arid environment (Hirth et al., 2017).

Some of the generic input parameters used in the current models for radiological environmental impact assessment may not be appropriate for the assessment of Australian native species in arid conditions. A study by Hirth et al. (2017), collated concentration ratio data of wildlife surrounding Australian mining sites. As shown in Figure 1.1.2, this study identified that 83% of the Australian species, reported higher concentration ratios compared with non-Australian data. This study outlined the importance of developing a larger Australian specific database for more accurate environmental impact assessments for the arid environment (Hirth et al., 2017). Figure 1.13 compares Australian CR data to CR data from other localities, this figure highlights the difference as the majority of Australian CR values are significantly higher.

1.4.10. Need for Australian specific concentration ratios

There is a need to develop further data for Australian specific species. More than 90% of available CRs$_{(WO-Media)}$ data for NHB originates from temperate climates of Europe and North America (Hirth et al., 2017). Yet two out of three active U mines in Australia are located in the arid zone of South Australia. This highlights the importance of the development of more Australian specific CRs$_{(WO-Media)}$ data for a more accurate radiological risk assessment of NHB within an arid environment (Hirth et al., 2017). A study by Wetle et al. (2020), focused on U uptake in desert plants from an abandoned U mine. The findings were that the desert species accumulated higher concentrations of U in comparison to the literature from other climates. The conclusion was this was due to the desert plants either accumulating U to a greater extent, or having fewer mechanisms to remove the elements (Wetle, Bensko-Tarsitano, Johnson, Sweat, & Cahill, 2020). A paper by Wood et al. (2013), compared studies which determined radionuclide concentration ratios for NHB, this paper concluded that there is a large variation between measured and predicted radionuclide concentrations calculated from different studies. This is most likely due to the great simplification of assessment models and

differences in the sampling sites. This study further highlighted the need for specific concentration ratio data for specific climates, ecosystems and species (Wood et al., 2013).

1.6. Radionuclide and elemental uptake in plants, anatomy and chemical processes in plants and cells

1.6.1. Leaf anatomy

The anatomy of a shrub consists of roots, stems, leaves, flowers and seedpods, depending on the species. The anatomy of a *Dodonaea viscosa* leaf is shown in Figure 1.14.

This image has been removed due to copyright restriction. Available online from [Venkatesh, S., Reddy, Y. R., Ramesh, M., Swamy, M., Mahadevan, N., & Suresh, B. (2008). Pharmacognostical studies on Dodonaea viscosa leaves. *African Journal of Pharmacy and Pharmacology*, 2(4), 083-088.]
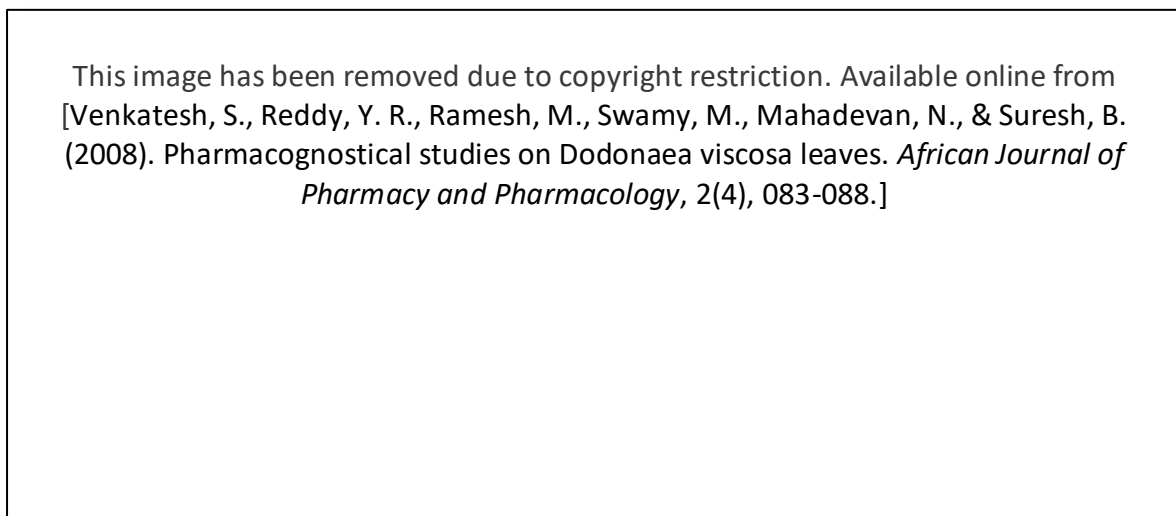
Figure 1.14. Dodonaea viscosa leaf anatomy identified from a transverse thin section (Venkatesh et al., 2008).

Figure 1.14 shows the typical anatomy of a *Dodonaea viscosa* leaf where the different structures are shown, and the different functions are discussed below. Xylem and phloem are the plants vascular system and are responsible for transport of nutrients and fluids around the plant, the xylem and phloem are referred to as 'vascular bundles' (Carlsbecker & Helariutta, 2005). The vascular bundles are circular in shape and are surrounded with chlorenchyma cells. This formation of cells in a leaf is referred to a Kranz anatomy, where Kranz anatomy is a characteristic of C4 plants (Sedelnikova et al., 2018). The chlorenchyma cells are surrounded by the palisade cells, which are then surrounded by the cuticle. Stomata are on the cuticle and are responsible for gas exchange in and out of the leaf (Chater et al., 2016).

1.6.2. Mechanism of radionuclide or element uptake into vegetation

The uptake of metals (including metalloids and some non-metals e.g., Se) in biota is dependent on the properties of the metals such as the oxidation and ligand binding. Metals in sediments tend to bind with ligands, therefore the metals available to interact with biota may only be a fraction of the total available metals in the sediment. Depending on the precipitation, complexation, inclusion, mediation and the water and solid sediment matrix, will determine if the metal will be obtainable for uptake and interaction with the biota. The transport mechanisms for metal uptake in vegetation include passive diffusion facilitated transport, active transport and endocytosis. Due to the range of different uptake mechanisms the prediction of uptake can be difficult to determine. Organic matter within the soil also can influence the uptake of elements into plants, where higher organic content in soils leads to higher Ra availability (Peijnenburg et al., 2014).

For a metal to interact with an organism, the metal must interact with the cellular membrane before it is taken up. The cell membrane is hydrophobic, however, transport proteins in the layer allow the movement of hydrophobic ions across the membrane, this may lead to interactions within the cell (Campbell et al., 2002). The transport across a cell membrane via passive diffusion can be responsible for the uptake of lipid soluble metal species including neutral, nonpolar, a few alkyl-metal compounds and inorganically complexed metal species (Peijnenburg et al., 2014).

A study by Boghi *et al.* 2018 stated that the mechanism of U uptake into plants remains poorly understood. The Boghi *et al*. 2018 study showed different chemical processes (Figure 1.15) within soil which may affect U mobility and potentially affect the uptake into roots (Boghi et al., 2018).

Figure 1.15. Summary of U speciation and uptake into vegetation through the root system (Boghi et al., 2018).

The uptake of a gas through leaves is controlled by three individual factors of resistance (Equation 1.10) (in s m^{-1}), stomata resistance (R_s), the Mesophyll resistance (R_m) and the cuticula (outside layer of cells) resistance (R_{ct}) (Gut et al., 2002).

$$\frac{1}{R_{leaf}} = \frac{1}{R_s + R_m} + \frac{1}{R_{ct}}$$

Equation 1.10. Total leaf resistance to uptake of trace gases (Gut et al., 2002).

Foliar uptake of elements from wet or dry deposition from atmospheric fallout. Foliar elemental intake can occur via penetration through stomata or penetration through cuticle via cracks however this method is less likely (Shahid et al., 2017). Intake of radionuclides via foliar uptake has previously been determined from the study of Po intake to tobacco plants. A study by Cankurt et al., 2020, determined the majority of Po accumulation in tobacco plants was the leaves and roots. Where they found 14.1 ± 1.1 Bg/kg in the leaves, 7.6 ± 0.8 in stems and 14.3 ± 1.2 in the roots (Skwarzec et al., 2001).

1.6.3. Bioavailability and translocation

The bioavailability of elements is essential to consider when discussing uptake to biota, bioavailability varies when considering different elements and different chemical states. The different chemical states and properties of elements of interest have been detailed in chapter 1 section 1.2.1. Movement of radionuclides or elements within an organism after it has been taken in is referred to as translocation. Within vegetation the main method of translocation is via the xylem and phloem. Translocation can occur following intake through the roots or

following foliar intake after the elements have been transported to the vascular bundles within the leaf (Shahid et al., 2017). The intake of radionuclides through foliar routes is shown schematically in Figure 1.16 below. Distribution and mobility of elements and radionuclides within an organism depends on the chemical properties of the element. For example, Ra and Ba behave similarly as they are both alkaline cations. Both Ra and Ba are more prominent in the stems compared to the other plant structures. The roots and the leaves are generally the structures with the highest concentration of elements, where the stems are primarily for transport (Favas et al., 2016). A study by Favas et al, (2016) analysed the U content in plants from an old U mine. The leaves, stems and roots of different vegetation species were analysed, higher concentrations of U were found in the leaves and roots in comparison to the stems (Favas et al., 2016).

This image has been removed due to copyright restriction.
Available online from [Koranda, J, J. & Robison, W, L. (1978) Accumulation of Radionuclides by Plants as a Monitor System, Environmental Health Perspectives, 27, 165-179]

Figure 1.16. Routes of foliar intake of radionuclides of vegetation (Koranda et al., 1978).

1.6.4. Roots and nutrients in arid Australia

A study by Dawson and Pate (1996), studied Australian native vegetation in arid environments with dimorphic root systems (deep-rooted) and they found that, when drought occurs, the lateral dimorphic roots remain hydrated (Dawson & Pate, 1996). In the arid Australian environment fire is the primary consumer of woody plant tissues which are typically low in nutrients. When fire occurs, nitrogen is lost as it is volatilised, therefore, nitrogen fixation is important, *Acacia spp.* are capable of N_2 fixation in the presence of a symbiotic relationship with rhizobia. The Great Sandy Desert in WA has phosphorous concentrations of < 2 $\mu g\ g^{-1}$ in the soil and <1 mg g^{-1} within some vegetation that have grown in the soil. Zn is another micronutrient for vegetation, this is also low in concentration in the arid Australian environment, Mn can be accumulated to high concentration in the leaves of vegetation, even

when the Mn concentration in the soil is low. Ni concentrations can be high in the arid zone, some vegetation are Ni-hyperaccumulators (He et al., 2018).

1.7. Radionuclide analysis

The analysis of radionuclide activity involves the detection of the energy of the emissions of specific radionuclides. Spectral interferences may occur when the energy of two radionuclides of interest overlap, for example the major gamma emission from ^{235}U occurs at 185.72 keV, this has some spectral interference with the ^{226}Ra radionuclide which has its major energy at 185.99 keV (Gilmore, 2008). When analysing ^{235}U and its decay series, in this decay scheme the ^{235}U is the only isotope that can easily be identified using gamma spectrometry. ^{227}Th, ^{223}Ra and ^{219}Rn can be identified and measured, however this is more difficult. When analysing ^{238}U and the decay series, not all of the radionuclides in the ^{238}U decay series emit gamma emissions, and not all gamma emissions are of high enough intensity to be detectable for identification using gamma spectrometry. The radionuclides that can be identified readily using gamma spectrometry are: ^{234}Th, ^{234m}Pa, ^{226}Ra, ^{214}Pb, ^{214}Bi, and ^{210}Pb. If these radionuclides are in equilibrium the activity of ^{234}Th, ^{234m}Pa, ^{226}Ra will be the same. There will also be the same activity between ^{214}Pb, ^{214}Bi, and ^{210}Pb, these radionuclides will achieve equilibrium faster due to their shorter half-lives (Gilmore, 2008).

A study by Taddei et al. 2001, analysed vegetables and faeces for U and Th isotopes. Initially samples were dissolved and separated using an ion exchange resin, followed by electrodeposition onto stainless steel plates for alpha spectrometry. Alpha spectrometry using an 'Ortec Soloist and 567 A' was then performed. This study used radioactive tracers to determine the % recovery of radionuclides a ^{232}U tracer was used, the % recovery was found between 80 and 97 %, the activity of ^{234}U and ^{238}U was identified in the vegetable and faeces samples. A ^{232}Th tracer was used to determine the recovery, this was found to be between 46 and 72 %, ^{232}Th and ^{228}Th activities were identified from the samples using alpha spectrometry (Taddei et al., 2001).

A study by Casacuberta et al. 2012 analysed U and Th from samples of NORM by using extraction chromatography using new and recycled UTEVA resins. This method is useful for

high activity samples in the magnitude of kBq kg^{-1}. U and Th require separation prior to analysis using alpha spectroscopy due to interfering alpha emissions. Liquid-liquid extraction and ion exchange methods are commonly used for this separation, however the large amount of organic waste that is produced by these techniques. The aim of this study was to find a separation method for radiochemical separation (Casacuberta et al., 2012).

1.7.1. Statistical issues with low activity radiation measurements

Environmental radionuclide activity in Non-Human Biota (NHB) is often very low and is commonly less than the limit of detection. Due to this, many datasets have adopted different ways to include data that is below the limit of detection. A previously used method is the LOD/2 substitution method, when no more than 20% of the values are below the LOD, they are included within the data set. However, this is only recommended when there is minimal impact on the results. Although this approach has previously been used in literature, there is a lack of statistical rationale behind the method (Hirth, 2014). A study by Wood et al. 2010, used data that was <LOD when assessing radionuclide transfer to reptiles. The statistical Kaplan-Meier method was used to calculate the mean and standard deviation. This method is appropriate with datasets that are up to 50% <LOD (Hirth, 2014; Wood et al., 2010). Other studies have used LOD values as absolute values in the calculation processes within ERICA (Wood et al., 2009). A study by Johansen et al. 2010, included values that were <MDA, where this is equivalent to <LOD (Hirth, 2014; Johansen & Twining, 2010). Data on radionuclide transfer to NHB providing CR$_{WO-media}$ values of less than the limit of detection is a wide issue. The review on Australian radionuclide concentration ratios for NHB, from Hirth, 2014 suggests that a more consistent approach to <LOD values be adopted by the radioecology community (Hirth, 2014). A detailed description of MDA and how to calculate the MDA is included below in section 3.2.2. To ensure analytical robustness, data presented within this thesis will be above the MDA unless indicated otherwise.

1.8. Elemental analysis for environmental impact assessments

Elemental data is also useful in determining the effect of mining activities on the environment. Previous studies have implemented elemental data into their environmental assessments. A short communication by Doering and Bollhofer, 2016, used elemental data

for a database used in ERISS these elements included Al, As, Ba, Ca, Cd, Co, Cr, Cu, Fe, Hg, K, Mg, Mn, Na, Ni, P, Pb, Rb, S, Sb, Se, Sr, Th, U, V and Zn. This was for the tropical environment of the Northern Territory in Australia (Doering & Bollhöfer, 2016). A study by Fisher et al. 2013, explored the Ranger U deposit in the Northern Territory, Australia. The study focused on 3D visualization of elemental data of REE mobility at the mine. Geochemical data enables the determination of geochemical architecture of the ore deposit. This was performed by collecting drill hole samples at 20-50 cm intervals. The drill hole samples were sectioned into thin layers, polished and were analysed. The analytical techniques that were used for this study include SEM/EDS mapping, XRF, ICP-MS and ICP-OES. (Fisher et al., 2013).An interlaboratory comparison study by Bürger et al. 2014, looked at the consistency of detection of trace elements in UOCs. Elemental impurity analysis is generally performed using ICP-MS for U materials as it is a multi-element analysis technique. The digestion of the samples was performed using a variety of methods, including hot plate and microwave digestion methods, HNO_3 only, mixtures of HNO_3 and HCl, and mixtures of HNO_3 and HF. For quality control, standard reference materials for each element of interest were used, the interlaboratory study found that the standard deviation of the detected REEs were within 30%, most not exceeding 15%. REEs were able to be identified to parts per trillion (ppt) concentrations. Issues with the analysis of Cl, Br, P, S and Si were identified, however the other 64 elements Ag, Al, As, Au, B, Ba, Be, Bi, Ca, Cd, Ce, Co, Cr, Cs, Cu, Dy, Er, Eu, Fe, Ga, Gd, Ge, Hf, Ho, In, Ir, K, La, Li, Lu, Mg, Mn, Mo, Na, Nb, Nd, Ni, Pb, Pr, Pt, Rb, Re, Rh, Ru, Sb, Sc, Se, Sm, Sn, Sr, Ta, Tb, Te, Th, Ti, Tl, Tm, V, W, Y, Yb, Zn and Zr were successfully identified using ICP-MS (Bürger et al., 2014).Soil is routinely analysed for elemental composition, a study by Melaku et at. (2005), compared different sample digestion methods for trace metal analysis. The Melaku et al. (2005) study determined the concentration of trace elements Cd, Co, Cr, Cu, Mn, Ni, Pb and Zn in samples of agricultural soil by using ICP-MS. The samples were prepared by air-drying and sieved (<63 μm) before digestion using acids. This study found the aqua regia microwave acid digestion (3:1 mixture of 2ml of HNO_3 (15.8 M) and 6 mL HCl (12 M)) to be the most safest and most accurate, this digestion provided an elemental analysis of between 91-110 % and 5% in most cases (Melaku et al., 2005). It has been shown that elemental data is important for environmental studies and UOC analysis. All three previously discussed studies have all implemented ICP-MS for elemental quantification.

41

1.9. Radiography, nuclear emulsions and alpha track analysis

Nuclear emulsions for particle physics applications were initially developed in the 1940s. Alpha track analysis uses nuclear emulsions; these emulsions are composed of silver halide, mostly AgBr crystals suspended in gelatine. The size of the silver halide crystals suspended throughout the gelatine will determine the sensitivity of the gel. Where the larger the crystals, the more sensitive to ionising radiation. Low sensitivity nuclear emulsions are often used for high energy radioactive particle detection as there is plenty of energy available from the ionizing radiation present to enable electron liberation from the electron deficient bromine atoms within the crystal. As high energy ionizing radiation particles move more quickly throughout a media a more sensitive emulsion may be required to visualize their effect as they deposit small amounts of energy within the silver halide crystals. This is the reason a more sensitive emulsion is required for high energy ionizing radiation. The theory behind this technique is fundamentally the same as the theory behind conventional silver halide photography. The silver halide crystals are very uniform in size, there is a higher amount of silver halide crystal to gelatine ratio and there is lower false positives (reduced chemical fog) compared to photography gels (Ilford, 2010).

Kinoshita, 1910 was the first study to use silver halide alpha track analysis and microscopy to identify radiation (Kinoshita, 1910). Since then, it has had many applications to mineral and biological samples. Kalnins 2019, used alpha-particle radiography to determine the spatial locations of alpha emitting radionuclides within mineral samples (Kalnins et al., 2019). A study by Zarubin (2016), used nuclear track emulsions to resolve low energy emissions, this research concluded that the technique is cumbersome with limited statistics. However, with the use of automated microscopes this technique becomes more viable (Zarubin, 2016).

A study by Katz and Pinkerton 1975 studied the response of nuclear emissions to ionising radiation, Ilford emulsions were used within this study (Katz & Pinkerton, 1975). A study by Noto et al. 2014, used alpha track analysis using nuclear emulsions to develop a method for environmental analysis for nuclear safeguards (Noto et al., 2014).

1.9.1. Alpha decay and alpha penetration energy

An alpha particle is composed of two neutrons and two protons, therefore is a doubly charged He nucleus. Alpha particles have high amounts of energy, due to this they can travel through, and cause damage to surrounding media. When considering alpha decay on a two-dimensional media need to understand the penetrating power of the radiation along with the absorption coefficients of the sample. We can use 'The infinite matrix assumption', where the sample counted is required to have a volume greater range than the penetrating power of the radiation in the sample, this assumes the rate of energy absorption and energy emission is equal (Figure 1.17). If we assume the sample is homogenous in both its radioactivity and absorption coefficients we can say that the absorption energy per unit mass and emission energy per unit mass are equal (Aitken, 1985).

This image has been removed due to copyright restriction. Available online from [Aitken, M. J. (1985). Thermoluminescence Dating: Academic Press]

Figure 1.17. Schematic of alpha particle emissions from a sample and the ideal sample thickness for alpha counting. R is the range the alpha particle will travel through the media. (Aitken, 1985)

When considering traditional alpha counting, for an alpha emission to be counted it must reach the zinc sulphide screen and produce a scintillation. When the particles are close to the screen, they reach a point where nearly half of the alpha emissions will cause a scintillation. However, for nuclei that are further away from the screen the proportion is reduced. And if the nuclei are a greater distance than R (range) no alpha particles will reach the screen. On average a quarter of alpha particles that are emitted from nuclei in the range will reach the screen, or the alpha track emulsion to form an image. The average range is 25 μm for the U and Th series for samples with a density of 2.6 g/cm^3. However, the alpha emitter with the highest energy, the value is twelve times this. A standard zinc sulphide screen is 42 mm in diameter, for this example the range layer contains about 0.2 g. It is recommended to use about 1 g of sample on the screen for even spreading over the screen. This same theory can be applied to alpha track analysis discussed below. A schematic of an alpha particle emission and the range that it may reach on a detector is shown below in Figure 1.18.
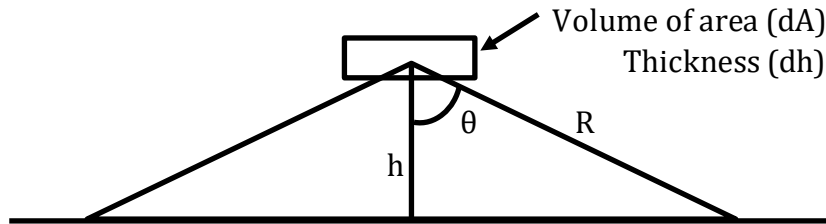
Figure 1.18. Thick sample alpha counting using a scintillation screen, R is the maximum range an alpha particle can travel, h is the height from the sample to the detection media and θ is the angle between R and h.

When a sample is placed onto the media, the thickness of the sample is required to be thicker than the penetration energy of the alpha radiation emitted from the sample. If we assume all alpha emissions are of equal energy to the alpha radiation emitted from the sample, a quarter will be within the range. Where the range is the area that the alpha emissions will reach the zinc sulphide screen as the alpha emissions are emitted isotopically. Therefore if c_α is the number of alpha particles emitted per unit mass in unit time, the count rate will follow Equation 1.11 (Aitken, 1985).

$$\dot{\alpha} = \frac{1}{4} AR\rho c_\alpha$$

Equation 1.11. Where: ρ is the sample density, A is the area of the zinc sulphide screen, where the range R is much smaller than the screen. Where $\dot{\alpha}$ is the count rate (per ksec). The count rate is proportional the emission rate from the sample and the R.

Where the higher energy of the alpha particle emission *(E)* from the nucleus gives a greater *R*. This is not linear, however the count rate from a higher energy emitter will be larger than the count rate from a lower energy emitter of the same activity. The alpha dose-rate is proportional to the product *(Ec$_\alpha$)*. Due to this the dependence on E for the conversion from count rate to dose rate is weakened. Therefore, the conversion factor is almost the same between the alpha emitting radionuclides from the U and Th decay series. The following Equation 1.12 is used when we have a sample that has radionuclides from a decay series containing *n* alpha emitters, this requires the assumption of equilibrium.

$$\dot{\alpha} = \frac{1}{4} A(R_1 + R_2 + R_3 + \dots)\rho c$$
$$\dot{\alpha} = \frac{1}{4} A\bar{R}\rho nc$$

Equation 1.12. Where c is the activity per unit mass of the parent and R1, R2 ... etc represent the ranges of the alpha particle emissions from the individual members of the series and $\bar{R}$ is the average range.

The individual and average alpha ranges are in the literature. The values of *Rρ* above are used as the average and the number of alpha emitting members in the decay series. When we substitute into the above equation, we get the Equation 1.13.

44

$$\dot{\alpha} = \frac{1}{4} A\{(70 * 6 * c_h) + (58 * 8 * c_u)\} * 10^{-6}$$

*Equation 1.13. Where c*h *and c*u *are the specific activities (Bq/k) for the Th and U series respectively. A in mm^2 and α is in counts per kilo second (ksec).*

1.10. Phase analysis of Australian uranium ore concentrates determined by variable temperature synchrotron powder X-Ray diffraction

The formation and transformation of U oxides are of considerable technological and scientific interest reflecting the role of U in the nuclear fuel cycle. There is the additional complication of radioactive materials being diverted for nefarious purposes (Mayer et al., 2013; Pastoor et al., 2021). U ore concentrate (UOC) is the feedstock for the nuclear fuel cycle and its production is dominated by a relatively small number of countries, notably Canada, Namibia, Australia, and Kazakhstan. Conventionally, the term yellow cake has been used to describe UOC regardless of its origin and colour, yet each facility produces UOC with unique characteristics, including phase composition, chemical, and isotopic distributions that can be used to identify its provenance (Edwards & Oliver, 2000; Mayer et al., 2013; Z. Varga et al., 2011). To investigate illicitly trafficked nuclear materials or nuclear materials found outside of regulatory control, it is crucial to identify the origin of the materials, and a range of characterization methods including chemical and structural analysis have been employed. In a recent X-ray diffraction study of 15 UOC samples, Su et al. found 11 different crystalline phases, with the majority of samples studied containing two or more crystalline phases (Su et al., 2018; Tamasi et al., 2015; Tamasi et al., 2017; Wilkerson et al., 2020). It has been documented that chemical speciation of U oxides can change with age, and is sensitive to the temperature and relative humidity during storage (Tamasi et al., 2015; Wilkerson et al., 2020). Structural analysis may be valuable for characterizing material provenance and may provide insights into its storage over time.

The anthropogenic corrosion of U oxide compounds is well known and can lead to a complex mixture of hydrated U oxides (Finch & Ewing, 1992; Wronkiewicz et al., 1996). For example, Sweet et al. reported that UO_3 is unstable when exposed to moisture and will transform into

$UO_2(OH)_2$, and that when this is heated to above 450 °C it dehydrates to γ-UO_3 (Sweet et al., 2011;Weck & Kim, 2014). Many of the hydrated U materials formed are related to the schoepite group with the general formula of $UO_3 \cdot 2H_2O$. Wilkerson et al. recently showed that the crystalline α-UO_3 material converted to schoepite upon storage (Wilkerson et al., 2020). Similarly, Hanson et al. observed the conversion of amorphous UO_3 to schoepite on storage, a process that was sensitive to ageing time, temperature, and relative humidity (Hanson et al., 2021). The storage of U oxides impacts their surface morphology and methods to link surface morphology to the processing history and storage have been reported (Hanson et al., 2019; Nizinski et al., 2020). The oxidation and hydration of U_3O_8 can lead to the formation of schoepite phases, thus with time and exposure to moisture, the phase assemblage of a UOC will evolve (Brugger et al., 2011; Tamasi et al., 2015). Schoepite is assumed to easily transition to meta-schoepite under ambient conditions and it has also been shown that metaschoepite can form on the surface of U_3O_8 when exposed to air and moisture (Oerter et al., 2020).

1.11. Research scope

In order to increase the understanding of uranium and naturally occurring radioactive materials (NORM) in a radioecology and nuclear forensic context for Australia, this research branches in two directions. The two topics this thesis explores is radiological environmental impact assessments for the arid Australian environment and UOC phase analysis for nuclear forensic applications.

Current environmental impact assessment methods lack sufficient Australian concentration ratio data for confident radionuclide assessments. This research will increase the data for Australian specific species. Therefore, increasing the confidence in understanding the impact of NORM and ionizing radiation on vegetation. This research will increase the understanding of how radionuclides behave within the arid Australian environment in terms of uptake within vegetation and permeation throughout surface soil from deposition. Chapter 3 of this thesis will describe and analyse the radionuclide activity concentrations from the soil and the flora. The environmental radioactivity focus of this research is solely on the sites located within the arid Australian environment, Olympic Dam and Beverley. Chapter 4 will use the data

described in Chapter 3, however, concentration ratios are calculated and described. This thesis will explore the usefulness of CRs for dose assessment predictions for vegetation when very low activity radionuclides are present within samples. The skew that low activity concentrations, close to the limit of quantification will be explored. This can impact on the concentration ratio calculations and effect the scale of the CR data.

Chapter five determines the broad elemental profile of arid Australian soils and the elemental and nutrient availability to Australian native vegetation. A comparison of NAA and ICP-MS methodologies for soil analysis was performed due to the complexity of the soil matrix and the low elemental concentration. NAA was also used to determine the elemental profile of soils and vegetation across a broad range of elements. These data will provide information regarding the uptake of elements and plant nutrients for Australian native species within the arid Australian Environment. Also, to determine whether the elemental data provides information regarding increased mechanical disturbance in the arid Australian environment.

Chapter 6 aims to explore stratified soil analysis by attempting to visualize the effect of the surface contamination within the soils from operational sites within Olympic Dam. This chapter aims to provide some insight as to the mechanisms of intake of radionuclides into vegetation in the arid Australian environment. This chapter also aims to spatially resolve the locations of radionuclide accumulation within the physiological structures of leaves. The focus species for this study are the Australian Native species *Dodonaea viscosa* and *Acacia ligulata* sampled from Olympic Dam. Overall, this chapter aimed to increase the understanding of the uptake mechanisms of radionuclides within Australian native vegetation species within an arid environment. This chapter explored whether the radionuclide distribution and accumulation can assist in understanding radionuclides. This chapter also aimed to identify the most likely transport and uptake mechanisms for radionuclides in plants.

Chapter 7 of this thesis will examine three UOCs from three different U mines from Australia. The UOCs will be analysed using synchrotron-XRD to determine the different phases of U species within each of the UOCs. This will be performed in an endeavour to define the individual characteristics of each UOC for nuclear forensic applications. This research will also determine crystal structure phase transformations through heating each of the samples.

Chapter 2. Environmental sample collection

2.1. Sample sites

The environment at the Olympic Dam region sample sites had sand dunes and sparse shrubs with minimal to no grasses. The soil is soft and sandy matrix with minimal rocks and plant matter. Samples of vegetation and soil were collected from the Flinders Ranges and Olympic Dam regions, both sites are within arid South Australia. The two regions are highlighted in Figure 1.4. The sample collection was bound to the established environmental monitoring sites for Olympic Dam and the Flinders Ranges regions by BHP and Heathgate respectively. The species of vegetation were limited to the availability and abundance within each environmental monitoring site.

2.1.1. Olympic Dam

The sample collection sites are detailed below for the Olympic Dam region, they are shown in Figure 2.1. Soil and vegetation samples were collected from each site within a 50-meter diameter. The species of vegetation collected are detailed in Chapter 2, section 2.1 and 2.2. The Olympic Dam sample sites were chosen as they were established BHP environmental monitoring sites. The variation of site locations provides a longitudinal variability across the mining site and the control sites, the sites are shown in Figure 2.1. The type of soil sampled at all Olympic Dam sites was from dunes, as this was where the vegetation was located. The north and south control sites were chosen to be control sites for the study as they are outside of the mining lease area. The arid site is located at the north mining lease boundary, the arid site is located within 'Arid Recovery' which is a wildlife sanctuary for Australian native vegetation and fauna (Recovery, 2019). The raise bore site is located within the mining operations; the raise bore is the underground mining ventilation. The pilot site is located to the southern side of the mining operations, within the lease. The pilot plant was an operational ore processing facility. The tailings site is located in the vicinity of the tailings dam within the mining operations. The Roxby Downs site is located near the Roxby Downs township.

Figure 2.1. Olympic Dam environmental monitoring site locations (Billiton, 2016), 1 is north control - 30.308508, 136.946221, 2 is arid recovery -30.385465, 136.873317, 3 is raise bore -30.444541, 136.882792, 4 is pilot plant -30.458479, 136.869588, 5 is tailings -30.446362, 136.845252, 6 is Roxby Downs -30.585122, 136.882372 and 7 is south control site -30.671103, 136.879758. The pink dots represent established environmental monitoring sites, the text next to them is the site code as used by BHP. (State figure, indication only, not to scale).

Vegetation diversity and abundance

BHP monitor the vegetation in the vicinity of the Olympic Dam mine, the annual BHP vegetation monitoring program is set up to monitor and assess any potential impacts that the mining activities may have on vegetation (Billiton, 2016). Native vegetation within South Australia is protected under the 'Native Vegetation Act 1991' (Billiton, 2016; Government, 1991). The dominant species of vegetation at Olympic Dam and the environment in the vicinity to the mine is 'Sandhill Wattle' (*Acacia ligulata*) and 'Hopbush' (*Dodonaea viscosa)*. The 'Barley Mitchell-grass' (*Astrebla pectinata)* is also present in the region, these species are shown in Figure 2.2. A study by Griffin and Dunlop (2012) found and suggested that both the

Dodonaea viscosa and *Acacia ligulata* species are appropriate for use as indicator species for atmospheric pollution.
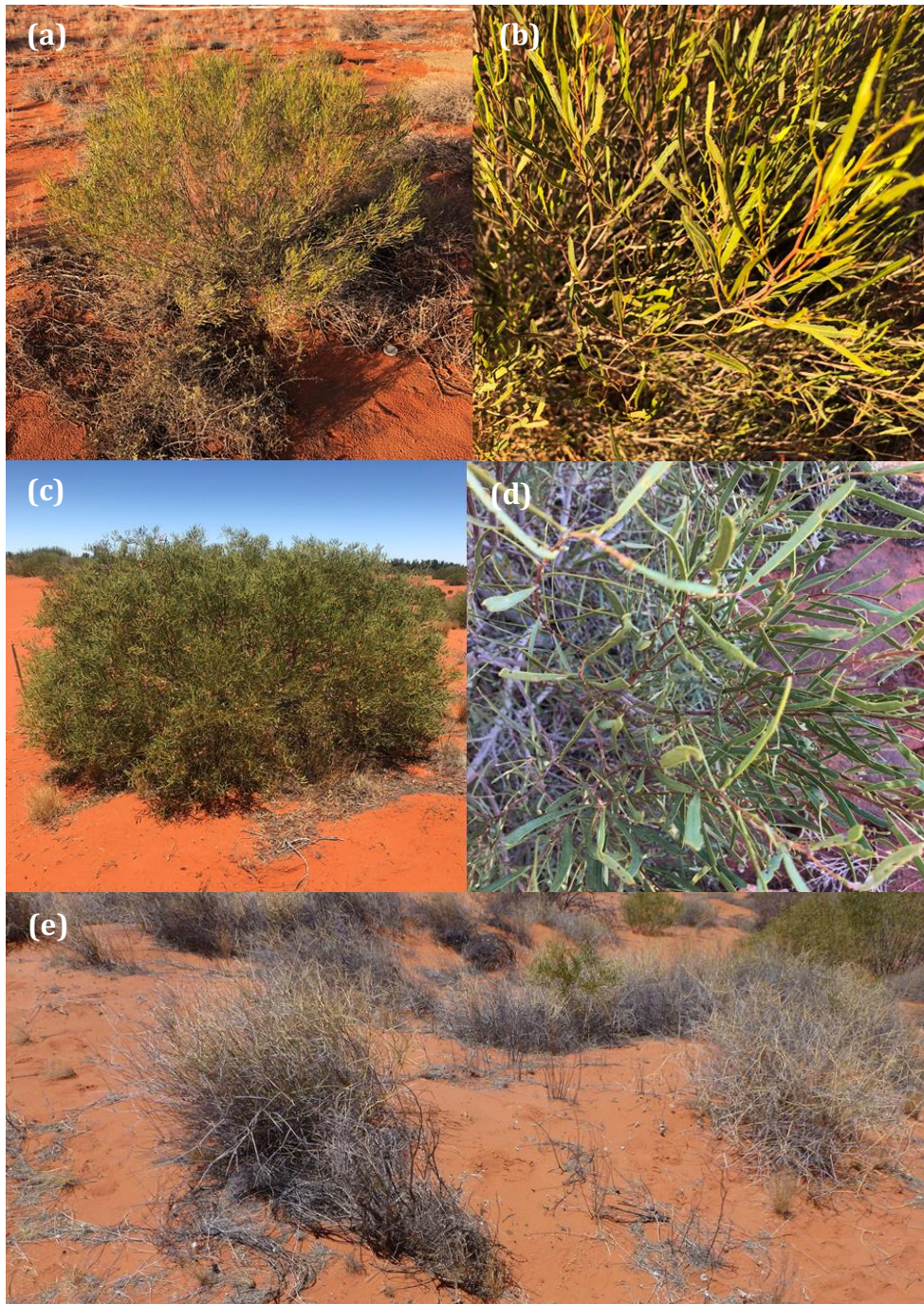
Figure 2.2. Olympic Dam species of vegetation. (a,b) Dodonaea viscosa, (c,d) Acacia ligulata and (e) Astrebla pectinata.

2.1.2. Flinders Ranges region sample sites

At the Flinders Ranges region sample collection sites, most of the ground is relatively flat and firm. The soil surface material is varied across sites, there is large boulders, gravel, silt, clays, small rocks and a large amount of dried *Astrebla pectinata*. The rainfall in the region is sparse and less than 70 mm annual rainfall has occurred in the last few years (Rea et al., 2021). Samples collected from the Flinders Ranges region were chosen as they were established environmental monitoring sites. The site coordinates are detailed in Table 2.1 below. Soil and vegetation samples were collected from each site within a 50-meter diameter. Site 3 overall had a low species abundance compared to other sites. Site 1 had no *Astrebla pectinata* however, this site had many *Acacia victoriae*. Site 2 had lower abundance of *Astrebla pectinata*.

Table 2.1. Flinders Ranges region sample site locations.

Sample Site	Site Coordinates
Site 1	S30° 15.958, E139° 33.785
Site 2	S30° 08.973, E 139° 30.169
Site 3	S30° 08.391, E 139° 31.364

Vegetation, diversity and abundance

Native vegetation observed within Lake Frome includes two distinctive groups of vegetation. When there is higher rainfall semi-succulent shrubs including *Nitraria shoberi* are present 'bladder saltbush' (*Atriplex vesicara*) and 'blue bush' (*Kochia sedifolia*) are often present in summers with a high rainfall. *Kochia astrotricha* and *Atriplex rhagodioides* are the most dominant shrubs. The other main plant community is the grasses. The 'cane grass', *Zygochloa paradoxa*, 'spinifex or porcupine grass', *Triodia basedowii* and 'Mitchell grass', *Astrebla pectinata* (Singh & Luly, 1991). The three vegetation species analysed from the Flinders Ranges region are shown below in Figure 2.3.
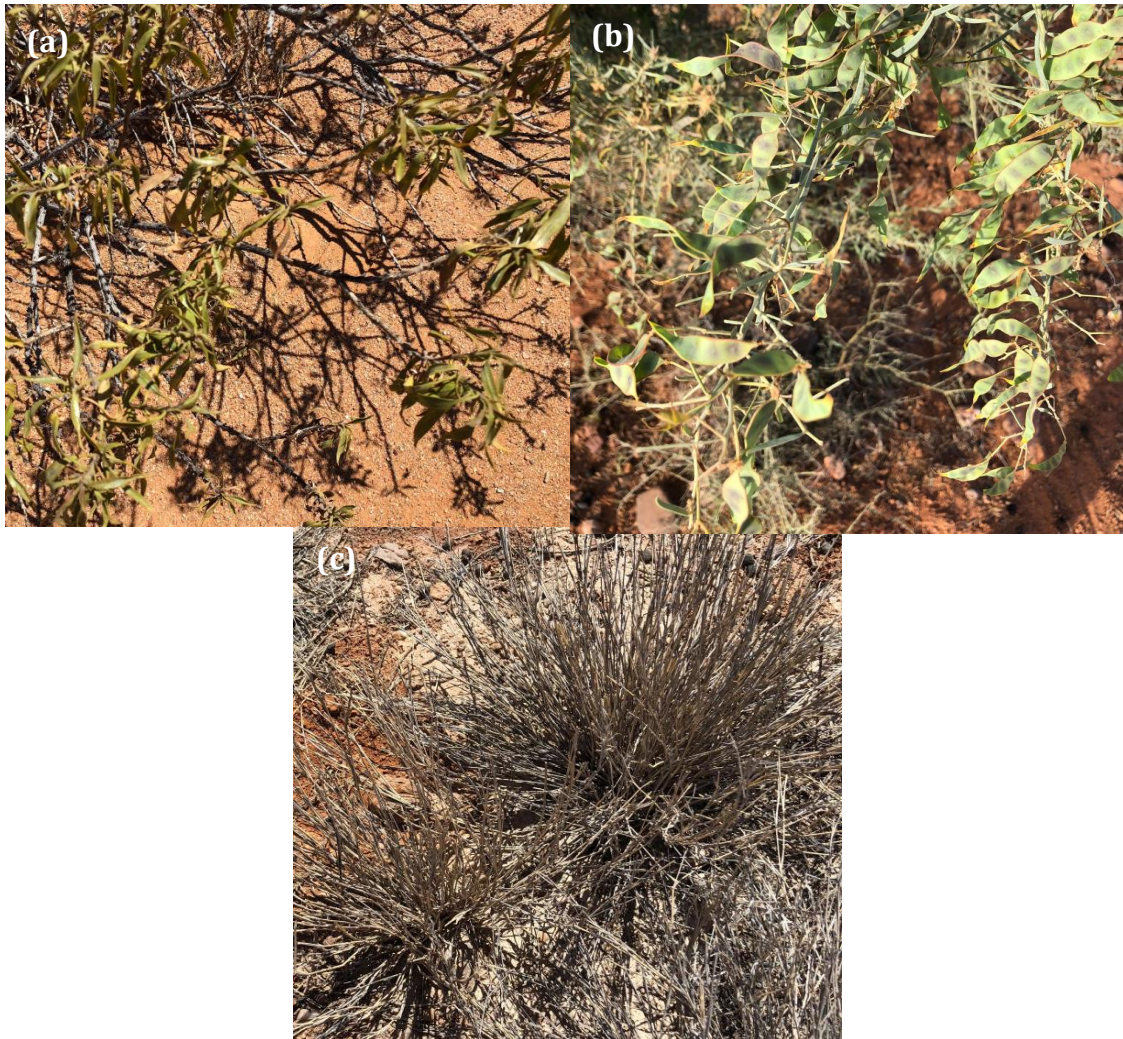
Figure 2.3. (a) Eremophila freelingii (Native Fuschia Bush), (b) Acacia victoriae (Elegant wattle, Prickly Acacia) (c) Astrebla pectinata (Barely Mitchell Grass).

Figure 2.5. shows the dominant vegetation species at the Flinders Ranges region. The three most dominant species at the Flinders Ranges sample sites were 'Barley Mitchell Grass' (*Astrebla pectinata*), 'Elegant Wattle or the Prickly Acacia' (*Acacia victoroae*) and the 'Native Fuschia Bush' (*Eremophilia freelingii*), these species were sampled for analysis, the details are below in Section 2.2.

2.2. Sample collection

Samples of soil and vegetation were collected from the sites identified in Tables 2.2 and 2.3. At each environmental sampling location, vegetation and soil samples were collected as pairs. For each vegetation sample collected a corresponding soil sample was taken within one meter from the trunk of the plant. The samples that have been collected were limited to the amount

of plants that had grown within the designated environmental sampling site, therefore, on some occasions different numbers of samples across sites are collected.

2.2.1. Soil collection

Soil samples were collected within a 50 m radius at each site. Composite samples taken from 0-10 cm depth were collected using core sampling with a PVC pipe of 100 mm length x 50 mm diameter that was pushed into the soil. Individual samples were then stored in a plastic BPA free polyethylene zip lock bag container and stored at room temperature and in the dark until analysis (Johansen et al., 2014; Medley et al., 2017).
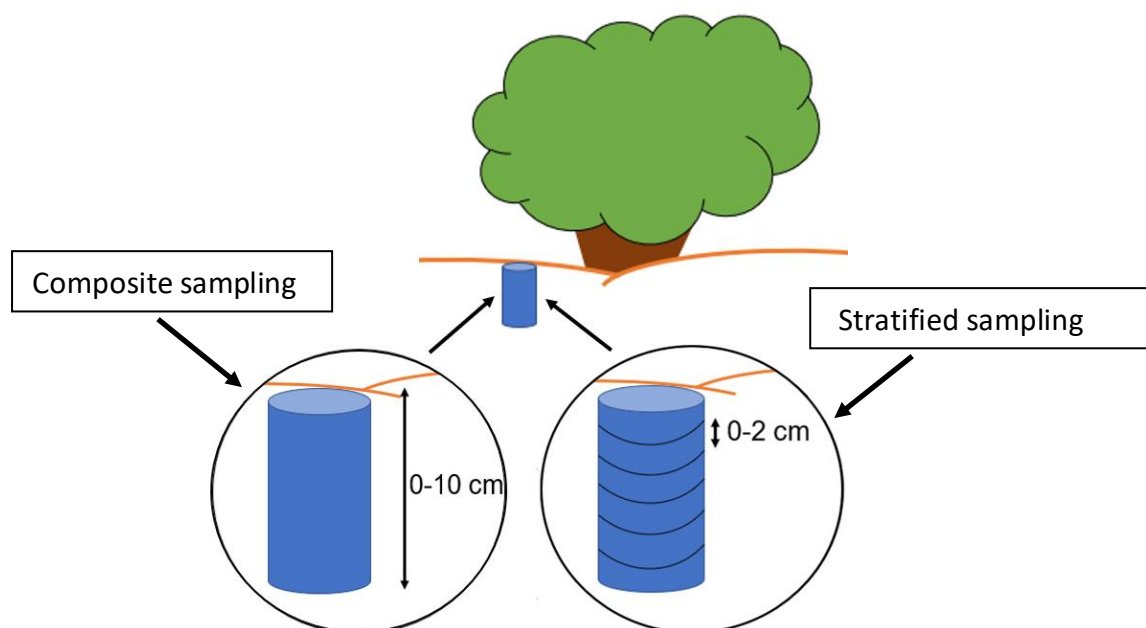
Figure 2.4. Soil sampling schematic, (left) 0-10 cm is concentration Ratio (CR) sampling, (right) 0-2 cm is stratified sampling.

Soil samples were collected using two different methods (Figure 2.4). The method shown on the left is the method that is used to collect a representative composite soil sample from 0-10 cm in depth. Samples collected using this method were used in conjunction with vegetation samples to determine concentration ratios. The method shown on the right was used to collect soil in 2 cm intervals from the surface soil to at least 10 cm depth. Samples collected using this method were used to determine any effect on surface deposition by collecting stratified samples of 0-2 cm, 2-4 cm, 4-6 cm, 6-8 cm, 8-10 cm and in some cases 10-15 cm. Tables 2.2, 2.3 and 2.4 describe the soil samples collected.

Table 2.2. Composite Soil Sample collection from Olympic Dam, Number of 0-10 cm composite samples from two different sampling times.

Site	May 2018		Dec 2018		
Associated Vegetation Species	*Acacia ligulata*	*Dodonaea viscosa*	*Acacia ligulata*	*Dodonaea viscosa*	*Astrebla pectinata*
North Control	3	0*	3	3	0
Arid Recovery	3	3	3	3	0
Raise Bore	4	4	3	3	0
Pilot Plant	3	3	3	3	0
Tailings	0	0*	3	0*	3
Roxby Downs	3	3	3	3	0
South Control	3	3	3	2	2

Table 2.3. Stratified Soil Sample collection from Olympic Dam of depth profile samples from two different sampling times depth samples of 0-2, 2-4, 4-6, 6-8, 8-10 and 10-15 cm.

Site	May 2018		Dec 2018	
Associated Vegetation Species	*Acacia ligulata*	*Dodonaea viscosa*	*Acacia ligulata*	*Dodonaea viscosa*
North Control	1^	0*	3	3
Arid Recovery	1	1	3	3
Raise Bore	1	1	3	3
Pilot Plant	1	1	3	3
Tailings	0	0	3	3
Roxby Downs	1	1	3	3
South Control	1	1	3	3

^2-5 cm and 5-8 cm, instead of 2-4 cm, 4-6 cm, 6-8 cm.

Table 2.4. Composite Soil Sample collection from the Flinders Ranges region of 0-10 cm composite samples, all samples collected in December 2018.

Site	Total Number of Samples Analysed
1	2
2	5
3	3

* There were not plants of this species at the sampling site.

2.2.2. Collection of vegetation

The details regarding the vegetation species selected have been discussed above. The species collected from Olympic Dam were *Acacia ligulata*, *Dodonaea viscosa* and *Astrebla pectinata*. The species collected from the Flinders Ranges region were *Astrebla pectinata*, *Acacia victoriae and Eremophila freelingii*. Vegetation samples were collected by trimming branches using secateurs, branches were collected to approximately 30 cm inwards from the end of the branches. The branch clippings were collected from different directions around each individual plant and were stored in paper bags. The radionuclide distribution within vegetation was assumed to be uniform throughout the plant (Beresford et al., 2008). Therefore, the stems, branches and leaves were not separated, and the samples were treated as a bulk sample, each individual plant that was sampled from was analysed separately unless otherwise stated. The vegetation samples were weighed as close in time as possible to the sample collection to minimise moisture loss, however, the exact amount of moisture loss from collection to weighing is a known limitation of this study. The samples of vegetation collected from the Olympic Dam region and the Flinders ranges regions are summarised in Tables 2.5 and 2.6 respectively.

Table 2.5. Number of samples of Acacia ligulata plants sampled from Olympic Dam during the two different sampling times.

Site	May 2018		Dec 2018		
	Acacia ligulata	*Dodonaea viscosa*	*Acacia ligulata*	*Dodonaea viscosa*	*Astrebla pectinata*
North Control	3	0*	3	3	0
Arid Recovery	3	3	3	3	0
Raise Bore	4	4	3	3	0
Pilot Plant	3	3	3	3	0
Tailings	0*	0*	3	3	14
Roxby Downs	3	3	3	3	0
South Control	3	3	3	3	8
Total	19	16	21	21	22

* There were not plants of this species at the sampling site.

Table 2.6. Flinders Ranges region species vegetation sample collection, all samples collected in December 2018.

Site	Associated Species of Vegetation		
	Astrebla pectinata	*Eremophila freelingii*	*Acacia victoriae*
1	1	N/A	2
2	1	3	N/A
3	1	3	N/A
Total	3	6	2

2.3. Sample preparation

This section describes the general sample preparation processes used throughout the research. Where changes have been made for specific analysis, this will be discussed in the specific chapter.

2.3.1. Soil sample preparation

Following sample collection, samples were subsequently air dried, then homogenized by mechanical stirring and sieved (1mm) to remove leaves and large particulate matter, this is the standard method for concentration ratio analysis (Shishkina et al., 2106). Further soil sample preparations will be discussed with the associated analytical methodology.

2.3.2. Vegetation sample preparation

Following the vegetation sample collection, plant samples were washed with distilled water and air dried and then freeze dried using a The Christ Beta 2-8 LD freeze dryer at -95 °C. The samples were freeze dried by first snap freezing the vegetation with liquid nitrogen, and then placed into the freeze dryer for at least 12 hours to ensure total dryness. Once the vegetation was dry the sample was ground to a fine powder using a spice grinder (Breville no. BCG200BSS) (Medley et al., 2017). Further vegetation sample preparations will be discussed with the associated analytical methodology.

2.3.3. Drying factors

The vegetation samples of *Acacia ligulata* and *Dodonaea viscosa* collected from the Olympic Dam Spring 2018 sample collection trip. The samples were collected and initially weighed to collect the fresh weight data. The samples were then air dried and re weighed to determine the wet to dry mass conversion. After the samples had been air dried the samples were freeze dried and re weighed to determine the wet to freeze dried mass conversion. The results from the experimentally determined wet to dry mass conversion is in appendix C.

Chapter 3. Bulk radionuclide transfer from soil to vegetation within the arid Australian environment

The data which are derived and discussed in detail in this chapter were the author's collaborative contribution to the paper titled "Radionuclides and stable elements in vegetation in Australian arid environments: Concentration ratios and seasonal variation" by M. A. D. Rea *et al*. that has been published in the *Journal of Environmental Radioactivity*. These data were obtained using the methodology discussed in the preceding chapters.

3.1. Introduction

This present research explored the transfer of radionuclides from soil to vegetation within the arid Australian environment. Two regions within the arid South Australian environment, Olympic Dam and the Flinders Ranges region were chosen for analysis. The two locations have been chosen as they have vastly different geological settings, this is detailed in Chapter 1 Section 1.3.2 and 1.3.3. Soil and vegetation samples from the two sites were collected to research the transfer of radionuclides within the environment. The transfer routes of radionuclides and elements within the environment from a source term to organism uptake and physical decay is shown in Figure 3.1.

This image has been removed due to copyright restriction. Available online from [Strans. P., Copplestone. D., Godoy. J., Jianguo. L., Saxen. R., Yankovich. T., Brown. J. (2009). Environmental Protection: Transfer Parameters for Reference Animals and Plants]

Figure 3.1. Radionuclide transport within the environment through biological and environmental processes (Strans, 2009).

Figure 3.1 shows the different pathways of radionuclide transfer within the environment, this chapter details the pathway from soil and sediment to plants. Radionuclides of interest in this research are the NORM radionuclides including ^{238}U, ^{230}Th, ^{226}Ra, ^{210}Pb and ^{210}Po. Analytical methods including alpha spectroscopy and gamma spectroscopy were used within this chapter. This chapter will describe results obtained with the methods of bulk analytical techniques to determine whole organism radionuclide activity to determine transfer from

soil. Soil analysis will use the internationally accepted method of CR determination and using 0-10 cm depth for soil collection (Beresford et al., 2008; Brown et al., 2008).

3.1.1. Chapter directions

Within this chapter, radionuclide transfer from soil to vegetation and from two distinctly different environments within the arid zone of South Australia are examined. During this research the radionuclide activity concentrations of soil and vegetation were determined, sample site and species comparisons were made to determine further information regarding the range of radionuclide concentrations. The variation of radionuclide concentrations within the same species collected from the same sample site was observed. A brief comparison of seasonality was performed for the two major shrub species from the Olympic Dam region. An overall comparison of the Olympic Dam and Flinders Ranges regions were performed due their different geological settings.

3.2. Experimental

All experimental methods used in this chapter have been detailed in below, refer to Chapter 2 for details regarding sample collection and preparation. Where the number of samples is referred to as 'n' this represents the number of individually collected samples analysed. Wet mass was used for all reference to vegetation within this chapter.

3.2.1. Experimental specific sample preparation

Alpha spectroscopy sample preparation

Vegetation samples had been prepared by freeze drying and grinding, soil samples had been sieved to 500 μm^2. Sample digestion is required before the solution is passed through the EICHROM columns that separate out the radionuclides of interest. However, prior to digestion tracers are added quantitatively to determine the recovery of the analysis.

Alpha spectroscopy was performed at two different locations and methods due to access of instrumentation at either the ANSTO or ARPANSA laboratories. The soil and vegetation

samples that were collected from Olympic Dam Mine during May 2018 were analysed at ANSTO laboratories; all of these samples were composited equally by mass. All of these samples were analysed for U and Th, separately from Po and Ra, both processes are described below. Where 10 g of sample for both soil and freeze dried vegetation were used for the U and Th analysis and 2 g of the samples were used for the Po and Ra analysis. All samples were weighed into 500 mL beakers, tracers were added. The EICHROM columns used for the composite samples were TRU and TEVA. Figure 3.2 below shows the resin setup.

The samples that were analysed in the ARPANSA laboratories were collected from Olympic Dam Mine during November 2018. All of these samples were analysed as individual soil and vegetation samples. The samples analysed at ARPANSA were analysed for Po and Ra as a separate batch to allow for lower temperatures of heating. However, the Ra and Po were also analysed from the samples that go through the columns for the U and Th analysis. 5 g of samples were weighed for Po and Ra analysis and 10 g was weighed for U, Th Ra and Po analysis. The EICHROM columns used for the radiochemical separations of each sample were the, TRU, TEVA or U/TEVA columns.
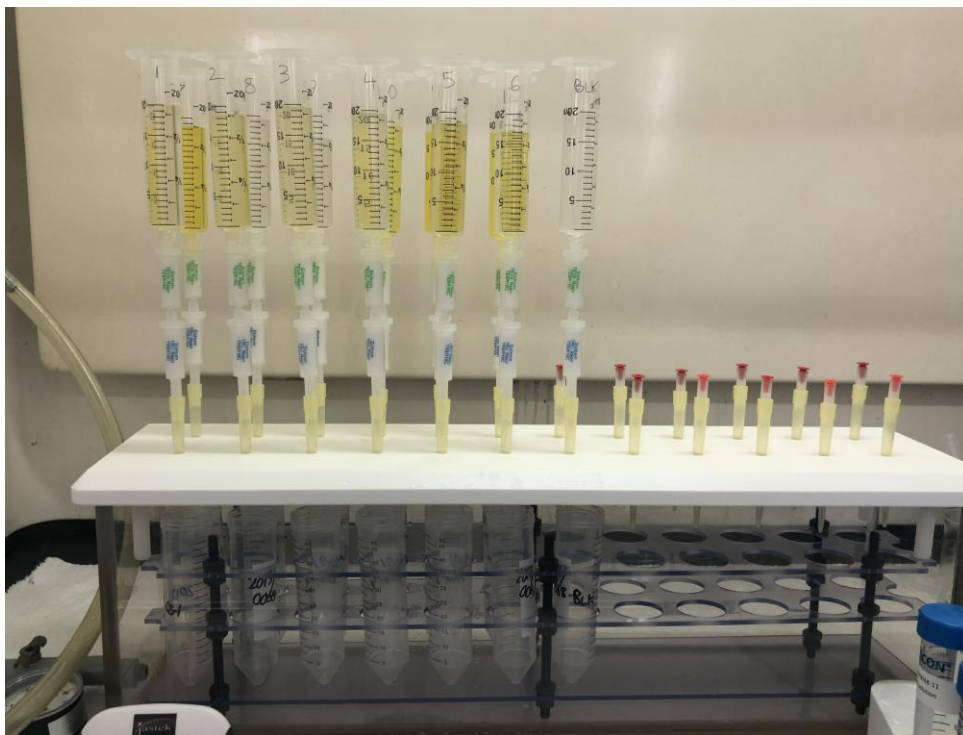
Figure 3.2. Vacuum box setup for alpha spectroscopy preparation using EICHROM TEVA and TRU columns.

The load solution, which is 10 mL at 3 M HNO_3, was added to the EICHROM columns to bind the U and Th. The U and Th were then eluted individually, and the micro precipitate was collected onto filters for counting.

Fe Precipitation Process (Vegetation)

The supernatant from the digestion steps was collected and 10 mg (1000 mg/L) Fe (Fe metal in HNO_3) was added to digests, concentrated ammonia solution was added as the sample was continuously stirred until the sample solution reached a pH of between 8 and 9. When the pH was between 8 and 9 a dark orange precipitate formed within the solution containing the soil samples. The Fe precipitate FeO(OH) that forms contains the radionuclides from the sample. The samples were left overnight to complete the precipitation process. The solution was colourless after the complete precipitation process; the precipitate was dark orange in colour. Digestion of vegetation samples and subsequent precipitation of the radionuclide species of interest was problematic and often required several cycles of re-digestion under different conditions before a satisfactory Fe co-precipitation of the alpha emitters was formed.

Gamma spectroscopy sample preparation

Sample preparation for gamma spectroscopy analysis follows the general soil and vegetation sample preparation methods detailed in section 2.3. However, prior to analysis via the SAGe well detector the samples were packed tightly into a 6 mL vial to a height level to the top of the detector. The remaining headspace was filled with glue from a hot glue gun to avoid radon emanation into the headspace of the vial. For the gamma spectroscopy analysis using the planar detector, the same sample preparation was performed however the samples were packed tightly into 65 mm petri dishes and silicon was used to seal the samples. Prior to analysis these samples were kept for equilibration for at least 38 days.

3.2.2. Radionuclide analysis

Radioactive elements decay via alpha (α), beta (β) or gamma (γ) emissions at specific energies. The specific decay energy can be used to identify specific radionuclides using analytical techniques such as alpha-particle spectroscopy and gamma-ray spectroscopy. This type of analysis works by measuring the energy emitted when the parent isotope undergoes

radioactive decay. The energy of gamma and X-rays varies from 1 to 3000 keV, whereas the energy of alpha particles ranges from 3 to 8 MeV (Murphy, 2005). Traditionally, radionuclide analysis is undertaken using Gamma-Ray Spectroscopy and Alpha spectroscopy as the methods quantify different radionuclides within NORM and are complementary. The details of both gamma spectroscopy and alpha spectroscopy are outlined below.

Alpha spectroscopy

Alpha spectroscopy is a radioanalytical technique that identifies alpha emitting radionuclides and quantifies the activity within a sample (Cadieux et al., 2015). Alpha spectroscopy is appropriate for the analysis of NORM materials as alpha emissions are associated with U and daughter radionuclides. Table 3.1 shows the main radionuclides and the energy of the associated alpha emission that were used for this analysis (Brookhaven). Alpha spectroscopy requires digestion and chemical separation prior to analysis. Tandem column extraction using EICHROM resins were used to isolate U and Th from the sample matrix. The radionuclides were then filtered onto a disk and placed into the vacuum chamber of the alpha spectrometer. Po is deposited onto a silver disk prior to counting (Horwitz et al., 1995).

Table 3.1. Primary alpha emissions and intensity of U and Th chain radionuclides (Brookhaven).

	^{232}Th Nuclide	Energy (MeV)	Intensity (%)	^{238}U Nuclide	Energy (MeV)	Intensity (%)	^{235}U Nuclide	Energy (MeV)	Intensity (%)
U				^{238}U	4.2	79	^{235}U	4.4	57.6
					4.15	21			
				^{234}U	4.77	72			
					4.72	28			
Th	^{232}Th	4.01	78	^{230}Th	4.69	76.3	^{227}Th	6.04	24.2
		3.95	22		4.62	23.4			
	^{228}Th	5.42	73.4						
		5.34	26						
Ra	^{224}Ra	5.69	95	^{226}Ra	4.78	93.8	^{223}Ra	5.72	51.6
		5.45	5		4.6	6.2	^{219}Ra	7.68	66.2
Rn	^{220}Rn	6.29	100	^{222}Rn	5.49	100	^{219}Rn	6.82	79.4
Po	^{216}Po	6.78	100	^{218}Po	6	100	^{215}Po	7.39	99.9
	^{212}Po	8.78	100	^{214}Po	7.69	100	^{211}Po	7.45	98.9
				^{210}Po	5.3	100			
Bi	^{212}Bi	6.05	25.2	^{210}Bi	4.94	55	^{211}Bi	6.62	83.54
		6.09	9.8		4.90	39.5			

The EICHROM Method

Alpha spectroscopy requires a chemical separation before analysis, followed by actinide separation using EICHROM columns before the alpha source preparation. Alpha spectroscopy requires sample digestion as part of the preparation. As the samples must be a solution to precipitate the radionuclides of interest. This needs to be done before the solution is passed

64

through the EICHROM columns that separate out the radionuclides of interest. The load solution preparation method is important for accurate and quantitative sample collection (Horwitz et al., 1995).

Considerations for handling samples containing Po

Different methods for handling samples which may contain Po were implemented within this chapter. When Po is in a HNO_3 matrix the major species is $Po(NO_3)_6^{2-}$, this converts to $Po(OH)_2^{2+}$, $Po(OH)_3^+$, and $Po(OH)_4$ with decreasing hydrogen ion concentration. When Po is in a HCl matrix it forms negative complexes such as $Po(OH)_2Cl_4^{2-}$, $Po(OH)_2Cl_3^-$. Po is very volatile, where the loss of Po within a sample has been reported to begin to volatilise at ~50°C, where others report loss begins at 100 °C and 90% loss by 300 °C (Thakur & Ward, 2020). The loss of Po through different sample digestion methods have been previously determined, ~13-17% loss when using a microwave digestor, and 30% loss in open beakers, dry ashing at 500 °C showed a loss of 62% and wet ashing with HNO_3 and $HClO_4$ at ~200 °C over 1 week resulted in negligible Po loss (Thakur & Ward, 2020).

Instrumentation

An alpha spectrometer is composed of many different components (Figure 3.3), it consists of a vacuum chamber where the sample is placed, this also contains the silicon detector. Many alpha spectrometers have multiple individual sample chambers for multiple consecutive analysis. Alpha spectrometers require a high voltage bias supply, they are also composed of a preamplifier, amplifier, a multichannel analyser and a computer to process and visualise the data (El Afifi et al., 2020).

This image has been removed due to copyright restriction. Available online from [El Afifi, E. M., Hilal, M. A., & Attallah, M. F. (2020). Performance characteristics and validation of alpha particle spectrometers for radiometric analysis of natural and anthropogenic radionuclides of environmental impacts. Applied Radiation Isotopes, 109548]

Figure 3.3. Alpha Spectrometer Schematic (El Afifi et al., 2020).

Quantitative analysis, precision and accuracy

When samples are counted by an alpha spectrometer a blank and a control count are also counted at the same time. Tracer addition to sample before digestion to ensure account for loss of sample or volatility.

Radioactive tracers have been added to each sample of soil, vegetation and blanks prior to digestion for alpha spectroscopy analysis. Samples digested prior to EICHROM separations have [229]Th and [232]U tracers added. Prior to Po and Ra analysis tracers [209]Po and [133]Ba were added to samples. Tracers were added to each sample to monitor the recovery of the radionuclides within the samples. This was to account for any potential sample loss throughout digestion.

Justification

Alpha spectroscopy is a useful method for this research and will provide quantitative results for the activity of the low-level U-chain alpha emitting radionuclides in the samples. The advantage of alpha spectroscopy includes a low LOD, alpha emitting radionuclides within NORM samples. By comparing the activity of parent and daughter isotopes, the isotopic equilibrium and disequilibrium in natural decay schemes can be identified (Tuovinen et al., 2015).

Alpha spectroscopy experimental methods

Alpha Spectroscopy was performed to determine the activity of alpha emitting radionuclides within samples of soil and vegetation. This was performed at two different locations and two different sample sets were analysed. At ANSTO Alpha spectroscopy was performed on samples collected from Olympic Dam from May 2018. Alpha spectroscopy follows the ANSTO procedure, alpha spectrometer 13321 ERMC Operation of Ortec Alpha Spectrometer method. Any variations to the method are detailed below. These samples were all analysed as composite samples. Each individual vegetation sample from a particular site and species was composited equally by weight to provide a representative result of the species within the site. The soil samples were also composited evenly by weight within the same sampling site.

Alpha Spectroscopy performed at ARPANSA was of environmental samples collected from Olympic Dam during November 2018. This analysis was performed on individual plant and soil samples. This analysis was performed in replicates. Therefore, data of three different plants of the same species were analysed and compared to their adjacent soil samples. This analysis allowed a comparison between activity within the same species within a site. The Alpha spectroscopy discussed below was performed at ARPANSA and the activity of the vegetation compared to the soil adjacent to the plants on interest have been used to calculate concentration ratios.

Load Solution Preparation

To achieve the optimum actinide sorption to the EICHROM column, the loading solutions should be as 3 M HNO_3. Chapter 2, Figure 2.13 details the necessity for the sample to be in 3M HNO_3. The pH of the samples was adjusted using either concentrated HNO_3 or NH_3 to reach 3 M. The samples were then filtered through 0.45 µm and 0.2 µm filters consecutively. The filters were washed with 5 mL of 3 M HNO_3 to ensure complete transfer of the sample. The sample were now ready to go through the EICHROM columns.

EICHROM Column Separation

To quantify U and Th within samples of soil and vegetation. The EICHROM method uses tandem column extractions to isolate U and Th from the matrix. A vacuum box was set up with two columns, EICHROM resins were used, TEVA for Th extraction and TRU for U extraction. The TEVA column is placed before the TRU column, so the load solution passes through the TEVA before the TRU column. 10 mL of 3 M HNO_3 was flushed through each set of columns at 3 mL/minute, to prepare the columns for the load solution. The columns were prepared by passing a rinse solution of 5 mL 3 M NHO_3 through the columns and monitoring the flow rate, the flow rate was then adjusted to a rate of 1 mL/minute. The load solution was added to the columns and flushed through at 1 mL /minute to ensure radionuclide binding to the columns. 3 mL of 3 M HNO_3 was added to the load solution vials, as a wash, this was followed by a column rinse of 5 mL NHO_3 directly to the column (Eikenberg et al., 2009).

Gamma-ray spectroscopy

Gamma spectrometry is routinely used for environmental analysis for analysis of NORM materials as it provides quantitative results for the activity of the low-level gamma emitting radionuclides in the samples (Tuovinen et al., 2015). Table 3.2 shows the main radionuclides and the energy of the associated gamma emission for analysis. The benefits of gamma spectroscopy include: minimal sample preparation required, low LOD, quantitative analysis with a reasonable accuracy of multiple radionuclides within a single analysis (Gilmore, 2008). By comparing the activity of parent and daughter isotopes, the isotopic equilibrium and disequilibrium in natural decay schemes can also be identified (Tuovinen et al., 2015). However, when using gamma spectrometry for analysing low activity NORM materials to obtain statistically significant results, long count times are often required. Not all of the radionuclides in the U decay series emit a gamma emission when they undergo radioactive decay. Some do however, they can be a very low intensity. This is often the case for natural samples including soil and water as they often have low activity, and the radionuclides of interest are found in the background. Gamma spectrometers often include the energy range of 30 to 2300 keV is the normal range (Gilmore, 2008).

Table 3.2 Radionuclide and instrumentation. Gamma spectrometry, radionuclide and associated energy emission for identification used at ANSTO. Primary gamma emissions and intensity of U and Th chain radionuclides (Brookhaven).

	^{232}Th Nuclide	Energy (keV)	Intensity (%)	^{238}U Nuclide	Energy (keV)	Intensity (%)	^{235}U Nuclide	Energy (keV)	Intensity (%)
U							^{235}U	185.6	57
Th				^{234}Th	63.3	3.7	^{227}Th	235.9	12.9
Ra	^{224}Ra	240.9	4.1				^{223}Ra	269.5	13.9
Rn							^{219}Rn	271.2	10.8
Po	^{212}Po	2610	2.6						
		570	2						
Bi				^{214}Bi	609.3	45.5			
				^{210}Bi	265.6	51			
					304.6	28			
Pb	^{212}Pb	238.5	43.6	^{214}Pb	351.8	35.6	^{211}Pb	832	3.5
					295.2	18.3	^{207}Pb	569.7	97.9
				^{210}Pb	46.5	4.2		1063.6	88.8
Tl	^{208}Tl	2614.5	99.7	^{210}Tl	799.6	98.96			
		583.2	85		296	79			
				^{206}Tl	453.3	93			
					265.7	96			

Other radionuclides can be measured and used to calculate others, ^{214}Pb at 351.9 keV can be used to calculate ^{226}Ra activity, ^{228}Ac at 911.2 keV can be used for ^{228}Ra, ^{212}Bi at 727.3 keV can be used for ^{228}Th activity and ^{234}Th at 63.3 keV can be measured to calculate ^{238}U activity. When using Gamma Spectroscopy for analysis of NORM radionuclides, it is ideal for them to

be in secular equilibrium. This will be achieved by preparing the samples and sealing them for 38 days prior to analysis. This is an appropriate method of achieving secular equilibrium for the radionuclides below radon in the U decay series.

Instrumentation

High purity germanium (HPGe) detectors are most commonly used for gamma spectrometry, as they have much higher resolution compared to NaI detectors (Hossain et al., 2012). Gamma spectrometers detect photons from X-rays or gamma rays. The energy of the photon is directly related to the decay event which, in turn, relates to the parent radionuclide. A schematic diagram of a typical gamma spectrometer is below (Figure 3.4). Central to the system is a liquid nitrogen cooled detector placed in close proximity to the sample. When ionizing radiation hits the detector, free electrons are generated, and a signal is measured. HPGe detectors are commonly set up within a Pb shield where these shielding limits the background radiation exposure to the detector, therefore ensuring the results are from the sample and are not background interference. Shielding is especially important when analysing low activity NORM samples as the radionuclides of interest may be present within the background, shielding reduces the background detection (Murphy, 2005).

Figure 3.4. Schematic of a gamma spectrometer, The HPGe detector sits on top of a liquid nitrogen dewer, the cold finger is attached below the detector and sits within the dewer. Liquid nitrogen is filled into the dewer as required through the fill/vent tubes, this is how the cryogenic temperatures are achieved (Wallbrink et al., 2002).

Ge detectors are sensitive to ionizing radiation particularly gamma and x-rays as they are both photons. The charge produced is proportional to the energy of the photon that is detected. This charge is then converted to a voltage pulse by a preamplifier (Figure 3.5). This voltage is proportional to the incident photon energy. When ionizing radiation interacts with the Ge crystal, free electrons are generated from the crystal as a response to the photons absorbed from the sample (Figure 3.5). The charge produced is proportional to the energy of the photon that is detected. This charge is then converted to a voltage pulse by a preamplifier (Canberra, 2016). This voltage is proportional to the incident photon energy. The energy from the photon is related by magnitude to the charge in the crystal (Wallbrink et al., 2002).

Figure 3.5. Schematic of a gamma spectrometer electronics (Wallbrink et al., 2002).

The crystal acts as a semiconductor as it has the ability to conduct voltage. They are semiconductor diodes that have a p-i-n structure, this intrinsic region is the radiation sensitive region. An electric field extends across the intrinsic or depleted region under reverse bias voltage. When ionizing radiation interacts with the detector, the photons from the sample interact with the depleted volume of the detector. This produces charge carriers (holes and electrons) which are then swept to the p and n electrodes by the electric field (Wallbrink et al., 2002). Ge detectors have a low band gap, due to this the detector must be cooled constantly by liquid nitrogen, (77 °K) to reduce the thermal generation of the charge carriers to an appropriate level. The detector is cooled as to protect the detector and to ensure a high resolution is achievable (Canberra, 2016). A schematic of a band gap is shown in Figure 3.6.
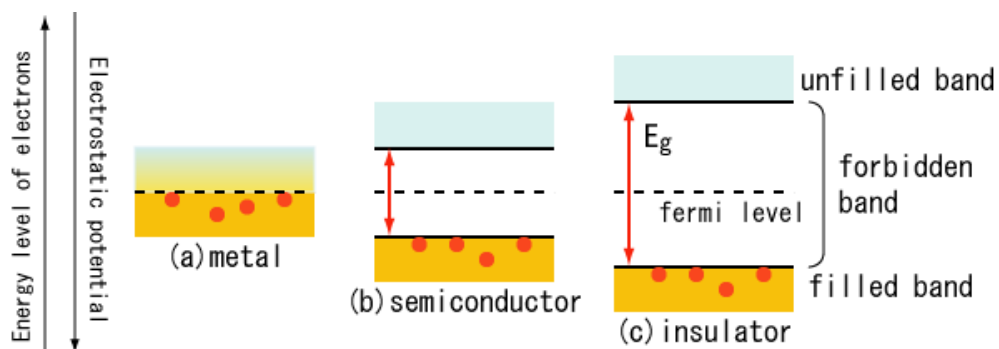
Figure 3.6. Schematic of the band gap for gamma spectrometers.

In this project two Ge detectors were used, one at Flinders University, one at ANSTO. both were high purity Ge, but the detector geometry and efficiency differed. The Flinders detector comprised a SAGe detector and the ANSTO detector was a planar HPGe detector, these are discussed separately below.

SAGe Well detector (Flinders University)

Figure 3.7 depicts a small anode germanium (SAGe) well detector. SAGe well detectors have a higher counting efficiency compared to standard Ge detectors, due to the near 4π geometry for small samples. As the sample sits inside of the detector, there is a larger surface area of the detector for the sample to interact with; therefore, more decay events will be detected (Technologies, 2016). For well type detectors, efficiency approaches 4π. These detectors have three options for sample positioning around the detector, including Marinelli containers. Round containers, (both used on top of the detector), and small vials used inside of the well. The gamma spectroscopy analysis performed at ANSTO used a planar HPGe gamma spectrometer.

This image has been removed due to copyright restriction. Available online from [Technologies, M. (2016). Small Anode Germanium Well Detector (SAGe)]
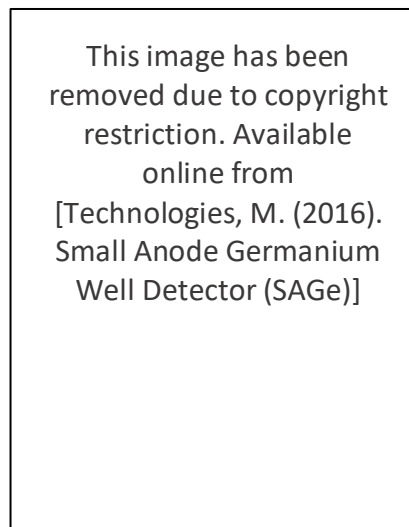
Figure 3.7. Small Anode Germanium (SAGe) Well Detector (Technologies, 2016).

LabSOCS and ISOCS for SAGe Well Detector

The method of calibration for gamma spectroscopy is the In-Situ Object Calibration Software (ISOCS) and Laboratory SOurceless Calibration Software (LabSOCS), these methods are now widely used in the gamma spectrometry community. ISOCS can be used to determine the full energy peak efficiency of the detector between the energy 45 keV and 7 MeV (Venkataraman et al., 2005). When LabSOCS is used for calibration of a SAGe gamma spectrometer, the detector is initially characterized in the factory. This is done by measuring a source from various different locations in the space surrounding the detector. Monte Carlo N-Particle Transport code (MCNP) model is used to model the efficiency from the response from the calibration source. This method provides a full efficiency calibration for the detector (Britton et al., 2015). The LabSOCS calibration method is then used with the geometry composer

software combined with the Genie2000 software to model the geometry of the sample against the detector. The geometry composer with the MCNP model is combined to calculate the efficiency and cascade summing corrections (Britton et al., 2015). The efficiency of the LabSOCS calibration is accurate to 4-5% at energy >400 keV (Bronson, 2003). In Situ Object calibration software of (ISOCS) Laboratory SOurceles Calibration Software (LabSOCS). CANBERRA has a mathematical method for calibration of the gamma spectroscopy (Adekola et al., 2016) as shown in Figure 3.8. The efficiency of the well detectors is higher than the semi planar detector from 30 keV to 10,000 keV.

This image has been removed due to copyright restriction. Available online from [Adekola, A., Colaresi, J., Douwen, J., Jäderström, H., Mueller, W., Yocum, K., & Carmichael, K. (2016). Characteristic performance evaluation of a new SAGe well detector for small and large sample geometries. *IEEE Transactions on Nuclear Science*, 63(3), 1570-1577]
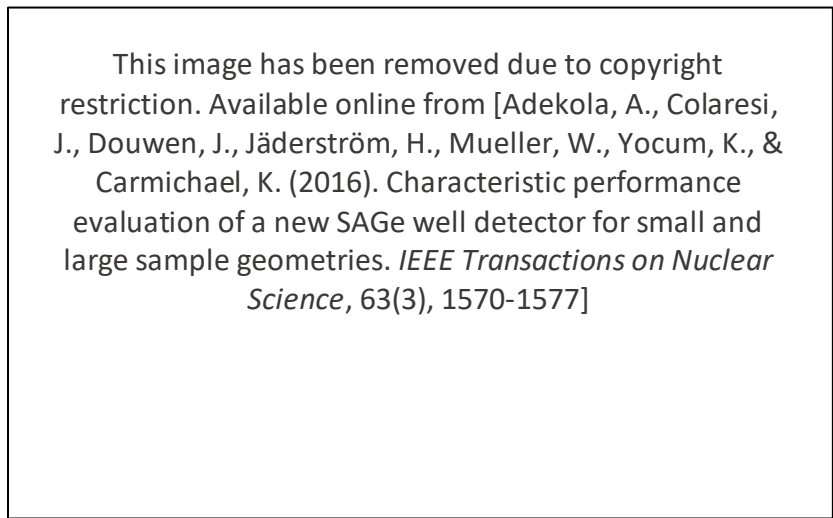
Figure 3.8. Efficiency of different gamma spectrometer detector types. (Adekola et al., 2016)

Quantitative analysis, precision and accuracy

Reference materials were analysed using the Flinders University gamma spectrometer, a seaweed radionuclide standard, NIST standard reference material 4359 was analysed (NIST; Outola et al., 2006) where the know ^{210}Pb activity from the NIST standard was 21.0 ± 3.0 mBq/kg and the measured activity from the SAGe well detector was 21.3 mBq/kg.

The MDA (Equation 3.1) determines the lowest activity of sample that can be detected by the instrument. This is often determined by the analytical software (Hwang et al., 1992). The method by Currie 1968, for determining the MDA is well established and recommended by the American National Standard For Performance Criteria for Radio-bioassay (ANSI N13.30) (Currie, 1968). The Currie method was designed for radioactivity measurements and is appropriate long and short-lived radionuclides. The MDA considers three factors 1. The decision limit, which determines whether the results indicate detection, 2. Limit of detection

(LOD) which determines if the detection is achieved by a given analytical procedure, and 3. The determination limit provides information on if the results are precise enough for quantitative analysis (Currie, 1968). The Currie method uses statistics based on a 5% probability of a non-detection risk, if the decay event occurs away from the detector and a 5% probability of the smallest amount of sample being detected (Hwang et al., 1992). The efficiency of the detector considers the number of counts from a given number of gamma rays from the sample (Gamma and X-Ray Detection, 2014). The Currie MDA estimate equation is shown in Equation 3.1.

$$MDA = \frac{\sigma\sqrt{B}}{\varepsilon PTW}(Bq\ kg^{-1})$$

Equation 3.1. MDA calculation. Where: σ = statistical coverage factor equal to 1.645 (confidence level 95%), B = Background, T = counting time (seconds), ε = Counting efficiency of the detector, P = absolute transition probability of γ-decay, W = the dried sample weight in kg (El Afifi et al., 2006).

Where the MDA is where the relative uncertainty equals + or – 100% at 95% probability level. When counting samples with very low activity, considering the Equation 3.2 is important when deciding on count times (NEA, 2006).

$$t_N/t_B = \sqrt{k}$$

Equation 3.2. Where tN = counting time of sample, tB = counting time of background and k = ratio of total count time to background rate (NEA, 2006).

Interferences

Background subtractions must be performed by counting the background and subtracting from the sample counts. When using the activity and half-life of radionuclides to calculate the activity of another radionuclide in the decay series, ^{234}U is not an ideal one to use. It has been shown that groundwater can cause natural leaching of ^{234}U from ore to the groundwater causing minor disturbances in the natural isotopic ratios (Murphy, 2005). Spectral interferences need to be considered when using gamma spectrometry, the majority of radionuclides will emit unique energies however, there are some interferences to consider when analysing NORM materials.

A study calculated the activity for ^{226}Ra and ^{232}Th from the activity of the measured daughter radionuclides, Equation 3.3. below was used. This is important as not all radionuclides from

the U and Th decay series are detectable by analytical methodology. Therefore, undetectable daughter activities can be predicted by the parent radionuclides.

$$A = \frac{C}{\varepsilon P W} (Bq\ kg^{-1})$$

Equation 3.3. Calculate activity of the measured daughter radionuclides. Where: A = activity of a radionuclide in Bq kg-1, C = Net counting rate of sample with background subtracted in (cps), ε = Counting efficiency of the detector, P = absolute transition probability of γ-decay, W = the dried sample weight in kg (El Afifi et al., 2006).

The activity of a sample can be calculated using the decay constant and the number of atoms (Equation 3.4).

$$A = N\ \lambda$$

Equation 3.4. Where: A = Activity, N = the number of atoms, λ = decay constant (s-1) of radionuclide (ln2/half-life) (El Afifi et al., 2006).

Chen et al. 2005, studied the transfer of ^{238}U, ^{226}Ra and ^{232}Th from soil to plants. Plant and soil samples were collected from a site contaminated with U mine tailings material, from south-eastern China. A Canberra HPGe gamma spectrometer was used for the analysis. This study identified a difference in the mobility of ^{238}U, ^{226}Ra and ^{232}Th from soil to root and that the uptake was plant specific. The mobility from the soil to root was found to be ^{238}U ~ ^{226}Ra > ^{232}Th (Chen et al., 2005).

Justification

The radionuclides of interest from the samples required to address the aims outlined in Chapter 1 Section 1.11 will be analysed using gamma spectroscopy. Gamma spectroscopy is a useful method for this research and will provide quantitative results for the activity of the low-level U-chain gamma emitting radionuclides in the samples. Minimal sample preparation is required as powdered solid samples can be analysed as-is within plastic vials. Gamma spectrometry identifies gamma-emitting radionuclides by detecting the energy of the photon emitted. Detectors that can be used for this analysis include Ge and NaI (Tuovinen et al., 2015). The benefits of gamma spectroscopy include: minimal sample preparation required, low LOD, quantitative analysis with a reasonable accuracy of multiple radionuclides within a single analysis (Gilmore, 2008). By comparing the activity of parent and daughter isotopes, the isotopic equilibrium and disequilibrium in natural decay schemes can be identified (Tuovinen et al., 2015). Therefore, gamma spectroscopy is an appropriate analytical instrument for analysis for this research.

Gamma-ray spectroscopy experimental methods

For the gamma spectroscopy analysis using the SAGe well detector, following the sample preparation outlined in section 2.3, the samples contained within the 7mm vial was placed into the SAGe well detector. For the gamma spectroscopy analysis using the planar Ge detectors the samples within the petri dish were placed on top of the planar Ge detector. For both types of detectors, the Pb shield was closed to minimize the interference from background radiation. The count time for soil was 24 hours, the count time for vegetation was 72 hours.

3.3. Results

3.3.1. Radionuclide activity from soil and vegetation from the arid Australian environment

The results and discussion following in this section result from alpha spectroscopy and gamma spectroscopy from two different seasons, Autumn and Spring 2018 at the Olympic Dam mine and one sampling time at the Flinders Ranges region at the beginning of Summer 2018. Analytical techniques including Alpha spectroscopy, gamma spectroscopy, NAA and ICP-MS have been implemented within the work described in this chapter.

Olympic Dam Autumn (May 2018) radionuclide results and discussion

Composite results

Composite soil (n=6) and vegetation (n=3) samples collected from Olympic Dam in May (Autumn) 2018 have been analysed for ^{232}Th, ^{230}Th, ^{238}U, ^{235}U, ^{234}U, ^{210}Po and ^{226}Ra activities, the results are shown in Figure 4.2 for soil and 4.3 for the vegetation results the complete dataset is in Appendix B Table B.2. Radionuclide activity within soil from the different sample collection sites are shown as a comparison in Figure 3.9.
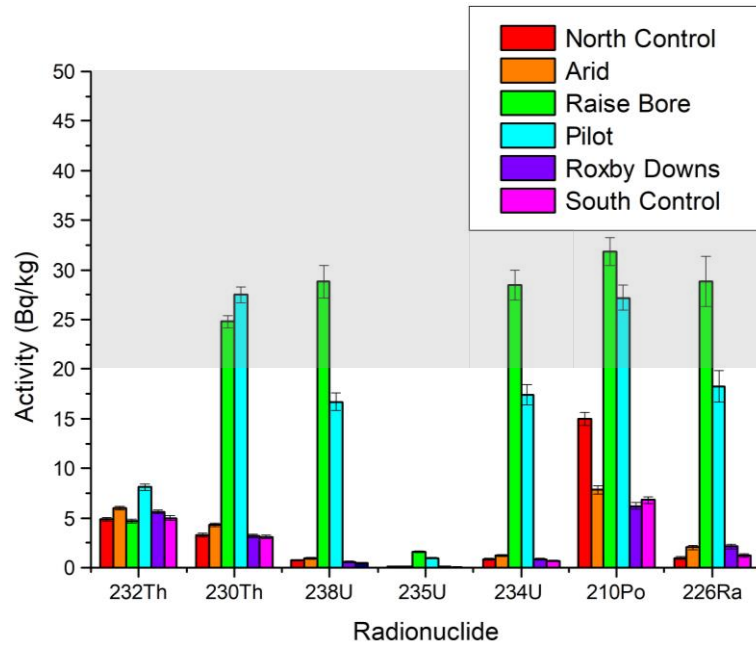
Figure 3.9. Alpha spectroscopy results of soil composite samples from May 2018, alpha spectroscopy performed at ANSTO (n=6). The Grey area indicates "normal ranges of radionuclides within soils (Long, 2012; Thakur & Ward, 2020).

Figure 3.9. shows that there is a large variation in activity between sites sampled within the Olympic Dam Region. The raise bore site had the highest activity of radionuclides ^{238}U, ^{235}U, ^{234}U, ^{210}Po and ^{226}Ra. The site with the highest activity of ^{232}Th and ^{230}Th was the pilot plant. The radionuclide that showed the highest activity over all sites samples was ^{210}Po with the exception of the pilot plant site, where ^{230}Th was the highest activity. The radionuclide with the lowest overall activity in soils from all sites was ^{235}U at a maximum of 1.6 ± 0.1 Bq/kg at the raise bore site and a minimum of 0.04 ± 0.02 Bq/kg at the south control site. The radionuclide with the highest overall activity was ^{210}Po at a maximum of 31.8 ± 1.42 Bq/kg at the raise bore site and a minimum of 6.18 ± 0.33 Bq/kg at the Roxby Downs site. The ^{210}Po activity are elevated in comparison with the other ^{238}U daughters, ^{210}Po follows ^{222}Rn gas within the series. The higher activity of ^{210}Po is due to ^{222}Rn and the deposition of radon on the environment (Mudd, 2008; Schmidt & Hamel, 2001). Disequilibrium within the system is inevitable as they are environmental soil samples, with dust deposition and radon progeny contribution (Eitrheim et al., 2016; Landsberger et al., 2017; Michalik et al., 2018). Due to α-recoil processes occurring from radioactive decay of ^{238}U and daughters, the mobility of ^{234}U within natural systems is often higher than its parent ^{238}U leading to an excess of ^{234}U in groundwater (Yanase et al., 1995). Any corresponding depletion of ^{234}U in the solid soil phase is generally less pronounced, this was not observed in these samples as the activity of ^{238}U and ^{234}U are in good agreement.

77

Overall, the difference in activity between the north control and the south control sites is minimal with a difference of between 0.02 Bq/kg and 0.28 Bq/kg from all radionuclides detected except for [210]Po. Where the difference of [210]Po is 8.2 Bq/kg, the north control site has higher activity compared to the south site. When comparing activity directionally, a comparison to wind direction was made from the Olympic Dam Aerodrome. The majority average wind direction annually is in a southern direction this is also the case for May and November (Australian Government, 2020). A schematic of the wind direction at Olympic Dam is shown in Figure 3.10.

This image has been removed due to copyright restriction. Available online from [Meteoblue, Simulated historical climate & weather data for Olympic Dam Airport, 2022]

Figure 3.10. Directionality of wind at Olympic Dam airport (Meteoblue, 2022).

Throughout all sites [235]U activity was low, with the highest activity at 1.6 ± 0.1 Bq/kg, this is expected in comparison to [238]U due to their natural abundance ratio. The radionuclide [232]Th was very consistent in activity across all sites with a range of 3.4 Bq/kg, where [232]Th is within an individual decay scheme to the other radionuclides, there is no observable influence from the sample site on [232]Th activity. The [235]U and [232]Th are not found within the [238]U scheme, as both [235]U and [232]Th show different trends and lower activity overall compared to the [238]U and

daughters. The soil composite (n=6) 0-10 cm samples analysed from the Olympic Dam region in Autumn 2018, overall displayed relatively low activity.

Radionuclide activities of ^{232}Th, ^{230}Th, ^{238}U, ^{235}U, ^{234}U, ^{210}Po and ^{226}Ra determined from Olympic Dam vegetation samples collected during Autumn 2018 from the same sites at the same time as the samples discussed above in Figure 3.9. *Dodonaea viscosa* composite (n=3) analysis from Olympic Dam samples from Autumn 2018 are shown in appendix B Table B.3. The results are also shown in Figure 3.11. (a) for the *Dodonaea viscosa* (n=3) and (b) for the *Acacia ligulata* (n=3).
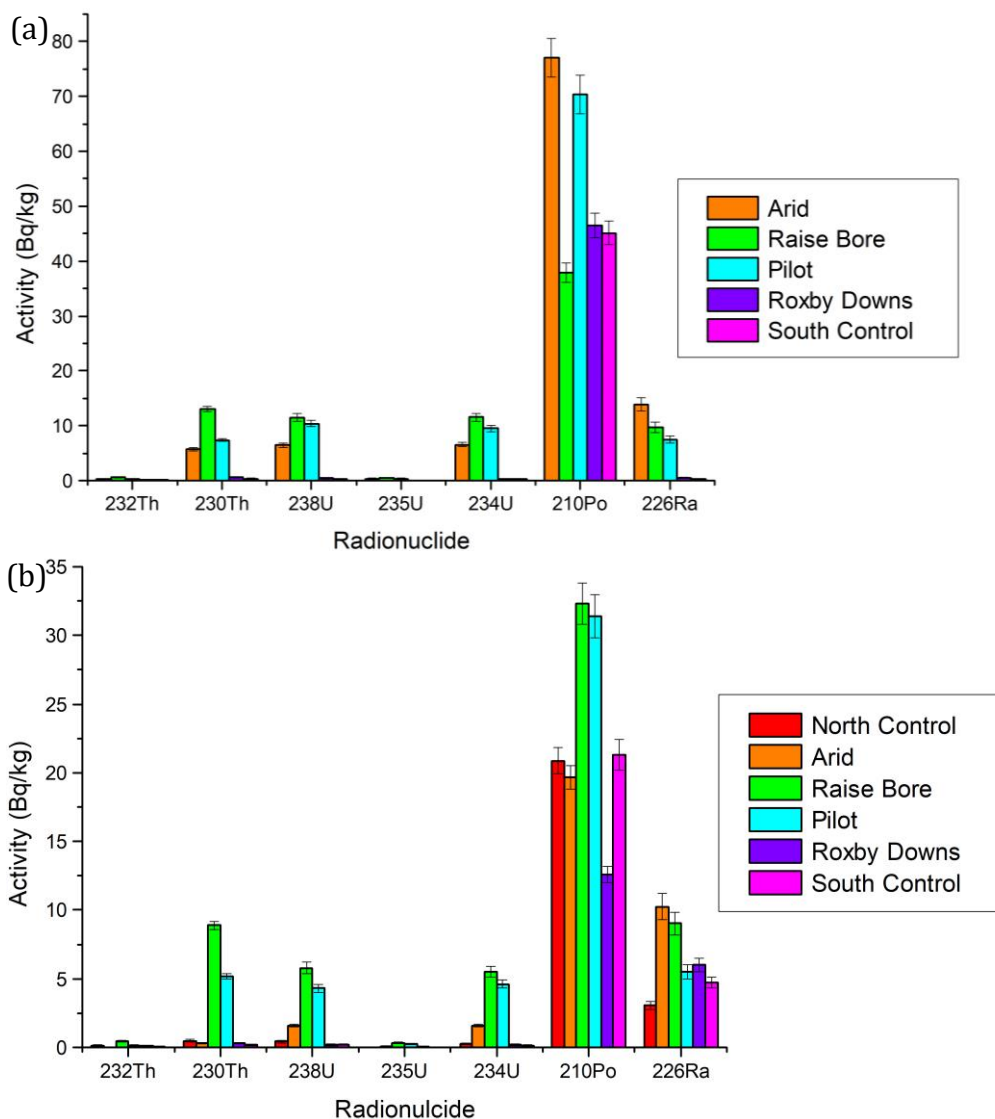
Figure 3.11. (a) Dodonaea viscosa alpha spectroscopy results from the Olympic Dam May 2018 composite, dry weight samples. (b) Acacia ligulata alpha spectroscopy results from the Olympic Dam May 2018 composite, dry weight samples (n=3).

Figure 3.11 shows the radionuclide analysis of Olympic Dam vegetation species *Dodonaea viscosa* and *Acacia ligulata* have shown overall consistent activities for the ^{238}U daughters for *Dodonaea viscosa*, with the exception of ^{210}Po. Where ^{210}Po is elevated in comparison within both species, the *Dodonaea viscosa* shows significantly higher activity of ^{210}Po at 77.0 ± 3.5 Bq/kg at the pilot plant compared to 32.30 ± 1.50 Bq/kg at the raise bore site for *Acacia ligulata*. As discussed previously the ^{210}Po is expected to be higher due to deposition from ^{222}Rn. The *Dodonaea viscosa* results from the arid site ^{226}Ra activity is elevated in comparison to the other ^{238}U daughters, with the exception of ^{210}Po. The activity of both ^{232}Th and ^{235}U is very low for both species with a maximum activity of 0.58 ± 0.08 Bq/kg. ^{230}Th, ^{238}U and ^{234}U are all relatively consistent when comparing operational sites and when comparing sites outside of the mining lease area for both species with the exception of the Arid Recovery site. No *Dodonaea viscosa* were located at the north control site, therefore, a direct control site comparison cannot be made. The comparison of vegetation activities to the soil media activities shown in Figure 3.11 shows that the *Acacia ligulata* has a close to 1:1 ratio of activity between soil and vegetation. However, the *Dodonaea viscosa* accumulates higher activities of radionuclides from the soil in comparison to *Acacia ligulata*.

Replicate results

Samples collected from Olympic Dam in Autumn 2018 have been analysed using gamma spectroscopy for ^{226}Ra, ^{228}Th, ^{235}U, ^{212}Pb and ^{214}Pb activities. The individual results are available in appendix B and are shown in Figure 3.12.
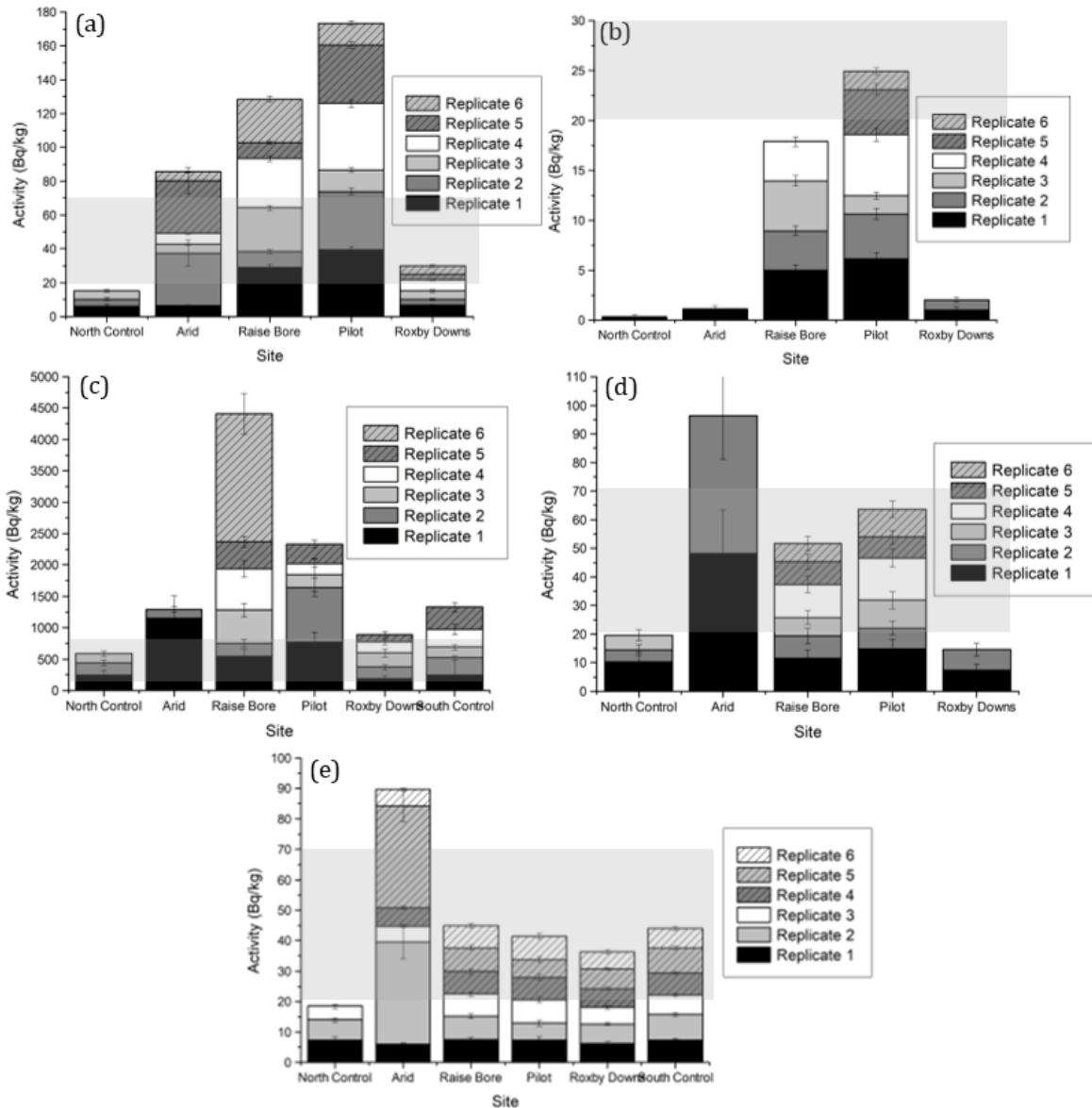
Figure 3.12. Replicate soil samples from Olympic Dam (May 2018) gamma spectroscopy results from Flinders university laboratories. (a) ^{226}Ra, (b) ^{235}U, (c) ^{214}Pb, (d) ^{212}Pb and (e) ^{228}Th. This figure shows there the activity concentrations sit regarding 'normal soil ranges' as the shaded boxes across the graphs shows the normal ranges of activity in soil(Long, 2012).

The individual activity results from Figure 3.12 shows that there is a large amount of variation of the activity between the sample sites, however, there is also a large variation in soil activity within the same sample site. When considering sites near the mining operations such as the raise bore and pilot sites this could be due to the mechanical disturbances of the environment. However, the variation in the sites outside of the mining activities, the variation is likely due to natural variability seen in the natural arid Australian environment. The range of results and statistics are discussed in Table 3.3 below.

Table 3.3. Olympic Dam Autumn soil replicate results from Gamma Spectroscopy analysis (n=3, 'uncert' is used as an abbreviation for uncertainty) (Flinders University).

Site		226Ra Activity (mBq/g)	Uncert ±	228Th Activity (mBq/g)	Uncert ±	214Pb Activity (mBq/g)	Uncert ±	212Pb Activity (mBq/g)	Uncert ±	235U Activity (mBq/g)	Uncert ±
North Control	Average	5.04	0.98	6.15	0.81	196.3	52.0	6.55	2.32	-	-
	Min	4.20	0.69	4.47	0.63	150.0	42.5	4.04	1.82	-	-
	Max	6.08	1.49	7.38	1.13	245.0	70.2	10.3	3.19	-	-
	Range	1.88	0.80	2.91	0.50	95.00	27.7	6.36	1.37	-	-
	SD	0.78	0.36	1.23	0.23	38.82	12.9	2.77	0.62	-	-
Arid	Average	10.3	1.82	11.0	1.34	644.5	202	-	-	-	-
	Min	3.17	0.51	5.28	0.49	139.0	47.7	-	-	-	-
	Max	31.2	7.58	33.4	5.39	1150	358	-	-	-	-
	Range	28.0	7.07	28.1	4.90	1011	310	-	-	-	-
	SD	9.48	2.58	10.1	1.81	505.5	155	-	-	-	-
Raise Bore	Average	21.3	1.37	7.49	0.85	734.5	136	8.62	2.70	4.48	0.51
	Min	9.38	1.01	7.22	0.79	214.0	58.8	6.45	2.44	3.95	0.47
	Max	29.1	1.64	7.85	0.91	2040	322	11.4	3.00	5.00	0.55
	Range	19.6	0.63	0.63	0.11	1826	263	5.05	0.56	1.05	0.08
	SD	8.62	0.26	0.26	0.05	599.6	86.1	2.12	0.23	0.53	0.04
pilot	Average	28.9	1.72	6.89	0.97	467.2	137	10.5	2.85	4.16	0.51
	Min	12.7	1.24	5.67	0.92	187.0	59.6	7.27	2.37	1.85	0.34
	Max	39.3	2.08	7.68	1.06	870.0	268	14.7	3.24	6.10	0.65
	Range	26.6	0.84	2.01	0.15	683.0	208	7.53	0.87	4.25	0.31
	SD	11.6	0.35	0.87	0.06	293.3	76.4	3.13	0.36	1.75	0.13
Roxby Downs	Average	5.01	0.63	6.04	0.57	178.2	46.2	-	-	-	-
	Min	3.36	0.51	5.49	0.49	117.0	39.6	-	-	-	-
	Max	6.70	0.74	6.50	0.69	224.0	61.9	-	-	-	-
	Range	3.34	0.23	1.01	0.21	107.0	22.3	-	-	-	-
	SD	1.36	0.10	0.42	0.09	34.66	7.98	-	-	-	-
South Control	Average	4.85	0.79	6.65	0.61	265.8	101	7.80	2.72	-	-
	Min	3.84	0.57	4.50	0.54	168.0	31.6	6.67	2.11	-	-
	Max	7.03	0.95	8.36	0.70	353.0	279	9.29	3.04	-	-
	Range	3.19	0.38	3.86	0.16	185.0	247	2.62	0.93	-	-
	SD	1.28	0.15	1.18	0.07	60.45	90.8	1.10	0.43	-	-

As the half-lives of ^{214}Pb and ^{212}Pb are very short, the activity concentrations of these radionuclides is not of concern in an environmental context, however, can be an indicator of radon presence as they are daughters. There was a result for the north control site, ^{214}Bi was 3.20E+02 ± 5.00E+01 (MDA = 1.33E+02). A sample from the south control site result for ^{214}Bi was 2.45E+02 ± 5.24E+01 (MDA = 1.56E+02). The pilot site had a result for ^{210}Pb at 6.77E+01 ± 1.31E+01 (MDA = 9.10E+00). The Roxby Downs site had ^{212}Pb at 7.34 ± 2.22 (MDA = 5.63). The North Control site showed ^{235}U and ^{226}Ra below the MDA. At the Roxby Downs, arid and North Control sites ^{226}Ra and ^{235}U were below the MDA. The arid site also had a sample with ^{212}Pb below the MDA. The activity range increases at sites within the mining operations. The range at the north and south control sites lower compared to the sites within the mining operations as the activities overall were very low. This is due to the nature of the arid Australian environment having highly variable elemental and radionuclide concentrations within close proximities due to phenomena of 'islands of fertility'. Where 'Islands of fertility' are small accumulated regions of soil near vegetation where plant nutrient cycling occur, this leads to heterogeneous spread of nutrients and elements within arid soils (He et al., 2018).

Vegetation samples from Olympic Dam in Autumn 2018 have been analysed using gamma spectrometry, the complete dataset is in appendix B. The range, average activity, minimum, maximum and SD are shown in Table 3.4 below. Figure 3.13 shows the vegetation activity results from the Olympic Dam Autumn samples of *Dodonaea viscosa* and *Acacia ligulata*.

| Species | Site | ^{210}Pb (Bq/kg) | | | | | | |
		Activity	Uncertainty ±	MDA	Min	Max	Range	SD
Acacia ligulata	North Control	18.13	2.39	8.48	7.14	9.96	2.82	1.16
Acacia ligulata	Arid	21.43	2.79	9.55	7.87	11.70	3.83	1.60
Acacia ligulata	Raise Bore	23.23	2.94	9.34	8.29	11.30	3.01	1.38
Acacia ligulata	Pilot	17.83	2.67	8.65	7.26	10.20	2.94	1.21
*Acacia ligulata**	Roxby Downs	16.15	2.17	7.55	7.53	7.56	0.03	0.01
Acacia ligulata	South Control	18.90	2.38	7.75	7.06	8.66	1.60	0.67
Dodonaea viscosa	Arid	26.93	3.59	12.44	8.01	17.90	9.89	4.10
*Dodonaea viscosa**	Raise Bore	18.85	14.01	11.00	10.30	11.70	1.40	0.70
Dodonaea viscosa	Pilot	21.27	2.96	9.37	8.03	10.30	2.27	0.97
Dodonaea viscosa	Roxby Downs	16.63	2.57	9.12	6.45	10.70	4.25	1.90
Dodonaea viscosa	South Control	11.04	2.51	7.85	6.44	8.92	2.48	1.04

*n=2
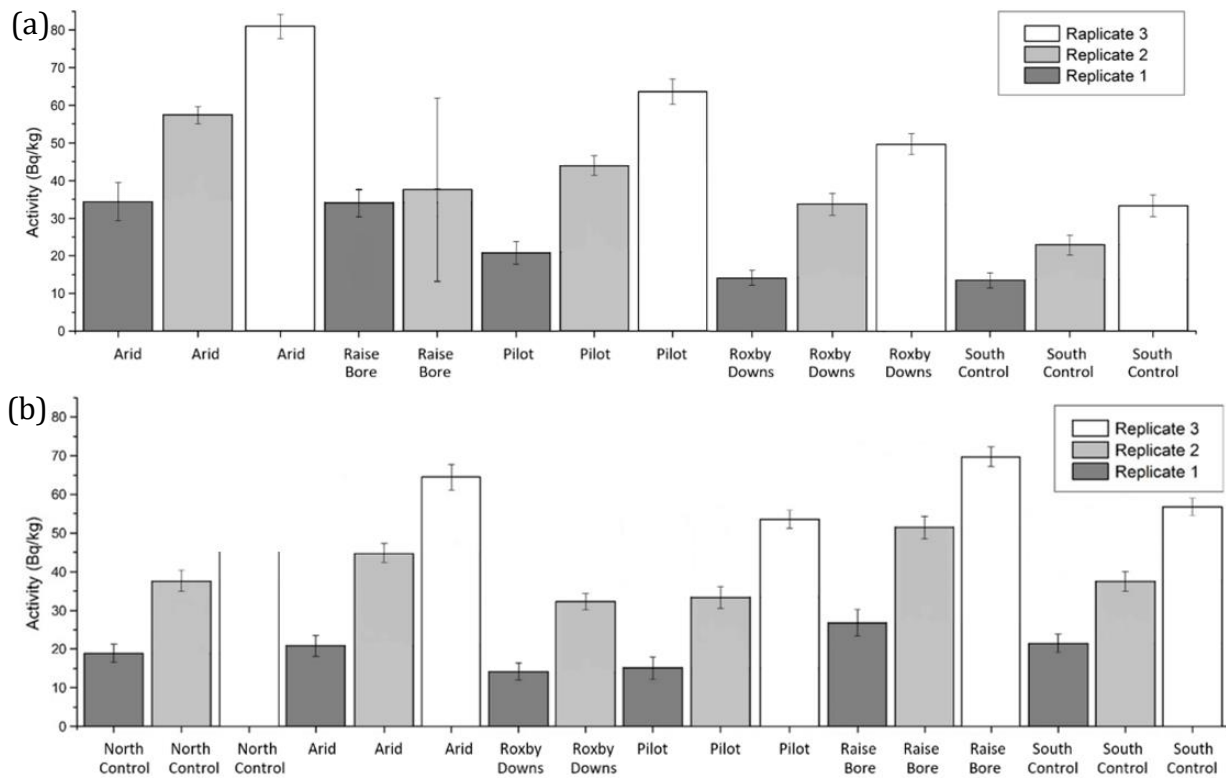
Figure 3.13. ^{214}Pb concentrations from vegetation Olympic Dam May 2018 Autumn replicate results from Gamma Spectroscopy analysis (Flinders University) (a) Dodonaea viscosa (b) Acacia ligulata (n=1), the error bars are representative of the uncertainty of the analysis.

Figure 3.13 shows the vegetation activity results from the Olympic Dam Autumn samples of *Dodonaea viscosa* and *Acacia ligulata*. The only radionuclide detected within these samples consistently was ^{214}Pb, as the activity overall was very low for the other radionuclides and

pushed the limit of detection. However, with the ^{214}Pb is taken up into the vegetation and was therefore, detected by the gamma spectrometer. The range within the *Dodonaea viscosa* was larger across the different sites in comparison to the *Acacia ligulata*, where the *Acacia ligulata* the range was similar between the three replicates across all sites. The uncertainty of the *Dodonaea viscosa* at the raise bore site was very large.

There were radionuclides under the MDA, ^{234}Th in *Acacia ligulata* from Pilot replicate 3 had activity below MDA. The *Dodonaea viscosa* at the south control site had ^{212}Pb detected at 20.000 ± 4.3800 (MDA 12.8) and ^{214}Bi at 11130.0 ± 275.0 Bq/kg. The raise bore *Dodonaea viscosa* had ^{226}Ra and ^{235}U below the MDA. The pilot *Acacia ligulata* has ^{234}Th below the MDA.

Olympic Dam Spring radionuclide results and discussion (November 2018)

Composite results

Composite soil (n=6) and vegetation (n=3) samples per site collected from Olympic Dam in Spring 2018 have been analysed for ^{232}Th, ^{230}Th, ^{238}U, ^{235}U, ^{234}U, ^{210}Po and ^{226}Ra activities. The results are shown in Figure 3.14 for soil and 3.15 for the vegetation results the complete dataset is in appendix B.
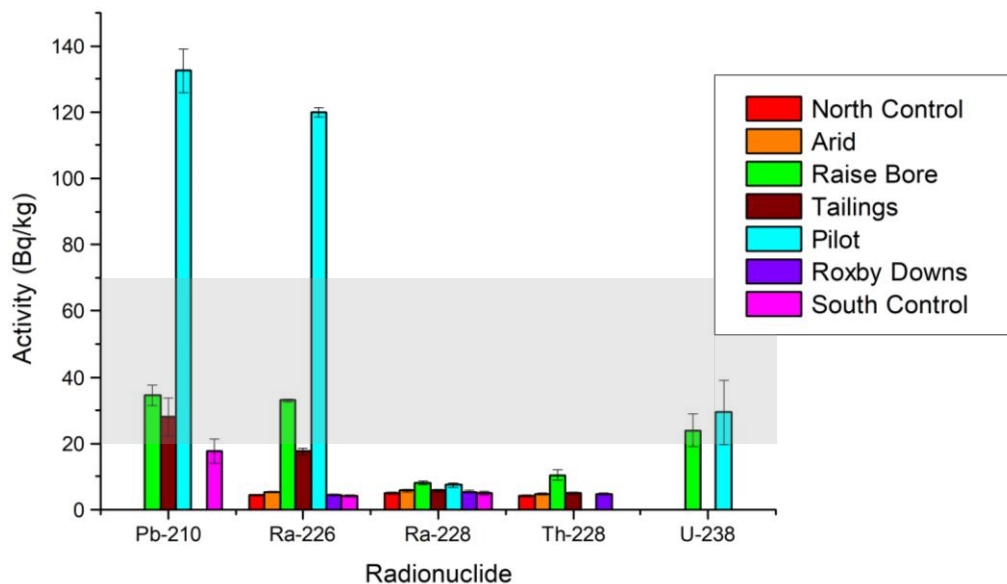
Figure 3.14. Olympic Dam Nov 2018 gamma spectroscopy soil activity composite (ANSTO/ARPANSA), The 'normal soil ranges' are represented as the shaded boxes across the graph (Long, 2012).

Figure 3.14 shows the radionuclide activities for soil samples from Olympic Dam in Spring 2018. The results show that the activity of ^{228}Ra and ^{228}Th are reasonably consistent across all

sample sites. ^{238}U was only detected at the raise bore and pilot sites, the activity of ^{210}Pb was higher than the normal soils range at the pilot site, the same was true for the activity of ^{226}Ra. However, all other sites and activities were either below or at the low end of the normal soil activity range of 20-70 Bq/kg (Long, 2012). There was a large variation of activity of ^{226}Ra and ^{210}Pb across the sampled locations.

In comparison of radionuclide activity of Olympic Dam sites between Autumn and Spring, ^{238}U was detectable at more sites in the Autumn samples, however there was a very similar activity within the raise bore and arid sites. ^{226}Ra showed much higher activity from the spring samples at the pilot site, all other sites were comparable across seasons. Further sampling and analysis need to be performed over a number of years before any conclusions are drawn from the seasonality comparison, particularly as the activities are low and generally close to the limit of quantification for the method.
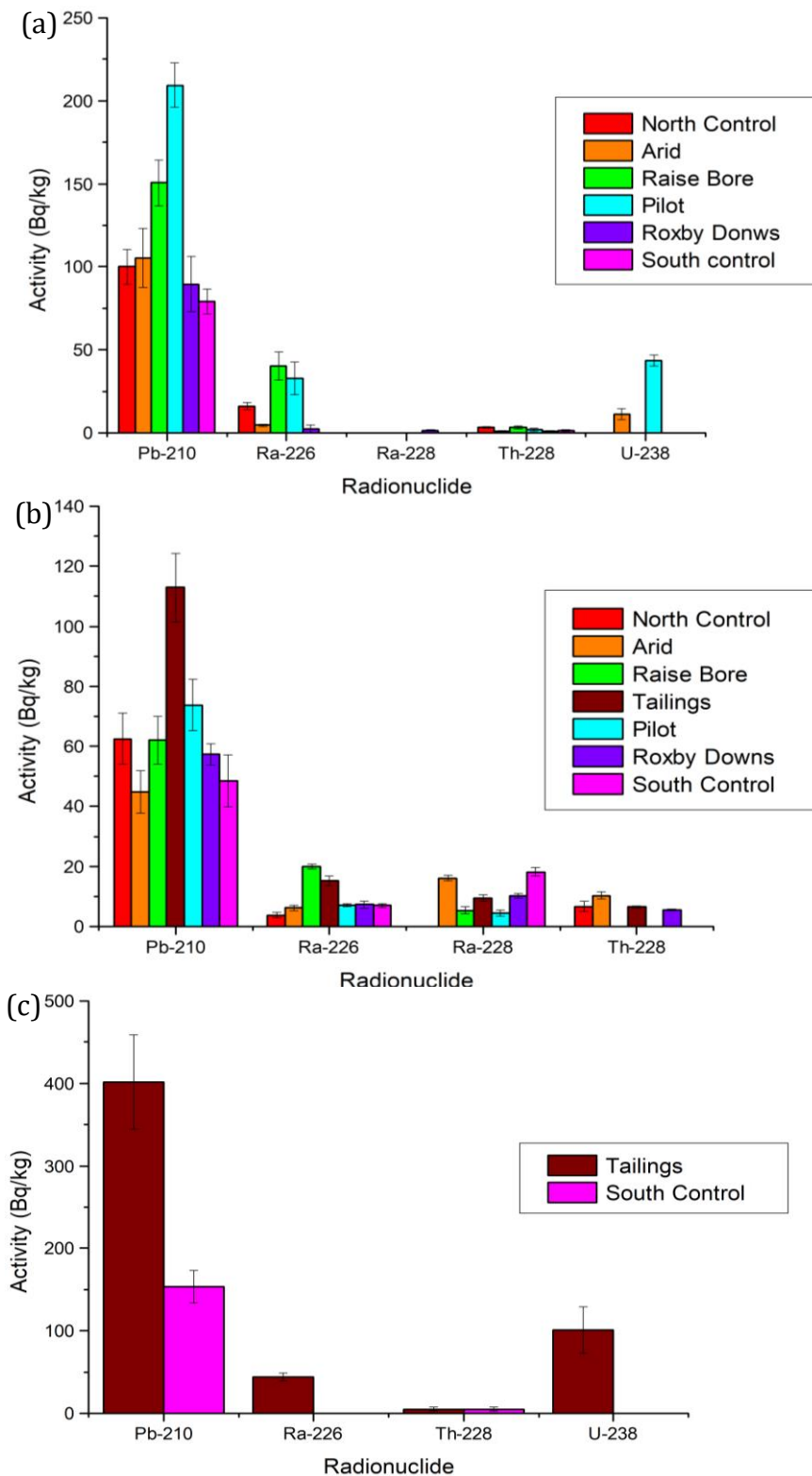
Figure 3.15. Vegetation from Olympic Dam, Nov 2018, gamma spectroscopy activity composite (ANSTO/ARPANSA) (a) Dodonaea viscosa, (b) Acacia ligulata) and (c) Astrebla pectinata.

Figure 3.15 shows the activity measured from vegetation from Olympic Dam in spring 2018. The results show the activity of ^{210}Pb to be consistently higher in the *Dodonaea viscosa* having a higher ^{210}Pb activity compared to *Acacia ligulata*. This is consistent with the activity of the

[210]Po activity being much higher in the *Dodonaea viscosa* as discussed previously. However, the *Astrebla pectinata* has the highest activity of ^{210}Pb at the tailings site. The activity of [238]U within the *Astrebla pectinata* was also higher than the other two species.

Replicate analysis

During the analysis of Olympic Dam samples from Spring using alpha spectroscopy, two different methods were used. The two methods included using a sub sample for the Po and Ra analysis, keeping this at low temperatures <70 °C for consideration of [210]Po volatility (Kim et al., 2012; Seiner et al., 2014). The other method was to take the column effluent from the UTEVA columns from the sample digestion at high temperatures and isolate [210]Po and [226]Ra from the column effluent. This was performed to determine which methodology works the best for environmental samples with a complicated matrix. The ability to use the effluent from the UTEVA column would save time and chemicals. Alpha spectroscopy analysis was performed on individual samples, the results from the UTEVA column for U, Th, Po and Ra are in appendix B Table B.3. The results from the individual Po and Ra are in appendix B Table B.4.

Following the sample digestion for the EICHROM column separation, an Fe precipitation process was followed. The vegetation samples did not form the FeO(OH) precipitate when following the suggested dilution with water to ~250mL (Lozano et al., 1999). However, when dilution to ~2L a precipitate formed readily.

The Ra microprecipitation step was also affected by the oily matrix of the vegetation samples. The Ra precipitation step was more successful on samples that had previously been eluted from the UTEVA column. There appeared to be matrix interference with the digested vegetation samples and the Ra microprecipitation formation. This interference was not observed on the soil samples digested under temperature control for [210]Po, this further indicates that there was matrix interference from the vegetation samples. Following a wet ash procedure with hydrogen peroxide and aqua regia reflux wax was still present within these samples. A comparison of [210]Po activities from the two methods have been made, the results are shown in Figure 3.16 below.
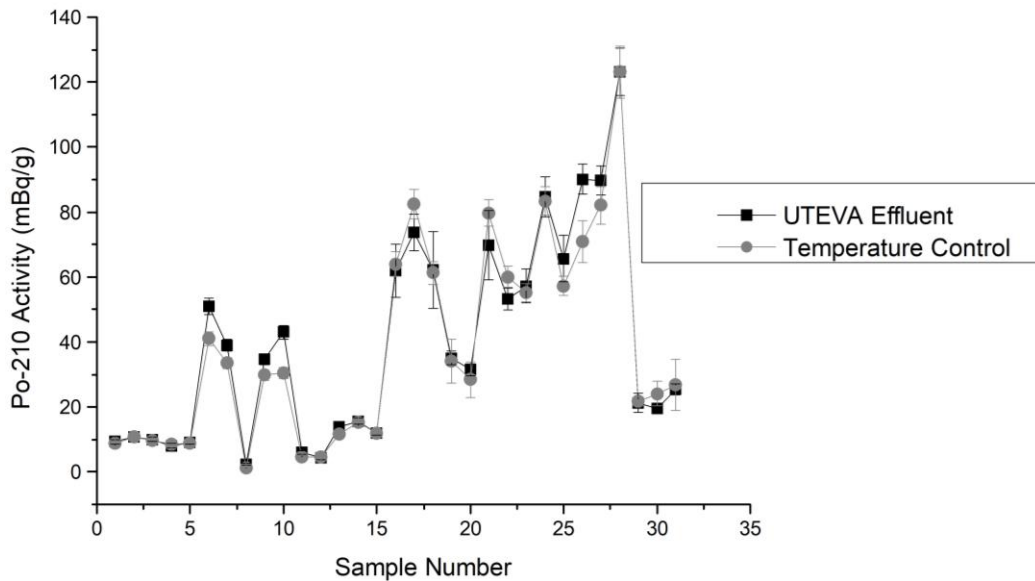
Figure 3.16. Comparison of activity measured of ^{210}Po from Alpha spectroscopy using two different methods, UTEVA column effluent and temperature-controlled digestion. Each sample number was analysed twice using both digestion methods.

The mean ^{209}Po tracer recovery was 46% from samples prepared for Po analysis from the columns, where the mean recovery of ^{209}Po from the temperature-controlled analysis was 56%. Therefore, the temperature-controlled Po method provided a higher percentage recovery. Disregarding the blanks, the soil vs vegetation recovery from the soil samples from the column separation was 57%, while the average column vegetation recovery was 28%. The average recovery from the Po analysis from the temperature-controlled digestions for soil was 67% recovery and from vegetation was 42% recovery. From Figure 3.16 above, the comparison of ^{210}Po activity from the two different methods, there is no clear trend between the two methods. Neither method consistently produced an activity of a higher or lower activity. Therefore, there is no clear advantage of using the temperature-controlled Po digestions. However, there is a benefit when considering the recovery factor, where the recovery for the temperature-controlled digestions is ~10% higher.

The nitrate form of ^{210}Po has previously been described to be involatile up to 400 °C (El-Daoushy et al., 1991; Thakur & Ward, 2020). Where the chloride form is more volatile, therefore when digesting with nitric acid this may assist with the ^{210}Po remaining involatile.

Replicate samples of vegetation and soil from Olympic Dam Spring (November 2018) were analysed by alpha spectroscopy. The results are shown in Appendix A and Figure 3.17 and 3.18, a summary table of the average results is shown in Tables 3.5 and 3.6.
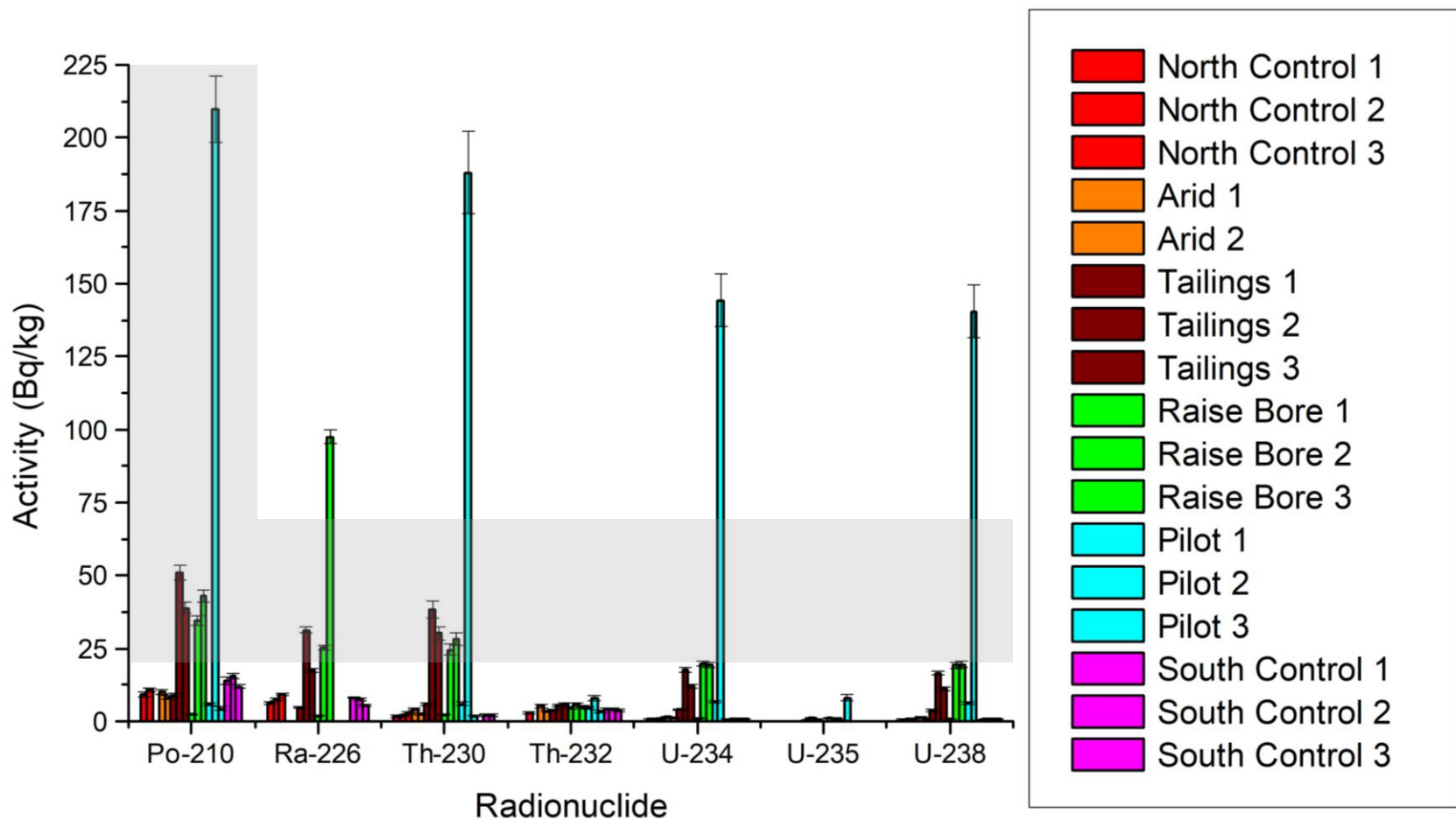
Figure 3.17. Soil Alpha spectroscopy results, ARPANSA Olympic Dam Nov 2018, replicate (Note, no arid 2 results). The 'normal soil ranges' are represented as the shaded boxes across the graph (Long, 2012; Thakur & Ward, 2020).

From Figure 3.17, there is variability of ^{238}U chain radionuclides across the different sampling sites. The activity of ^{232}Th and ^{235}U were reasonably consistent across the different sites.

Replicate vegetation activities are shown in Figure 3.18, the activities were determined using alpha spectroscopy and the samples were collected in association with the soil samples shown in Figure 3.17.
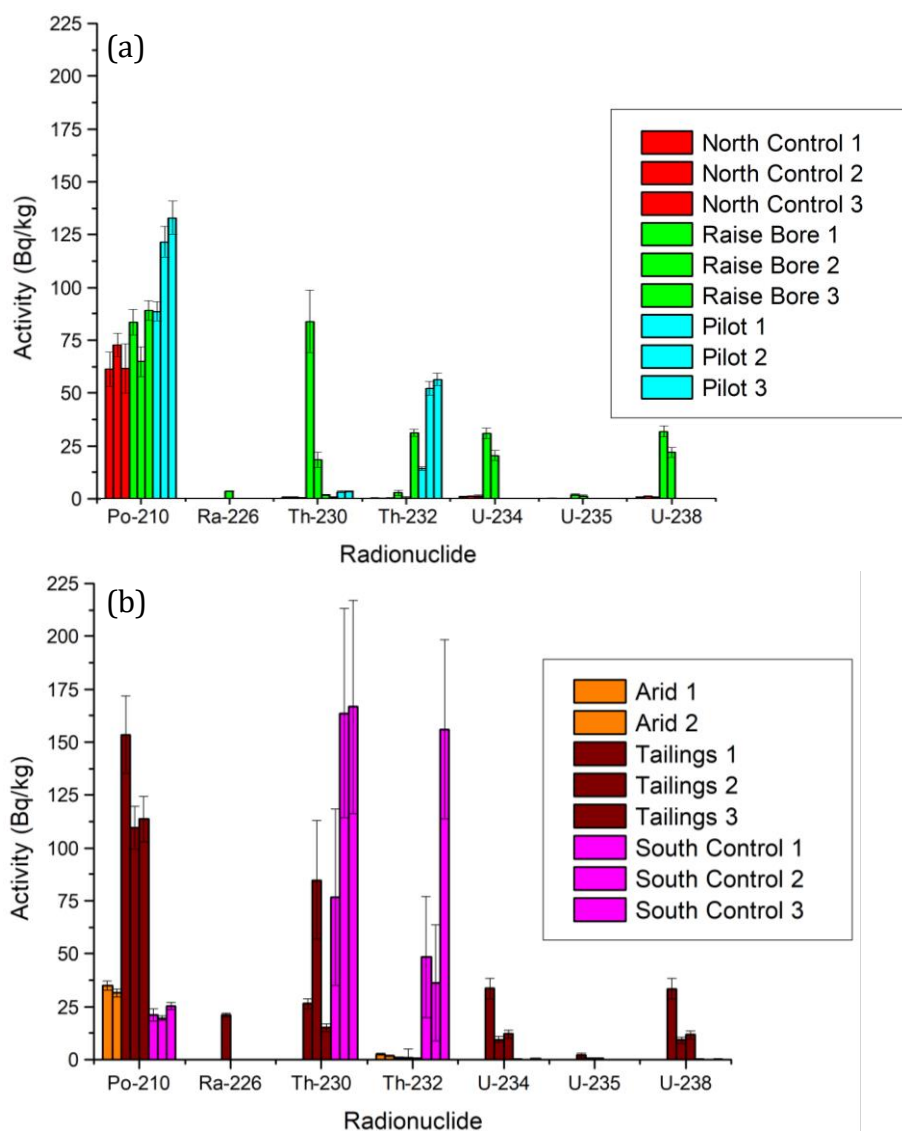
Figure 3.18. (a) Dodonaea viscosa alpha spectroscopy results replicate Nov 2018 (ARPANSA Laboratories). (b) Acacia ligulata alpha spectroscopy results replicate Nov 2018 (ARPANSA Laboratories).

Figure 3.18 shows the second *Dodonaea viscosa* sample from the pilot site is higher than the other pilot results for the ^{238}U daughters. This may be due to the soil being mechanically disturbed and it may have contained some process material from when the pilot plant was operational. This is consistent with the appearance of the soil, containing dark purple and light material mixed in with the deep orange of the soil from that region, if ore or slag was

mixed in with the soil from this sample, this may explain the higher concentration of ^{238}U chain radionuclides. The analysis of ^{226}Ra was not successful for the pilot and arid site samples therefore they are not included within the figure and no conclusions can be made regarding these. However, the same trend of the ^{238}U can be assumed for the pilot and arid samples. The ^{210}Po was significantly higher than the other radionuclides for *Dodonaea viscosa* except for the ^{230}Th at a raise bore site. The *Acacia ligulata* showed large variability for the ^{230}Th and ^{232}Th.

The average results from Figures 3.17 and 3.18 are calculated and shown in Tables 3.5 and 3.6 below. The average results show that the soil activities from the sites outside of the mining lease area are consistent in activity of each radionuclide. ^{226}Ra was below the limit of detection in half of the samples analysed. The average results follow the same trends as discussed previously for the Olympic Dam samples.

Table 3.5. Olympic Dam Nov 2018 soil results, replicate analysis mean summary table, alpha spectroscopy results, 'uncert' is used as an abbreviation for uncertainty. (ARPANSA laboratories) n=3 (Arid n=2).

Site	^{210}Po Activity (Bq/kg)	Uncert ± (Bq/kg)	^{226}Ra Activity (Bq/kg)	Uncert ± (Bq/kg)	^{230}Th Activity (Bq/kg)	Uncert ± (Bq/kg)	^{232}Th Activity (Bq/kg)	Uncert ± (Bq/kg)	^{234}U Activity (Bq/kg)	Uncert ± (Bq/kg)	^{235}U Activity (Bq/kg)	Uncert ± (Bq/kg)	^{238}U Activity (Bq/kg)	Uncert ± (Bq/kg)
North Control	10.01	0.695	7.641	0.357	2.157	0.296	3.091	0.458	0.869	0.097	0.037	0.020	0.718	0.083
Arid	9.065	0.680	-	-	3.392	0.370	4.442	0.435	1.336	0.160	0.079	0.040	1.15	0.145
Tailings	32.94	1.607	17.87	0.562	24.81	1.907	5.045	0.467	11.23	0.582	0.637	0.087	10.539	0.55
Raise Bore	26.66	1.307	41.48	1.057	18.42	1.422	5.208	0.452	13.40	0.682	0.716	0.092	13.19	0.673
Pilot	73.42	4.127	-	-	65.27	4.927	5.296	0.502	50.55	3.272	2.859	0.330	49.29	3.180
South Control	13.79	1.050	7.141	0.330	2.112	0.278	4.074	0.488	0.777	0.090	0.034	0.020	0.663	0.076

Table 2.6. Olympic Dam Nov 2018 vegetation results, replicate analysis mean summary table, alpha spectroscopy results, 'uncert' is used as an abbreviation for uncertainty. (ARPANSA laboratories) n=3 (Arid n=2).

Site	Species	^{210}Po Activity (Bq/kg)	Uncert ± (Bq/kg)	^{226}Ra Activity (Bq/kg)	Uncert ± (Bq/kg)	^{230}Th Activity (Bq/kg)	Uncert ± (Bq/kg)	^{232}Th Activity (Bq/kg)	Uncert ± (Bq/kg)	^{234}U Activity (Bq/kg)	Uncert ± (Bq/kg)	^{235}U Activity (Bq/kg)	Uncert ± (Bq/kg)	^{238}U Activity (Bq/kg)	Uncert ± (Bq/kg)
North Control	*Dodonaea viscosa*	65.95	8.570	-	-	0.552	0.204	0.201	0.091	0.985	0.312	0.052	0.127	0.753	0.250
Raise Bore	*Dodonaea viscosa*	80.11	6.040	3.508	0.240	35.03	6.300	11.52	1.120	25.87	2.44	1.532	0.430	27.14	2.540
Pilot	*Dodonaea viscosa*	115.7	6.647	-	-	2.396	0.290	41.42	2.350	-	-	-	-	-	-
Arid	*Acacia ligulata*	33.24	1.98	-	-	0.114	0.060	2.171	0.235	-	-	-	-	-	-
Tailings	*Acacia ligulata*	125.6	13.00	21.01	0.900	42.10	10.72	0.732	1.542	18.35	2.74	0.993	0.547	18.04	2.730
South Control	*Acacia ligulata*	22.05	1.932	-	-	0.136	0.046	0.080	0.033	0.207	0.052	0.015	0.017	0.174	0.046

Flinders Ranges region Summer radionuclide results analysis and discussion (December 2018)

Replicate results

Samples collected from the Flinders Ranges region in Summer 2018 have been analysed for radionuclide activity. Radionuclides of ^{210}Pb, ^{137}Cs, ^{226}Ra, ^{228}Th, ^{235}U, and ^{238}U are of interest for the Flinders Ranges region analysis, the results from the soil samples are shown in Figure 3.19 and the vegetation results are shown in Figure 3.20.
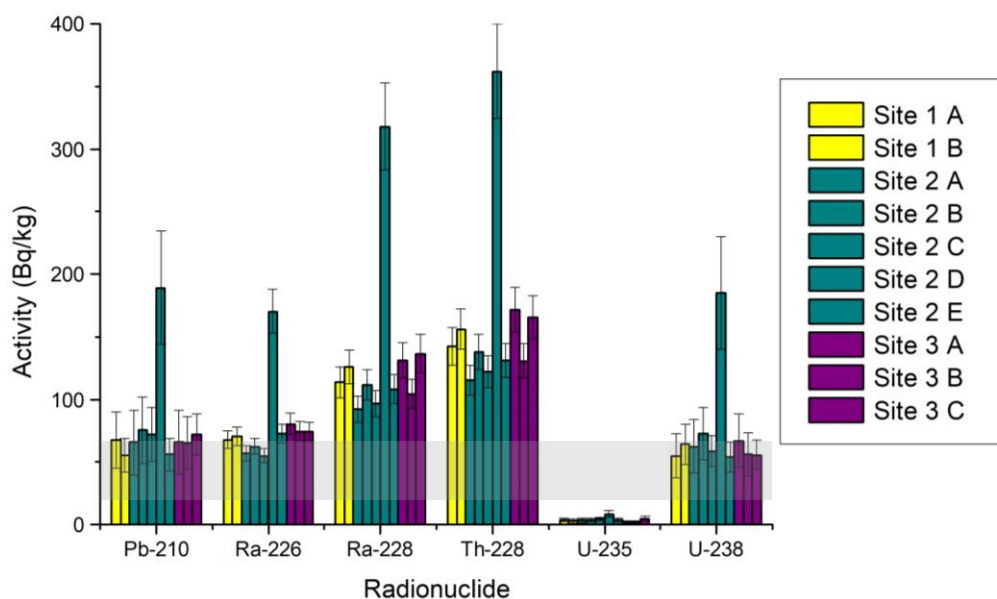
Figure 3.19. Average activity Flinders Ranges region soil analysis using gamma spectroscopy, average activity of each radionuclide at each sampling site (ARPANSA) (Long, 2012).

The radionuclide activity from the Flinders Ranges region soil samples collected in Summer are in Figure 3.19. These results show that there is a reasonable amount of uniformity of each of the radionuclides across each of the sampled sites. Overall, the activity of radionuclides within the soil samples are towards the upper end of the normal soils range for ^{210}Pb, ^{226}Ra and ^{238}U. The ^{228}Ra and ^{228}Th radionuclides are higher across all sites than the normal range. However, the ^{235}U activity across all sites is below the lower normal range. Except for one sample from site 2, where the activity of ^{238}U and ^{232}Th progeny are much higher than the rest of the samples. The activity range of ^{210}Pb across all sites is 55.5 to 189.0 Bq/kg, ^{226}Ra is 54.9 to 170.2 Bq/kg, ^{228}Ra 92.1 to 317.6 Bq/kg, ^{228}Th 115.4 to 362.1 Bq/kg, ^{235}U 2.1 to 8.3

94

Bq/kg and ^{238}U is 54.0 to 54.0 Bq/kg. The activity mean from each site is shown in Table 3.7 below. The activity of vegetation from the Flinders ranges region is in Figure 3.20 below.

Table 3.7. Mean soil samples for Flinders Ranges region summer (site 1 n=2, site 2 n=5 and site 3 n=3 (ARPANSA)).

Radionuclide	Site 1		Site 2		Site 3	
	Activity (Bq/kg)	Uncertainty ± (Bq/kg)	Activity (Bq/kg)	Uncertainty ± (Bq/kg)	Activity (Bq/kg)	Uncertainty ± (Bq/kg)
^{210}Pb	61.34	17.98	91.65	26.54	67.51	20.93
^{226}Ra	68.91	7.188	83.44	8.765	76.24	8.002
^{228}Ra	119.7	12.82	145.3	15.90	124.1	13.71
^{228}Th	149.3	15.55	173.7	18.18	155.8	16.38
^{235}U	3.660	1.470	4.718	1.854	2.995	1.063
^{238}U	59.53	16.86	86.50	22.40	59.63	16.88

The Flinders ranges region soil activities are in most cases sitting in the higher end of the normal ranges. ^{228}Ra and ^{228}Th activities are higher than normal soil ranges. ^{235}U is well below the lower end of the normal range. One site 2 soil sample is higher at all radionuclides except for ^{235}U overall.
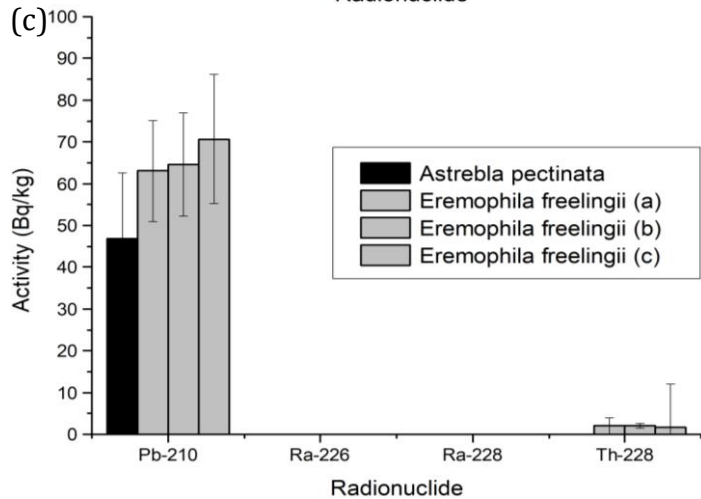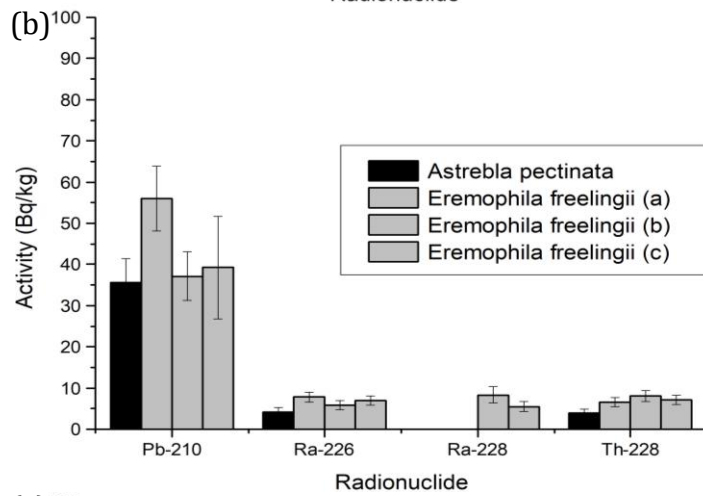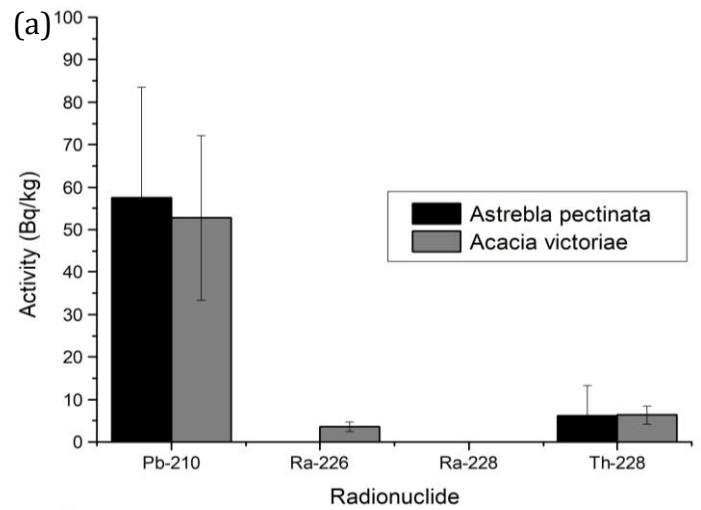
Figure 3.20. Flinders Ranges vegetation gamma spec results (n=1), (a) site 1, (b) site 2, (c) site 3 (ARPANSA).

Figure 3.20 shows the radionuclide activity of the three species: *Astrebla pectinata* (1), *Eremophila freelingii* (2) and *Acacia victoriae* (3) were measured from the Flinders Rangers region. The samples were measured using gamma spectroscopy, the results show that the activity each radionuclide is consistent across the same species. The abundance of vegetation

was low, not all species were located at each sampling site, limiting the study. Overall, the activity of the radionuclides determined within this research is low, however, the uncertainty on the activity of the ^{210}Pb is large. As with the Olympic Sam samples the ^{210}Pb is higher in activity in comparison to the other ^{238}U radionuclides. From site 3 the ^{210}Pb and ^{228}Th were the only radionuclides detected, where no ^{228}Ra was detected at all in either species.

3.4. Discussion

NORM series radionuclide activities have been determined for soil and vegetation samples from Olympic Dam and Flinders Ranges regions, the samples analysed were soil from 0-10 cm and vegetation branch clippings. Overall, Olympic Dam radionuclide activity concentration is low in comparison to 'normal soil' ranges. Often at the sites outside of the mining lease area the activity is well below the low end of the normal range i.e., <20 Bq/kg for soil. This has provided an instrumental and statistical challenge in quantifying the activities due to the very low activities. All of the soil activity results from Olympic Dam in Autumn 2018 have been below or on the lower side of the normal range of activity for soils. There was a large variability in soil activity from the ^{238}U decay series results across different sites, however, also within the same sampling sites. The large variability is likely due to the very low activity near the LOD, this creates greater statistical variability. This is also true for the activity of the vegetation at Olympic Dam, where the activity was very close to the LOD, there were multiple cases where activities were below the LOD and therefore, not reported.

From the Olympic Dam region three different vegetation species have been compared from the same sites and, *Dodonaea viscosa* tends to accumulate higher activity of radionuclides compared to *Acacia ligulata*. *Astrebla pectinata* overall contained the highest levels of ^{210}Pb and ^{212}Pb, except the lowest activity of the other radionuclides. *Astrebla pectinata* did not contain detectable ^{228}Ra at any of the sample sites. The activity of radionuclides in most cases is below the lower end of the normal activity range for soil of 20 Bq/kg. With the exception of a sample from the pilot site being above the high end of the normal range for ^{230}Th, ^{234}U and ^{238}U, this is likely due to the sample containing some mining process material such as ore or processed ore, due to the nature of the sampling site. The Read and Pickering (1997) results

in comparison to the present study, when comparing to the tailings site, the results from the raise bore site are higher overall. However, the results from the Read and Pickering tailings site are in close agreement with the pilot site from the present study. The comparison to the Read and Pickering 1999 study showed close agreement of the activity of radionuclides from their tailings site to the pilot site from this present study (Read & Pickering, 1999). The comparison of the control site, the Read and Pickering is 5km away from the tailings site therefore is comparable to the Roxby Downs site of this present study.

From the Flinders Ranges region, the activity concentration overall has been found to be around the higher end or above the 'normal ranges' however the activity across the different sampling sites was found to be very consistent. The level of activity is attributed to the natural background radiation in the region. Further analysis of the *Astrebla pectinata* from both the Olympic Dam and Flinders Ranges Region is required to make conclusions regarding the activity of radionuclides within this species. At sample site 3, the only radionuclide detectable for *Astrebla pectinata* was ^{210}Pb and no ^{226}Ra or ^{228}Ra were detectable in *Eremophila freelingii*. The activity variation of radionuclides within the same site and across all sites within the Flinders ranges region is very consistent within each radionuclide.

Flinders ranges soils and plants fall within the normal range and the results are much more consistent. This highlights the issues at Olympic Dam and its low levels, near detection limits in low levels greater statistical variability. At the Flinders Ranges region the soils are in part derived from weathering of the granite in the Flinders Ranges which are high in U minerals, leading to higher activities and higher natural background radiation at this site. Other rocks which are rich in U in this region include gneisses which may have high U and Th content. The area near the Paralana spring within the region contains palaeosol which has U concentrations of 150 ppm, this palaesol is also rich in lanthanides (Hill & Hore 2011). Olympic Dam on the other hand, the soils are largely quartz-based sands, the U orebody in the associate granites are over 300 m below the surface. From the Flinders ranges region, the activity overall has been found to be around the higher end or above the 'normal ranges' however, the Flinders ranges region in Australia has a high natural background due to the geological composition of the site (Brugger et al., 2005).

Another major difference between the two sites is the vastly different methods implemented for mining the U ore. As Olympic Dam implements an underground stope mining method, followed by transporting the ore to the surface, milling it to a powder followed by chemical processing. Dust deposition and contribution from Rn and daughters is of consideration for this site, whereas the Beverley site which is adjacent to the Flinders Ranges implement the ISR method for mining the U ore. The ISR method is preferred when considering the environmental disturbance as minimal surface interruptions occur as a result (Woods, 2011). Therefore, a different profile of radionuclides is present from both sites is observed, less contribution from Rn and daughters are observed from the Flinders Ranges region and radioactive equilibrium is more established within the soils from this region. When considering the differences in radionuclide activity concentrations at the different environmental sites at Olympic Dam, they were generally higher as the pilot and raise bores sites as this was the closest sites to the mining activities.

Radionuclides below radon in the decay series, for NORM radionuclides, overall, were higher in concentration in comparison to the early radionuclides in the ^{238}U decay series. This is likely due to the contributions of radon daughters and wet and dry fallout deposition from the atmosphere (Eitrheim et al., 2016; Landsberger et al., 2017; Michalik et al., 2018). Overall, the activity of the samples analysed from the Olympic Dam region are lower in comparison to the Flinders Ranges region, however, they are far more inconsistent across site and species and individual samples in comparison to the results from the Flinders Ranges region. In general, there was more of consistency in the activity measured from the Flinders Ranges region. The analysis of the activity of environmental NORM samples has proven challenging, this is due to the overall low activity of the samples. as the activity is low, or close to the MDA. The activities determined above will be used to determine concentration ratios for the arid Australian environment. Two distinctly different arid environments, the Olympic Dam and Flinders Ranges regions were analysed.

The conclusions from the alpha spectroscopy results were based on a comparison of the two methods for ^{210}Po analysis show that in some cases, the activity is outside of the uncertainty for the ^{210}Po analysis. This further emphasises the statistical issues with very low activity samples. A paired T-test was performed, and the results show that P = 0.149 (two tail). This

indicates that there is statistically no difference within the activities measured from the samples using both methods. Therefore, it is the recommendation when dealing with vegetation samples of complex matrix using the effluent from the UTEVA column for Po and Ra analysis instead of digesting a separate sample at a controlled temperature. Another suggestion is performing a hexane wash following the vegetation digestion step to remove the oils from the sample. This research has shown that the effect of the ^{210}Po volatility on alpha spectroscopy sample digestion is negligible when comparing the extraction from UTEVA column effluent when dealing with complex sample matrices, whilst remaining in an aqueous form.

Disequilibrium within the system is inevitable as they are environmental soil samples, with dust deposition and radon progeny contribution (Eitrheim et al., 2016; Landsberger et al,, 2017; Michalik et al., 2018). Due to α-recoil processes occurring from radioactive decay of ^{238}U and daughters, the mobility of ^{234}U within natural systems is often higher than its parent ^{238}U leading to an excess of ^{234}U in groundwater (Yanase et al., 1995). Any corresponding depletion of ^{234}U in the solid soil phase is generally less pronounced, this was not observed in these samples as the activity of ^{238}U and ^{234}U are in good agreement.

A study by Mamand *et al*. (2020) found *Dodonaea viscosa* to accumulate higher concentrations of Pb form polluted soil in comparison to three other species. The reason for *Dodonaea viscosa* accumulation was proposed to be due to the fibrous root system, with a large surface area (Mamand et al., 2020). This is consistent with the finding from this present study, as *Dodonaea viscosa* accumulating a higher concentration of radionuclides in comparison the *Acacia ligulata*.

The activity of ^{232}Th within vegetation is very low within both species, where the soil ^{232}Th activity is ~5 Bq/kg. The activity of ^{230}Th is also lower in vegetation compared to soil, this is likely due to the low solubility of Th (Yanase et al., 1995). Elements with low solubility will be present within the vegetation at much lower concentrations in comparison to the media. There is higher activity of ^{210}Po in the *Dodonaea viscosa* compared to the *Acacia ligulata* and the soil. As ^{210}Po follows radon gas in the ^{238}U decay series, there is potential for the radon to

be taken in by gas exchange from the vegetation and then decay through the series within the plant (Li et al., 2018).

There are limited literature values of radionuclides within vegetation from the arid Australian environment, however a previous study by Read and Pickering 1997, found *Acacia ligulata* activity from the Olympic Dam region results for the control site were (n=3) ^{238}U <2 Bq/kg, ^{230Th} <5 Bq/kg, ^{226}Ra <18 Bq/kg, ^{210}Pb 13±1.3 Bq/kg and ^{210}Po <3 Bq/kg. The control sites from this study were at least 5 km from the TRS. The *Acacia ligulata* results for the tailings site were (n=3) ^{238}U = 5.2±0.5 Bq/kg, ^{230}Th 23±5 Bq/kg, ^{226}Ra <18 Bq/kg, ^{210}Pb 40 ±16 Bq/kg and ^{210}Po 8.7 ±1.6 Bq/kg (Read & Pickering, 1999). The results from the Read and Pickering 1997 study, in comparison to the present study show the ^{210}Po activity is in agreement with the Tailings site activity to the present study. Other radionuclides from this present study are lower than the Read and Pickering (1999) study.

A study by Toro Energy in 2011, have previously reported radionuclide concentrations for Acacia species from the Wiluna U project, there the average activity of ^{238}U was 9 Bq/kg, ^{230}Th is 1.0 Bq/kg, ^{226}Ra is 2.5 Bq/kg, ^{210}Pb is 95 Bq/kg, ^{210}Po is 52 Bq/kg and ^{228}Ra is 2.1 Bq/kg (Toro Energy, 2011). The results from this present study show that in comparison to the *Acacia* species from Wiluna, ^{238}U was in good agreement, ^{230}Th was in good agreement across all sites except for the raise bore and pilot sites and the ^{226}Ra activity for the present study are higher than reported by Toro.

Overall, the composite samples provide a good idea of the activity of the vegetation within the Olympic Dam mining area and surrounding vicinity. However, it is important to also understand the variation of radionuclide activity within the same species at the same environmental site. Therefore, individual plants of the same species within the same environmental monitoring site have been analysed and are discussed in the next section. This is also paired with replicate soil results from the same environmental sites to understand the variability of radionuclide concentration throughout the soil of the same location.

From the alpha spectroscopy method development section, further dilution of the sample may allow for the Fe coprecipitation to occur due to a dilution of the complex matrix. This

may reduce the chance of wax hindering the Fe from precipitating. However further studies are required to explain this in detail. A solution to the problem of the complex matrix which contains oils would be to perform a liquid-liquid extraction on the sample following the digestion step. A hexane wash should remove the oils within the samples, however, further work would be required to determine whether the hexane wash removes any radionuclides from the sample (Islam et al., 2020). Using a furnace to incinerate the samples prior to analysis may have removed the wax causing the interference within the samples, however this method would not be appropriate for the analysis of ^{210}Po due to volatility (Kim et al., 2012; Seiner et al., 2014). This further emphasises the use of the UTEVA effluent as an alternative. As the digestions never reach a full dryness and the samples remain in solution, lowering the risk of ^{210}Po loss, compared to incineration. A previous study by Seiner et al., 2014, studied the loss of Po during digestions, this study concluded that Po loss was minimised when using a wet ash in comparison to a dry ash. However, the interference of organic matter within the sample was not discussed (Seiner et al., 2014). Other studies have explored closed vessel microwave digestion prior to alpha spectroscopy analysis, a study by Salar 2007, used this for soil digestions (Amoli et al., 2007).

When considering the activity of U, Th and Ra in 'normal' soils to be 20-70 Bq/kg, the activity of the soils at Olympic Dam are very low (Long, 2012; Nations, 2000). The normal range of ^{210}Po is 20-240 Bq/kg in soil (Thakur & Ward, 2020). This is due to the nature of the arid Australian environment with 'islands of fertility' this is also as the activity is very low. Therefore, there appears to be a large variation, but in comparison to the activity range of 'normal soils' the activities are all reasonably similar, when considering the context of the scale. Overall, there is a high variation of activity within the same species from the same sampling site, this may be due to the age, size, lifespan and surface area of the individual plants. A brief seasonal comparison was performed on the alpha spectroscopy data collected on soil and vegetation. In most cases the soil results showed higher activities for the samples collected in Spring in comparison to those collected in Autumn. This is possibly due to the differences in the plant growth cycles between seasons (Rea et al. 2021). The *Acacia ligulata* vegetation shows no observable variability with season of collection. The *Dodonaea viscosa* has shown to have higher activity of radionuclides in Autumn in comparison to the samples collected in Spring.

The UNCEAR worldwide background range of ^{238}U is on average 0.035 Bq/g (35 Bq/kg) and ranges from 0.016-0.110 Bq/g and ^{232}Th an average of 0.030 (30 Bq/kg) with a range of 0.011 to 0.064 Bq/g (UNSCEAR, 2000). The IAEA worldwide background ranges state ^{238}U at an average of 0.025 Bq/g (25 Bq/kg) with a range of 0.010-0.050 Bq/g and ^{232}Th with an average of 0.025 Bq/g (25 Bq/kg) and range of 0.007-0.050 Bq/g (IAEA, 2000).

3.5. Conclusions

Overall, the Olympic Dam radionuclide concentration results show that the activity concentration is very low in comparison to the normal ranges. In most cases the radionuclide concentration at Olympic Dam is well below the normal ranges of 20 Bq/kg outlined by Long (2012). When comparing to other literature background ranges, the data from this study, on most occasions, is either in agreement or well below (UNSCEAR, 2000; IAEA, 2000)).

Overall, from the Olympic Dam results there are higher concentrations of radionuclides present in the vegetation in comparison to the soil, this indicates that the vegetation are accumulating radionuclides within them. The radionuclides within the same decay series analysed from the Olympic Dam region are not in equilibrium, especially the radionuclides below radon. This suggests there may be contribution to the overall radionuclide concentrations in environmental soils from Radon progeny within the region. The possibility for deposition of fallout from radon daughters within the atmosphere causing a higher activity concentration of Po within the vegetation, this concept will be explored further in chapter 7 (Matthews et al., 2007; Shahid et al., 2017; Skwarzec et al., 2001; Thakur & Ward, 2020). The soil from the Olympic Dam region will be studied further in Chapter 4 to understand the radionuclide contribution from radon progeny and from dust deposition.

There are activity results from the Flinders ranges region samples are more consistent overall. The activity concentration of radionuclides within this region is due to the natural geology and the soil composition including weathered granite from the Flinders Ranges. The activity concentration across the Flinders Ranges region was consistent.

An important consideration to make when reviewing the data is that the activities are low in comparison to. Especially for the Olympic Dam region, where there is very low background radioactivity, to the point where it becomes a statistical challenge to quantify. Due to this, the range in the activity across the samples is quite large, however, this may be skewed due to the statistical issues with measurements very close to the MDA.

Chapter 4. Radionuclide concentration ratios from soil to vegetation and ERICA dose assessments

The data which are derived and discussed in detail in this chapter are from the author's collaborative contribution to the paper titled "Radionuclides and stable elements in vegetation in Australian arid environments: Concentration ratios and seasonal variation" by M. A. D. Rea *et al*. that has been published in the *Journal of Environmental Radioactivity*. These data were obtained using the methodology discussed in the preceding chapters.

4.1. Introduction

The activity results from section 3.3.1, from the arid Olympic Dam and Flinders Ranges regions will be used to calculate concentration ratios. These concentration ratios will be used within the ERICA software to predict dose rates to the organisms analysed. This research will determine whether the activity of radionuclides transferring from soil to organism in the Australian arid climate compares to literature values. This data will also determine where the organisms sit within the dose response curve for biota, discussing whether the radionuclides will impact the vegetation.

A case study was performed to determine whether the radionuclide transfer from soil to vegetation in the arid Australian context is consistent with other localities and the WTD. Therefore, determining whether the current CR data within the WTD is appropriate for estimation of radiological dose using the ERICA tool for Australian species in the arid Australian environment (Beresford et al., 2008; Brown et al., 2008; Hirth et al., 2017).

4.1.1. Chapter directions

Within this chapter, a case study of samples from the Olympic Dam and Flinders Ranges Regions were analysed to determine whether the current internationally accepted environmental radiation monitoring tools are acceptable for use within the arid Australian environment. This chapter develops a set of radionuclide concentration ratios for shrubs within the arid Australian environment. Vegetation to soil concentration ratios were calculated for soil and vegetation from the Olympic Dam and Flinders Ranges regions within the arid zone of South Australia. The activities used within the concentration ratio calculations were determined in chapter 3.

Overall, this chapter research will determine whether ERICA assessments using the generic averages from the current WTD data are appropriate for native Australian species within the arid Australian environment. To use the developed soil to vegetation concentration ratios and use the ERICA tool to model the predicted dose that the organism would receive using the newly developed concentration ratios. To determine whether the activity of radionuclides transferring from soil to organism in the Australian arid climate compares to literature values.

4.2. Experimental

The data from the alpha and gamma spectroscopy from chapter 3 are analysed and interpreted to obtain CRs and ERICA assessments. Where the number of samples is referred to as 'n' this represents individually collected samples. Wet mass was used for all reference to vegetation within this chapter.

4.2.1. CR Determination

An example CR determination equation is shown below in Equation 4.1. for the CR of the ^{210}Po from the arid mine within *Acacia ligulata* from the composite samples composed of the May 2018 samples.

$$CR_{WO} = \frac{Plant\ Mass_{Dry}}{Plant\ Mass_{Fresh}} * \frac{Plant\ Activity_{Dry}}{Soil\ Activity}$$

$$CR_{WO} = \frac{0.0026\ kg}{0.0036\ kg} * \frac{19.65\ (Bq/kg)}{7.823\ (Bq/kg)}$$

$$CR_{WO} = 0.69 * 2.51$$

$$CR_{WO} = 1.75$$

Equation 4.1. Concentration ratio equation (CR$_{WO}$ = Concentration ratio of the whole organism).

Therefore, the concentration ratio of ^{210}Po for the *Acacia ligulata* composite sample to soil is 1.75.

4.2.2. Environmental risk from ionising contaminants: assessment and management (ERICA) tool

Tier 1 assessment

Tier 1 assessments were performed using the ERICA software, version 1.3.1.51 (Brown et al., 2016). The ecosystem input chosen was 'terrestrial' which automatically assigns the reference organism as 'lichen and Bryophytes', where the reference organism details can be found at (Brown et al., 2008; UNSCEAR). The dose rate screening value was selected as 10 µGy h^{-1} (Andersson et al., 2009). The measured site-specific media concentrations were entered into the software as Bq/kg. The output from the tier 1 assessment was a risk quotient value and a dose rate value which determines whether the dose received by the organism is above or below the screening value. If the results are below the screening value, then the assessment

is finished, if the results are above the screening value, then a tier 2 assessment is recommended.

Tier 2 assessment

Tier 2 assessments were performed, as there is an option to choose the reference organism here, the reference organism chosen was either 'grasses and herbs' or 'shrub or tree' depending on the species. There is an option for either a 'single point', spatial series of data (multi-site assessment in the same ecosystem), or a temporal series of data (times series assessment for a single site) or combination of spatial and temporal series. Single point assessments were performed within this study. The dose rate screening value of 10 µGy h^{-1} was selected with an uncertainty factor of 3 which allows for a 5% probability of exceeding the dose screening value. The default concentration ratios from the WTD were used along with the CRS determined from this study. The activity of the media and organism was included. The occupancy factor was 1 for all vegetation. The radiation weighting factors were left as the default values; therefore, alpha was 10, beta/gamma was 1 and low beta was 3.

The results from the tier 2 assessment include extremal dose rates, internal dose rates, total dose rates, activity concentration in organism, activity concentration in soil or air, risk quotient and total dose rate per organism. At the end of the assessment a risk quotient is provided based on the input data, if the dose rate is determined to be higher than the screening value, a tier 3 assessment is recommended. Tier 3 ERICA assessments involve the same input parameters at tier 2 assessments however, the assessment is run probabilistically and is therefore, out of the scope of this present research.

4.3. Results

To determine concentration ratios (CR) of radionuclides from corresponding soil and vegetation samples, wet to dry mass calculations must be known for vegetation. The radionuclide analysis was performed on dry samples therefore, a conversion to fresh mass is required prior to CR calculations (Johansen & Twining, 2010). Therefore, drying factors for the vegetation species of interest were determined experimentally and the results from this are detailed below.

4.3.1. Vegetation drying factors

Olympic Dam vegetation drying factors

The experimentally determined wet to dry mass conversion is in appendix C. The average mass lost between wet samples and freeze-dried samples of *Acacia ligulata* is 43.73 % (SD = 1.43) and an average % mass loss from air drying of 39.65% (SD = 1.35) of mass lost from wet weight to air dried weight for *Acacia ligulata*. The average mass lost between wet samples and freeze-dried samples of *Dodonaea viscosa* is 26.68 % (SD = 0.806). With an average % mass loss from air drying of 21.47 % (SD = 0.705) of mass lost from wet weight to air dried weight for *Dodonaea viscosa*. The wet to dry mass loss conversion for the *Astrebla pectinata* was 11.02%. This experiment was performed on the Flinders Rangers Region samples however the same mass was used here. Therefore, the experimentally determined values of 43.73%, 26.68% and 11.02% for *Acacia ligulata, Dodonaea viscosa* and *Astrebla pectinata* respectively will be used in all concentration ratio equations.

Flinders Ranges vegetation drying factors

The results from the drying experiment for the Flinders Ranges species, *Astrebla pectinata , Eremophila freelingii* and *Acacia victoriae* are found in appendix C. The average wet to dry mass lost from the *Astrebla pectinata* was 11.02%. The wet to dry mass loss of *Eremophila freelingii* was 9.06% and the mass loss of *Acacia victoriae* was 10.45% when freeze dried. These mass loss conversions were used for concentration ratio calculations.

Concentration ratios (CRs)

Using the results from the vegetation drying factors and alpha and gamma spectroscopy CRs are calculated below. The CRs calculated within this section are from the data from chapter 3, this includes the results from the autumn and spring collections as well as the composite and replicate results. Concentration ratio determination for the species of interest and the corresponding soil analysis were calculated. The vegetation drying factor of a mass loss from wet to freeze dry of 26.67% for *Dodonaea viscosa* and 43.75% for *Acacia ligulata*. From the composite samples that were analysed for different radionuclide activity using alpha spectroscopy, soil and vegetation results have been used to calculate concentration ratios.

The concentration ratios for the composite samples from Olympic Dam collected in May 2018 are shown below in Table 4.1.

4.3.2. Olympic Dam Autumn (May 2018) CRs

Composite CRs

CRs were determined using the vegetation activity and the corresponding soil 0-10 cm from Autumn (May) 2018. The individual CR calculations are in the appendix D. However, the summary of the composite CRs is in Table 4.1 below. The concentration ratios determined from alpha spectroscopy from the Olympic Dam samples collected from during May 2018 and are composited are shown below in Figure 4.1.

Table 4.1. Alpha spectroscopy samples composite from May 2018 sampling CR Summary Table.

Site	Species	Concentration Ratios						
		^{232}Th	^{230}Th	^{238}U	^{235}U	^{234}U	^{210}Po	^{226}Ra
South Control	*Dodonaea viscosa*	0.024	0.093	0.412	0.789	0.337	5.238	0.215
Pilot	*Dodonaea viscosa*	0.027	0.211	0.492	0.282	0.431	2.044	0.323
Roxby Downs	*Dodonaea viscosa*	0.020	0.141	0.573	0.262	0.291	5.928	0.181
Raise Bore	*Dodonaea viscosa*	0.118	0.506	0.385	0.283	0.394	1.046	0.298
Arid	*Dodonaea viscosa*	0.052	1.290	6.593	5.425	5.355	8.692	6.010
Arid	*Acacia ligulata*	0.002	0.048	1.158	0.893	0.927	1.747	3.491
Raise Bore	*Acacia ligulata*	0.067	0.250	0.139	0.156	0.133	0.706	0.218
North Control	*Acacia ligulata*	0.020	0.102	0.415	N/A	0.225	0.967	2.257
South Control	*Acacia ligulata*	0.007	0.052	0.457	N/A	0.196	0.136	0.168
Roxby Downs	*Acacia ligulata*	0.016	0.090	0.347	0.637	0.235	1.679	2.296
Pilot	*Acacia ligulata*	0.018	0.180	0.247	0.243	0.252	22.233	0.245
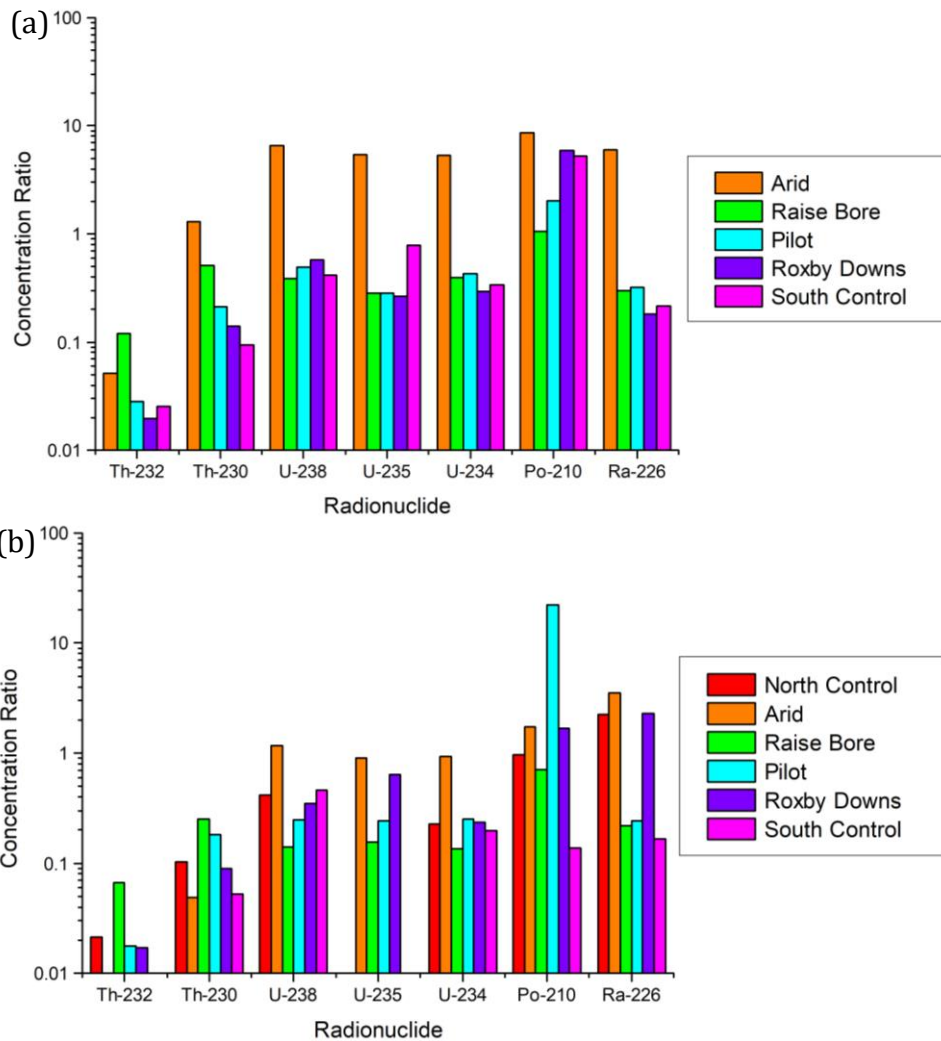
Figure 4.1. CRs from Olympic Dam vegetation species from composite samples May 2018, measured using alpha spectroscopy (a) Dodonaea viscosa (b) Acacia ligulata.

Figure 4.1. shows that there is a difference overall between the CRs from the two species. The data also show substantial within-species variation as the data ranges over 3 orders of magnitude for both species. The CRs are slightly more consistent for the *Dodonaea viscosa* in comparison to the *Acacia ligulata*. For the *Dodonaea viscosa*, there is consistency across the raise bore, pilot, Roxby Downs and south control sites. The arid zone site shows significantly higher CRs across all radionuclides excluding [232]Th. The *Dodonaea viscosa* CRs for [210]Po were consistent across the arid, Roxby Downs and Pilot sites. This is consistent with the activity of [210]Po in *Dodonaea viscosa* being higher in comparison to the *Acacia ligulata*.

Replicate CRs

CR from Autumn (May) 2018 Replicate Samples were determined using the vegetation activity and the corresponding soil 0-10 cm. The CRs are calculated from the activities measured from the Flinders University gamma spectrometer. The individual CR calculations are in Table 4.2 below. The replicate CRs are shown below in Figure 4.2.

Table 4.2. CRs from Olympic Dam May 2018 Replicate analysis, gamma spectroscopy.

Species	Site		CRs	
			^{214}Pb	^{212}Pb
Acacia ligulata	North Control	1	0.054	-
Acacia ligulata	North Control	2	0.066	3.494
Acacia ligulata	North Control	3	0.078	-
Acacia ligulata	Arid	2	0.014	-
Acacia ligulata	Raise Bore	1	0.034	-
Acacia ligulata	Raise Bore	2	0.080	-
Acacia ligulata	Raise Bore	3	0.023	2.071
Acacia ligulata	Pilot	1	0.014	1.108
Acacia ligulata	Pilot	2	0.015	-
Acacia ligulata	Pilot	3	0.052	-
Acacia ligulata	Roxby Downs	2	0.067	-
Acacia ligulata	Roxby Downs	3	0.071	1.820
Acacia ligulata	South Control	1	0.061	-
Acacia ligulata	South Control	2	0.040	-
Dodonaea viscosa	Arid	1	0.194	-
Dodonaea viscosa	Raise Bore	2	0.062	-
Dodonaea viscosa	Raise Bore	3	0.001	-
Dodonaea viscosa	Pilot	2	0.096	-
Dodonaea viscosa	Pilot	3	0.050	-
Dodonaea viscosa	Roxby Downs	1	0.050	-
Dodonaea viscosa	Roxby Downs	2	0.085	-
Dodonaea viscosa	Roxby Downs	3	0.108	-
Dodonaea viscosa	South Control	1	0.062	-
Dodonaea viscosa	South Control	2	0.024	-
Dodonaea viscosa	South Control	3	0.022	1.670
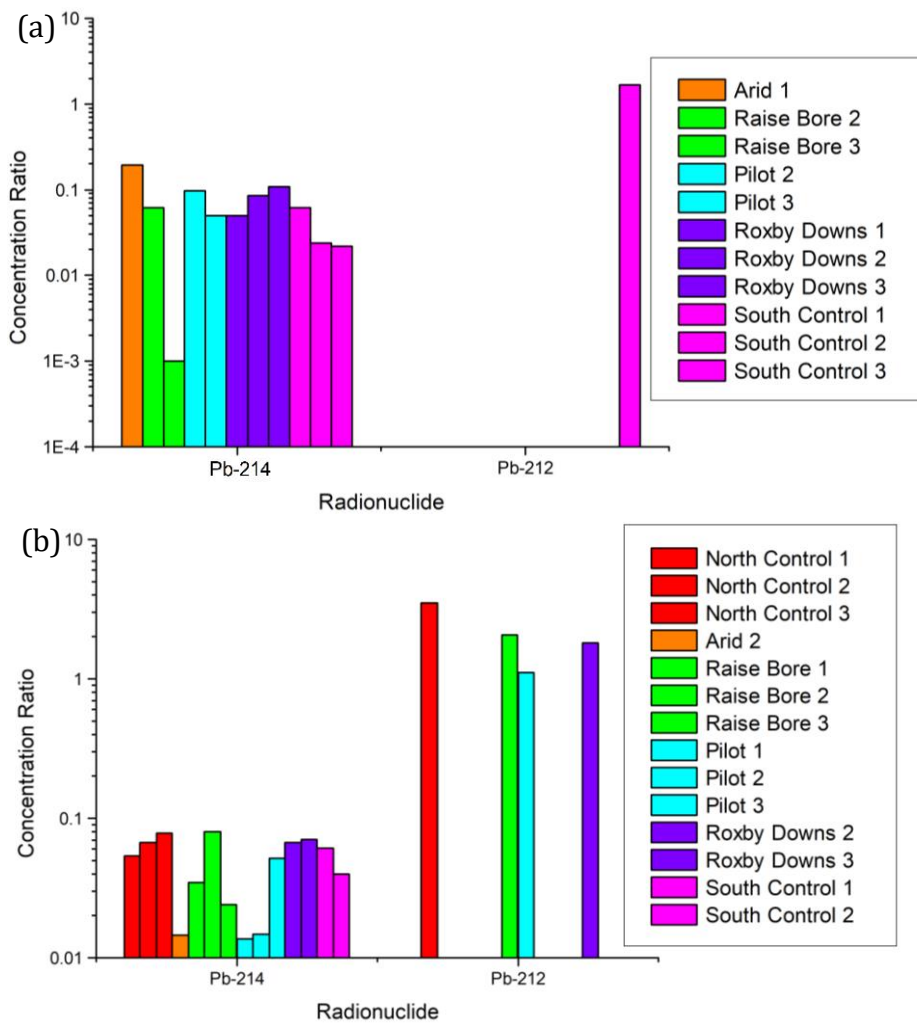
Figure 4.2. CRs from Olympic Dam May 2018 Replicate analysis, gamma spectroscopy. (a) Dodonaea viscosa, (b) Acacia ligulata.

The CRs shown in Figure 4.2 shows a large amount of variability, spread over greater than one order of magnitude for the *Acacia ligulata*. The *Dodonaea viscosa* CRS are spread over 3 orders of magnitude. This is consistent with the Olympic Dam results. The only *Dodonaea viscosa* sample that has [212]Pb detectable above the MDA for both the soil and vegetation, and therefore, a CR was determined, was south control 3.

4.3.3. Olympic Dam Spring (November 2018) CRs

Composite CRs

CR from Spring (Nov) 2018 Composite Samples were determined using the vegetation activity and the corresponding soil 0-10 cm. The CRs are calculated from the activities measured from the ANSTO gamma spectrometer. The individual CR calculations are in the appendix D. However, the summary of the composite CRs is in Table 4.3 below. The composite CRs are shown below in Figure 4.3.

Table 4.3. Olympic Dam Spring (Nov 2018) CRs.

Site	Species	^{210}Pb	^{226}Ra	^{228}Ra	^{228}Th	^{238}U
North Control	*Dodonaea viscosa*	-	2.906	-	0.613	-
Arid	*Dodonaea viscosa*	-	0.652	-	0.167	-
Raise Bore	*Dodonaea viscosa*	3.433	0.957	-	0.252	-
Pilot	*Dodonaea viscosa*	1.248	0.216	-	-	1.170
Roxby Downs	*Dodonaea viscosa*	-	0.381	0.217	0.166	-
South control	*Dodonaea viscosa*	3.501	-	-	-	-
North Control	*Acacia ligulata*	-	0.577	-	1.577	-
Arid	*Acacia ligulata*	-	0.771	1.871	1.097	-
Raise Bore	*Acacia ligulata*	1.230	0.451	0.451	-	-
Tailings	*Acacia ligulata*	2.746	0.585	1.090	0.880	-
Pilot	*Acacia ligulata*	0.394	0.412	0.421	-	-
Roxby Downs	*Acacia ligulata*	-	1.104	1.298	0.770	-
South Control	*Acacia ligulata*	1.930	1.164	2.600	-	-
Tailings	*Astrebla pectinata*	12.99	2.470	-	0.894	-
South Control	*Astrebla pectinata*	7.817	-	-	-	-
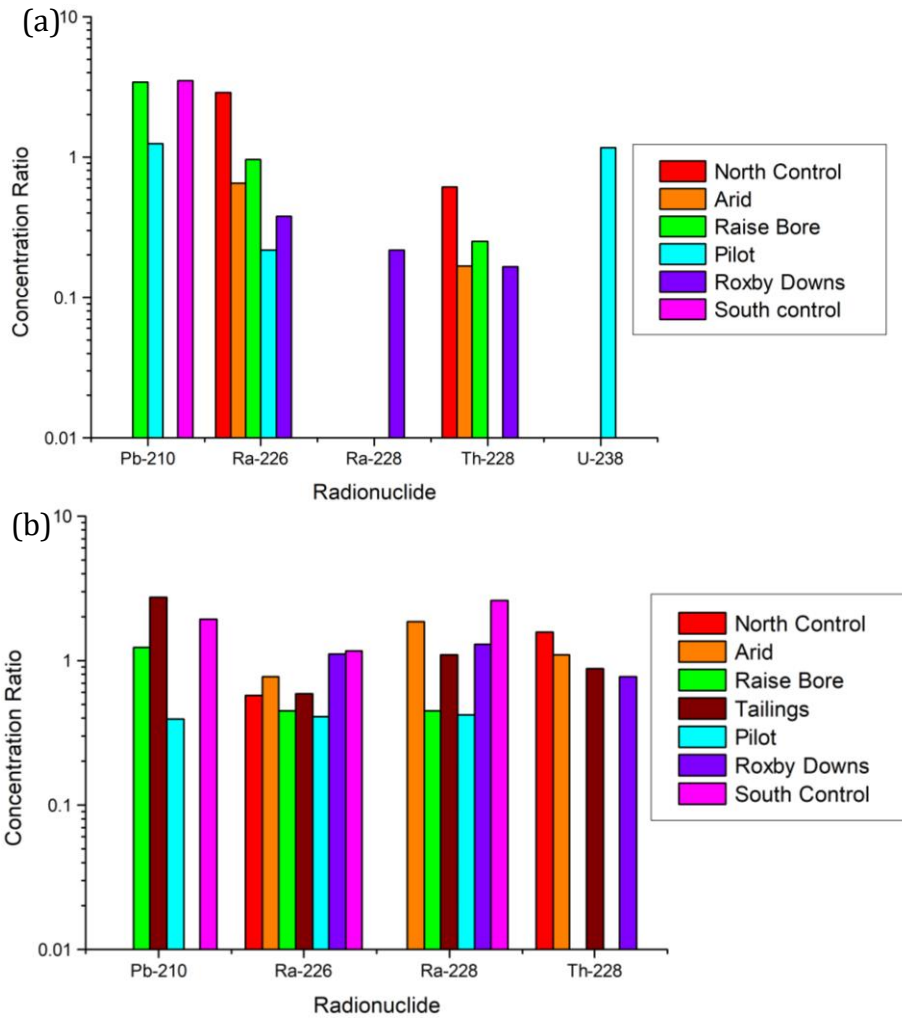
Figure 4.3. Olympic Dam Spring (Nov 2018) CRs (a) Dodonaea viscosa (b) Acacia ligulata.

The CR results from Figure 4.3 show that the *Dodonaea viscosa* shows more variation in comparison to the *Acacia ligulata*. The *Acacia ligulata* CRs are spread over one order of magnitude, and the *Dodonaea viscosa* CRs are over 2 orders of magnitude.

Replicate CRs

CR from Spring (Nov) 2018 replicate Samples were determined using the vegetation activity and the corresponding soil 0-10 cm, The CRs are calculated from the activities measured from the ARPANSA alpha spectrometer. The individual CRs are shown in Table 4.4 below. The replicate CRs are shown below in Figure 4.4.

115

Table 4.4. CRs Alpha spectroscopy (ARPANSA).

Site	Species	Replicate	^{230}Th	^{232}Th	^{234}U	^{235}U	^{238}U	^{210}Po	^{226}Ra
Tailings	*Acacia ligulata*	1	3.087	0.150	2.721	3.159	2.995	6.460	-
Tailings	*Acacia ligulata*	2	0.335	0.064	0.424	0.361	0.413	0.728	0.107
Tailings	*Acacia ligulata*	3	0.349	7.243	0.669	0.792	0.717	0.033	-
Raise Bore	*Dodonaea viscosa*	1	29.389	0.458	23.947	26.975	27.554	28.17	-
Raise Bore	*Dodonaea viscosa*	2	0.592	0.046	0.825	0.911	0.910	1.499	0.110
Raise Bore	*Dodonaea viscosa*	3	0.046	4.807	-	-	-	1.652	-
Pilot	*Dodonaea viscosa*	1	0.090	2.500	-	-	-	11.84	-
Pilot	*Dodonaea viscosa*	2	0.013	-	-	-	-	0.462	-
Pilot	*Dodonaea viscosa*	3	1.503	13.641	-	-	-	24.41	-
Arid	*Acacia ligulata*	1	0.019	0.337	-	-	-	2.420	-
Arid	*Acacia ligulata*	2	0.031	0.345	-	-	-	2.713	-
South Control	*Acacia ligulata*	1	0.026	0.008	0.100	0.122	0.120	1.069	-
South Control	*Acacia ligulata*	2	0.053	0.006	0.102	0.155	0.108	0.869	-
South Control	*Acacia ligulata*	3	0.056	0.028	0.266	0.609	0.227	1.472	-
North Control	*Dodonaea viscosa*	1	0.305	0.068	0.831	2.670	0.794	5.275	-
North Control	*Dodonaea viscosa*	2	0.253	0.032	1.023	0.921	1.290	5.405	-
North Control	*Dodonaea viscosa*	3	0.105	0.042	0.831	-0.039	0.533	-	-
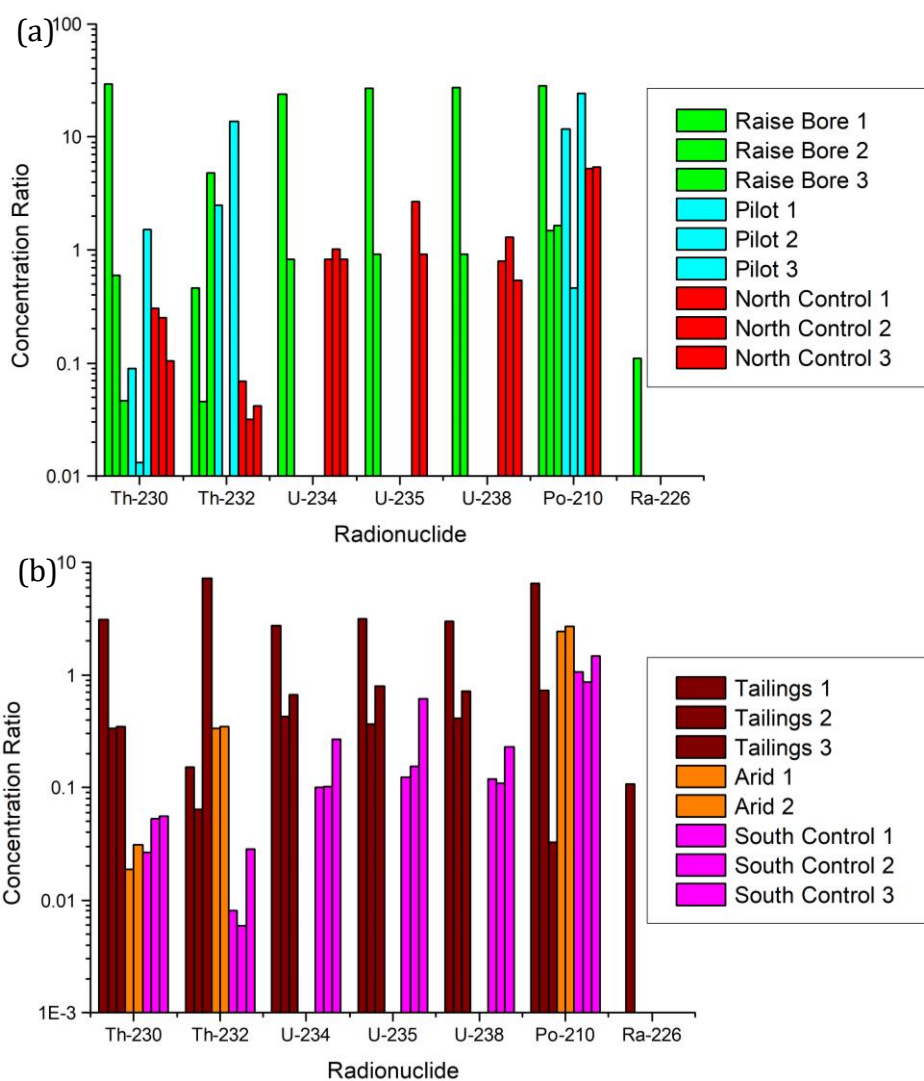
Figure 4.4. CRs Olympic Dam, November 2018, (a) Dodonaea viscosa, (b) Acacia ligulata.

In some cases, the *Dodonaea viscosa* was an order of magnitude higher than the *Acacia ligulata*. The *Dodonaea viscosa* CRs are spread over 3 orders of magnitude. The *Acacia ligulata* CRs are also inconsistent and spread over a large variability, around 3 orders of magnitude.

4.3.4. Flinders Ranges CRs

The drying factors for the Flinders Ranges species that were determines experimentally in this study are from wet to freeze dried is for *Astrebla pectinata* 11.02%, *Eremophila freelingii* 9.06% and *Acacia victoriae* 10.45%. These drying factors are used to calculate the concentration ratio values later within this thesis. The concentration ratios for vegetation from the Flinders Ranges Region are shown in Table 4.5 and Figure 4.5.

Table 4.5. Concentration ratios from the gamma spectroscopy results for Flinders Ranges Eremophila freelingii, Astrebla pectinata and Acacia victoriae.

Species	Site	Plant	Concentration Ratios				
			^{210}Pb	^{226}Ra	^{228}Ra	^{228}Th	^{235}U
Eremophila freelingii	3	1	0.767	-	-	0.013	-
Eremophila freelingii	3	2	0.822	-	-	0.015	-
Eremophila freelingii	3	3	1.155	-	-	-	-
Eremophila freelingii	2	4	0.548	0.078	0.038	0.038	0.403
Eremophila freelingii	2	5	0.525	0.072	0.073	0.057	-
Astrebla pectinata	1	1	0.770	-	-	0.053	0.039
Astrebla pectinata	3	2	0.641	-	-	-	-
Acacia victoriae	1	1	0.860	0.045	-	-	0.037
Acacia victoriae	2	2	0.713	0.096	-	-	0.036
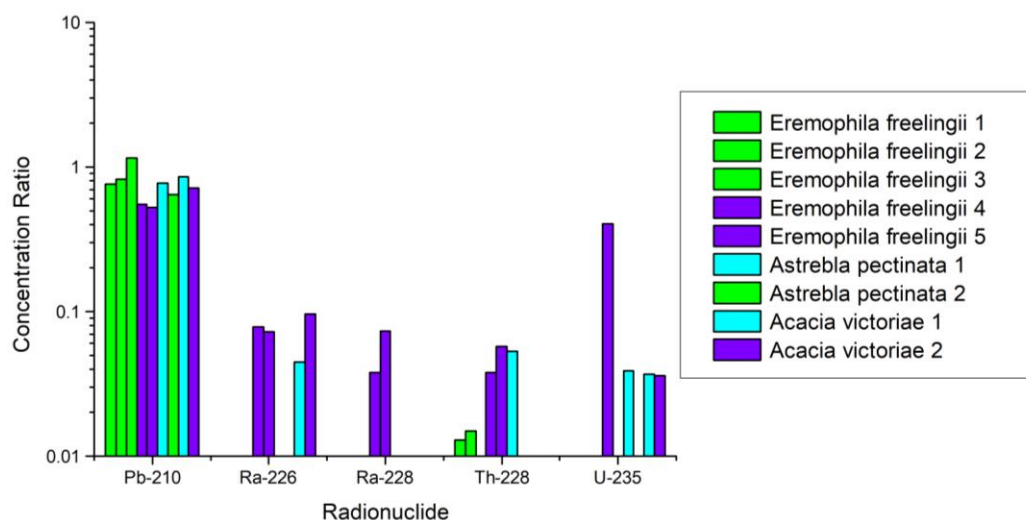
Figure 4.5. Flinders Ranges vegetation concentration ratios (n=1).

Figure 4.5 shows the concentration ratios calculated from the Flinders Rangers region. Overall, the concentration ratios of vegetation from the three species from the Flinders Ranges region are relatively consistent within each radionuclide. The CRs are all below 1.2

and are reasonable consistent. With the exception of ^{210}Pb and a single [235]U result, all CR values are below 1.

4.3.5. Proposed arid Australian shrub CRs

From this study the proposed CRs for use within the ERICA tool for arid Australian shrubs are shown below. The AM, SD, GM and GMSD was calculated for *Astrebla pectinata* for ^{210}Pb only. The [210]Pb (n=2), the minimum is 1.817 and the maximum is 12.99, the AM is 10.404, SD is 2.586, GM is 10.077 and the GMSD is 1.431. The tailings site had [226]Ra at 0.894 and [228]Th at 0.894.

For the Olympic Dam vegetation species, the CRs were analysed statistically, the results for the AM, SD, GM and GMSD have been calculated for each species as a comparison to literature values. The data below is the collation of all CR data collected above, it considers the different seasons and sites. The average CR data is shown in Tables 4.6 and 4.7. This table shows the proposed CR values for the Australian arid environment for shrubs.

Table 4.6. CRs statistical analysis Olympic Dam for the shrubs Dodonaea viscosa and Acacia ligulata.

Species	Radionuclide	n	Min	Max	AM	SD	GM	GMSD
Dodonaea viscosa	[214]Pb	11	0.0014	0.194	0.070	0.051	0.045	3.721
	[230]Th	14	0.013	29.39	2.466	7.480	0.283	6.349
	[232]Th	13	0.020	13.63	1.680	3.710	0.153	9.147
	[234]U	10	0.291	23.95	3.427	6.987	1.022	3.997
	[235]U	10	0.039	26.96	3.855	7.862	0.857	6.207
	[238]U	11	0.385	27.54	3.701	7.732	1.152	3.738
	[210]Po	13	0.462	28.17	7.819	8.503	4.262	3.387
	[226]Ra	11	0.110	6.010	1.114	1.724	0.488	3.406
	[228]Th	4	0.166	0.613	0.299	0.183	0.256	1.849
	[210]Pb	3	1.248	3.501	2.726	1.045	2.465	1.804
Acacia ligulata	[214]Pb	14	0.014	0.080	0.048	0.022	0.041	1.925
	[212]Pb	4	1.108	3.495	2.124	0.867	1.954	1.603
	[230]Th	14	0.019	3.087	0.333	0.770	0.103	3.845
	[232]Th	14	0.001	7.243	0.594	1.848	0.042	8.186
	[234]U	12	0.100	2.721	0.520	0.703	0.307	2.628
	[235]U	10	0.122	3.159	0.712	0.857	0.431	2.743
	[238]U	12	0.108	2.995	0.611	0.772	0.372	2.633
	[210]Po	14	0.033	22.22	3.087	5.526	1.165	4.696
	[226]Ra	14	0.107	3.492	0.988	0.971	0.616	2.964
	[228]Th	4	0.77	1.577	1.081	1.060	1.040	1.368
	[228]Ra	6	0.421	2.600	1.288	0.769	1.046	2.100
	[210]Pb	4	0.394	2.746	1.575	0.868	1.266	2.326

Species	Radionuclide	N	Min	Max	AM	SD	GM	GMSD
Eremophila freelingii	^{210}Pb	5	0.525	0.822	0.762	0.207	0.730	1.382
	^{226}Ra	2	0.072	0.078	0.074	0.001	0.075	1.057
	^{228}Ra	2	0.038	0.073	0.055	0.013	0.053	1.587
	^{228}Th	4	0.013	0.073	0.031	0.015	0.025	2.047
Astrebla pectinata	^{210}Pb	2	0.641	0.770	0.705	0.064	0.701	1.137
Acacia victoriae	^{210}Pb	2	0.713	0.860	0.786	0.073	0.782	1.142
	^{226}Ra	2	0.045	0.096	0.070	0.025	0.066	1.709
	^{235}U	2	0.036	0.037	0.036	0.001	0.036	1.020

4.3.6. Environmental risk from ionising contaminants: assessment and management (ERICA) tool

The concentration ratios determined within this thesis were used within the ERICA tool. The results were then compared to the literature values, other localities, and similar species. The ERICA modelling was performed using version 1.3.1.51. The individual inputs are outlined below.

ERICA limitations, activity calculations and 10-day half-life cut off

To provide a reasonable prediction of the dose the organism is receiving, the activity of the unmeasured radionuclides within the decay scheme needs to be calculated. The ERICA tool includes a <10 day half-life cut off period for progeny for inclusion of dose within the parent for the assessment (Hosseini et al., 2011). In ERICA the radionuclide progeny nuclides activity is assumed to be in equilibrium for the <10 day half-life, these progeny are not included in ERICA as options to assign an activity value within the assessment (Hosseini et al., 2011). Therefore, the dose rate under ^{226}Ra, this is the sum of the dose rates for ^{226}Ra, ^{218}Po, ^{214}Po, ^{214}Bi and ^{214}Po are combined. ^{222}Rn is not considered within the model as it is a gas and assumed to contribute very little dose. Therefore, where a radionuclide is not measured, if it's not included within the <10 day cut off, it must be calculated. Dose assessments will be made using only the measured radionuclides, this will be referred to as the 'lower estimate'. The ERICA assessments where all radionuclides are considered within the decay series is referred to as the 'upper estimate'.

234Pa has a much shorter half-life compared to the [234]Th parent, the [234]Th has a much shorter half-life compared to the [238]U parent, therefore radioactive equilibrium can be assumed between these three radionuclides. Therefore, adding uncertainty to the activities of the remaining [236]Ra group radionuclides. The ^{210}Pb group can all be assumed to be in radioactive equilibrium. From the [235]U chain we also need to consider [231]Pa, [227]Ac, [227]Th and [223]Ra, however, ERICA doesn't have options to include [227]Ac or [223]Ra. For the [232]Th chain we also need to consider [228]Ra and [228]Th. Equations 1.2 to 1.5 detail the activity of radionuclides within a decay scheme. Therefore, the activity of the unmeasured radionuclides needs to be accounted for within the ERICA assessments.

ERICA results

ERICA assessments are usually used to assess potential impacts of operations or industrial activity. The results presented here are from ERICA assessments using the currently widely used default ERICA input parameters. The ERICA assessments were performed on all radionuclide data collected for concentration ratio analysis. The same data was processed through ERICA through tier 1 and 2 to determine the variability in the estimated dose assessment. ERICA modelling has been performed on the CR data collected experimentally (detailed in chapter 3) and was calculated and described earlier within this chapter. The activity concentration of the media determined above was put through the ERICA tool, the tier 1 assessment results are shown below, tier 1 assessments use the activity of the media only. The reference organism used for all Tier 1 assessments is 'Lichen & Bryophytes'. Tier 2 assessments are preformed using the Default CRs available in ERICA and the CRS developed throughout this research, a comparison is made between the dose results from both. Tier 2 parameters included; single point, screening 10 µGy/hr, UF=3, terrestrial, shrub or grass, default radiation weighting factors of α 10. β 1, low β 3. The default CRs used in the tier 2 assessments are Th 6.10E-2, U 6.10E-2, Po 3.30E-1 and Ra 3.30E-1.

ERICA results from Olympic Dam Autumn (May 2018 composite)

Tier 1 assessments for the Olympic Dam May 2018 composite results from alpha spectroscopy detailed above were put through the ERICA tool. The risk assessment is shown below in Table 4.8.

Table 4.8. Olympic Dam Autumn 2018 Composite ERICA Tier 1 results (May 2018) where the reference organism is 'Lichen & Bryophytes', this is calculated using soil activity values.

Site	Lower estimate		Upper estimate	
	Risk Quotient	Risk Colour	Risk Quotient	Risk Colour
North Control	0.411	Green	0.543	Green
Arid	0.303	Green	0.460	Green
Raise Bore	2.329	Red	2.483	Red
Pilot	1.679	Red	1.911	Red
Roxby Downs	0.257	Green	0.405	Green
South Control	0.235	Green	0.365	Green

Tier 2 assessments for the Olympic Dam May 2018 composite results from alpha spectroscopy detailed above were put through the ERICA tool. The calculated dose and risk assessment for *Dodonaea viscosa* are shown below, Table 4.9 contains the lower estimate values and Table 4.10 contain the upper estimate values.

Table 4.9. ERICA tier 2 dose results for the Olympic Dam May 2018 composite results. Dodonaea viscosa from default CRs with ERICA lower estimate.

Site	Radionuclide	External (μGy h^{-1})	Internal (μGy h^{-1})	Total (μGy h^{-1})	RQ	Total dose rate per organism (μGy h^{-1})	Risk Colour
South Control	^{232}Th	2.50E-07	3.68E-03	3.68E-03	0.146	1.457	Green
	^{230}Th	2.42E-07	1.35E-03	1.35E-03			
	^{238}U	1.84E-08	5.76E-03	5.76E-03			
	^{235}U	1.12E-06	1.03E-03	1.03E-03			
	^{234}Th	2.92E-06	1.16E-04	1.19E-04			
	^{210}Po	1.09E-08	1.40E+00	1.40E+00			
	^{226}Ra	3.94E-04	4.64E-02	4.68E-02			
Pilot	^{232}Th	4.05E-07	6.67E-03	6.67E-03	0.366	3.673	Yellow
	^{230}Th	2.15E-06	2.00E-01	2.00E-01			
	^{238}U	6.68E-07	2.50E-01	2.50E-01			
	^{235}U	2.74E-05	9.02E-03	9.04E-03			
	^{234}Th	7.48E-05	3.80E-03	3.88E-03			
	^{210}Po	4.35E-08	2.18E+00	2.18E+00			
	^{226}Ra	5.82E-03	1.02E+00	1.02E+00			
Roxby Downs	^{232}Th	2.80E-07	3.22E-03	3.22E-03	0.154	1.535	Green
	^{230}Th	2.50E-07	1.54E-02	1.54E-02			
	^{238}U	2.20E-08	9.60E-03	9.60E-03			
	^{235}U	1.68E-06	5.15E-04	5.17E-04			
	^{234}Th	3.48E-06	1.20E-04	1.23E-04			
	^{210}Po	9.89E-09	1.44E+00	1.44E+00			
	^{226}Ra	6.82E-04	6.55E-02	6.61E-02			
Arid	^{232}Th	3.00E-07	7.36E-03	7.36E-03	0.46	4.612	Yellow
	^{230}Th	3.35E-07	1.54E-01	1.54E-01			
	^{238}U	3.84E-08	1.56E-01	1.56E-01			
	^{235}U	1.96E-06	1.00E-02	1.00E-02			
	^{234}Th	5.16E-06	2.64E-03	2.65E-03			
	^{210}Po	1.25E-08	2.39E+00	2.39E+00			
	^{226}Ra	6.53E-04	1.90E+00	1.90E+00			
Raise Bore	^{232}Th	2.35E-07	1.33E-02	1.33E-02	0.315	3.163	Green
	^{230}Th	1.93E-06	3.51E-01	3.51E-01			
	^{238}U	1.15E-06	2.76E-01	2.76E-01			
	^{235}U	4.48E-05	1.21E-02	1.22E-02			
	^{234}Th	1.23E-04	4.64E-03	4.76E-03			
	^{210}Po	5.07E-08	1.17E+00	1.17E+00			
	^{226}Ra	9.18E-03	1.32E+00	1.33E+00			

Table 4.10. ERICA tier 2 dose results for the Olympic Dam May 2018 composite results. Dodonaea viscosa from default CRs with ERICA upper estimate.

Site	Radionuclide	External (µGy h^{-1})	Internal (µGy h^{-1})	Total (µGy h^{-1})	RQ	Total dose rate per organism	Risk Colour
South Control	^{232}Th	2.50E-07	3.68E-03	3.68E-03	0.151	1.510	Green
	^{230}Th	2.42E-07	1.35E-03	1.35E-03			
	^{238}U	1.84E-08	5.76E-03	5.76E-03			
	^{235}U	1.12E-06	1.03E-03	1.03E-03			
	^{234}Th	4.01E-08	8.12E-03	8.12E-03			
	^{210}Po	1.09E-08	1.40E+00	1.40E+00			
	^{226}Ra	3.94E-04	4.64E-02	4.68E-02			
	^{231}Pa	2.78E-07	1.15E-03	1.15E-03			
	^{227}Th	7.60E-07	1.35E-03	1.35E-03			
	^{228}Ra	9.00E-04	6.61E-05	9.66E-04			
	^{228}Th	1.35E-03	2.96E-02	3.09E-02			
	^{210}Pb	1.36E-06	1.03E-02	1.03E-02			
	^{234Th}	1.98E-06	9.60E-05	9.80E-05			
Pilot	^{232}Th	4.05E-07	6.67E-03	6.67E-03	0.402	4.033	Yellow
	^{230}Th	2.15E-06	2.00E-01	2.00E-01			
	^{238}U	6.68E-07	2.50E-01	2.50E-01			
	^{235}U	2.74E-05	9.02E-03	9.04E-03			
	^{234}Th	1.03E-06	2.66E-01	2.66E-01			
	^{210}Po	4.35E-08	2.18E+00	2.18E+00			
	^{226}Ra	5.82E-03	1.02E+00	1.02E+00			
	^{231}Pa	6.81E-06	1.01E-02	1.01E-02			
	^{227}Th	1.86E-05	1.18E-02	1.18E-02			
	^{228}Ra	1.46E-03	7.99E-05	1.54E-03			
	^{228}Th	2.19E-03	5.36E-02	5.58E-02			
	^{210}Pb	5.44E-06	1.61E-02	1.61E-02			
	^{234Th}	7.18E-05	4.16E-03	4.23E-03			
Roxby Downs	^{232}Th	2.80E-07	3.22E-03	3.22E-03	0.157	1.583	Green
	^{230}Th	2.50E-07	1.54E-02	1.54E-02			
	^{238}U	2.20E-08	9.60E-03	9.60E-03			
	^{235}U	1.68E-06	5.15E-04	5.17E-04			
	^{234}Th	4.78E-08	8.40E-03	8.40E-03			
	^{210}Po	9.89E-09	1.44E+00	1.44E+00			
	^{226}Ra	6.82E-04	6.55E-02	6.61E-02			
	^{231}Pa	4.17E-07	5.74E-04	5.75E-04			
	^{227}Th	1.14E-06	6.74E-04	6.75E-04			
	^{228}Ra	9.90E-05	1.10E-04	2.09E-04			
	^{228}Th	1.51E-03	2.59E-02	2.74E-02			
	^{210}Pb	1.24E-06	1.06E-02	1.06E-02			
	^{234Th}	2.37E-06	1.60E-04	1.62E-04			
Arid	^{232}Th	3.00E-07	7.36E-03	7.36E-03	0.480	4.902	Yellow
	^{230Th}	3.35E-07	1.54E-01	1.54E-01			
	^{238}U	3.84E-08	1.56E-01	1.56E-01			
	^{235}U	1.96E-06	1.00E-02	1.00E-02			
	^{234Th}	7.08E-08	1.85E-01	1.85E-01			
	^{210}Po	1.25E-08	2.39E+00	2.39E+00			
	^{226}Ra	6.53E-04	1.90E+00	1.90E+00			
	^{231}Pa	4.87E-07	1.12E-02	1.12E-02			
	^{227}Th	1.33E-06	1.31E-02	1.31E-02			
	^{228}Ra	1.08E-03	8.82E-05	1.17E-03			
	^{228}Th	1.62E-03	5.92E-02	6.08E-02			
	^{210}Pb	1.56E-06	1.76E-02	1.76E-02			
	^{234Th}	4.13E-06	2.60E-03	2.60E-03			

Site	Radionuclide	External (µGy h^{-1})	Internal (µGy h^{-1})	Total (µGy h^{-1})	RQ	Total dose rate per organism	Risk Colour
Raise Bore	^{232}Th	2.35E-07	1.33E-02	1.33E-02	0.364	3.635	Yellow
	^{230}Th	1.93E-06	3.51E-01	3.51E-01			
	^{238}U	1.15E-06	2.76E-01	2.76E-01			
	^{235}U	4.48E-05	1.21E-02	1.22E-02			
	^{234}Th	1.68E-06	3.25E-01	3.25E-01			
	^{210}Po	5.07E-08	1.17E+00	1.17E+00			
	^{226}Ra	9.18E-03	1.32E+00	1.33E+00			
	^{231}Pa	1.11E-05	1.35E-02	1.35E-02			
	^{227}Th	3.04E-05	1.58E-02	1.59E-02			
	^{228}Ra	8.46E-04	1.60E-04	1.01E-03			
	^{228}Th	1.27E-03	1.07E-01	1.08E-01			
	^{210}Pb	6.34E-06	8.67E-03	8.68E-03			
	^{234}Th	1.24E-04	4.60E-03	4.72E-03			

Tier 2 assessments for the Olympic Dam May 2018 composite results from alpha spectroscopy detailed above were put through the ERICA tool. The calculated dose and risk assessment for *Acacia ligulata* are shown below, Table 4.11 contains the lower estimate values and Table 4.12 contain the upper estimate values.

Table 4.11. ERICA tier 2 dose results for the Olympic Dam May 2018 composite results. Acacia ligulata from default CRs with ERICA lower estimate.

Site	Radionuclide	External (µGy h⁻¹)	Internal (µGy h⁻¹)	Total (µGy h⁻¹)	RQ	Total dose rate per organism (µGy h⁻¹)	Risk Colour
South Control	^{232}Th	2.50E-07	9.20E-04	9.20E-04	0.130	1.312	Green
	^{320}Th	2.42E-07	4.59E-03	4.59E-03			
	^{238}U	1.84E-08	5.28E-03	5.28E-03			
	^{235}U	1.12E-06	1.03E-03	1.03E-03			
	^{234}Th	2.92E-06	5.60E-05	5.89E-05			
	^{210}Po	1.09E-08	6.60E-01	6.60E-01			
	^{226}Ra	3.94E-04	6.41E-01	6.41E-01			
Pilot	^{232}Th	4.05E-07	3.45E-03	3.45E-03	0.197	1.985	Green
	^{230}Th	2.15E-06	1.40E-01	1.40E-01			
	^{238}U	6.68E-07	1.03E-01	1.03E-01			
	^{235}U	2.74E-05	6.44E-03	6.47E-03			
	^{234}Th	7.48E-05	1.84E-03	1.92E-03			
	^{210}Po	4.35E-08	9.73E-01	9.73E-01			
	^{226}Ra	5.82E-03	7.50E-01	7.56E-01			
Roxby Downs	^{232}Th	2.80E-07	2.30E-03	2.30E-03	0.122	1.2264	Green
	^{230}Th	2.50E-07	8.10E-03	8.10E-03			
	^{238}U	2.20E-08	4.80E-03	4.80E-03			
	^{235}U	1.68E-06	1.03E-03	1.03E-03			
	^{234}Th	3.48E-06	1.60E-05	1.95E-05			
	^{210}Po	9.89E-09	3.91E-01	3.91E-01			
	^{226}Ra	6.82E-04	8.18E-01	8.19E-01			
Arid	^{232}Th	3.00E-07	2.30E-04	2.30E-04	0.204	2.037	Green
	^{230}Th	3.35E-07	8.10E-03	8.10E-03			
	^{238}U	3.84E-08	3.84E-02	3.84E-02			
	^{235}U	1.96E-06	2.32E-03	2.32E-03			
	^{234}Th	5.16E-06	6.40E-04	6.45E-04			
	^{210}Po	1.25E-08	6.11E-01	6.11E-01			
	^{226}Ra	6.53E-04	1.38E+00	1.38E+00			
Raise Bore	^{232}Th	2.35E-07	1.04E-02	1.04E-02	0.263	2.642	Green
	^{230}Th	1.93E-06	2.40E-01	2.40E-01			
	^{238}U	1.15E-06	1.39E-01	1.39E-01			
	^{235}U	4.48E-05	9.27E-03	9.32E-03			
	^{234}Th	1.23E-04	2.20E-03	2.32E-03			
	^{210}Po	5.07E-08	1.00E+00	1.00E+00			
	^{226}Ra	9.18E-03	1.23E+00	1.24E+00			
North Control	^{232}Th	2.45E-07	3.45E-03	3.45E-03	0.110	1.098	Green
	^{230}Th	2.57E-07	1.32E-02	1.32E-02			
	^{238}U	2.88E-08	1.03E-02	1.03E-02			
	^{235}U	1.68E-06	9.27E-03	9.28E-03			
	^{234}Th	3.57E-06	1.08E-04	1.12E-04			
	^{210}Po	2.40E-08	6.48E-01	6.48E-01			
	^{226}Ra	2.98E-04	4.15E-01	4.15E-01			

Table 4.12. ERICA tier 2 dose results for the Olympic Dam May 2018 composite results. Acacia ligulata from default CRs with ERICA upper estimate.

Site	Radionuclide	External (μGy h⁻¹)	Internal (μGy h⁻¹)	Total (μGy h⁻¹)	RQ	Total dose rate per organism (μGy h⁻¹)	Risk Colour
South Control	^{232}Th	2.50E-07	9.20E-04	9.20E-04	0.132	1.330	Green
	^{320}Th	2.42E-07	4.59E-03	4.59E-03			
	^{238}U	1.84E-08	5.28E-03	5.28E-03			
	^{235}U	1.12E-06	6.28E-05	6.40E-05			
	^{234}Th	4.01E-08	3.92E-03	3.92E-03			
	^{210}Po	1.09E-08	6.60E-01	6.60E-01			
	^{226}Ra	3.94E-04	6.41E-01	6.41E-01			
	^{231}Pa	2.78E-07	2.58E-04	2.58E-04			
	^{227}Th	7.60E-07	8.22E-05	8.30E-05			
	^{228}Ra	9.00E-04	1.10E-05	9.11E-04			
	^{228}Th	1.35E-03	7.39E-03	8.74E-03			
	^{210}Pb	1.36E-06	4.87E-03	4.87E-03			
	^{234}Th	1.98E-06	8.80E-05	9.00E-05			
Pilot	^{232}Th	4.05E-07	3.45E-03	3.45E-03	0.217	2.166	Green
	^{230}Th	2.15E-06	1.40E-01	1.40E-01			
	^{238}U	6.68E-07	1.03E-01	1.03E-01			
	^{235}U	2.74E-05	6.44E-03	6.47E-03			
	^{234}Th	1.03E-06	1.29E-01	1.29E-01			
	^{210}Po	4.35E-08	9.73E-01	9.73E-01			
	^{226}Ra	5.82E-03	7.50E-01	7.56E-01			
	^{231}Pa	6.81E-06	7.18E-03	7.19E-03			
	^{227}Th	1.86E-05	8.42E-03	8.44E-03			
	^{228}Ra	1.46E-03	4.13E-05	1.50E-03			
	^{228}Th	2.19E-03	2.77E-02	2.99E-02			
	^{210}Pb	5.44E-06	7.18E-03	7.19E-03			
	^{234}Th	4.21E-06	1.00E-04	1.04E-04			
Roxby Downs	^{232}Th	2.80E-07	2.30E-03	2.30E-03	0.124	1.252	Green
	^{230}Th	2.50E-07	8.10E-03	8.10E-03			
	^{238}U	2.20E-08	4.80E-03	4.80E-03			
	^{235}U	1.68E-06	1.03E-03	1.03E-03			
	^{234}Th	4.78E-08	1.12E-03	1.12E-03			
	^{210}Po	9.89E-09	3.91E-01	3.91E-01			
	^{226}Ra	6.82E-04	8.18E-01	8.19E-01			
	^{231}Pa	4.17E-07	1.15E-03	1.15E-03			
	^{227}Th	1.14E-06	1.35E-03	1.35E-03			
	^{228}Ra	1.01E-03	2.76E-05	1.04E-03			
	^{228}Th	1.51E-03	1.85E-02	2.00E-02			
	^{210}Pb	1.24E-06	2.88E-03	2.88E-03			
	^{234}Th	2.37E-06	8.00E-05	8.24E-05			
Arid	^{232}Th	3.00E-07	2.30E-04	2.30E-04	0.210	2.098	Green
	^{230}Th	3.35E-07	8.10E-03	8.10E-03			
	^{238}U	3.84E-08	3.84E-02	3.84E-02			
	^{235}U	1.96E-06	2.32E-03	2.32E-03			
	^{234}Th	7.08E-08	4.48E-02	4.48E-02			
	^{210}Po	1.25E-08	6.11E-01	6.11E-01			
	^{226}Ra	6.53E-04	1.38E+00	1.38E+00			
	^{231}Pa	4.87E-07	2.58E-03	2.59E-03			
	^{227}Th	1.33E-06	3.03E-03	3.03E-03			
	^{228}Ra	1.08E-03	2.76E-06	1.08E-03			
	^{228}Th	1.62E-03	1.85E-03	3.47E-03			
	^{210}Pb	1.56E-06	4.51E-03	4.51E-03			

Site	Radionuclide	External (µGy h^{-1})	Internal (µGy h^{-1})	Total (µGy h^{-1})	RQ	Total dose rate per organism (µGy h^{-1})	Risk Colour
	^{234}Th	4.13E-06	6.40E-04	6.44E-04			
Raise Bore	^{232}Th	2.35E-07	1.04E-02	1.04E-02	0.290	2.910	Green
	^{230}Th	1.93E-06	2.40E-01	2.40E-01			
	^{238}U	1.15E-06	1.39E-01	1.39E-01			
	^{235}U	4.48E-05	9.27E-03	9.32E-03			
	^{234}Th	1.68E-06	1.54E-01	1.54E-01			
	^{210}Po	5.07E-08	1.00E+00	1.00E+00			
	^{226}Ra	9.18E-03	1.23E+00	1.24E+00			
	^{231}Pa	1.11E-05	1.03E-02	1.03E-02			
	^{227}Th	3.04E-05	1.21E-02	1.22E-02			
	^{228}Ra	8.46E-04	1.24E-04	9.70E-04			
	^{228}Th	1.27E-03	8.32E-02	8.45E-02			
	^{210}Pb	6.34E-06	7.39E-03	7.40E-03			
	^{234}Th	1.24E-04	2.32E-03	2.44E-03			
North Control	^{232}Th	2.45E-07	3.45E-03	3.45E-03	0.112	1.133	Green
	^{230}Th	2.57E-07	1.32E-02	1.32E-02			
	^{238}U	2.88E-08	1.03E-02	1.03E-02			
	^{235}U	1.68E-06	9.43E-05	9.60E-05			
	^{234}Th	4.90E-08	7.56E-03	7.56E-03			
	^{210}Po	2.40E-08	6.48E-01	6.48E-01			
	^{226}Ra	2.98E-04	4.15E-01	4.15E-01			
	^{231}Pa	4.17E-07	3.87E-04	3.88E-04			
	^{227}Th	1.14E-06	1.23E-04	1.24E-04			
	^{228}Ra	8.82E-04	4.13E-05	9.23E-04			
	^{228}Th	1.32E-03	2.77E-02	2.91E-02			
	^{210}Pb	3.00E-06	4.78E-03	4.78E-03			
	^{234}Th	3.10E-06	1.72E-04	1.75E-04			

There is a small difference between the lower and upper dose estimates for both *Acacia ligulata* and *Dodonaea viscosa*.

4.4. Discussion

4.4.1. Concentration ratio discussion

The transfer of radionuclides from soil to vegetation is complex and depends on many variables including the soil type and organic component, clay component of the soil, which radionuclides are of interest and the species (Hegazy & Emam, 2010). The CRs developed for the Olympic Dam region show that they have substantial variability. The CRs span over 3 orders of magnitude. This is consistent with literature which reflects highly variable uptake between individual organisms of the same species (Beresford, 2010). It also likely reflects some variability due to the activity of the samples being very low, as discussed in chapter 3. When the activity is very low and close to the MDA the uncertainties for the values are very

large, a small difference in the activity leads to a very large difference statistically. When comparing the different species *Acacia ligulata* and *Dodonaea viscosa* the CRs from this study show the CRs for *Acacia ligulata* are far more consistent. This is due to the *Dodonaea viscosa* having a large variation in activity data, therefore, impacting the range of CRs produced. The CRs for *Dodonaea viscosa* are also generally higher compared to the *Acacia ligulata*. When comparing the CRs produced from this study to the default CRs from the WTD used in ERICA. There is a significant difference when comparing the CRs from the WTD to the Olympic Dam site specific values, observed below in Table 4.13.

Table 4.13. CR comparison table, comparison of CRs developed from this present study to the WTD and Read and Pickering Study (Read & Pickering, 1999).

	CRs				
Location	Th	U	Po	Ra	Pb
WTD	0.061	0.061	0.33	0.33	0.32
Olympic Dam	1.070	2.140	5.45	1.13	1.13
Flinders Ranges	0.030	0.030	-	0.07	0.75
Read and Pickering	1.2-3.2	2.3-9.1	0.2-0.9	-	1.5-5.6

This present study overall has higher CRs compared to the Read and Pickering (1999) study. This is likely due to the samples and the vicinity of some sample sites to surface operations from the Olympic Dam mine and the potential of the soil samples containing process materials such as ore or slag material. CRs from the Olympic Dam region are often greater than one. Where a CR is greater than one, this indicates that the vegetation is accumulating the radionuclides at a higher concentration than the soil. This could be due to several reasons including, disequilibrium from radon progeny fallout, the extra contribution from dust deposition or the plants themselves having high affinity for the radionuclides of interest.

As discussed in chapter 3, there is an issue with activity concentrations when they are very low and close to the MDA. When the activity is very low the relative errors are large, a small increase in activity may appear as though there is a very large CR. This may not necessarily be representative of the environmental conditions. When comparing our studies of both regions to the ERICA default values, the Flinders Ranges region values are reasonably consistent to the default ERICA values. However, the CRs developed from the Olympic Dam region are significantly higher than the default values as shown in Table 4.12. Due to the problems associated with using the very low activity values noted above.

This research proposes *Acacia ligulata* to be used as a model organism for radioactivity environmental monitoring due to the consistency in radionuclide data and high species abundance in the Olympic Dam region. Further data is required for the Flinders Ranges region to propose a model organism for environmental radionuclide monitoring. However, the high abundance of the *Astrebla pectinata* makes this organism a likely choice for the region.

4.4.2. ERICA discussion

A paper by Anderson et al. 2009, outlined the need for regulatory benchmarks for μGy h^{-1} doses of environmental radiation. That paper outlined that there is a 10 μGy h^{-1} threshold for dose response to species (Andersson et al., 2009). The results from this present study indicate that the dose rate to the species of interest is in most cases well below the 10 μGy/h dose screening limit. However, the radionuclides not included within ERICA that are present within the decay series need to be considered in the total does estimate. It is important to consider the radionuclides in the ^{238}U, ^{235}U and ^{232}Th decay series (Figures 1.1 to 1.3) when considering the total activity and dose to organism. The un-measured radionuclides in the series need to be considered, as they are not able to be measured using the techniques available within the scope of this research. They need to be considered as they will be present in the sample.

When ERICA calculates the internal vs. external dose rate, the type of radiation is considered, ^{234}U and ^{235}U are primarily alpha emitters and the dose received would be primarily internal. The main contributors to the internal dose are ^{210}Po and ^{226}Ra due to their high energy alpha emissions which are reflected in their ERICA dose conversion coefficients (DCCs). These results are consistent with other studies which indicate that ^{210}Po and ^{226}Ra are major dose contributors to living organisms when considering NORM in environmental samples (Thakur & Ward, 2020).

There was a negligible difference between the upper and lower estimate values for the Olympic Dam dose estimates. This is likely due to the overall low activity concentrations; therefore, minimal additional dose will be included once the missing radionuclides are accounted for. The organisms analysed in this study have calculated total dose rates lower

that the 10 µGy h^{-1} screening value, therefore there is unlikely to be any adverse effects to the organism from ionising radiation exposure.

4.5. Conclusions

Overall, new site specific CRs specific for shrubs within the arid Australian environment have been proposed from this study. Tables 4.6 and 4.7 provide the proposed CR values for native Australian shrubs from the Olympic Dam and Flinders Ranger regions respectively. There is higher confidence in the Olympic Dam values due to there being more available data from this present study. The activity of radionuclides transferring from soil to organism in the Australian arid climate compares to literature values from other localities. The two different regions studied are vastly different radiological environments and therefore, cannot be considered under the same model. The activity of samples in most cases were very low and close to the MDA, there this can make Concentration ratios seem high when the activities themselves are very low. Due to this there is a large range in CRs from the different sites. This research has shown that site specific CRs are appropriate for impact assessments. This research proposes the use of site-specific CR data when available for the most accurate organism dose assessment results.

The CRs determined from the Flinders Ranges region are consistent with the WTD. The CRs from Olympic Dam are higher than the WTD, therefore, site specific CRs for the Olympic Dam region would be of benefit to use in future radiological risk assessments for that region. There is a large amount of apparent variation from site to site. However, also large variation within the 100 m diameter the samples were collected from within the same sample site. This is a reflection of the generally very low activity of the samples from the Olympic Dam region and the challenges with quantifying this low activity. This is consistent with literature regarding the elemental concentrations within soils of the arid Australian environment (He et al., 2018). Overall, the consistency in activities and CRs for the *Acacia ligulata* makes it a desirable reference organism for monitoring arid environment shrubs. The abundance of the species in the environment is also high and useful for widespread monitoring, but the very low activities in the region make this inherently difficult.

Chapter 5. Elemental uptake into Australian native vegetation and nutrient availability

5.1. Elemental profile of vegetation and soil in the arid Australian environment

Nutrient availability to vegetation may be reduced in drought and heat stressed environments, this is an important factor when analysing vegetation from the arid Australian environment (Sánchez et al., 2020). Soil from the arid zone in Australia is typically low in nutrients such as P, K and N. Trace nutrients, including the elements of interest when studying plant nutrient uptake include S, Ca, N, P, K and Mg. The distribution of nutrients within the soil is often heterogeneous, as 'islands of fertility' is a prominent feature of the arid Australian soil. 'Islands of fertility' arise due to nutrient cycling from the decomposition of leaf litter, which typically occurs when bacteria and cyanobacteria are active following a rain event (He et al., 2018).The islands of fertility may also result from microtopography which is surface roughness which may provide potential for water, seeds and sticks to accumulate (Eldridge et al., 2011)

5.1.1. Chapter directions

This chapter determines the broad elemental profile of arid Australian soils and the elemental and nutrient availability to Australian native vegetation. A comparison of NAA and ICP-MS methodologies for soil analysis was performed due to the complexity of the soil matrix and the low elemental concentration. A direct comparison of ICP-MS and NAA was performed for U, Th and Pb due to the different limitations and benefits of each technique discussed in chapter 3. NAA was also used to determine the elemental profile of soils and vegetation across a broad range of elements.

These data will provide information regarding the uptake of elements and plant nutrients for Australian native species within the arid Australian Environment. This formed a pilot study to determine whether plant nutrient uptake can be influenced by other elements in the environment. Further to this, analysis of whether plant nutrient uptake can be influenced by the presence of other elements in the environment. Also, to determine whether the elemental data provides information regarding increased mechanical disturbance in the arid Australian environment.

The chapter directions were achieved by implementing the following analysis. Soils were sampled from the Olympic Dam region, sites detailed in Chapter 2. This was completed to also show the elemental variation when considering the distance from the mining operations. Two different species of vegetation were analysed, *Acacia ligulata* and *Dodonaea viscosa*, each individual plant was analysed independently in most cases. Some vegetation analysis was performed on samples that were composites of multiple plant samples from the same sites, this was done when access to instrumentation was limited. It is outlined in the results section when an individual plant or a composite sample is being discussed. The elemental data from associated soil and vegetation samples will detail the transfer from soil to plant. The focus elements in this chapter are long lived elements from the NORM series such as U and Th, lanthanides and the stable Pb. Plant nutrients such as P and K and other trace nutrients such as Mg, Ca, S, Na, Mn, Fe, Cu and Zn and other elements of interest were targeted. Elemental results of soil and flora from Olympic Dam were collected using ICP-MS and NAA. This research provides data regarding vegetation nutrient and elemental uptake within the arid Australian environment, also if nutrient uptake is influenced by other elements in the environment.

This chapter will report the outcome of experiments to measure the activity from stratified soil samples and compare these to the results from the bulk chapter (chapter 4). The depth profile of soils will be analysed by determining the radionuclide and elemental contents of the soil from each interval from each site. The suitability of using the standard 0-10 cm soil sampling methodology for ERICA assessments will be scrutinised for environments of NORM deposition from dust. Soil samples from Olympic Dam have been analysed to show the effect of the deposition of dust containing NORM radionuclides and ^{222}Rn from mechanical disturbances in the Olympic Dam region. This chapter aims to determine whether the 0-10 cm is appropriate for CR determination in environments where mechanical disturbance occurs such as the Olympic Dam region. The location of the Olympic Dam soil samples will be considered as it is expected that the stratified soil profiles will vary significantly within the mining lease area compared to the control samples. This will be used to determine whether the ERICA modelling is appropriate for the arid Australian environment generally or within a mining lease area.

5.2. Experimental methods

Dry weights have been used for all vegetation analysis within this chapter. Where the number of samples is referred to as 'n' this represents individually collected samples, except for ICP-MS results, where each sample was analysed three times, therefore 'n=9' represents three samples analysed three times each from within the same environmental site.

NAA sample preparation

Samples of soil and vegetation were prepared by the standard methods found in section 2.3. However, soil samples were further sieved to 500 µm prior to analysis. Composite samples were created by selecting equal mass of soil from the same site, from the individual sub samples. Vegetation sample was composed of both leaves and branches to be representative of the whole organism, they were prepared using the method outlined in section 2.3. These samples were then sent to ANSTO for analysis.

ICP-MS sample preparation

Samples of soil and vegetation were prepared by the standard methods found in section 2.3. However, further preparation was performed prior to ICP-MS analysis. Samples were digested using an 'Anton Paar Microwave Digestion System Multiwave ECO'. This method was used before analysis with instrumentation such as ICP-MS that requires a liquid sample. To digest environmental samples from solids e.g., soil to a liquid from for ICP-MS analysis, acid digestion is sufficient. This process will dissolve most biotite, clay and amorphous Fe oxides; however, many silicates and oxide minerals don't dissolve with this mix of acids. HF will dissolve silicates and is commonly used for this purpose however, was deemed not to be appropriate due to safety concerns for this application, and also because it can damage the torch of the ICP-MS (Tuovinen et al., 2015). Microwave digestion was used for sample digestion as it reduces the acid digestion time and increases the recovery of volatile elements in samples, lower contamination levels, minimal volumes of reagents and more reproducible yield (Agazzi & Pirola, 2000; Tuovinen et al., 2015).

Soil samples prepared as described in Section 2.3 and were prepared further for ICP-MS analysis. For soil samples 250 mg were weighed into digestion vials and 5 mL of aqua regia

((1:3) HNO$_3$ (15.6 M) and HCl (18.4 M)) was added. The samples were placed into the microwave digester and run for 15-minutes ramp time, followed by a 30-minute digestion at 175 °C. The samples were then quantitatively transferred to centrifuge tubes to remove any remaining insoluble sample fraction. The insoluble fraction was dried and weighed to account for the insoluble mass.

Samples of vegetation were prepared as in section 2.3.2 were prepared further for ICP-MS analysis. Samples were weighed to 250 mg in a digestion vial. 5 mL of H$_2$O$_2$ (9.8 M) and HNO$_3$ (15.6 M) were added to the sample to digest using a wet ash process. The microwave programmed run was 100 °C for 15 minutes. The entire vegetation sample was digested via this method.

5.2.1. Elemental analysis

When radionuclides have a long half-life they may be more suited to analysis using chemical analysis including mass spectrometry (Murphy, 2005). The elemental analysis performed on the samples required to address the thesis aims are NAA and ICP-MS, these are detailed below.

Neutron activation analysis (NAA)

NAA is a multi-elemental quantitative analysis, with a limit of detection is in the ppb range. NAA is both a quantitative and qualitative technique capable of multielement analysis (Glascock & Neff, 2003). NAA at ANSTO works by irradiating a sample using the OPAL reactor. Radionuclides with short half-lives (min/hr) are best measured after a short irradiation (e.g. Al, Ca, Cl, Cu, Dy, I, In, Mg, Mn, Na, Rh, S, Ti and V) and those with long half-lives (day/yr) are irradiated for a longer time (e.g. Ag, As, Au, Ba, Br, Ca, Ce, Cd, Co, Cr, Cs, Er, Eu, Fe, Ga, Ge, Gs, Hf, Hg, Ho, In, Ir, K, La, Lu, Mo, Nb, Nd, Os, Pd, Pr, Pt, Rb, Re, Ru, Sb, Sc, Se, Sm, Sn, Sr, Ta, Tb, Te, Th, Tm, U, W, Yb, Zn and Zr).

The activation process follows as a sample is placed into the reactor where it is bombarded with neutrons the energy that is given off is identified by the characteristic energy of the gamma rays that are produced. Figure 5.1 describes the reaction when the neutron interacts

with a nucleus. This figure describes the reaction when an incident particle is absorbed by a nucleus, followed by gamma rays being emitted from the nucleus.

This image has been removed due to copyright restriction. Available online from [Glascock, M. D., & Neff, H. (2003). Neutron activation analysis and provenance research in archaeology. Measurement Science Technology, 14(9), 1516]
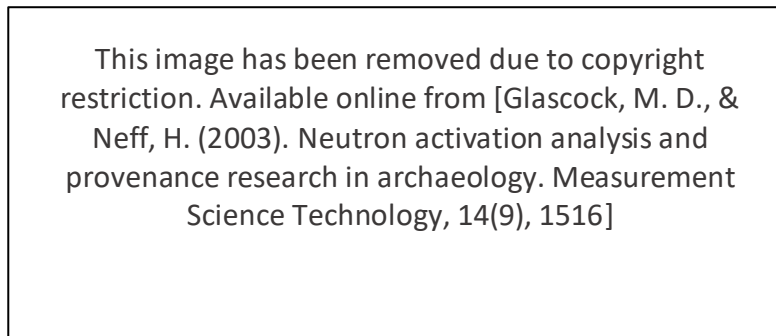
Figure 5.1. Activation process for Neutron Activation Analysis (NAA), the interaction of the incident neutron with a nucleus (Glascock & Neff, 2003).

When the material of interest is irradiated with a neutron beam, an incident particle (neutron) interacts with a nucleus of the material analysed, this neutron interacts with the target nucleus by either scattering or absorption. When absorption of the incident particle occurs, a radioactive nucleus and gamma rays are produced. The reaction of neutron activation is detailed below in Equation 5.1 (Glascock & Neff, 2003).

$$a + A \,[X] \rightarrow b + B + Q$$

Equation 5.1. The reaction of neutron activation. where, A is the target nuclide, [X] is the compound nucleus in the excited state, B is the product nuclide which is ofter radioactive, b is the exciting particle and Q is the amount of energy released or absorbed from the reaction.

Instrumentation

Following the sample preparation detailed in section 2.3. Samples are irradiated using the Open-pool Australian light water research reactor (OPAL) at ANSTO. The reactor is shown in Figure 5.2 below. OPAL is a 20 MW multipurpose research reactor, with irradiation capabilities for NAA. The reactor is 13 meters below demineralised light water. The reactor core contains heavy water which acts as a neutron reflector which provides neutrons at a high volume (Bennett, 2008).

Figure 5.2. OPAL Reactor, ANSTO (OPAL multi-purpose reactor, 2020)

Following irradiation, the samples are then counted using an ORTEC GEM high-purity Ge gamma-ray detector (P-type, 25% relative efficiency) Coupled to an ORTEC DSPEC-50 digital spectrometer (Martin et al., 2017).

Quantitative Analysis, Precision and Accuracy

Kayzero method

Samples were analysed by neutron activation analysis using the k_0-method of standardization (Martin et al., 2017). Long irradiations use Au wires as a flux monitor between the samples, these Au wires are also known as k_0 wires. The k_0-method allows for 3.5% error and reduces the need for SRM analysis (Bennett, 2008).

Certified Reference Materials (CRM)

Two Certified reference materials were analysed using NAA for comparison. A soil and a plant material reference material were each chosen to represent each of the different sample matrices of the analysed samples. The soil sample was NIST Standard Reference Material SRM2711a Montana II Soil (NIST, 2018). The other Standard Reference Material was NIST

SRM1547 Peach leaves (NIST, 2019). The Peach leaves standard was chosen as it is a matrix match to the vegetation samples with similar concentration ranges.

Table 5.1. Results in concentration mg/kg from NAA compared to the values form the NIST Standard reference material 2711a Montana II Soil (NIST, 2018).

Element	Measured Concentration (mg/kg)	Certified Concentration (mg/kg)	Reference Concentration (mg/kg)	% Variation
Mn	670.5 ± 40.45	675 ± 18.0		0.66
Co	9.945 ± 0.611	9.89 ± 0.20		0.54
As	100.1 ± 6.107	107 ± 5.00		6.88
Rb	112.7 ± 22.96		120 ± 3.0	6.48
Sr	223.8 ± 38.99	242 ± 10.0		8.12
Cd	46.36 ± 5.003	54.1 ± 0.50		16.7
Sb	23.75 ± 1.550	23.8 ± 1.40		0.20
Ba	662.0 ± 50.13	730 ± 15.0		10.3
Nd	41.66 ± 5.571		29 ± 2.0	30.4
Sm	6.113 ± 0.370	5.93 ± 0.28		2.98
Eu	1.003 ± 0.060		1.1 ± 0.2	9.66
Hf	9.892 ± 0.618		9.2 ± 0.2	6.99
Th	15.68 ± 0.971		15 ± 1.0	4.34
U	3.032 ± 0.378	3.01 ± 0.12		0.72

The measured results from the NAA analysis from the NIST Standard reference material 2711a Montana II Soil were all in agreement with the data collected.

Table 5.2. Peach leaves NAA results compared to the certified values (NIST, 2019).

Element	Measured (mg/kg)	Certified (mg/kg)	% Variation
Na	39.06 ± 2.584	23.80 ± 1.60	39.1
Mg	4641 ± 347.2	4320 ± 150.0	6.92
Al	253.8 ± 20.41	248.9 ± 6.50	1.92
Cl	381.1 ± 26.75	361.0 ± 14.0	5.26
K	25260 ± 1706	24330 ± 380	3.67
Ca	16880 ± 1044	15590 ± 160	7.63
Mn	103.6 ± 6.714	97.80 ± 1.80	5.60
Fe	227.8 ± 14.09	219.8 ± 6.80	3.50
Se	0.126 ± 0.018	0.120 ± 0.02	5.14
Rb	20.30 ± 1.989	19.65 ± 0.89	3.20
Sr	56.40 ± 4.181	53.00 ± 5.00	6.03
Ba	116.6 ± 7.364	123.7 ± 5.50	6.09

The measured results from the NAA analysis from the NIST Standard reference material 1547 Peach leaves were all in agreement with the data collected except Na.

Justification

NAA simplifies sample preparation of complex natural materials, eliminating a number of sample preparation steps required for ICP-MS analysis. NAA methods have been established and verified for both soil and dried plant material. Acid digestion of soil is complicated by the presence of silicates, requiring harsh acid conditions (i.e., high concentration and with multiple acids) at high temperatures, which ultimately may not result in the complete digestion of the sample. The complexity and variability of natural samples also makes matrix-matching of calibration standards for ICP-MS difficult, as well as potentially featuring isobaric interferences for the analytes of interest.

As NAA is matrix-independent, analysis of trace and REE elements within the samples is simplified as the only sample preparation required is the homogenisation of solid material. NAA provides a multi-element analysis with high accuracy, precision and low limits of detection. Within Australia, NAA is only performed at the world-class OPAL reactor at ANSTO.

NAA is ideal for analysis of the samples required in this research as it has the advantage of not needing to digest the sample. NAA is a multi-elemental technique that allows for the analysis of many elements, this is useful when looking for pathfinder elements as calibration curves are not necessary to set up for each element as techniques such as ICP-MS are. A benefit to NAA is that matrix interferences are minimised, and no sample digestion is required, therefore, limiting the chances of contamination, sample loss or the use of HF in cases of soils (Glascock & Neff, 2003).

NAA Experimental Methods

Samples were weighed and placed into containers for irradiation, ~500 mg mass of each sample used in this experiment. The sample size is chosen to provide good relative accuracy of around 4 to 5% for multi elemental capabilities. Solid powder samples are prepared in high density polyethylene (HDPE) capsules of an 8X5mm size for the sample (ANSTO, 2016). The density and volume of sample is taken into consideration as the gamma spectrometers that are used to count the sample are calibrated to the mass and geometry of the samples, the software that is used for the counting takes this into consideration.

Samples are analysed using both short and long irradiations, this allows for the greatest number of elements analysed from the samples. Samples analysed for a long irradiation are packed into Al cans in stacks of 12 samples. The Al cans used are shown in Figure 5.3. These Al cans are used as the sample enters the low flux area within the OPAL reactor. Long irradiations use Au wires (k0 wires) as a flux monitor between the samples in the Al can for the long irradiations. This is done to monitor the neutron flux throughout the can.

Figure 5.3. Al can used in NAA for long sample irradiation times.

The short irradiation samples are irradiated for 3 seconds at a flux of approximately 2.7×10^{13} $cm^{-2}s^{-1}$ (Bennett, 2008). Short irradiation samples were analysed using the gamma-ray spectrometers as soon as they were irradiated. The gamma spectroscopy measurement is performed for 3 minutes at the furthest position to the detector. The sample is then counted 18 minutes after the initial count finishes for a further 12 minutes on the closest position to the detector. The break in the count time is to allow for the Al and other elements to decay away as they swamp the detector signal, leading to high dead times. Gamma-ray spectra were analysed using the software HyperLab 2005 (HyperLabs Software, Budapest), elemental concentration in mg kg^{-1} are determined using (Kayzero) k$_0$-method (Bennett, 2008).

Long irradiations are for 4 minutes at a flux of approximately 3.4×10^{12} to 1.3×10^{14} cm^{-2}s^{-1}. The samples were then counted using an ORTEC GEM high-purity Ge gamma-ray detector (P-type, 25% relative efficiency) coupled to an ORTEC DSPEC-50 digital spectrometer (Bennett, 2008; Martin et al., 2017). Short irradiations are performed for 30 seconds, these are then counted using a Ge detector (on the highest position away from the detector) for three minutes about 1 minute following irradiation. Then samples decay for 18 minutes then counted again for 12 minutes. The break in the count time is to allow for the Al and other elements to decay away

as they swamp the detector. This accounts for activated isotopes with high count rates, however short half-lives.

Inductively coupled plasma mass spectrometry (ICP-MS)

ICP-MS is commonly used for elemental analysis, for the detection and quantification of long-lived radionuclides at trace levels. ICP-MS has excellent sensitivity, good precision and accuracy. ICP-MS has previously been used for the determination of nuclear materials. E.g. spent nuclear fuel, radioactive waste (Becker, 2005). The limit of detection for ICP-MS is around the ppb-ppt concentration for elements which have low natural background abundance (Murphy, 2005; Tuovinen et al., 2015). The samples need to be in solution prior to analysis using ICP-MS. (Tuovinen et al., 2015).

Instrumentation

The acidified aqueous sample enters the spray chamber, where the sample is ionized by an argon plasma at the torch (Figure 5.4). The sample is then transferred to the quadrupole where the ions are separated based on their m/z ratio. They are then counted by the detector (Linge & Jarvis, 2009; UC Davis, 2015).

This image has been removed due to copyright restriction. Available online from [UC Davis Interdisciplinary Center for Inductively-Coupled Plasma Mass Spectrometry (2015). Retrieved from http://icpms.ucdavis.edu/facilities-procedures]

Figure 5.4. ICP-MS schematic (UC Davis, 2015).

Quantitative Analysis, Precision and Accuracy

To obtain quantitative data from ICP-MS results, a calibration curve must be run before the samples. Standard samples of known concentration of the elements of interest must be prepared in multiple concentrations in a linear correlation. These concentrations must be above and below the concentrations of all the elements from all samples analysed to obtain quantitative data. If the concentration of our measured samples is within the highest and lowest concentration of the calibration, this provides higher confidence in the accuracy and precision of the determined concentration. Figure 5.5. shows the calibration curve for U, where ^{238}U was used as it has the highest natural abundance of the U isotopes and quadrupole ICP-MS is not isotope specific. However due to the long half-lives of U the elemental analysis of U is often used for quantitative analysis.
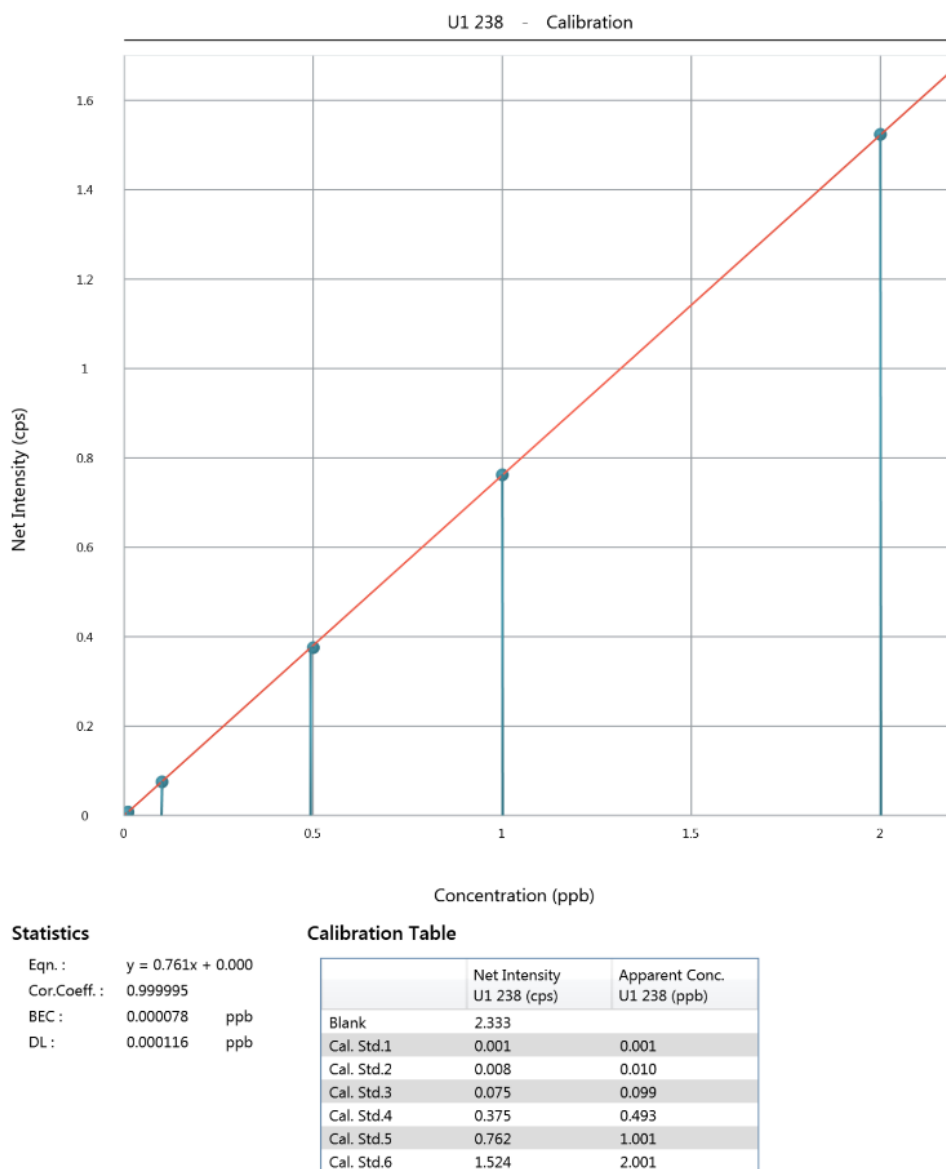
Figure 5.5. ICP-MS concentration curve of known standards for quantitative U analysis.

An internal standard is run at the same time as the calibration, blanks and all sample analysis. This monitors the matrix effects as it is a consistent concentration throughout the entire analysis. The internal standard plot from one of the ICP-MS runs performed is shown below in Figure 5.6. Samples need to be composed of the same matrix otherwise the internal standard will have a lot of disruption throughout the analysis which may interfere with the results. The internal standard is measured at each analysis to determine if there is drift occurring within the analysis run. This is important when running long batches of samples. In this research [115]In was used for the internal standard as it was not an element of interest and is in very low background concentrations.
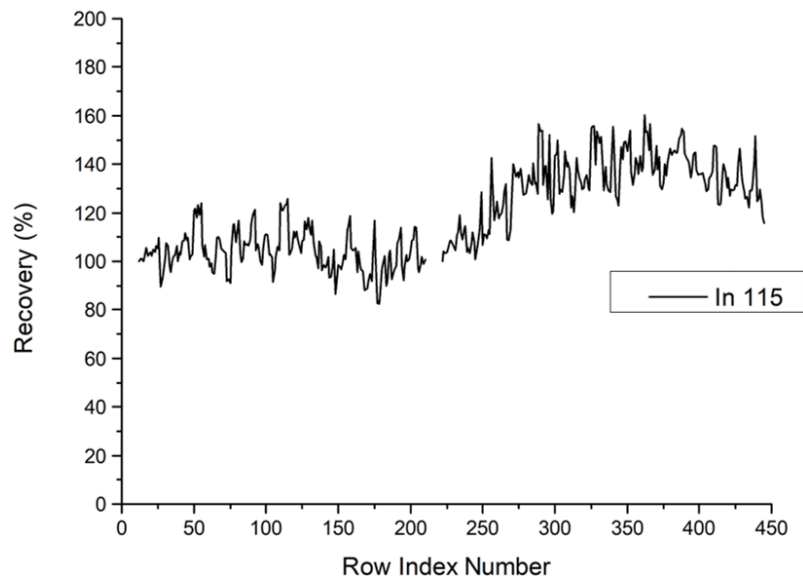
Figure 5.6. ^{115}In internal standard used for ICP-MS analysis.

Quality control and quality assurance (QAQC) is important to consider when using analytical techniques for quantitative analysis. Especially when dealing with low concentrations such as in the parts per billion range. There are many ways to show quality control and quality assurance within an analysis, some examples of this include, spikes and spike recoveries, digest blanks, calibration checks throughout the analysis, analysis of certified reference materials (CRM) and calculating the limit of detection (LOD) and limit of quantification (LOQ).

Running blanks is important for ICP-MS analysis as it shows if there is any potential contamination of the elements of interest from the sample preparation considering the vials and pipettes. The blank samples are the same matrix as the samples, in this study the blanks were 5% aqua regia when running soil samples or (5% HNO3 and H_2O_2) when running the vegetation samples. Digestion blank, same matrix as the samples however the digestion blank sample also undergoes the microwave digestion step that the samples undergo. This determines whether there is any potential contamination to our samples from the microwave digestion of the digestion vials.

The LOD for the ICP-MS analysis performed during the sample analysis run for this research is shown below. The LDO and LOQ for U and Th were determined experimentally following the method outlined by Yuksel & Arica, 2018. The LOD was calculated by 3.3 X SD/slope of the calibration curve and LOQ was calculated by 10 X SD/slope (Yuksel & Arica, 2018). The results are, U LOD=0.001 ppb, LOQ=0.01 ppb, Th LOD=0.003 ppb, LOQ=0.010 ppb. The LOQ is

144

defined as the lowest concentration that the measured analyte can be within a sample that is still reliably detected via the instrument. Where the LOD is defined as how sensitive the desired instrument must be in order to determine the presence of the desired analyte within the sample (Rajaković et al., 2012). The LOD and LOQ are necessary to determine experimentally to determine whether the analysis performed is sensitive enough to provide the desired results. This is achieved by analysing ten consecutive blank samples.

Justification

ICP-MS was used to determine the concentrations of U and Th within soil and vegetation samples. ICP-MS was used as it has a very low detection limit for U and Th. The LOD is within the high parts per trillion (ppt) range. ICP-MS was used to determine total elemental U and Th. This technique is complementary to NAA as ICP-MS will reach lower detection limits compared to NAA.

ICP-MS Experimental Methods

Following sample digestion outlines within the section 2.3.2 the samples were placed into the autosampler of the Perkin Elmer nexION ICP-MS paired with Syngistix software. Calibration standards and samples were loaded into the autosampler. An internal standard solution of In was prepared. The pump and chiller were turned on and the pump tubes were placed around the peristaltic pump under tension. The vacuum was turned on and the tuning process was performed. The ICP-MS was run in KED mode and the tuning was performed, following a tune that passes the reference values the samples were run through the ICP-MS. The procedure follows the Flinders University NexION ICPMS method (Young, 2015).

5.3. Results

5.3.1. Actinide and Pb results of soil and vegetation from Olympic Dam by NAA and a comparison of U and Th concentrations using ICP-MS

Soil results for actinides and Pb

An analytical comparison of the concentration of U and Th was performed using both NAA and ICP-MS. The benefits and limitations of both techniques have been discussed previously.

However, ICP-MS was used as low limit of detection, within the high parts per trillion (ppt) range for the elements of interest can be achieved (Becker, 2005; Kosior et al., 2020; Moens & Dams, 1995; Xu et al., 2011). The limit of detection for NAA ranges significantly for each element, the individual LOD values are detailed below and, in the appendices E and F. The LOD ranges for U have previously been reported at approximately 0.4-0.8 ppm (Osborne et al., 2012; Simsek & Aykut, 2007). The average insoluble silica fraction from soil digestions was determined and the results are in Table 5.3.

Table 5.3. The average insoluble fraction is while digesting with a microwave under aqua regia, soil samples used were 0-10 cm composites.

	Insoluble soil content %	Insoluble soil content in 250 mg (mg)	Soluble soil content %	soluble soil content in 250 mg (mg)
Maximum	98.26	245.7	1.72	4.2
Minimum	57.75	144.3	42.23	105.6
Average	86.66	216.7	13.33	33.2

Table 5.3 shows the soil samples had an average soluble fraction value of 13.33% and an insoluble fraction of 86.66%. The soluble fraction was used to calculate the elemental concentrations within soil samples analysed using ICP-MS. The U and Th LOD and LOQ were determined experimentally, the results showed, U LOD = 0.001 ppb, LOQ = 0.001 ppb, Th LOD = 0.003 ppb, LOQ = 0.010 ppb, the data can be found in appendix F.

The elemental results for U, Th and Pb from the ICP-MS analysis of soils are also found in appendix F. A summary of the results is shown below in Table 5.4.

Table 5.4. Soil ICP-MS concentrations, replicates of 6 soil samples are averaged in each instance, samples from Dec 2018, the average uncertainty is the uncertainty from the instrument.

Site	Element	Average Concentration (mg/kg)	Average Uncertainty (mg/kg)	Min (mg/kg)	Max (mg/kg)	Range (mg/kg)	SD
North Control	U	0.085	0.010	0.185	2.651	2.464	0.900
	Th	1.092	0.054	0.010	0.148	0.138	0.058
	Pb	4.661	0.159	0.085	3.281	N/A	N/A
Arid	U	0.170	0.015	0.105	0.223	0.118	0.034
	Th	1.715	0.068	1.427	1.928	0.501	0.151
	Pb	5.333	0.199	4.453	6.249	1.796	0.557
Raise Bore	U	3.281	0.148	0.108	12.72	12.60	4.763
	Th	2.539	0.111	1.225	6.136	4.908	1.772
	Pb	13.86	0.525	4.928	43.58	38.65	14.79
Tailings	U	1.993	0.079	0.549	2.877	2.327	1.022
	Th	2.021	0.096	1.351	2.525	1.173	0.438
	Pb	11.41	0.435	5.350	14.51	9.170	4.386
Pilot	U	4.520	0.223	0.098	23.26	23.16	8.663
	Th	2.106	0.086	1.438	3.321	1.885	0.645
	Pb	13.71	0.463	4.843	48.28	43.45	16.33
Roxby Downs	U	0.130	0.017	0.074	0.183	0.107	0.034
	Th	2.072	0.119	1.347	2.839	1.492	0.536
	Pb	6.884	0.369	4.982	9.127	4.147	1.239
South Control	U	0.111	0.011	0.068	0.188	0.122	0.031
	Th	1.562	0.049	1.102	2.607	1.505	0.455
	Pb	5.601	0.201	4.464	7.157	2.691	0.783

The results from the NAA analysis of the composite 0-10cm soil samples are in appendix E. Replicate results for actinide concentration within the replicate 0-10 cm soil samples results are in appendix E. The average results are also summarised in Table 5.5 below.

Table 5.5. NAA Actinide soil replicate analysis average and summary table.

		Average concentration (mg/kg)	Average uncertainty (mg/kg)	Min (mg/kg)	Max (mg/kg)	Range (mg/kg)
Raise Bore	**Th**	2.577	0.158	1.264	3.471	2.207
	U	1.448	0.133	1.104	2.084	0.980
South Control	**Th**	2.023	0.124	1.755	2.343	0.588
	U	0.429	0.070	0.374	0.466	0.092
North Control	**Th**	1.736	0.106	1.248	2.080	0.832
	U	0.339	0.054	0.274	0.453	0.179
Pilot	**Th**	2.856	0.176	2.057	4.173	2.116
	U	2.347	0.195	0.914	4.564	3.649

The actinide results show that the concentrations of Th are consistently higher than U in all cases except for one sample from the pilot mine. The concentration of U and Th was very consistent when comparing the north control site and the south control site, where Th had a

larger range compared to U at each site. The pilot mine had higher concentrations of U and Th compared to the raise bore site. The range for the pilot plant is the largest.

The results from Figure 5.7 (a) show that there is consistency across the Th elemental data. The U results show that there is a higher concentration of U at the raise bore site in comparison to the other sites, U was not detected at the South Control site. Overall, the Th results were very consistent across both the NAA and ICP-MS analysis, however, the U results vary. The U concentrations within the mining lease area detected using ICP-MS were higher than the NAA results. However, the sites outside of the lease area, arid, raise bore and north control, the results were lower when using ICP-MS compared to the NAA results, except for the South control site, as this was not detectable in the NAA data.
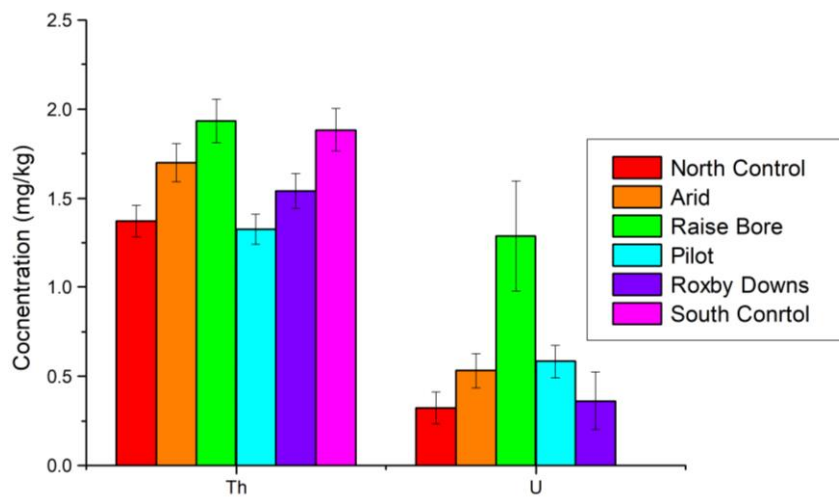
Figure 5.7.a Actinide concentration from soil composite results from NAA analysis.

148
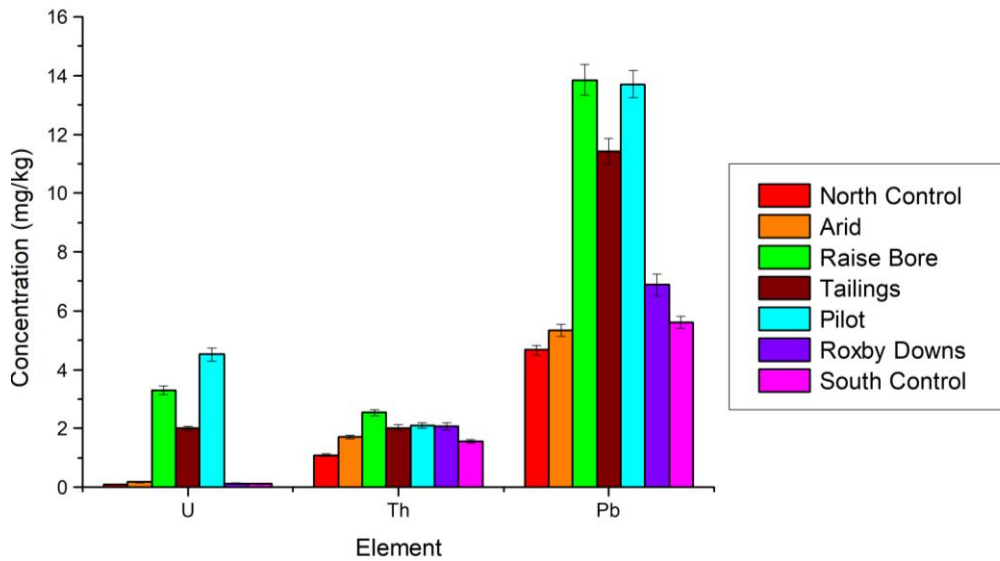
Figure 5.7.b Olympic Dam soil composite 0-10 cm interval elemental analysis using ICP-MS (n=6 samples 18 results).

Figure 5.7.b shows the ICP-MS results for U, Th and Pb from the different sample sites from Olympic Dam. The highest mean concentration overall was Pb at all sites. U was significantly higher in the raise bore, tailings and pilot sites, where Th was very consistent in concentration across all sites.

Vegetation results for actinides and Pb

The actinide concentrations within the *Dodonaea viscosa* and *Acacia ligulata* vegetation species from multiple sites in the Olympic Dam region were compared using ICP-MS and NAA. The elemental results for U, Th and Pb from the ICP-MS analysis of the *Dodonaea viscosa* and *Acacia ligulata* are found in appendix E. A summary of the results is shown below in Figure 5.8 and Table 5.6.

149
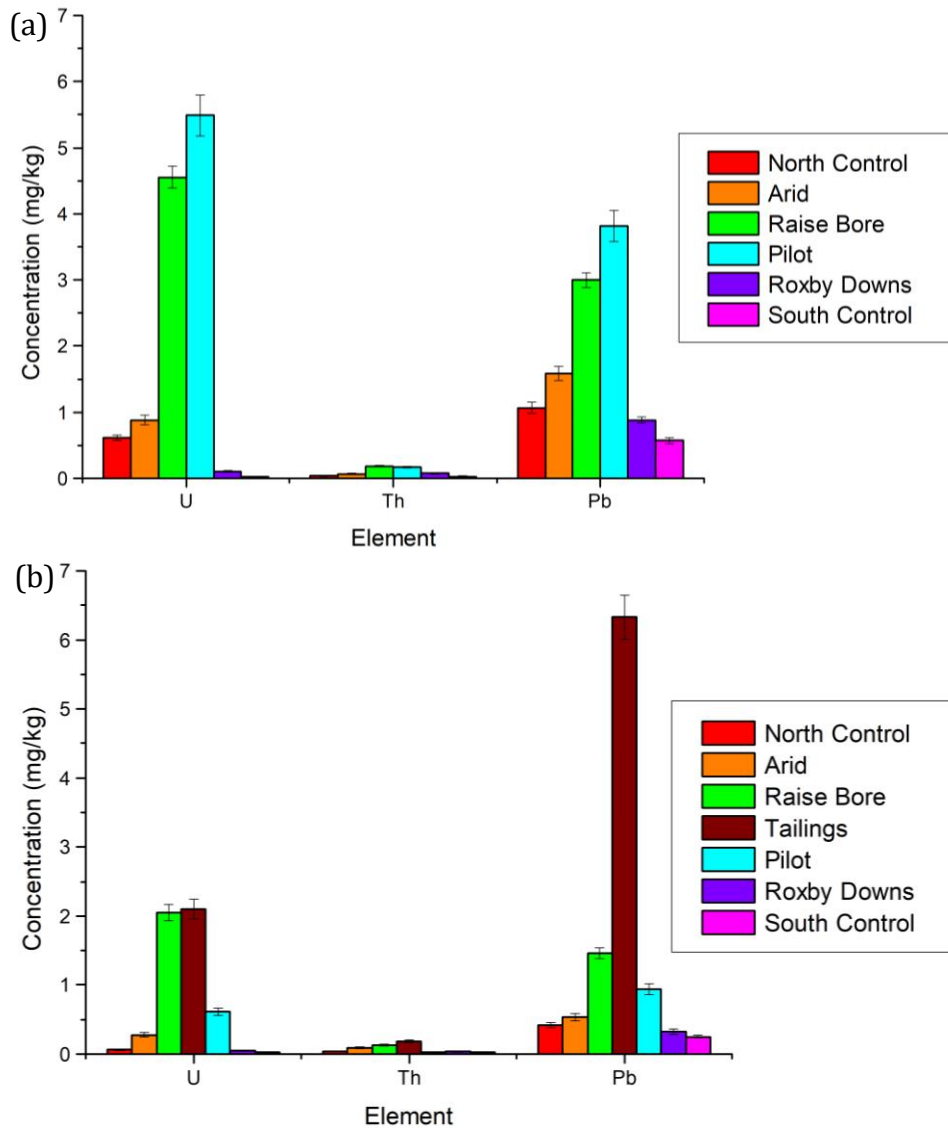
Figure 5.8. (a) Dodonaea viscosa ICP-MS concentrations (n=9) from 3 samples Dec 2018. (b) Acacia ligulata ICP-MS concentrations (n=9) from 3 samples Dec 2018.

The ICP-MS results for *Dodonaea viscosa* and *Acacia ligulata* show that there is a difference in uptake of U and Pb between the two species; the *Dodonaea viscosa* species has higher concentration of U compared to the *Acacia ligulata* species. A summary table of the average concentration is presented below in Table 5.6.

150

Table 5.6. Dodonaea viscosa ICP-MS concentrations (n=9) from 3 samples Dec 2018. Acacia ligulata ICP-MS concentrations (n=9) from 3 samples Dec 2018, 'uncert' was used as an abbreviation for uncertainty.

			Concentration (mg/kg)	Uncert (mg/kg)	Min (mg/kg)	Max (mg/kg)	Range (mg/kg)	SD
Acacia ligulata	North Control	U	0.060	0.010	0.039	0.077	0.038	0.011
		Th	0.038	0.004	0.016	0.089	0.073	0.026
		Pb	0.418	0.040	0.370	0.449	0.079	0.029
	Arid	U	0.279	0.033	0.156	0.474	0.318	0.123
		Th	0.092	0.008	0.070	0.129	0.059	0.019
		Pb	0.536	0.047	0.355	0.806	0.451	0.170
	Raise Bore	U	2.049	0.120	1.270	2.778	1.508	0.570
		Th	0.132	0.010	0.086	0.212	0.126	0.045
		Pb	1.463	0.078	0.873	2.216	1.344	0.498
	Tailings	U	2.106	0.143	1.718	2.794	1.076	0.472
		Th	0.187	0.016	0.160	0.240	0.080	0.027
		Pb	6.331	0.322	4.869	8.298	3.429	1.383
	Pilot	U	0.617	0.051	0.396	0.893	0.497	0.192
		Th	0.029	0.003	0.023	0.034	0.011	0.003
		Pb	0.943	0.078	0.726	1.262	0.536	0.214
	Roxby Downs	U	0.047	0.011	0.028	0.059	0.031	0.009
		Th	0.036	0.004	0.019	0.071	0.051	0.021
		Pb	0.326	0.034	0.213	0.418	0.206	0.082
	South Control	U	0.025	0.005	0.015	0.037	0.022	0.006
		Th	0.028	0.003	0.014	0.059	0.045	0.014
		Pb	0.252	0.017	0.170	0.341	0.171	0.065
Dodonaea viscosa	North Control	U	0.613	0.039	0.084	4.640	4.556	1.424
		Th	0.034	0.004	0.014	0.099	0.085	0.028
		Pb	1.063	0.084	0.634	3.091	2.457	0.730
	Arid	U	0.884	0.076	0.783	1.032	0.249	0.095
		Th	0.071	0.007	0.050	0.107	0.057	0.024
		Pb	1.585	0.108	1.405	1.787	0.382	0.135
	Raise Bore	U	4.552	0.162	3.564	5.588	2.023	0.775
		Th	0.190	0.012	0.114	0.351	0.237	0.075
		Pb	3.000	0.111	2.325	3.661	1.337	0.558
	Pilot	U	5.486	0.313	1.994	8.167	6.173	2.522
		Th	0.168	0.017	0.074	0.236	0.162	0.055
		Pb	3.818	0.236	2.718	5.084	2.365	0.079
	Roxby Downs	U	0.108	0.012	0.096	0.118	0.022	0.007
		Th	0.073	0.008	0.032	0.142	0.109	0.046
		Pb	0.883	0.049	0.751	1.080	0.329	0.133
	South Control	U	0.023	0.004	0.018	0.029	0.012	0.004
		Th	0.032	0.004	0.016	0.043	0.027	0.011
		Pb	0.573	0.046	0.498	0.655	0.156	0.051

*n=9

Actinide concentration within the samples using NAA were analysed and the results are in appendix E. The composite samples of vegetation from Olympic Dam May 2018 for *Acacia ligulata* and *Dodonaea viscosa* of U and Th are summarised and shown below in Figure 5.9.
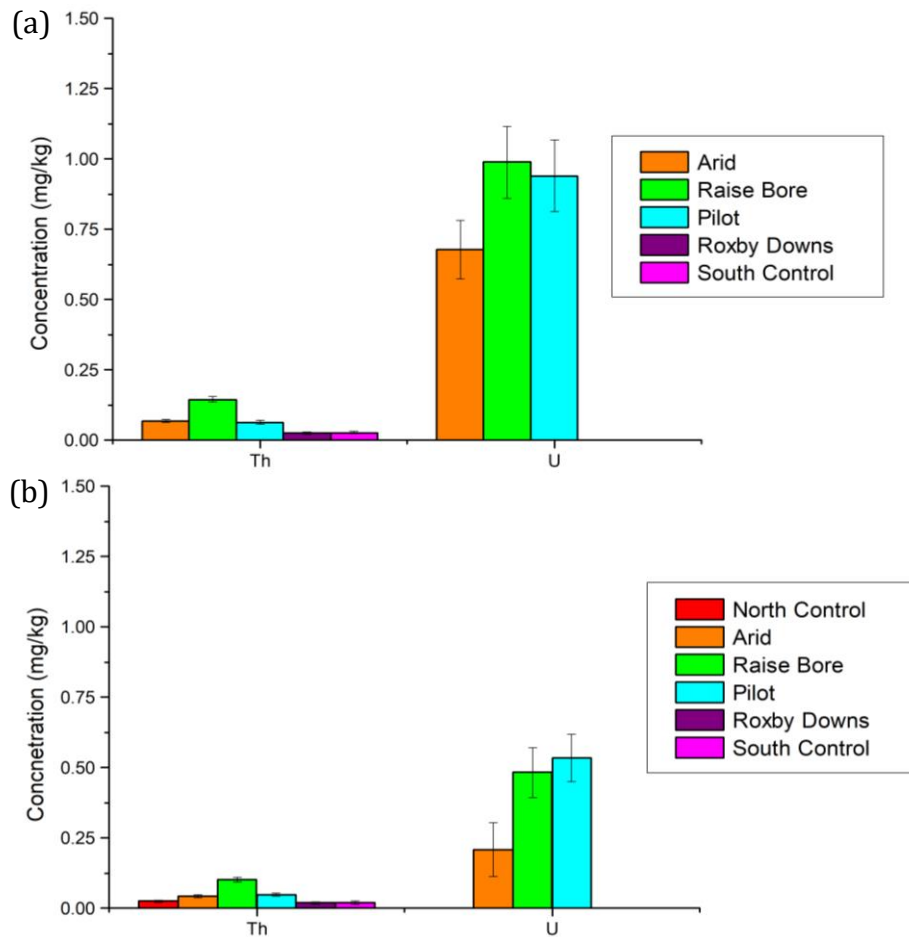
Figure 5.9. Actinides results for vegetation composite samples analysed using NAA results. (a) Dodonaea viscosa and (b) Acacia ligulata.

The results from Figure 6.4 shows the *Dodonaea viscosa* sample has higher concentration of U compared to *Acacia ligulata*, this is consistent with the activity data from chapter 4 and the ICP-MS results from above. U was not detected in the composite sample from the north control, Roxby Downs or south control samples. The highest concentration of U was identified at the pilot mine. The highest concentration of Th was identified at the raise bore site. Th was identified at all sites above the LOD.

5.3.2. Lanthanide results of soil and vegetation from Olympic Dam

Soil lanthanide NAA results

Lanthanide concentrations of composite soil samples from Autumn (May 2018) are shown below in Figure 5.10 as chondrite normalised plots. These data were normalized by chondrite values from Taylor and McLennan 1985 (Taylor & McLennan, 1985).
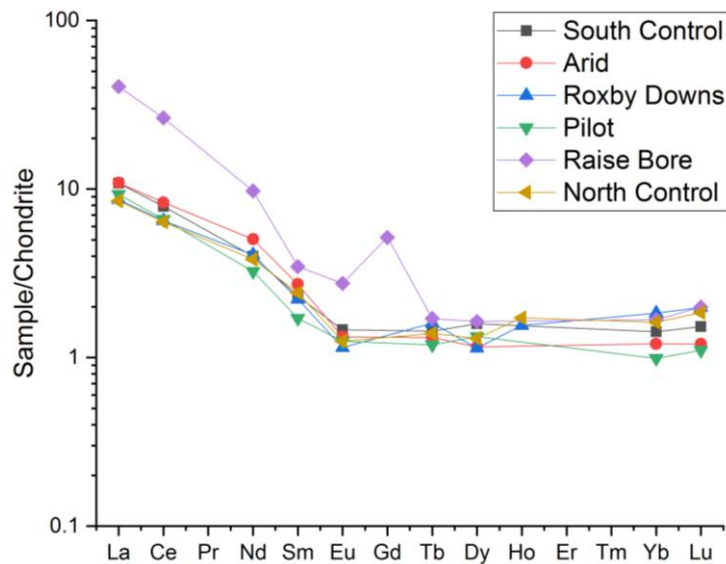
Figure 5.10. NAA Lanthanide results from soil 0-10 cm collection, 2018 may composite samples, chondrite normalised plot (Taylor & McLennan, 1985).

Figure 5.10 shows chondrite normalised NAA results for Olympic Dam composite soil samples from 0-10 cm collection during Autumn (May 2018) (Taylor & McLennan, 1985). Figure 5.10 shows an enrichment of the light REEs (LREEs) in comparison to the heavy REEs (HREEs) consistently across all sites analysed. The raise bore site is more highly enriched in the light REEs in comparison to the other sites. The arid site is more enriched in the LREEs in comparison to other sites. However, is more depleted in HREEs in comparison to sites except for the pilot and Roxby Downs sites. The Roxby Downs site is enriched in Gd, where Gd was not detected in the samples from all other sites. A minor depletion of Dy at the Roxby Down site was also observed. Pr is a radioactive element and is not found naturally in the environment, therefore was not detected at any of the sites. A negative anomaly of Eu was observed for the raise bore site. However, it was only detectable at that site, with the elevation of Sm in all other sites in comparison to Eu, it is assumed that there is a negative anomaly of Eu across all sites (Ticianelli et al., 2013). This indicates that the Eu is in the Eu^{2+} state as the concentration is lower than the Sm and Gd neighbours, the Eu^{2+} is readily incorporated within feldspars and is therefore shown as a depletion in Figure 5.10.

153

A comparison of chondrite normalised results from composite 0-10 soil samples from three different sites over two different time periods have been performed, the results are in Figure 5.11.
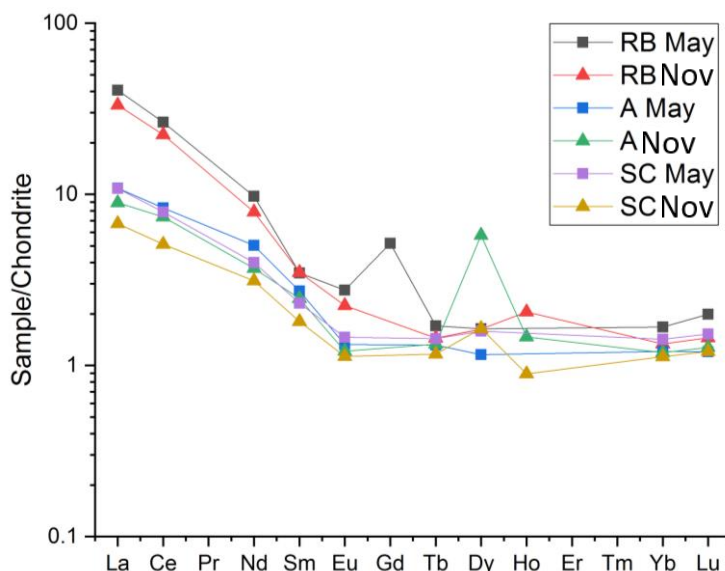
Figure 5.11. NAA lanthanide chondrite normalised plots 0-10 cm composite samples 6X sample each sample. Squares represent spring (May 2018), triangles represent (November 2018) results (Taylor & McLennan, 1985)

Figure 5.11 above shows a chondrite normalised NAA results of a comparison of Olympic Dam composite soil samples from 0-10 cm collection during Autumn (May 2018) and Spring (November 2018) (Taylor & McLennan, 1985). Overall, the results from the Spring samples show lower concentrations in comparison to the samples taken in Autumn. Dy in the arid and South control samples from Spring is enriched compared to the other samples and sites. Gd in the RB Autumn raise bores site is enriched, it is also the only sample where detectible Gd was present.

The samples were analysed in replicates to determine whether there was much variability within the same sample collection sites. The chondrite normalised NAA results for four different Olympic Dam sites are shown below in Figure 5.12.
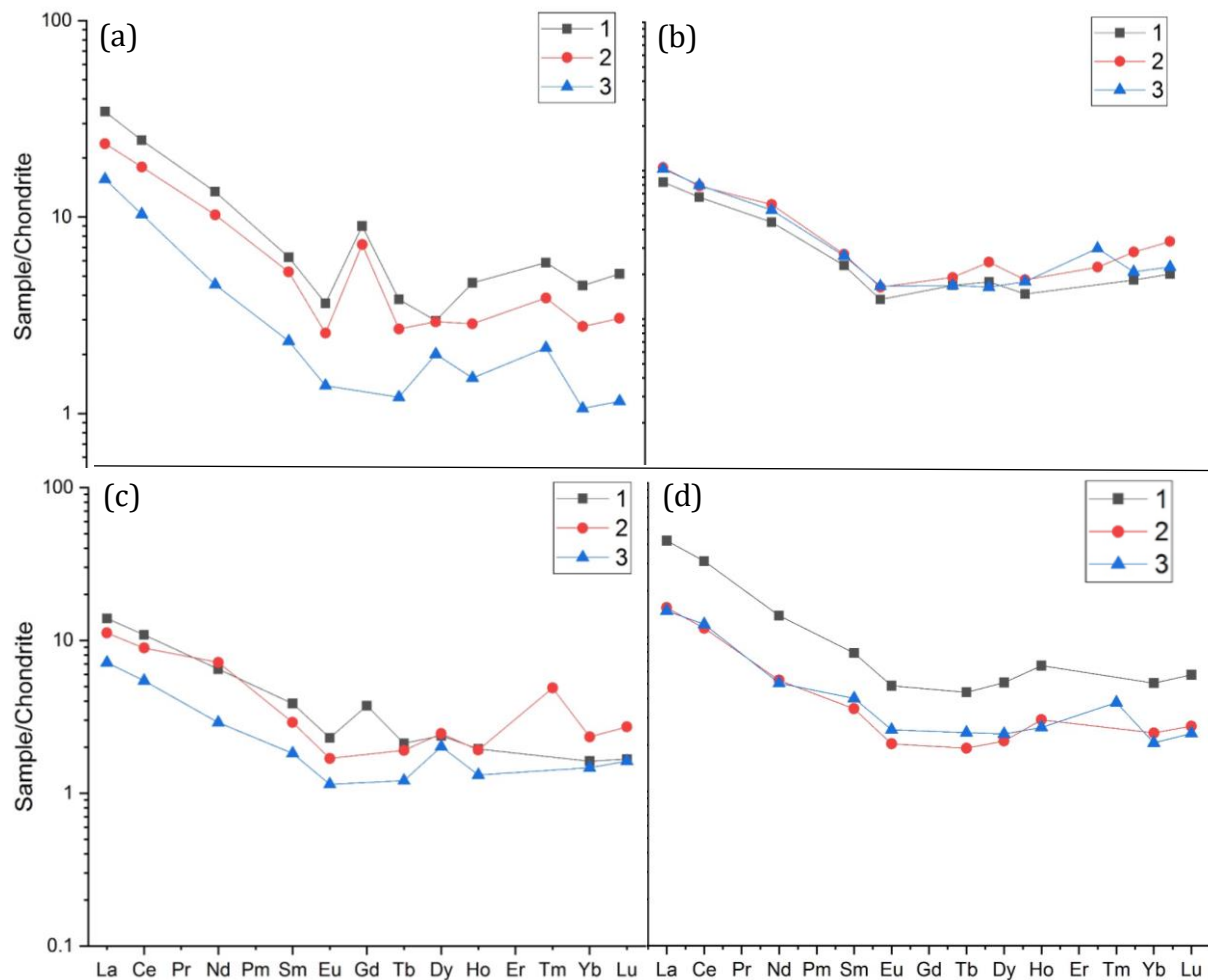
Figure 5.12. Olympic Dam lanthanide REE, chondrite normalised, plot 0-10 cm composite samples for CR analysis (replicates) NAA data. (a) raise bore (b) South Control (c) North control (d) Pilot (Taylor & McLennan, 1985).

The chondrite normalized plots from the NAA results for soil collected for concentration ratios from 0-10 cm is shown above in Figure 5.12. This figure shows data for the raise bore site, south control site, north control site and the pilot plant site. The replicate results from all sites shows that there is variation within the concentration of lanthanides from soil samples taken from within the same site. The South control site shows the least variation between replicates. The raise bore site showed Gd concentrations detectable within two of the three replicates. However, the only other sample where Gd was detected was one north control sample. In all sites the Eu anomaly shows the samples are depleted in Eu assuming the Gd trend remains the same for the rest of the samples. Tm is enriched in the sample it was detectable in from the raise bore, north control and the pilot sites. However, it is only enriched in one of the two South control samples it was detected in.

155

Vegetation lanthanide NAA results

NAA results for lanthanides are represented as chondrite normalized plots in Figure 5.13 (Taylor & McLennan, 1985).
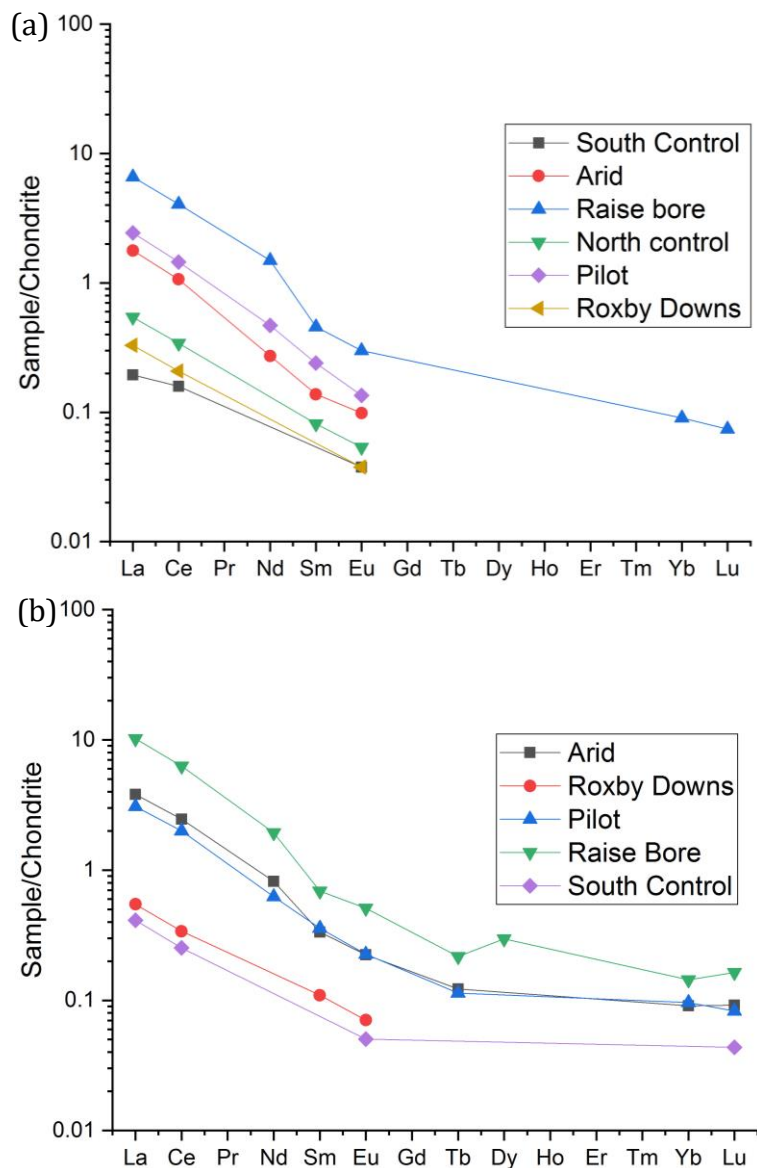
Figure 5.13. (a) Acacia composite NAA samples chondrite plot. (b) Dodonaea viscosa composite vegetation all sites NAA chondrite all samples are composites.

The NAA results of the vegetation samples is shown above in Figure 5.13. The HREE results from both *Acacia ligulata* and *Dodonaea viscosa* were not above detectable concentrations in many cases. Only the *Acacia ligulata* from the raise bores site had a detectible level of Yb and Lu, these were the only HREEs detected within the Acacia Ligulata samples from all sites. The LREE results from the *Acacia ligulata* were enriched in comparison to the HREEs. There is a depletion of Eu compared to Sm, however, no Gd results are available to comment on. The site with the highest concentration of LREEs is the raise bore site, this is consistent with the

soil results from above. The *Acacia ligulata* species has higher concentrations of LREEs at the Pilot plant in comparison to *Dodonaea viscosa*. Where *Dodonaea viscosa* showed samples from the arid site to be higher than the *Acacia ligulata* arid site. The south control site showed the lowest concentration of LREEs for both species. The North control site could not be compared due to the lack of *Dodonaea viscosa* at this site.

A direct comparison of lanthanide concentrations from both species at each site is shown below in Figure 5.14.
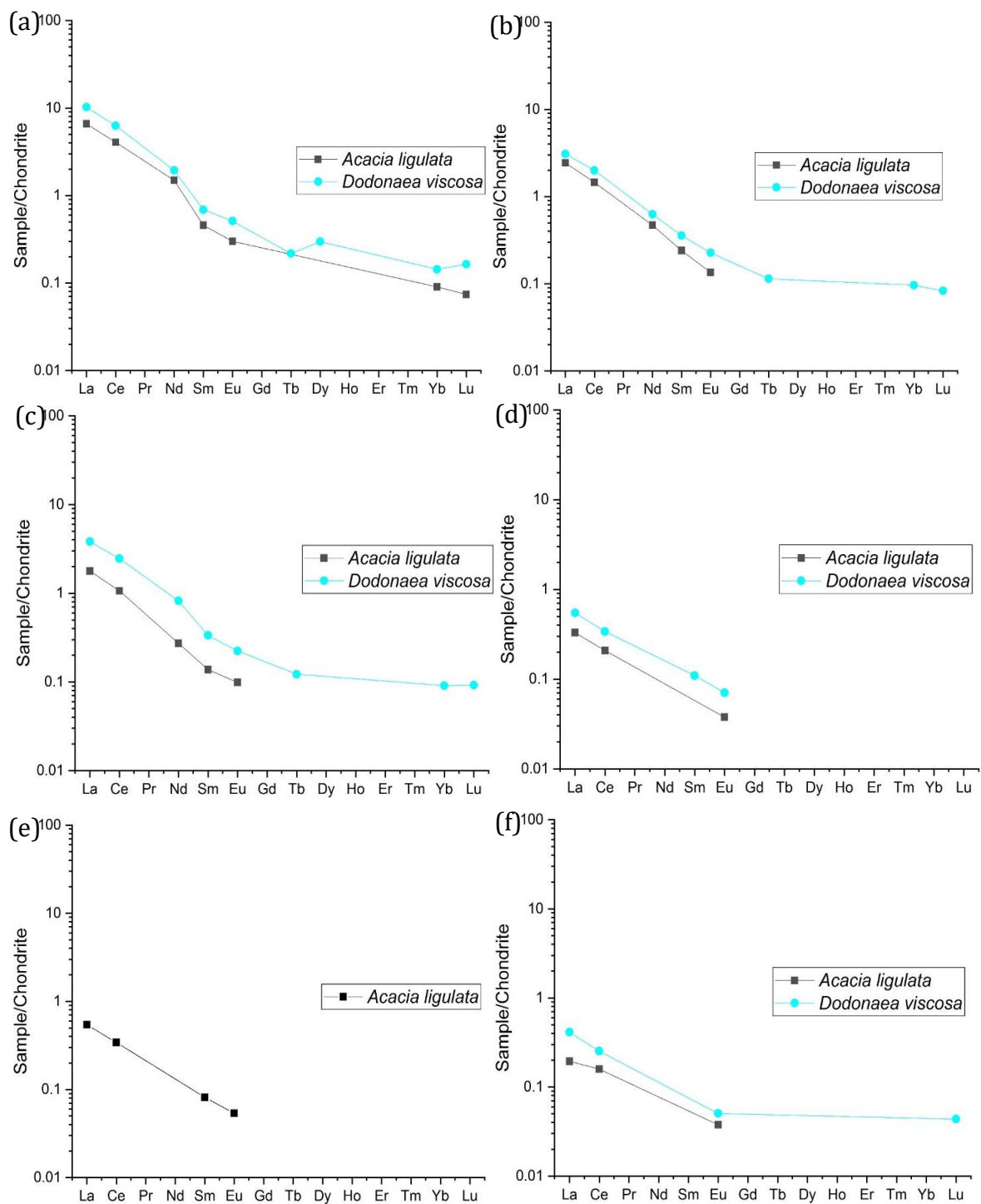
Figure 5.14. NAA chondrite normalised results from composite vegetation samples. Comparison of Species within sample sites. (a) Raise Bore, (b) Pilot, (c) Arid, (d) Roxby Downs, (e) North Control and (f) South Control. Note, no Dodonaea viscosa were found at the north control site therefore there were none available for analysis

The results from NAA analysis on the vegetation samples show that at all sites *Dodonaea viscosa* had higher concentrations of detected elements compared to *Acacia ligulata*, with the exception of the North Control, in which no comparison can be made due to the lack of

available *Dodonaea viscosa*. When comparing to Sm only, Eu appears to have a negative anomaly for all species at all sites. There were no other enrichments or depletions with regards to lanthanides compared to the chondrite value. There is little difference in the measured concentration lanthanide elements within the same sites.

5.3.3. Elemental results of soil and vegetation from Olympic Dam

Soil results for vegetation nutrients and trace elements from NAA

From the same soil sample analysis as discussed previously, soil nutrients and trace elemental concentrations have been determined, this is discussed below. Elemental concentrations of soil samples that are of potential interest when considering soil nutrients and trace elements. A summary table is shown below in Table 5.7.

Table 5.7. NAA soil composite samples (0-10 cm) element concentrations.

	South Control		Arid		Roxby Downs		Pilot		Raise Bore		North Control	
	Concentration (Mg/kg)	LOD (mg/kg)	Concentration (Mg/kg)	LOD (mg/kg)	Concentration (Mg/kg)	LOD (mg/kg)	Concentration (Mg/kg)	LOD (mg/kg)	Concentration (Mg/kg)	LOD (mg/kg)	Concentration (Mg/kg)	LOD (mg/kg)
Na	166.0 ± 34.46	0.101	121.0 ± 12.81	0.102	121.7 ± 8.534	0.127	118.5 ± 7.551	0.106	335.6 ± 49.52	0.216	177.4 ± 12.44	0.079
Mg	626.1 ± 52.70	0.460	837.1 ± 62.78	0.359	681.6 ± 54.78	0.451	784.8 ± 113.2	0.349	865.1 ± 63.99	0.444	568.2 ± 48.62	0.346
K	1766 ± 595.7	128.1	1279 ± 349.4	116.7	1494 ± 166.4	115.4	1001 ± 103.6	116.1	1584 ± 254.5	200.0	1280 ± 126.6	126.4
Ca	446.8 ± 83.31	2.607	1029 ± 117.9	1.820	387.9 ± 87.97	2.629	1016 ± 169.6	2.069	712.5 ± 143.0	3.064	255.5 ± 88.08	31.79
Rb	10.00 ± 1.589	2.417	6.825 ± 1.364	2.163	7.205 ± 1.368	2.109	5.225 ± 1.247	1.956	10.93 ± 1.869	2.630	6.067 ± 1.277	2.097
Cs	0.517 ± 0.057	0.111	0.397 ± 0.048	0.096	0.421 ± 0.048	0.097	0.316 ± 0.079	0.089	0.519 ± 0.060	13.69	0.317 ± 0.044	0.093
Ba	180.1 ± 11.79	0.234	175.7 ± 11.45	0.170	156.4 ± 14.33	0.301	152.2 ± 10.94	0.163	295.9 ± 49.55	0.563	210.2 ± 13.62	0.161
Al	8015 ± 492.7	7.934	6232 ± 395.9	7.192	7842 ± 476.0	11.97	6060 ± 366.1	7.823	7737 ± 475.9	9.275	6004 ± 364.5	11.33
Cl	12.98 ± 3.417	3.404	25.69 ± 4.017	3.536	12.34 ± 3.832	4.252	29.91 ± 4.379	3.739	120.0 ± 9.016	5.677	20.73 ± 4.256	3.729
As	1.490 ± 0.133	0.149	1.151 ± 0.113	0.139	1.101 ± 0.107	0.130	1.053 ± 0.103	0.126	6.590 ± 0.511	0.426	1.144 ± 0.114	0.139
Br	0.537 ± 0.090	0.231	0.514 ± 0.081	0.212	0.378 ± 0.076	0.202	0.487 ± 0.075	0.197	0.790 ± 0.195	0.548	0.436 ± 0.080	0.215
Sb	0.150 ± 0.031	0.059	0.114 ± 0.040	0.039	0.141 ± 0.025	0.051	0.102 ± 0.024	0.048	0.822 ± 0.071	0.164	0.097 ± 0.028	0.052
Sc	1.621 ± 0.097	0.002	1.206 ± 0.073	0.002	1.300 ± 0.078	0.002	1.043 ± 0.063	0.001	1.643 ± 0.098	0.002	1.100 ± 0.065	0.002
Ti	673.7 ± 62.32	39.96	398.9 ± 32.91	36.93	608.5 ± 47.76	47.99	476.8 ± 42.64	38.82	797.5 ± 56.35	46.74	658.2 ± 50.37	46.18
V	19.35 ± 1.240	0.254	17.65 ± 1.374	0.228	17.80 ± 1.179	0.275	16.70 ± 1.092	0.244	19.37 ± 1.251	0.292	15.86 ± 1.069	0.278
Cr	10.23 ± 0.704	0.548	7.361 ± 0.532	0.476	8.878 ± 0.611	0.468	7.099 ± 0.507	0.433	10.21 ± 0.761	0.600	6.876 ± 0.506	0.488
Mn	37.98 ± 2.328	0.080	23.71 ± 1.501	0.075	31.29 ± 1.963	0.091	23.18 ± 1.488	0.076	41.66 ± 2.550	0.092	24.32 ± 1.548	0.084
Fe	6865 ± 415.4	29.56	5157 ± 312.8	26.51	5789 ± 350.5	26.19	4954 ± 300.4	24.13	11220 ± 677.0	32.81	4365 ± 265.4	26.62
Co	1.073 ± 0.073	0.035	1.117 ± 0.076	0.031	0.874 ± 0.060	0.030	1.055 ± 0.071	0.028	1.542 ± 0.102	0.036	0.857 ± 0.061	0.030
Cu	ND	ND	69.40 ± 10.75	2.941	ND	ND	72.66 ± 11.28	2.977	38.96 ± 11.35	5.500	ND	ND
Zn	10.26 ± 1.486	1.148	8.758 ± 1.332	1.150	10.00 ± 1.329	1.082	8.126 ± 1.233	0.896	11.98 ± 1.678	1.380	6.114 ± 1.139	1.116
Zr	66.77 ± 22.50	7.373	78.31 ± 39.03	3.182	66.29 ± 17.38	5.594	52.27 ± 24.62	3.028	106.6 ± 20.34	10.48	149.6 ± 17.95	3.018
Hf	1.894 ± 0.129	0.046	1.630 ± 0.123	0.042	1.374 ± 0.100	0.041	0.928 ± 0.076	0.038	2.347 ± 0.181	0.052	3.714 ± 0.240	0.043
Ta	0.131 ± 0.041	0.035	0.083 ± 0.034	0.037	0.100 ± 0.310	0.035	0.072 ± 0.030	0.027	0.165 ± 0.041	0.043	0.143 ± 0.031	0.036

Results for Vegetation Nutrients and Trace Elements from NAA

Some plants within the arid Australian environment have shown to accumulate elements such as Mn within their foliage (He et al., 2018). Elements that are important for plant nutrients include N, P, K, Ca, Mg, Zn, and Mn (He et al., 2018). Therefore, an elemental screening analysis was preformed using NAA on the vegetation samples from the Olympic Dam region. N is not detectable using NAA and therefore, was not included within the results and discussion. The results from the *Acacia ligulata* samples from the Olympic Dam Autumn (May 2018) samples analysed from the different sites are shown below in Table 5.8.

Table 5.8. Fora NAA results composite Acacia ligulata elements

	South Control		Arid		Roxby Downs		Pilot		Raise bore		North control	
	Concentration (Mg/kg)	LOD (mg/kg)	Concentration (Mg/kg)	LOD (mg/kg)	Concentration (Mg/kg)	LOD (mg/kg)	Concentration (Mg/kg)	LOD (mg/kg)	Concentration (Mg/kg)	LOD (mg/kg)	Concentration (Mg/kg)	LOD (mg/kg)
Na	287.9 ± 18.13	0.004	518.5 ± 31.89	0.078	201.8 ± 12.27	0.004	1216 ± 77.68	0.098	1891 ± 123.7	3.057	433.9 ± 26.25	0.003
Mg	3089 ± 192.5	80.13	3178 ± 218.1	103.8	3635 ± 258.1	115.7	3772 ± 233.8	88.94	3534 ± 227.2	102.8	3357 ± 208.4	77.52
K	7553 ± 506.3	120.2	8318 ± 598.1	195.9	4979 ± 384.9	103.6	7047 ± 546.4	264.1	7650 ± 531.3	324.2	7745 ± 499.5	155.4
Ca	59700 ± 3675	155.8	60980 ± 3719	160.7	56010 ± 5453	137.6	57060 ± 3486	167.2	58880 ± 3691	174.4	59990 ± 3636	153.1
Rb	1.898 ± 0.281	0.309	2.347 ± 0.288	0.291	1.225 ± 0.232	0.268	2.161 ± 0.276	0.286	2.314 ± 0.304	0.330	2.661 ± 0.286	0.264
Sr	870.0 ± 55.12	5.784	807.4 ± 49.11	5.444	781.7 ± 47.83	4.932	723.7 ± 46.93	5.253	583.4 ± 36.99	5.882	506.9 ± 35.02	4.699
Cs	ND	ND	0.019 ± 0.004	0.011	0.016 ± 0.005	0.113	0.023 ± 0.005	0.011	0.033 ± 0.005	0.014	0.020 ± 0.005	0.011
Ba	46.97 ± 3.166	3.508	51.14 ± 3.393	0.178	50.56 ± 3.301	3.018	33.30 ± 2.400	0.144	57.50 ± 3.776	0.159	40.27 ± 2.739	2.881
Sc	0.023 ± 0.002	0.001	0.031 ± 0.001	0.001	0.025 ± 0.002	0.001	0.030 ± 0.001	0.001	0.052 ± 0.002	0.001	0.026 ± 0.002	0.001
V	0.243 ± 0.106	0.086	0.394 ± 0.140	0.126	0.218 ± 0.086	0.067	0.373 ± 0.112	0.084	0.669 ± 0.148	0.103	0.311 ± 0.103	0.082
Cr	0.625 ± 0.067	0.096	0.501 ± 0.060	0.093	0.374 ± 0.052	0.084	0.431 ± 0.056	0.089	0.692 ± 0.069	0.095	0.385 ± 0.049	0.078
Mn	11.56 ± 0.767	0.145	17.65 ± 1.126	0.187	11.82 ± 0.783	0.101	10.13 ± 0.694	0.151	14.88 ± 0.958	0.187	23.78 ± 1.473	0.140
Fe	98.50 ± 8.403	5.186	192.7 ± 12.53	5.197	107.5 ± 7.266	4.478	206.3 ± 13.17	4.887	458.9 ± 28.26	5.213	116.5 ± 7.816	4.431
Co	0.152 ± 0.017	0.007	0.178 ± 0.017	0.007	0.172 ± 0.012	0.007	0.244 ± 0.020	0.007	0.264 ± 0.017	0.009	0.135 ± 0.015	0.005
Cu	ND	ND	ND	ND	ND	ND	41.42 ± 11.18	ND	28.58 ± 10.56	9.370	ND	ND
Zn	9.298 ± 0.651	0.320	8.241 ± 0.591	0.305	7.795 ± 0.553	0.267	7.290 ± 0.528	0.298	7.787 ± 0.565	0.326	8.054 ± 0.569	0.270
Mo	4.467 ± 0.730	1.394	5.028 ± 0.883	0.922	3.741 ± 0.710	1.318	20.66 ± 1.526	0.735	6.384 ± 0.989	0.823	10.17 ± 1.093	1.581
Hf	ND	ND	ND	ND	ND	ND	0.008 ± 0.003	0.008	0.021 ± 0.005	0.009	ND	ND
Au	ND	ND	0.002 ± 0.001	ND	ND	ND	0.002 ± 0.001	0.001	0.002 ± 0.001	0.001	ND	ND
Al	142.5 ± 10.63	1.321	191.7 ± 13.58	1.772	147.2 ± 10.74	0.899	196.3 ± 16.54	1.255	387.3 ± 24.36	1.721	169.0 ± 11.92	1.088
S	28640 ± 5609	7493	24590 ± 8966	9619	22760 ± 5225	6693	22930 ± 4885	8309	29920 ± 6897	9382	22840 ± 5524	6920
Cl	4830 ± 293.5	11.21	3800 ± 235.4	19.96	2632 ± 160.4	9.290	3929 ± 244.1	11.42	6542 ± 398.4	13.57	3686 ± 222.2	12.29
Se	1.709 ± 0.111	0.101	0.630 ± 0.053	0.099	2.260 ± 0.141	0.088	1.405 ± 0.093	0.096	0.968 ± 0.070	0.100	0.221 ± 0.036	0.086
Br	55.65 ± 3.347	0.295	31.66 ± 1.913	0.376	42.31 ± 2.551	0.228	20.29 ± 1.238	0.517	28.85 ± 1.756	0.704	25.00 ± 1.510	0.266
Sb	ND	ND	ND	ND	ND	ND	ND	ND	0.038 ± 0.006	0.019	ND	ND
I	2.229 ± 0.692	1.337	ND	ND	37.75 ± 2.469	1.409	ND	ND	ND	ND	4.839 ± 0.759	1.334

The results from the *Dodonaea viscosa* samples from the Olympic Dam Autumn (May 2018) samples analysed from the different sites are shown below in Table 5.9.

Table 5.9. Fora NAA results composite Dodonaea viscosa elements

	South Control Concentration (Mg/kg)	LOD (mg/kg)	Arid Concentration (Mg/kg)	LOD (mg/kg)	Roxby Downs Concentration (Mg/kg)	LOD (mg/kg)	Pilot Concentration (Mg/kg)	LOD (mg/kg)	Raise Bore Concentration (Mg/kg)	LOD (mg/kg)
Na	789.6 ± 48.51	0.003	2247 ± 144.8	0.125	372.0 ± 23.23	0.003	1559 ± 96.32	0.179	5029 ± 310.2	0.172
Mg	2232 ± 146.6	98.77	3076 ± 195.0	100.3	2190 ± 134.5	37.01	2586 ± 168.2	105.3	2641 ± 178.3	188.0
K	8676 ± 577.5	269.5	8390 ± 597.0	308.3	8721 ± 549.3	128.6	8268 ± 687.9	342.7	8037 ± 709.9	625.5
Ca	12910 ± 808.3	121.8	11960 ± 729.2	113.0	8698 ± 542.9	130.7	10740 ± 690.7	129.6	11430 ± 714.5	163.9
Rb	0.969 ± 0.183	0.253	1.193 ± 0.223	0.305	0.737 ± 0.171	0.237	1.110 ± 0.203	0.280	1.386 ± 0.260	0.348
Sr	131.3 ± 8.785	4.459	102.4 ± 7.274	5.444	70.57 ± 5.117	4.130	91.96 ± 6.533	4.911	66.84 ± 5.519	6.126
Cs	ND	ND	0.021 ± 0.004	0.013	ND	ND	0.016 ± 0.005	0.012	0.029 ± 0.007	0.015
Ba	15.30 ± 1.434	2.710	20.23 ± 1.804	0.180	12.85 ± 1.266	2.517	14.80 ± 1.945	3.065	39.33 ± 3.269	0.216
Al	206.4 ± 14.26	1.404	294.3 ± 20.36	1.290	182.1 ± 12.42	0.969	304.1 ± 20.42	1.700	488.4 ± 30.17	1.408
Cl	2821 ± 172.1	12.91	4939 ± 308.7	13.50	1771 ± 106.8	5.196	2956 ± 179.7	14.81	7762 ± 471.0	26.40
Se	0.603 ± 0.047	0.080	0.302 ± 0.040	0.098	0.393 ± 0.036	0.073	0.511 ± 0.046	0.089	0.252 ± 0.039	0.105
Br	24.11 ± 1.465	0.426	16.26 ± 1.013	0.712	17.53 ± 1.062	0.227	13.34 ± 0.830	0.513	20.70 ± 1.297	0.991
Sb	ND	ND	0.025 ± 0.012	0.017	0.040 ± 0.006	0.014	0.026 ± 0.009	0.017	0.058 ± 0.009	0.021
I	ND	ND	ND	0.916	0.983 ± 0.317	0.616	ND	ND	ND	ND
Sc	0.033 ± 0.001	0.001	0.050 ± 0.002	0.001	0.033 ± 0.001	0.001	0.048 ± 0.002	0.001	0.073 ± 0.004	0.001
V	0.320 ± 0.125	0.103	0.494 ± 0.122	0.081	0.297 ± 0.092	0.061	0.525 ± 0.151	0.121	0.812 ± 0.150	0.097
Cr	0.310 ± 0.045	0.070	0.552 ± 0.061	0.088	0.293 ± 0.042	0.065	0.577 ± 0.057	0.081	0.885 ± 0.076	0.094
Mn	22.34 ± 1.397	0.175	24.87 ± 1.537	0.178	17.85 ± 1.119	0.067	23.59 ± 1.471	0.187	37.30 ± 2.287	0.354
Fe	118.8 ± 7.945	4.15	330.4 ± 20.60	5.100	119.3 ± 7.878	3.848	306.6 ± 19.07	4.601	656.7 ± 40.11	5.340
Co	0.178 ± 0.011	0.005	0.363 ± 0.023	0.007	0.359 ± 0.023	0.005	0.370 ± 0.023	0.006	0.450 ± 0.029	0.002
Cu	ND	ND	65.02 ± 11.27	8.791	ND	ND	87.87 ± 14.79	9.314	61.91 ± 14.85	12.88
Zn	15.66 ± 1.015	0.264	12.00 ± 0.803	0.311	9.919 ± 0.665	0.237	15.52 ± 1.002	0.288	12.24 ± 0.821	0.335
Mo	ND	ND	ND	ND	ND	ND	1.964 ± 0.990	1.116	ND	ND
Hf	0.012 ± 0.002	0.007	0.016 ± 0.004	0.008	0.011 ± 0.002	0.005	0.014 ± 0.002	0.006	0.024 ± 0.003	0.009
Au	ND	ND	0.003 ± 0.000	0.001	ND	ND	0.005 ± 0.001	0.001	0.007 ± 0.001	0.001

From the composite NAA analysis, the average concentration of Mg within *Dodonaea viscosa* across all sites is 2545 ± 164.52 mg/kg and the average Ca is 11147.6 ± 697.12 mg/kg, where n=5X 3 composites. The average Mg concentration of *Acacia ligulata* across all sites is 3427.5 ± 223.0 mg/kg. The average Ca is 58770 ± 3943.3 mg/kg. The uncertainty of Ca measurements using NAA is high. Na concentrations of *Dodonea viscosa* were significantly higher at the Raise bore site in comparison to the other sites and in comparison, to *Acacia ligulata*. The Na concentrations for *Acacia ligulata* across all sites showed minimal variation. The *Acacia ligulata* species only showed Cu above the LOD at the Raise Bore and Pilot sites. Both species showed similar concentrations of Cu.

Elemental analysis of stratified soil by NAA

Thorough elemental analysis of soil will provide data on available plant nutrients for uptake (He et al., 2018). Within this study NAA and ICP-MS were used to provide quantitative elemental data throughout the stratified soil samples. ICP-MS was used to determine the very low concentrations of U and Th. As ICP-MS does require sample digestion prior to analysis, the silica component of the soil was assumed to not contain any U, Th or Pb for this study.

Stratified soil samples from Olympic Dam sites outlined in Chapter 2 were analysed using NAA to provide a broad range of elemental data through the stratified soil. NAA analysis was performed on the soil samples to determine the elemental profile throughout the depth of the soil. This was used to determine the likelihood of uptake into vegetation and the influence of dust deposition. The elements which are of nutritional value to the plants were studied through depth, this was performed to determine whether there is any competition occurring from the NORM series.

Stratified actinide concentrations of soil by NAA

The actinides concentrations of U and Th within stratified soil samples from the different Olympic Dam sites were analysed using NAA, the results are shown in Figure 5.15.
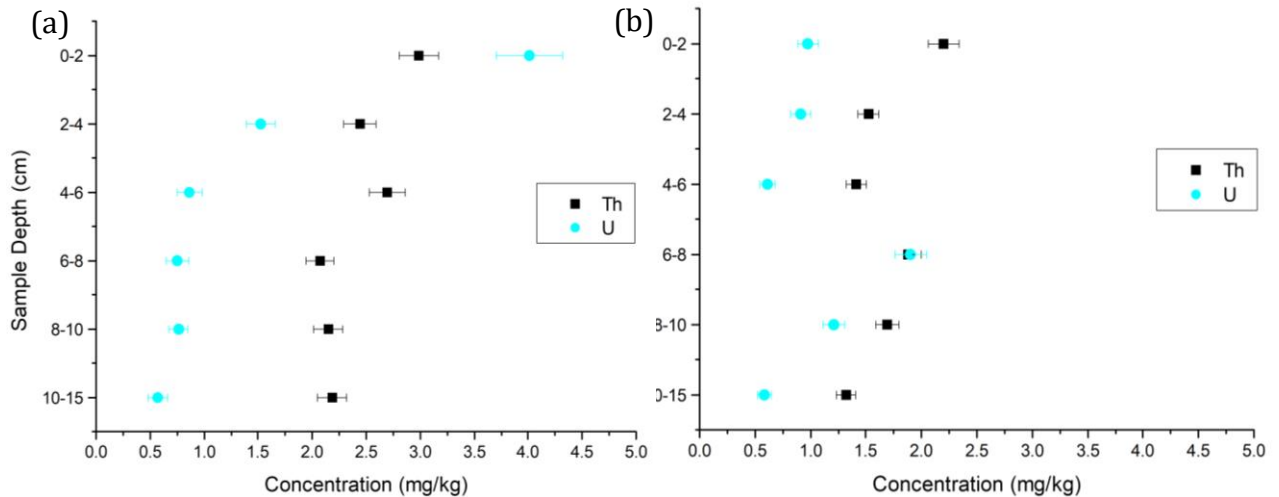
Figure 5.15. NAA U and Th results from the depth profile analysis of soil from Olympic Dam (a) raise bore, (b) pilot.

Figure 5.15 above shows the variation of U and Th concentrations detected using NAA within soil samples of decreasing depth from the raise bore site (Figure 5.15 (a) and the pilot site Figure 5.15 (b)). From the raise bore site results, the only soil depth that has U concentrations greater than Th was soil 0-2 cm. The 0-4 cm interval shows U at a higher concentration compared to the 4 to 15 cm intervals. The pilot site interval 6-8 cm is the interval with the highest concentration of U. The 6-8 cm interval also has U and Th concentrations within the uncertainty of each other.

The variation of U and Th within each site for the arid, Roxby Downs, north control and south control sites were minimal through depth. The results from these can be found in the appendix E. There was no clear trend of U and Th concentration throughout the depth of the soil samples from these sites. The ranges of the U and Th concentrations from these sites are in Table 5.10 below.

Table 5.10. Actinide concentration ranges Olympic Dam Autumn (May 2018) NAA results.

Site	U max conc (mg/kg)	U min conc (mg/kg)	U conc range (mg/kg)	Th max conc (mg/kg)	Th min conc (mg/kg)	Th conc range (mg/kg)
Raise Bore	4.010	0.568	3.441	2.987	2.074	0.913
Pilot	1.903	0.587	1.315	2.200	1.320	0.880
Arid	0.364	0.194	0.172	1.697	1.142	0.555
Roxby Downs	0.340	0.199	0.140	1.661	1.127	0.534
North Control	0.287	0.000	0.287	1.554	1.054	0.500
South Control	0.357	0.244	0.111	1.846	1.289	0.557

U was below the LOD for the north control sample at 0-2 cm. Overall, U concentrations outside of the mining lease area is relatively consistent throughout all sites. The results in

165

Figure 5.15 show that the contribution of U to the soil through depositional contribution is observed as the concentration of U decreases with the decrease in depth of soil (bhpbilliton, 2013). The results from Figure 5.15 (b) show the U and Th from the pilot mine soil depth profile, the results throughout the depth do not show any clear trends. The soil at this location has been highly disturbed by the mining activities therefore, the effect of surface deposition is not observed, likely due to the turnover and movement of soil and that the surface deposition in minimal in comparison to the turnover and movement of soil. The actinide concentrations throughout the soil samples from Olympic Dam show that at the north control and south control sites there is no significant difference between the depths of soil and the difference in concentration.

Stratified lanthanide concentrations of soil by NAA

The stratified lanthanide results from the NAA analysis are shown below in Figure 5.16. The data has been normalized against chondrite values from Taylor and McLennan, 1985 (Taylor & McLennan, 1985).
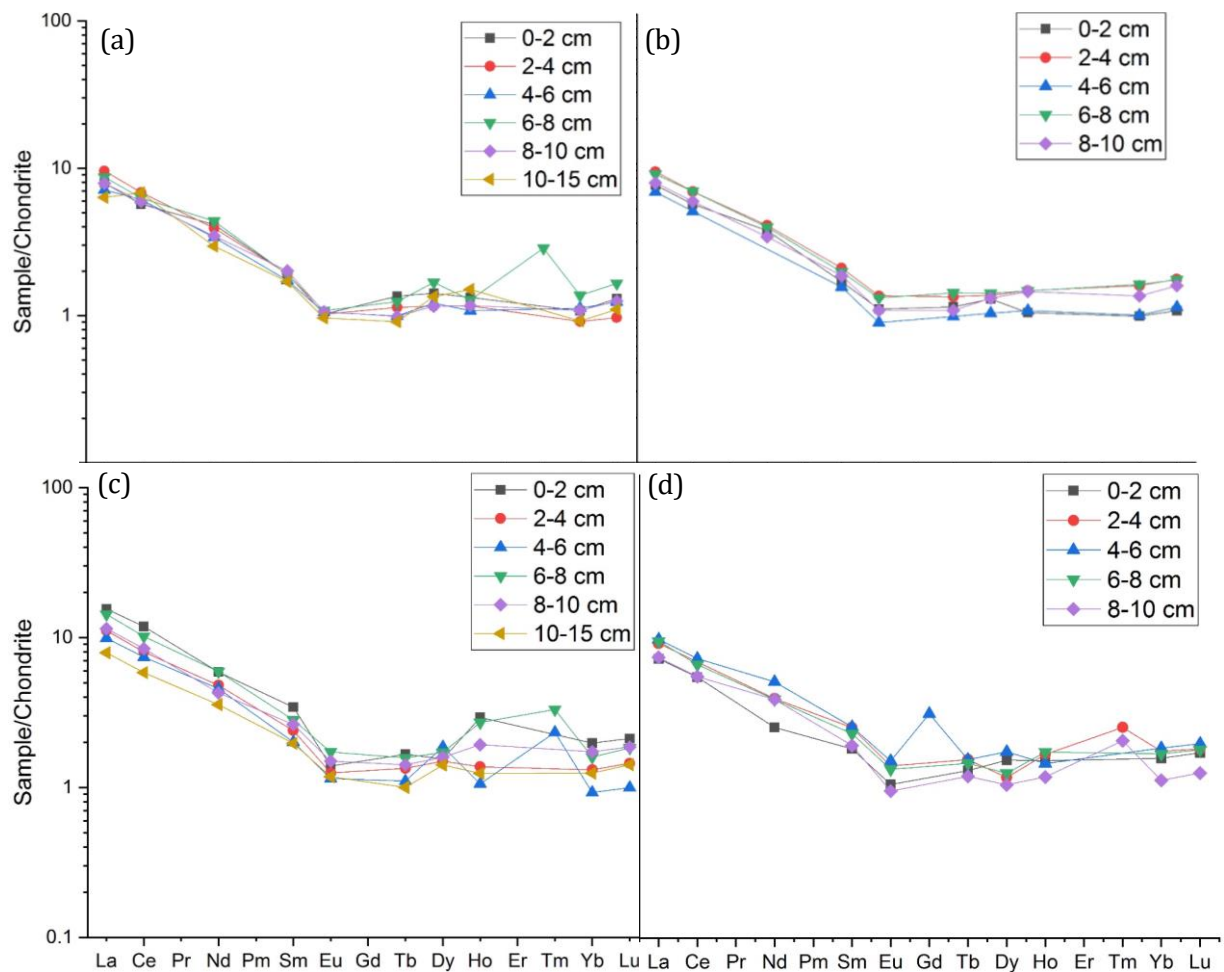
Figure 5.16. NAA results from the lanthanide chondrite normalised from Olympic Dam soil depth profiling. (a) arid, (b) Roxby Downs, (c.) pilot and (d) south control (Taylor & McLennan, 1985).

The results from Figure 5.16 show that the pilot, arid, Roxby Downs and south control sites all show enrichment of the LREEs in comparison to the HREEs. The pilot site has higher concentrations of the LREEs compared to the arid, Roxby Downs and south control sites. The south control Sites is the only sites where Gd was measured. Gd was only identified in the 4-6 cm fraction from the south control site, however, was measured in all soil fractions except for the 0-2 cm fraction. On every occasion where Gd was measured it shows enrichment in the chondrite normalised plots. Sm is enriched on every occasion it was measured except for the raise bore site where the 4-6 cm and 10-15 cm fractions are depleted. Therefore, if using the Sm and the available Gd data, we can assume there is a negative Eu ammonily within our system on every occasion except for the 4-6 cm and 10-15 cm fractions from the raise bore site. This indicates that the Eu is in the Eu^{2+} state in each sample except for the 4-6 cm and 10-15 cm fractions where the Eu^{3+} is assumed. A Tm enrichment is observed in all sties except for the Roxby Downs site, where no Tm was identified. The arid site (c) shows an enriched Tm

167

at the 6-8 cm depth, however this was the only depth where Tm was above the LOD for the arid site. Pr, Eu and Tm were not identified in any of the (d) Roxby Downs samples from any depth of soil. The (f) south control sample at 4 to 6 cm soil depth sample was the only sample to have Gd. Pr, Pm and Er were not identified in any samples.

Stratified nutrients and elemental concentrations by NAA

A variety of elements have been discussed below due to their role in vegetation nutrients or of potential interest from mining operations (He et al., 2018). Elements of interest when considering vegetation nutrients include Ca, Mg, Zn and Mn (He et al., 2018). Elements known to be in elevated concentrations within the ore deposit such as Al, Cu are also analysed. The stratified results for Zn and Mn in soil from the different sites at Olympic Dam are shown in Figure 5.17.
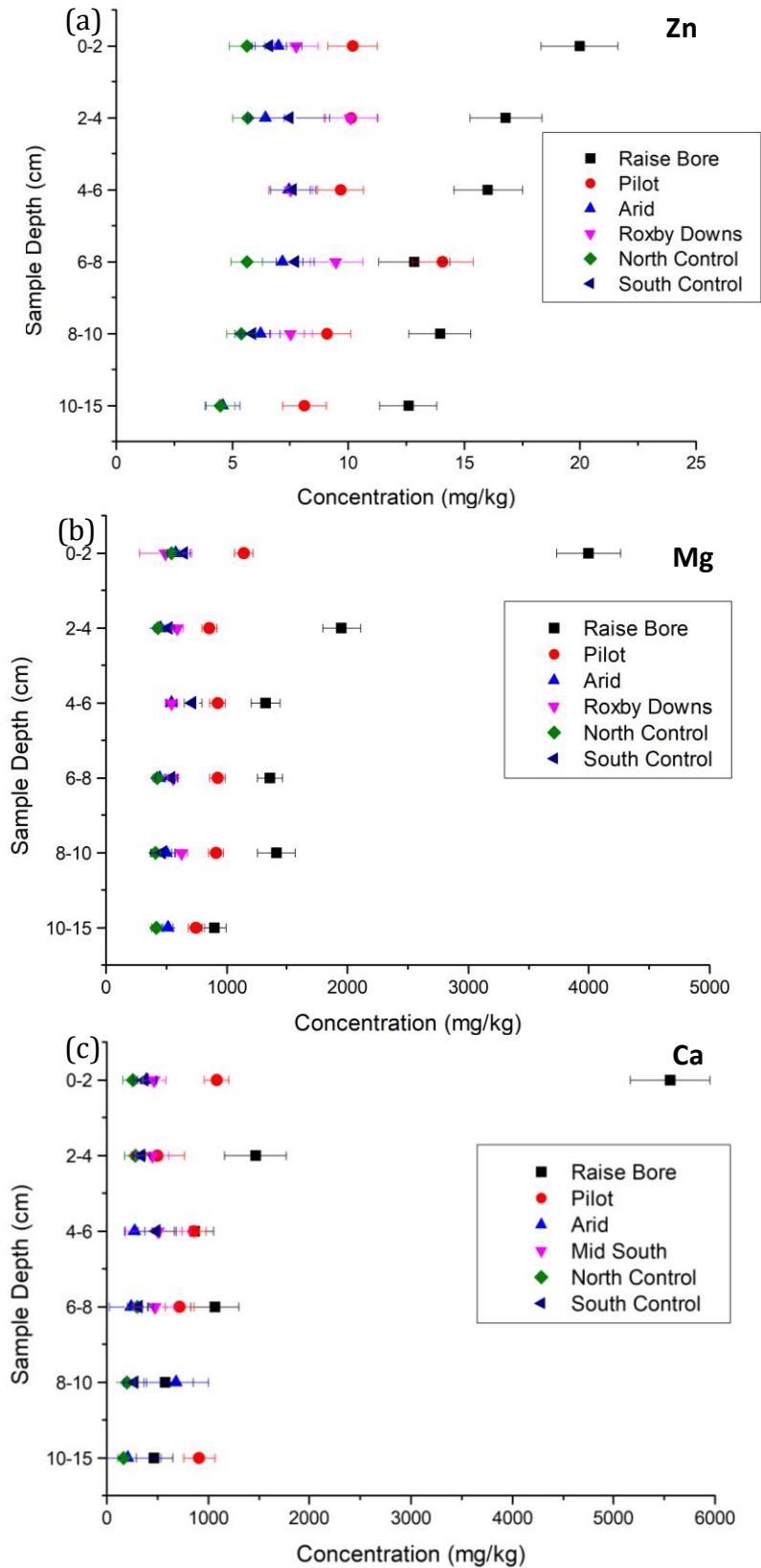
Figure 5.17. Concentration of elements within stratified Olympic Dam soils by NAA analysis. (a) Zn, (b) Mg and (c) Ca.

The stratified results from Zn in soil shown in Figure 5.17 (a) show that there is a much higher concentration of Zn in the soil from the raise bore site in comparison to all other sites at each depth except for the 6-8 cm interval where the raise bore, and the pilot concentrations are within the uncertainties. The north and south control sites have the lowest concentration of Zn at most depths, at 4-6 cm the north control site Zn was not detected. There are elevated levels of Zn in the arid and Roxby Downs sites. This indicates that there may be some influence of the Zn concentration from the mine at these sites or the natural geology as it is closer to the ore deposit. The Mg results from Figure 5.17 (b) shows that there is elevated Mg at the raise bore site and arid site. The raise bore site concentrations are affected by depth as the 0-2 cm interval has the highest concentration followed by the 2-4 cm interval. There is no clear trend in the concentrations of Mg from the other sites. The concentration of Ca across the different sites and depth intervals were consistent except for the 0-2 cm interval at the raise bore site. The concentration of Na and Cl through depth at different Olympic Dam sample sites is shown in Figure 5.18 below.
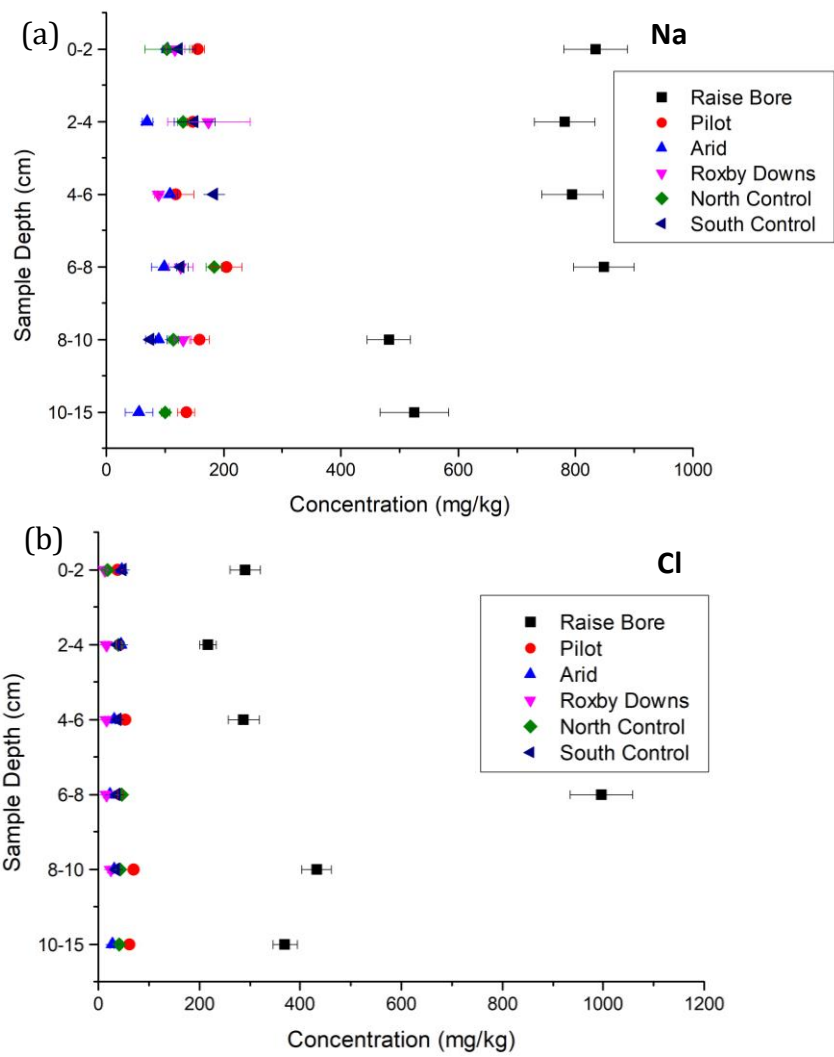
Figure 5.18. Concentration of (a) Na and (b) Cl throughout soil depth

The NAA results for Na and Cl from the soil depth profile are shown in Figure 5.18. The concentration of Na is less than 200 mg/kg from the pilot, arid, Roxby Downs, north control and south control sites. There is no clear trend of Na concentration through the depth profiling from any of the sites, with the exception of the raise bore site. The raise bore site has Na concentrations as high as 848.3 ± 51.88 mg/kg. The raise bore site shows a slight trend of Na concentration towards the higher concentrations being at the surface soil in comparison to lower soil depths. However, the concentration of Na and Cl at the lower depths are twice those at other sites. However, the 6-8 cm depth interval had the highest concentration of Na from all samples analysed. The highest concentration of Cl measured within in stratified soil from the raise bore samples is the 6-8 cm sample at 996 ± 62.29 mg/kg. The next highest concentration was the 8-10 cm interval at 432.4 ± 29.1 mg/kg. Figure 5.18 shows the trend of Cl concentration with soil depth increases in comparison to the Na concentrations. The pilot,

171

arid, Roxby Downs, north control and south control sites all showed concentration of Cl of less than 100 mg/kg.

The concentration of Cu, Fe and Al through depth at different Olympic Dam sample sites is shown in Figure 5.19 below.
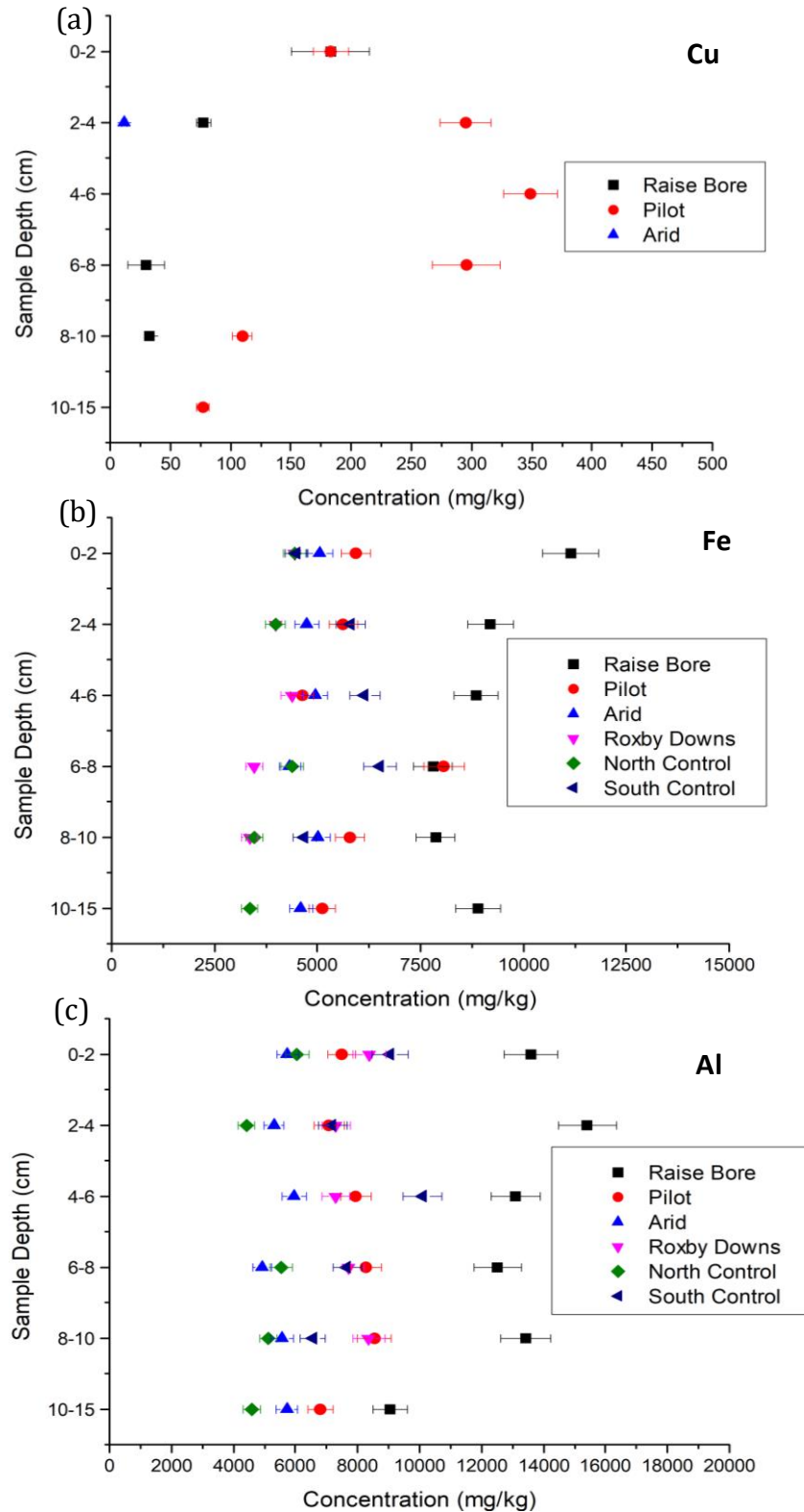
Figure 5.19. NAA results of stratified soil samples (a) Cu, (b) Fe and (c) Al.

No Cu results were above LOD for Roxby Downs, south control or north control Sites. The pilot plant had the highest concentrations of Cu compared to all other sites. The other sites potentially contained Cu however, the LOD is high for NAA therefore there is likely to be Cu

present at below LOD levels. As the pilot site once was a fully operational ore processing plant, elevated Cu concentration nearby is expected.

5.4. Discussion

5.4.1. Elemental analysis comparison of U and Th by ICP-MS and NAA and the concentration of Pb

Soil sample digestion is complicated by the presence of silicates, where, breaking down the silicate matrix is difficult and requires HF. The use of high concentrations of acids at high temperatures, may ultimately not result in the complete digestion of the sample (Falciani et al., 2000; Gaudino et al., 2007). The comparison of the U and Th analysis using ICP-MS and NAA shows that the methods are comparable when concentrations are above >1 ppm. This has been determined with the high level of consistency between the concentrations of Th and U between the NAA and ICP-MS analysis for the soil. Where there is variation in concentration of the soil samples this is likely due to the sample preparation where no digestion is required for analysis using NAA. Where a large proportion of the sample, ~85% is insoluble due to the silica fraction of the soils. This was determined experimentally through the mass difference between the undigested samples pre and post digestion with aqua regia in a microwave digester. There is a consistency in the concentration results, this indicates that there is a negligible U and Th bound within the silicate mineral structures. The large difference in the concentrations of both U and Th from the vegetation analysis is likely due to the limit of detection of the instrumentation used and the low concentration of U and Th.

There is a significant benefit to using NAA as there is a very broad range of elemental data that is obtainable from a single analysis. The ability to analyse the sample without the potential for loss of some fractions of the sample through processing is of large benefit. This provides a more precise analysis, particularly for the application to soil analysis. However, the downside of using NAA is the availability and access to the technique, as a neutron source is required.

ICP-MS also has its benefits as a technique for environmental analysis, ICP-MS is capable of the detection of Pb which is not possible using NAA. ICP-MS is also capable of reaching lower LODs for some elements. A major influencing factor of using ICP-MS over NAA is the accessibility of the technique as the ICP-MS instruments are generally more accessible in comparison to access for NAA.

5.4.2. Elements in the arid environment

Lanthanide concentrations

Enrichment of the LREEs is consistent with the Olympic Dam region. Overall, the lighter lanthanides are higher in concentration across the sites measured in May than the November replicate. This could be related to the soil moisture, pH and redox potential (Rea et al., 2021). As it has previously been established that at high pH when hydrolysis occurs the species $REE(OH)_2^+$, $REE(OH)_3(aq)$, and $REE(OH)_4^-$ are formed and at low pH REE_3^+ and $(REE)SO_4^+$ are formed. The solubility of REEs is generally low (Kahn et al., 2017). However, the difference between the replicates from the raise bore, pilot, south control and north control sites show that there is a difference between the replicates as large as the difference between the seasonal difference. Therefore, the difference in the seasonal data is most likely due to the heterogeneity of the soil and not related to the difference in seasonal variation. Further data is required over a long period of time to determine whether there is seasonal variation in the elemental data, particularly considering the nature of the arid environment, a long sampling period would be required to capture the influence of large rain events. Lanthanides can transfer to vegetation via sorption through the leaves or though the roots and transported through the xylem to other parts of the plant. The atomic radii of lanthanides is similar to calcium; therefore, lanthanides can competitively replace calcium in many biological processes. The lanthanides were of interest to this present study as the majority of the previous studies on lanthanide uptake into vegetation is based around different climates (Kotelnikov et al. 2021).

Elemental concentrations

The elements within the soil samples from multiple sites and replicates within the same site were heterogeneous in terms of elemental concentration. This is consistent with the nature

of soils from an arid climate, and the resulting 'islands of fertility', which result from nutrient cycling from leaf litter decomposition. This provides locations where there is sufficient nutrients to sustain vegetation, and other areas where there are lower concentrations of nutrients required to sustain vegetation. 'Islands of fertility' arise due to nutrient cycling beneath long-lived perennial plants. This is due to leaf litter, from the existing vegetation. When rain events occur, there is a flush of microbial activity which promotes the decomposition of organic material and leaf litter which promotes nutrient availability for plants (He et al., 2018). This explains the inconsistency and variation of soil concentrations within the same sampling location, for instance, the variability observed within the control sites. Na was found to be elevated especially near the Raise bore site ant the *Dodonaa viscosa* has been shown to be an accumulator of Na, particularly in comparison to the *Acacia liguata* species. Al was also high near the Raise Bore site, this is consistent with elements that are in the ore being higher at this site. K was much higher in concentration in within the vegetation in comparison to the soil as K is a vital plant nutrient. Samples were all very high in concentration of Fe, Fe is known to be high in Australian soils and provides the characteristic red colour.

5.4.3. Elemental profile from Olympic Dam

ICP-MS results around Olympic Dam

The soil ICP-MS results show that there is a significant difference in the U and Pb concentrations from the mining lease area of Olympic Dam in comparison to the arid, Roxby Downs, north control and south control sites. The concentration of U overall is low, but variable across sites analysed. The concentration of Th overall at all sites was very consistent with a range of only 1.45 mg/kg across all sites.

NAA results around Olympic Dam

The elemental results from the different sites samples from the vicinity of the Olympic Dam mine are varied, Na is high in soil around the raise bore site. This is likely to be an influence of the raise bore, which expel NaCl from the raise bore itself. No Cu results were above LOD for Roxby Downs, South Control or North Control Sites. The pilot plant had the highest concentrations of Cu compared to all other sites. This is likely to be due to residual Cu in the

area from Cu production from the pilot ore processing site. As the pilot site once was a fully operational ore processing stream, elevated Cu concentration nearby is expected. Al was an element what was found in relatively high concentration at all sites. This is consistent with what is expected in this kind of environment. However, there is a clear trend of the raise bore site showing a higher concentration at all depths compared to all other sites analysed. The South control and North control site are consistently the lowest concentration of Al analyses. Fe showed high concentrations from all sites, this is expected as the natural soil in the region is Fe rich.

The literature shows previous *Acacia spp.* Ca concentration to range between 6.4 mg/g to 72.0 mg/g across a variety of *Acacia spp.* from the Great Sandy Desert, which is found within arid Australia. Mg concentrations ranged from 0.7 mg/g to 11.1 mg/g. The study by Reid et al, 2016 showed *Acacia ligulata* results from Australian sites from showed concentrations of Mg 0.460 ± 0.08 %. 5.28 ± 0.63 % and K 1.11 ± 0.27 % (Reid et al., 2016) (He et al., 2018).

5.4.4. Stratified soil elemental discussion

Overall, the raise bore and the pilot sites are the only sites that show any significant variability of concentration of various elements throughout the depth of the soil samples. There is no significant different in elemental concentration through the 0-10 cm depth of soil from all sites outside of the mining lease area, as the majority of the results were within the uncertainty at each depth. Therefore, the 0-10 cm sampling for environmental monitoring is sufficient for use for CR calculations in the Australian arid environment assuming there is no dust deposition from mining activities.

The variation of U and Th within each site for the arid, Roxby Downs, north control and south control sites were minimal through depth. The results from these can be found in the appendix E. U was below the LOD for the north control sample at 0-2 cm. Therefore, indicating that the impact from the depositional contribution of U is not observed at the north control site. Overall, U concentrations outside of the mining lease area is relatively consistent throughout all sites. The results in Figure 5.15 (a) show that the contribution of U to the soil through depositional contribution is observed as the concentration of U decreases with the

decrease in depth of soil. The results from Figure 5.15 (b) show the U and Th from the pilot mine soil depth profile, the results throughout the depth do not show any clear trends, the soil at this location has been highly disturbed by the mining activities.

5.5. Conclusions

The elemental data detailed in section 5.3 has provided a comprehensive elemental profile of soil and vegetation from the arid Australian environment. However, stratified soil analysis is required to fully understand the soil profile from the Olympic Dam region due to surface deposition, the stratified soil analysis is explored in detail in chapter 6. This present research establishes a lanthanide concentration dataset for the arid Australian climate and maps the transfer from soil to vegetation. There is a lack of HREEs within the vegetation analysed in comparison to the soils, this was not observed for the LREEs. This shows that there is less uptake of HREEs into the vegetation in comparison to LREES.

The elemental results from vegetation show the concentration of elements that has been taken up into the plants. Therefore, the elements that have been detected in the vegetation were in a bioavailable state. Nickel and Mn hyperaccumulators are possible in the arid Australian environment (He et al., 2018).

Chapter 6. Radionuclide and elemental concentration of stratified soil from Olympic Dam and spatially resolved radionuclides within vegetation using radiography techniques

6.1. Radionuclide and elemental analysis of stratified soil and radiography techniques for vegetation analysis introduction

Chapters 2, 4, 5 and 6 have demonstrated the importance of understanding the uptake of radionuclides is of importance for Australian Native vegetation (Hirth, 2014). The CR measurements detailed in chapter 4 have quantified the radionuclide transfer from soil to vegetation. The CR calculations were performed using surface soil samples of a 0-10 cm depth which is the internationally accepted standard method. Radiography techniques were used to analyse the stratified soil samples from different intervals of soil to provide a visual representation of the radioactivity. These data will also show the radioactivity in terms of soil fractionation by visualising the distribution of radionuclides throughout the samples. This will show if there are radioactive particles or whether the radionuclides are present within the fine fractions of the samples. Elemental analysis was used to determine if there was a trend in the elements through the depth of soil that could be indicative of nutrient uptake.

The mechanism of foliar metal transfer is not well understood however, it has been previously shown that elements or radionuclides can enter a plant via fallout from wet or dry deposition onto leaves. Intake may occur when there is penetration through the cuticle layer of cells on the outside of the leaf or entry via the stomata (Shahid et al., 2017). There has been significant previous research regarding the intake method of ^{210}Po in tobacco plants, however, the mechanism is still uncertain. The direct deposition of ^{210}Po and ^{210}Pb on the surface of a leaf appears to be the major pathway for accumulation by the plant. (Matthews et al., 2007; Skwarzec et al., 2001; Thakur & Ward, 2020). The study by Skwarzec et al. 2001 have shown that the most likely intake mechanism for ^{210}Po is generally through the intake from the dry or wet deposition into the plant, therefore, foliar intake is the method of transport into the plant (Skwarzec et al., 2001). Pietrzak-Flis & Skowrońska-Smolak (1995) studied the transfer of ^{210}Po and ^{210}Pb within plants and found that majority of the activity was in the leaves and roots, with minimal in the stems. The location of radionuclides within vegetation can be spatially resolved using radiography techniques. Autoradiography is primarily sensitive to beta radiation and is observed on a macroscopic level. Alpha-particle radiography analysis is sensitive to alpha radiation and is observed on a microscopic level. This technique uses the theory from Ag halide photography, the first study to use Ag halide alpha-particle radiography

analysis and microscopy was in 1910 by Kinoshita (Kinoshita, 1910). This technique is still used today for particle physics research across broad research applications (Kalnins et al., 2019; Noto et al., 2014; Zarubin, 2016).

6.1.1. Chapter directions

This chapter aims to explore stratified soil analysis by attempting to visualize the effect of the surface contamination within the soils from operational sites within Olympic Dam. This chapter aims to provide some insight as to the mechanisms of intake of radionuclides into vegetation in the arid Australian environment.

This chapter also aims to spatially resolve the locations of radionuclide accumulation within the physiological structures of leaves. The focus species for this study are the Australian Native species *Dodonaea viscosa* and *Acacia ligulata* sampled from Olympic Dam. The alpha-particle radiography method was used to determine if the radionuclides accumulate in specific structures within the leaves, this should also provide some insight as to if the result of alpha decay within vegetation is of concern to the surrounding tissues. This research provides a visual representation of the radioactivity taken up by vegetation within the arid Australian environment and to determine whether there is surface contamination on the outside of the vegetation by comparing washed and unwashed samples. This was performed as the environment at the Olympic Dam region has a moderate amount of dust. This research identifies whether different radiography techniques are sensitive enough for low level NORM radiation detection to provide spatial information on environmental samples of soil and vegetation. This was achieved by developing the alpha-particle radiography method for biological samples, and to determine whether it is sensitive enough to be used on environmental samples of vegetation.

Overall, this chapter aimed to increase the understanding of the uptake mechanisms of radionuclides within Australian native vegetation species within an arid environment. This chapter explored whether the radionuclide distribution and accumulation can assist in understanding radionuclides. It also aimed to identify the most likely transport and uptake mechanisms for radionuclides in plants. To compare the activity of bulk soil samples to the

stratified soil samples from Olympic Dam to determine the validity of using the 0-10 cm sample within concentration ratio calculations for use within ERICA assessments. To determine whether the current environmental impact assessment method is appropriate for use with Australian native vegetation species within the arid environment.

6.2. Experimental

The experimental methods used within this chapter include Alpha-particle radiography analysis, autoradiography, gamma spectroscopy which was discussed in Chapter 3 and NAA which was discussed in Chapter 5.. Soil samples from the Olympic Dam mine were collected and analysed using autoradiography. Soil samples were analysed in 2 cm depth intervals following collection via the methodology detailed in Chapter 2 section 2.2.1. Where the number of samples is referred to as 'n' this represents individually collected samples. Dry mass was used for all reference to vegetation within this chapter.

The samples of vegetation used within this chapter are *Dodonaea viscosa* and *Acacia ligulata* sampled from the Olympic Dam site, the details of samples and collection sites is outlined in Chapter 2 section 2.2.2 and the samples were prepared by resin embedding and microtomy followed by the alpha track method detailed below.

Autoradiography sample preparation
Soil samples prepared following the method outlines in Section 2.3.1. the soil was then added to a sugar water mixture and placed onto an autoradiography plate. For autoradiography the vegetation samples were air dried at 25 °C and were not ground as to retain the original structures of the plant. The samples were either kept as they were when collected from the field or washed with deionised water and dried prior to analysis. The vegetation samples were laid flat onto the autoradiography plate for imaging. Autoradiography is primarily sensitive to Beta radiation.

Alpha-particle radiography

Samples of *Acacia ligulata* and *Dodonaea viscosa* from Olympic Dam were analysed using the alpha-particle radiography method combined with microtomy preparation. The alpha-particle radiography method was used to determine where radionuclides were located spatially within the microstructures in the leaf (Kalnins et al., 2019). This research provides information regarding the route of radionuclide intake and transport into the leaf and translocation within the plant. This information will provide data regarding route of entry and to assess the potential of radiation induced damage to the vegetation from the alpha emission.

This experimental method required extensive method development for use on biological samples, following method development, analysis of the Olympic Dam samples was performed. Vegetation samples were collected and processed, embedded in resin, cut with the microtome, and coated with the alpha track emulsion in two separate batches, one batch prepared and coated within 38 days from sample collection. The other batch was coated with the emulsion after 38 days. The time period of 38 days was used as the half-life of ^{222}Rn is 3.8 days therefore, following the 10 half-lives the activity of radon is negligible (Basunia et al., 2020). To assess the impact the radon has on the number of tracks the vegetation samples, the two separate batches of samples were prepared from the same plant samples and coated. One batch was coated before 38 days and one batch coated following the 38 days. This was performed to determine if there was a statistical significance within the number of alpha tracks were found between samples from the two batches. This will provide some insight as to the contribution of alpha tracks from the ^{222}Rn and the short lives radionuclides following its decay.

The presence of an alpha track within the sample identifies that a radioactive nucleus was present within the sample and an alpha decay event has occurred in the direction of the

emulsion where the nucleus is close enough to the surface of the sample that is in contact with the emulsion. An example of this is shown graphically in Figure 6.1 below.
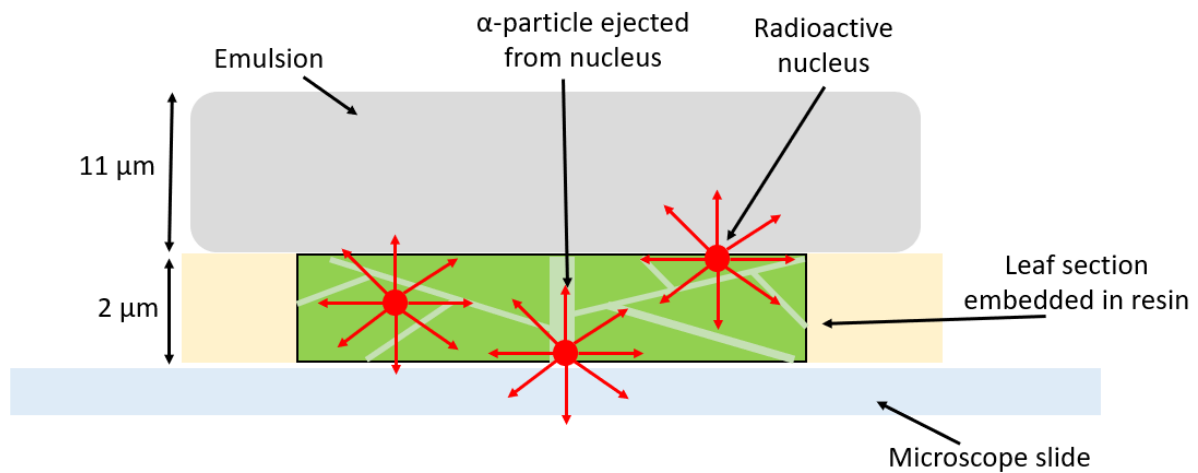

Figure 6.1. Alpha-particle radiography experimental setup and schematic of alpha decay within the sample.

Figure 6.1 shows the influence of the thickness of the leaf sample and the depth of the radioactive nucleus on the chances of an alpha particle reaching the emulsion. Referring to Equation 1.11, this shows that a quarter of alpha emissions within a sample will be visible, three quarters of the alpha tracks will not reach the emulsion (Aitken, 1985). Therefore, the tracks observed, it can be assumed that there would be 4 times more tracks if three-dimensional analysis through the sample was possible. The alpha penetration distance depends on the energy of the alpha emission and the density of the media that the alpha particle travels through. The highest energy alpha particle of interest is ^{212}Po at 8.78 MeV and ^{214}Po at 7.69 MeV and the lowest energy alpha particle is ^{235}U at 4.4 MeV and ^{238}U at 4.2 MeV (Brookhaven). The length of the track will depend on the energy of the emission and the angle of emission from the radioactive nuclei to the objective.

To determine information regarding the uptake mechanisms and the translocation within the species, the anatomy of the leaf was identified for *Dodonaea viscosa*. An annotated image of a *Dodonaea viscosa* thin section is shown in Figure 6.2 below.
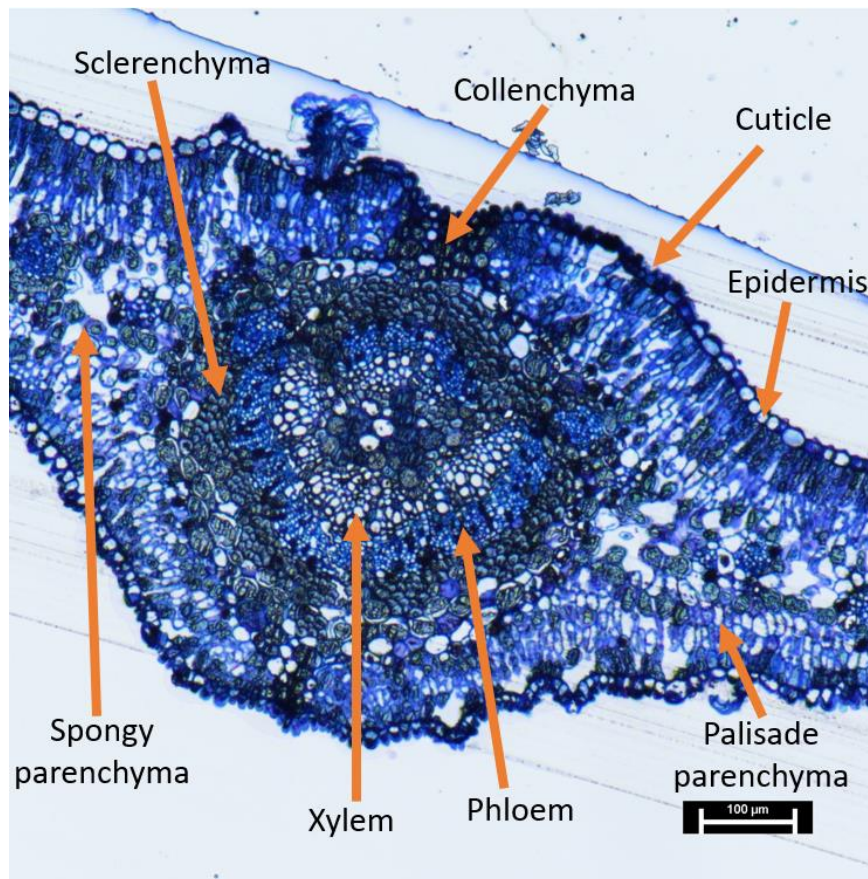
Figure 6.2 Leaf anatomy of Dodonaea viscosa species, 2 μm thin section stained with toluidine blue, vascular strands were not located within this image.

Figure 6.2 shows the different biological structures within the leaf of a *Dodonaea viscosa*. Where vascular strands can be thought of as the veins of the leaf, no vascular strands were located within Figure 6.2 (Venkatesh et al., 2008). The different structures of the leaf will be referred to within the discussion of the Olympic Dam samples and the track locations. The centre stem section of the leaf which contains the xylem and Phloem will be referred to as the midrib if indistinguishable within the microscopy image.

Alpha-particle radiography sample preparation

Samples of vegetation were collected fresh from the field and placed into Electron Microscopy (EM) fixative (4% paraformaldehyde/1.25% glutaraldehyde in PBS, + 4% sucrose, pH7.2) and stored in a cooler with ice until a 4°C fridge was available after the fieldwork was complete.

Resin embedding

After the samples had been in the refrigerator for 24 hours, the leaf sample was removed from the EM fixative and placed onto a glass slide in a few drops of phosphate buffer (PBS + 4% sucrose). The leaf was cut into small sections, approximately 2 mm^2 using a blade. These sections were then submerged into a phosphate buffer solution. The leaves were left in the phosphate buffer until fully submerged and the leaf sections sank to the bottom of the vial (Figure 6.3). This shows that the ethanol solutions will infiltrate the sample effectively leading to an effective dehydration process. Samples were placed on an agitator plate throughout the ethanol and resin stages of the sample preparation method. Samples were then dehydrated using a gradient ethanol series to remove all moisture from the sample before it is embedded in resin. All buffer solution was removed from the leaves and 70% ethanol was added, this was left for 30 minutes. After 30 minutes the 70% ethanol solution was changed for fresh 70% ethanol solution, this was repeated 3 times for 30 minutes each. The ethanol wash procedure was repeated with 3 changes of 90% ethanol for 30 minutes each. This was followed with 3 changes of 100% ethanol for 30 minutes each. After the final 100% ethanol rinse, propylene oxide was placed into the leaves for 25 minutes, this step begins the infiltration process. Resin was mixed using DDSA 22 mL (hardener), araldite 6 mL, (procure) 10 mL and DMP30 0.560 mL (catalyst). A subsample of the resin was removed from the stock solution and a 1:1 propylene oxide resin solution was made. This 1:1 propylene oxide:resin solution replaced the propylene oxide solution for 1 hour. This was followed with the 100% resin solution for 1 hour, this step was repeated and left overnight. The resin was replaced with fresh resin and placed into an oven for at least 24 hours for the resin to set at 70 °C. After the resin had set the samples were cut with a rotary microtome using a glass knife by transverse sectioning to 2 µm thick sections (Tajuddin et al., 2013).
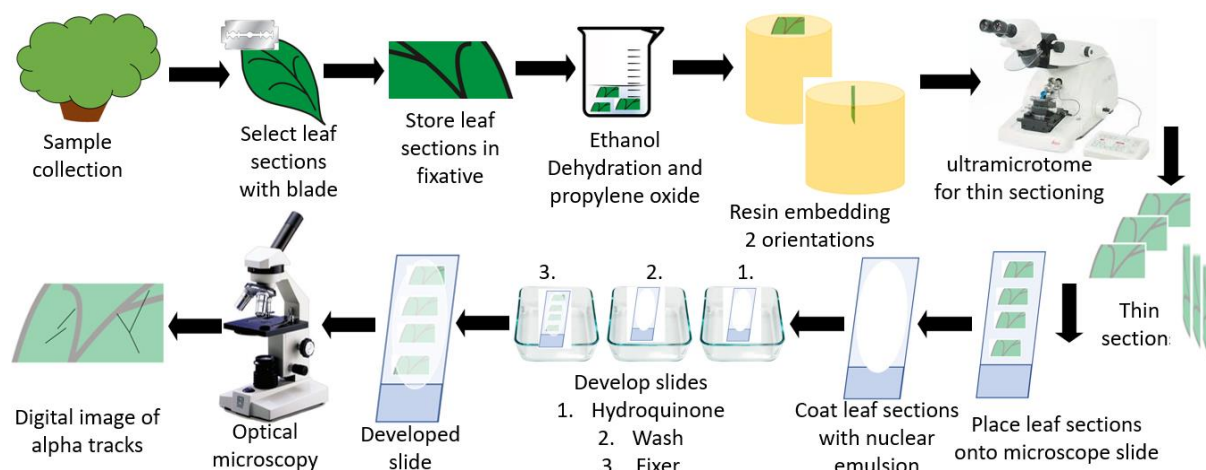
Figure 6.3. Vegetation alpha track analysis sample preparation process schematic.

Acacia ligulata floated in the resin therefore the dehydration steps were extended, and the propylene oxide:resin mixture exposure times were extended at each 50:50, 75:25, 80:20 and 90:10 step. However, when the leaf sections were placed into the 100% resin they floated. These sections were embedded upside down for microtomy. The *Dodonaea viscosa* sunk in the resin, therefore, was much easier to process and cut with the microtome.

Embedding biological samples in epoxy resin for electron microscopy has been used extensively. This method was first developed by Glauert and Glauret, 1957 (Glauert & Glauert, 1958; Richardson et al., 1960). Araldite (electron microscopy sciences) has shown no detectable damage to the tissue it infiltrates during polymerization; araldite also doesn't sublime in the electron microscope. Araldite enables the production of micron thick sections. The standard technique includes fixing, washing and then dehydration using a gradient ethanol series, placed in either toluene of xylene for an hour followed by resin infiltration using araldite resin, polymerization using heat (Richardson et al., 1960). The sample preparation method also used a fixative followed by a wash, a gradient ethanol series for dehydration, prefiltration and infiltration with resin. The resin used in this study was Technovit 7100 resin. A rotary microtome with a glass knife was used for sectioning the sample (Kalve et al., 2015).

*Microtomy*

In this research microtomy was performed on the resin embedded leaves using an 'Reichert OmU3' Ultramicrotome was used for thin sectioning glass knives were used to cut the sections, a boat was glued to the glass knife and the boat was filled with deionized water. The

sections were cut into the water and were collected using an eyelash brush, the thin sections were placed onto a microscope slide and dried on a warm hot plate (~50 °C). The sections are stained using toluidine blue and rinsed with deionized water, the slides were then dried further at ~50 °C on a hotplate.

Alpha-particle radiography method development results

Following the anatomy identification, initial method development for the alpha-particle emulsion involved coating the outside of a whole dried leaf to determine whether the alpha-particle radiography method was appropriate for use on vegetation. Initial experiments were performed to test the alpha track emulsions air dried leaves attached to microscope slides using different adhesives. Different adhesives were used to determine which would withstand the emulsion development process and to determine if interference with the emulsion and the adhesive occurred. The different adhesives used were used with the intention of attaching the leaf to the slide and not interfering with the alpha-particle emulsion. Whole air-dried leaves were adhered to a microscope slide and coated in the alpha track emulsion, the sample was exposed to the emulsion for four days, then developed. The results from these samples are shown in Figure 6.4 below.
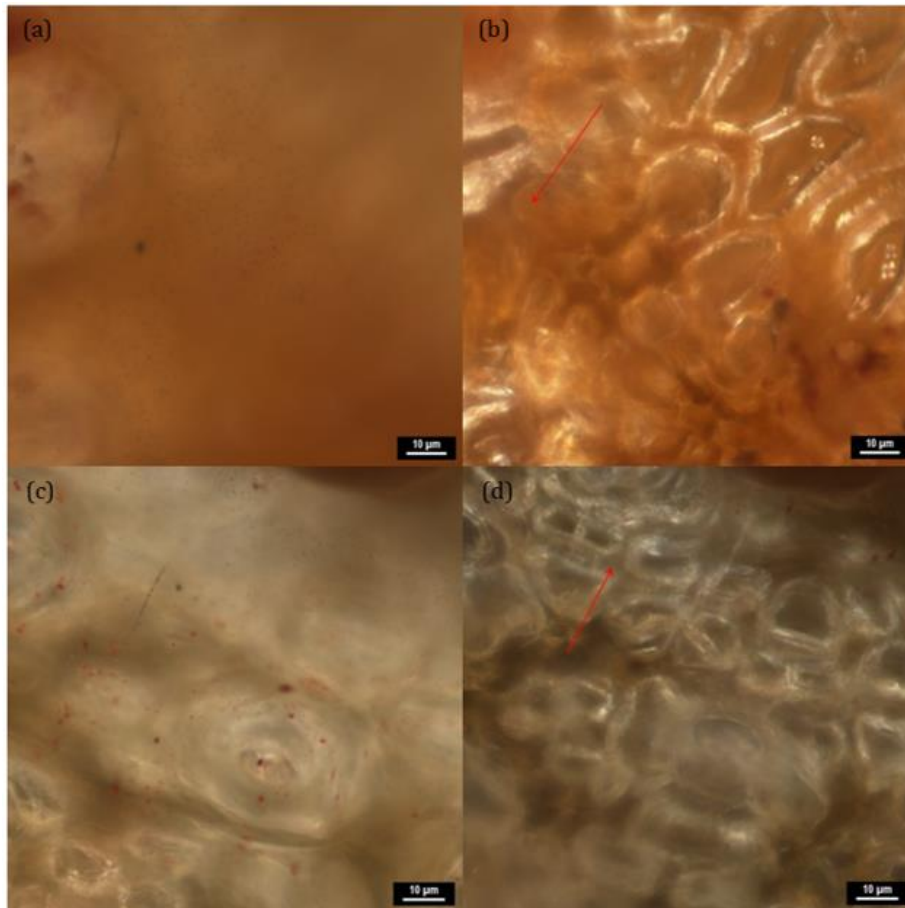
Figure 6.4. Acacia ligulata air dried whole leaf, nuclear emulsion applied to surface for alpha track visualisation. (a) alpha track in focus, (b) leaf in focus where the alpha track shown in (a) is, the arrow indicates alpha track and directionality. (c) alpha track in focus, (d) leaf in focus where the alpha track was represented by an arrow.

The results from the initial alpha-particle radiography on a whole leaf are shown in Figure 6.4. The samples were imaged using an optical petrographic microscope, the results show that the alpha tracks can be identified using the alpha-particle radiography method. However, the alpha tracks were difficult to locate and visualise as the leaf surface was uneven and lumpy. The different biological structures on the surface of the leaf were also difficult to identify. When imaging the tracks scrolling the z-axis through the focal plane of the 3-dimensional emulsion allowed the track directionality to be determined. Collecting images through the z-axis of the focal plane allowed for the identification of the alpha tracks however, this method did not allow for easy visualisation of the tracks and their original location. Reflection of the transmitted light from the lumpy sample surface further complicated the track identification. Subtle twisting of the tracks was also observed, this may have been due to the unevenness of the surface.

The results from the initial method development shows that alpha tracks can be visualised from the leaf samples using the alpha-particle radiography method. However, to address the aims of determining the location of radionuclides within the structures of the leaf, a flatter surface on a microscopic scale is required. Therefore, further method development was required and microtomy was explored to cut into the leaf to provide a flat surface for application of the emulsion. The results from the microtome are shown in Figure 6.5 below.
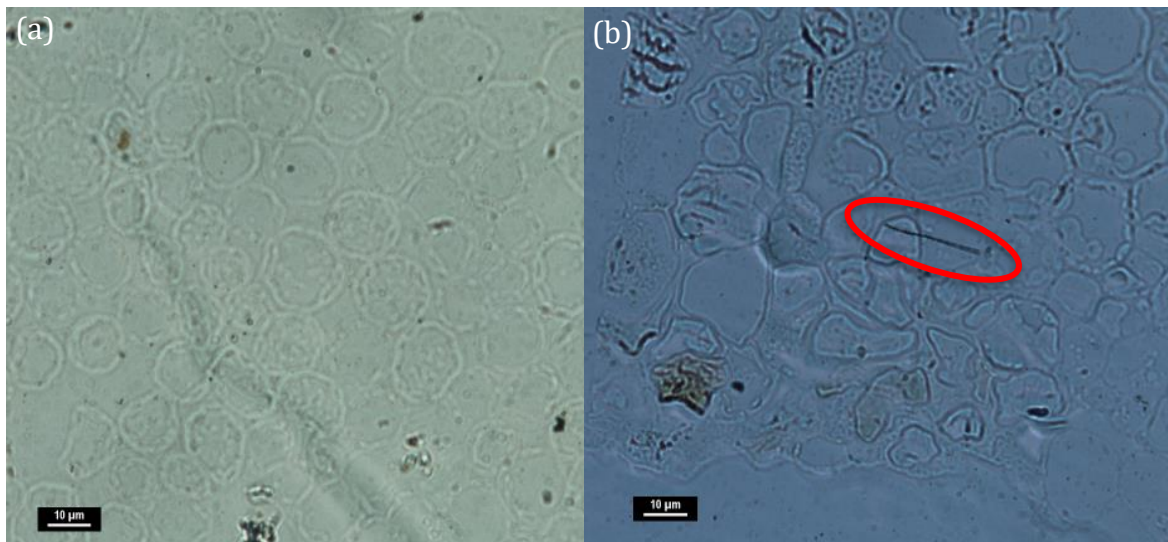

Figure 6.5. A leaf from an unidentified species from Adelaide University for method development (a) leaf cells uncoated, (b) sample exposed to emulsion for 1 month, leaf cells and alpha track.

The results from the microtome trial are shown above in Figure 6.5. The alpha track emulsion was exposed for a month before development of the gel. The results of the microtome trial allowed for significantly more efficient microscopy work and clearer images of the sample below when comparing to the results from Figure 6.5 above. Due to the promising results from the microtome trial the microtome method was continued for the remaining of the experiment and the Olympic Dam analysis.

Figure 6.6 (a.) shows the *Acacia ligulata* samples that had not fully been embedded with resin. Figure 6.6 (a.) shows air bubbles within the resin and (b.) shows the leaf torn into two sections down the mid rib area. When the *Acacia ligulata* was cut with the glass knife the cells through the middle of the leaf broke away as they were brittle with no resin. Therefore, due to the resin embedding issue with *Acacia ligulata* the *Dodonaea viscosa* was the focus species of interest for this experiment as the *Acacia ligulata* requires a more extensive resin infiltration steps to fully embed.
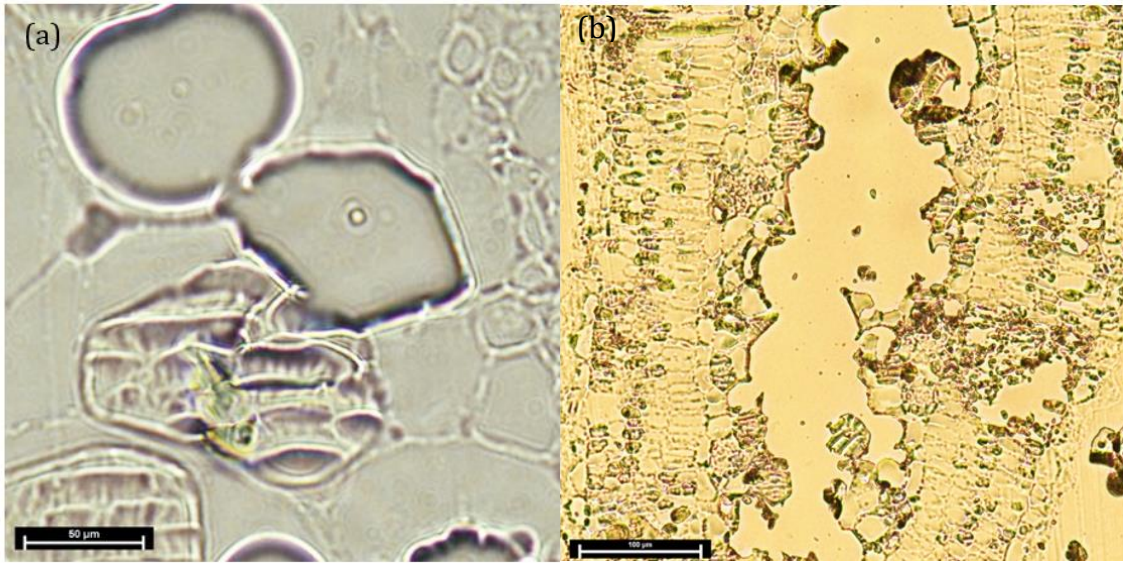
Figure 6.6 (a) Air pockets in the acacia ligulata samples. (b) Acacia ligulata thin section that had split into two sections due to not being fully embedded with resin.

The thin sectioned samples have provided the best outcome in terms of alpha track finding using optical microscopy and clarity of sample however, further visualizing the structures of the cells within the leaves would be beneficial. Staining of the cells within the sample was explored. Toluidine blue is a commonly used biological stain that Is used to stain the membranes of cells (de Campos Vidal & Mello, 2019; O'Brien, Feder, & McCully, 1964).

Toluidine blue stain was added to the sample sections after they had been cut with a microtome. The excess stain is rinsed with deionized water. The results from the staining of the leaf sections are shown below in Figure 6.7.
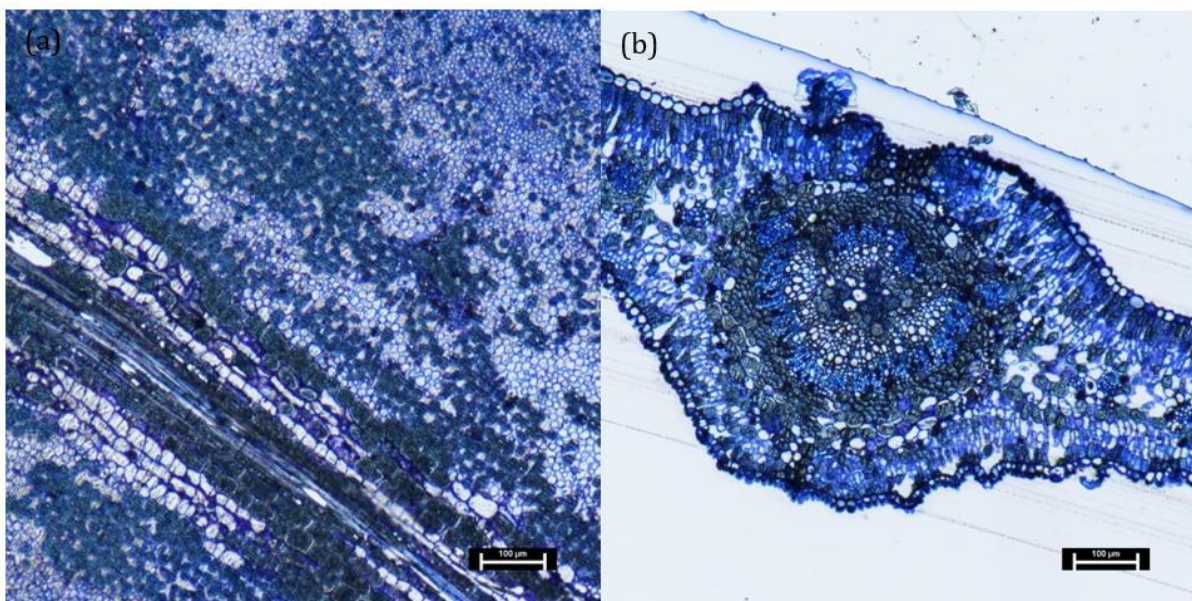

Figure 6.7. Dodonaea viscosa leaf cross sections in two orientations (left longitudinal, right is transverse).

Figure 6.7 above show the results of the toluidine bule stain on the *Dodonaea viscosa* sections that have been cut with a microtome. The cells are easily to visualize with the toluidine blue stain. Figure 6.7. shows the two different orientations, transverse and longitudinal of the leaf that have been cut and coated with the alpha track emulsion. Using the two different orientations will provide us with two different perspectives to determine where the alpha tracks are origination and therefore provide data as to where the radionuclides are accumulating within the structures of the leaves of the vegetation of interest. The stained sections were then coated with the alpha track emulsion. The toluidine blue stain interfered with the alpha-particle emulsion; a high background interference was observed in the plane closest to the sample. Figures of the interference are shown in appendix G, the stain was used as a reference for each sample, however, was not able to be used in conjunction with the alpha-particle emulsion.

6.2.1. Radiography analysis

Spatial analysis including Autoradiography and alpha track analysis were performed on samples to provide data on the spatially resolved locations of radiation within the samples.

Autoradiography

Autoradiography is a non-quantitative technique that enables the visualization of radioactivity within the sample analysed. This technique results in a grey scale image of the sample, where the intensity of the pigmentation produced in the image is related to the activity of radiation relative to the other parts of the sample. The darker areas in the image indicate higher activity of ionising radiation as radioactive decay interacts with the autoradiography plate.

Instrumentation

This technique uses photo stimulated luminescence (PSL) imaging plates. The specific plates used are Fujifilm imaging plate AAS-SR 2040 BAS-IP SR 2040. These photographic plates are composed of three layers, a protective layer at the top of the plate, which is in contact with the sample, followed by a photo-stimulable phosphor layer, followed by a support layer (Figure 6.8).
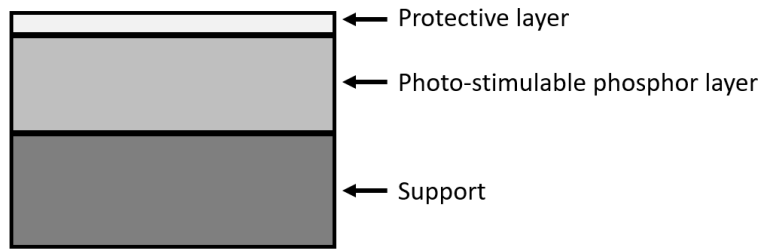
192

Figure 6.8. Schematic of autoradiography plate layers.

The photo-stimulable phosphor layer in the plates used in this experiment are composed of 5 µm Ba fluorobromide crystals with trace Eu. This acts as the luminescence centre, where the formula is BaFBr: Eu^{2+}(X = Cl, Br or I). Figure 6.9. shows the mechanism of the luminescence within the imaging plate.
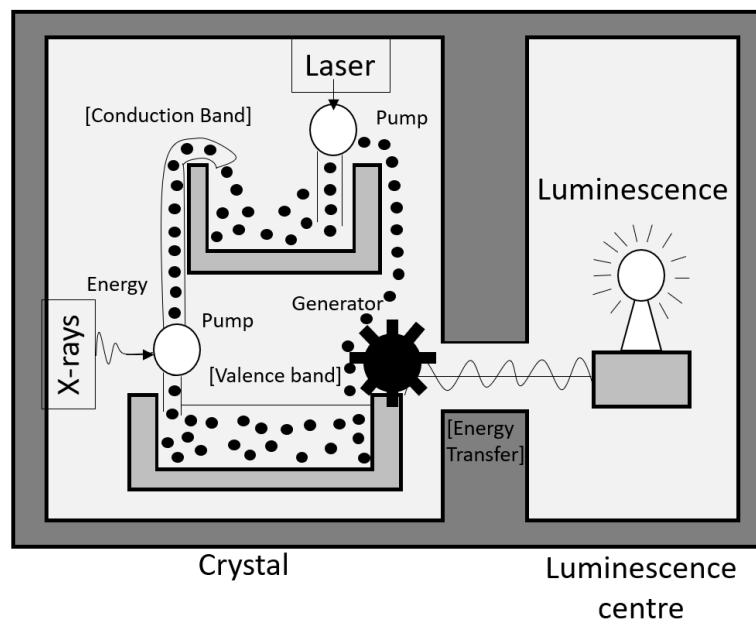

Figure 6.9. Schematic of the mechanism of the autoradiography imaging plate luminescence.

The active crystal centres within the imaging plate when irradiated release electrons which trap within the crystal lattice which then produces a colour centre. Electrons are released into the conduction band and X-rays excite the Eu^{2+} ions to Eu^{3+}. The excited electrons are then trapped within the Br ion empty lattices where there are defects present within the crystals. The mechanism of the luminescence is described in Figure 6.10. When the imaging plate is developed (Figure 6.10) a laser scans and irradiates the imaging plate again exciting the electrons within the colour centre. The plate is conveyed in a phosphor reader (Figure 6.10), the PSL released by the reaction from the laser is detected using the photomultiplier tube through the light collection guide. The recombination energy within the electron hole is transferred to the Eu ion within the luminescence centre resulting in luminescence. However, the exact mechanism still remains unclear.
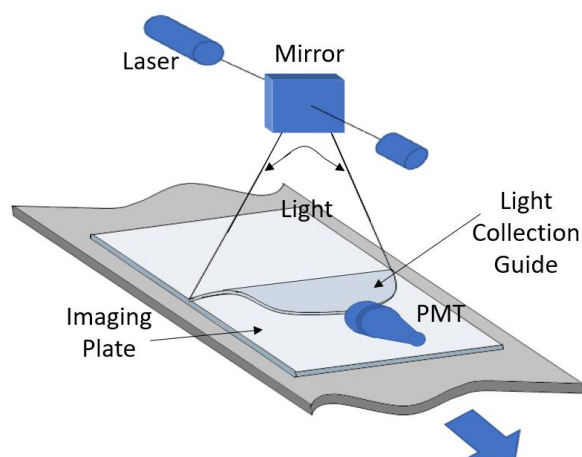
193

Figure 6.10. Schematic of reading the information from the autoradiography plate.

The resolution of the image can range from 5 to 40 pixels/mm. A blue/purple light at 400 nm is released when excited by the laser. The result is a grey scale image where darker areas are representative of higher activity of radiation. Beta radiation is the main source of images on these types of plates. The imaging plate is irradiated at 633 nm with a He-Ne laser.

Qualitative Analysis

Autoradiography is a qualitative technique; it spatially resolves the location of beta emitting radionuclides. It provides a level of intensity by the depth of greyscale image that is produced.

Justification

Autoradiography is useful for this research as it will provide data on the spatial distribution of beta radioactivity within the soil and vegetation samples. The use of autoradiography will provide details as to the radionuclide accumulation throughout different soil fractions. Autoradiography will show if there is an obvious difference between the activity of washed and unwashed vegetation. This will provide information on the effects of surface contamination at Olympic Dam.

Autoradiography Experimental Methods

Following the sample preparation methodology detailed above for autoradiography, samples were exposed to the imaging plates for seven days. After the exposure time the image plates

194

were analysed using a biomolecular imager (Typhoon 7000) with a laser at 650 nm to image the plate.

Alpha-particle radiography analysis

Alpha track analysis is a method that implements the theory behind black and with Ag halide photography for the analysis of radiation. This technique involves coating the sample of interest with the Ag halide emulsion and where alpha decay occurs within the sample a visible line appears within the emulsion. This technique was used to determine where within the different structures of the leaves from vegetation samples from where alpha radiation was emitted.

Latent image formation

The nuclear emulsion is placed onto a sample, this is left for the decay events to occur within the sample. When ionizing radiation travels through the AgBr crystals, latent image centres are formed within the gel. These are not visible until after development. These latent image centres are the result of the ionizing radiation ionising the AgBr to produce Ag+ and Br-. The latent image is essentially a cluster of Ag^+ atoms.

<div align="center">

Ionising Radiation

$$AgBr \quad \rightarrow \quad Ag^+ \; + \; Br^-$$

</div>

When ionizing radiation is absorbed by the AgBr crystal it forms a positive electron hole, this can affect the AgBr crystal by liberating an electron from the electron deficient Br atoms. When light from ionizing radiation is absorbed by the AgBr crystal in the emulsion, an electron is liberated from the crystal lattice. Electron transfer from an adjacent bromine ion in the crystal lattice can occur, creating electron deficiency from the donor ion. From this activity the electron holes (or positive hole) can move through the crystal lattice. Latent image formation requires positive holes and electrons to be separated within the system to avoid recombination. The free Ag^+ ions within the system are able to move through the lattice, then the Ag^+ ion and a trapped electron occurs their charges neutralize, and metallic Ag^0 is produced.

<div align="center">

hv

$Ag^+ |Dye \rightarrow Ag^+|Dye^* \rightarrow Ag^0 |Dye^{\cdot+}$

</div>

195

When this occurs the metallic Ag is not very stable, however, the site becomes an electron trap which encourages more Ag atoms be built up, this creates the latent image centre, which can later be reduced to metallic Ag.

$$hv$$

$$Ag^+|Dye \rightarrow\rightarrow\rightarrow Ag_n^0 \text{ (latent image formation } n \geq 4)$$

AgBr is a semiconductor. Depending on the halide composition, they generally absorb strongly only below ~450 nm. Therefore this process is required to be performed in a dark room with only red light at around 700 nm (Gould et al., 2000).

Instrumentation and Emulsion Details

Red light was the only visible light used in the room at 700 nm. The Ilford nuclear emulsion gel L4 that contains 0.162 g Ag/g emulsion. The Ag is present as AgBr crystals at a diameter of 0.11 μm in gelatine, it was prepared by placing in a beaker and adding deionized water as a 1:2 water to gel ratio.

After the slides containing the sample and the nuclear emulsion gel have been developed the alpha tracks are visualized using light microscopy. The Nikon Eclipse LV100 POL Petrographic Microscope was used. The alpha tracks are visible in the gel above the sample. Scanning the gel using the fine focus is the easiest way to locate the alpha tracks as they appear throughout the different focal planes in the gel. Images and videos are collected of the alpha tracks using the NIKON NIS-Elements software (Version BR 5.11.00).

Further characterization of the alpha track emulsion was performed, an optical profiler was used to determine the thickness of the emulsion. The results from the optical profiler are shown below in Figure 6.11. The emulsion is prepared consistently to a 2:1 emulsion to deionized water ratio. The thickness of the emulsion was determined to be approximately 11 μm.
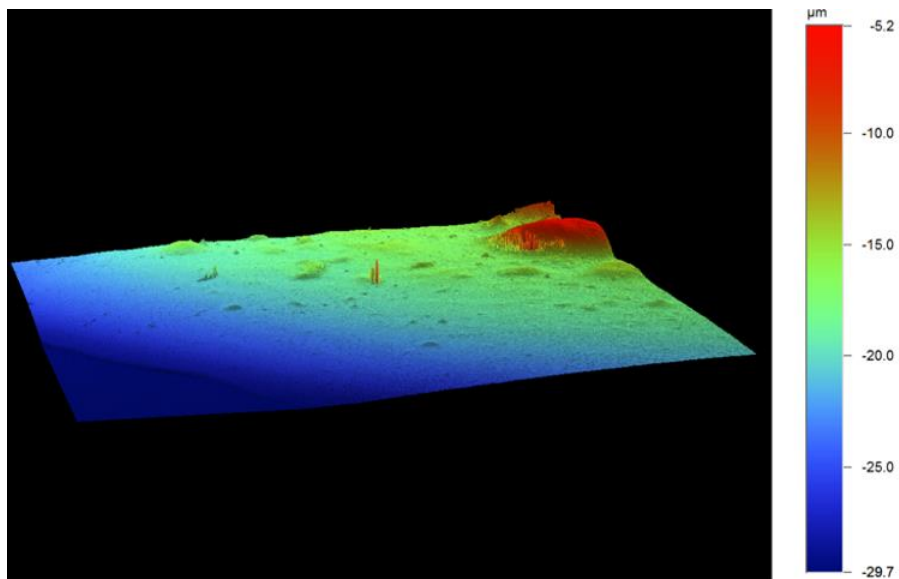
Figure 6.11. Results from the optical profiler, this shows the thickness of the alpha track emulsion.

Qualitative Analysis, Precision and Accuracy

Positive Control

Alpha track analysis is a qualitative method where the tracks visualized from the sample can indicate that an alpha decay occurred the originating nuclei cannot be determined. A positive control sample of ^{210}Po a primarily α emitter at the energy of 5304.33 keV was applied to the alpha track emulsion. The results from the ^{210}Po source are shown below in Figure 6.12.

Figure 6.12. (a-c) ^{210}Po known source positive control results on blank alpha track emulsion. The black lines in the image are the alpha 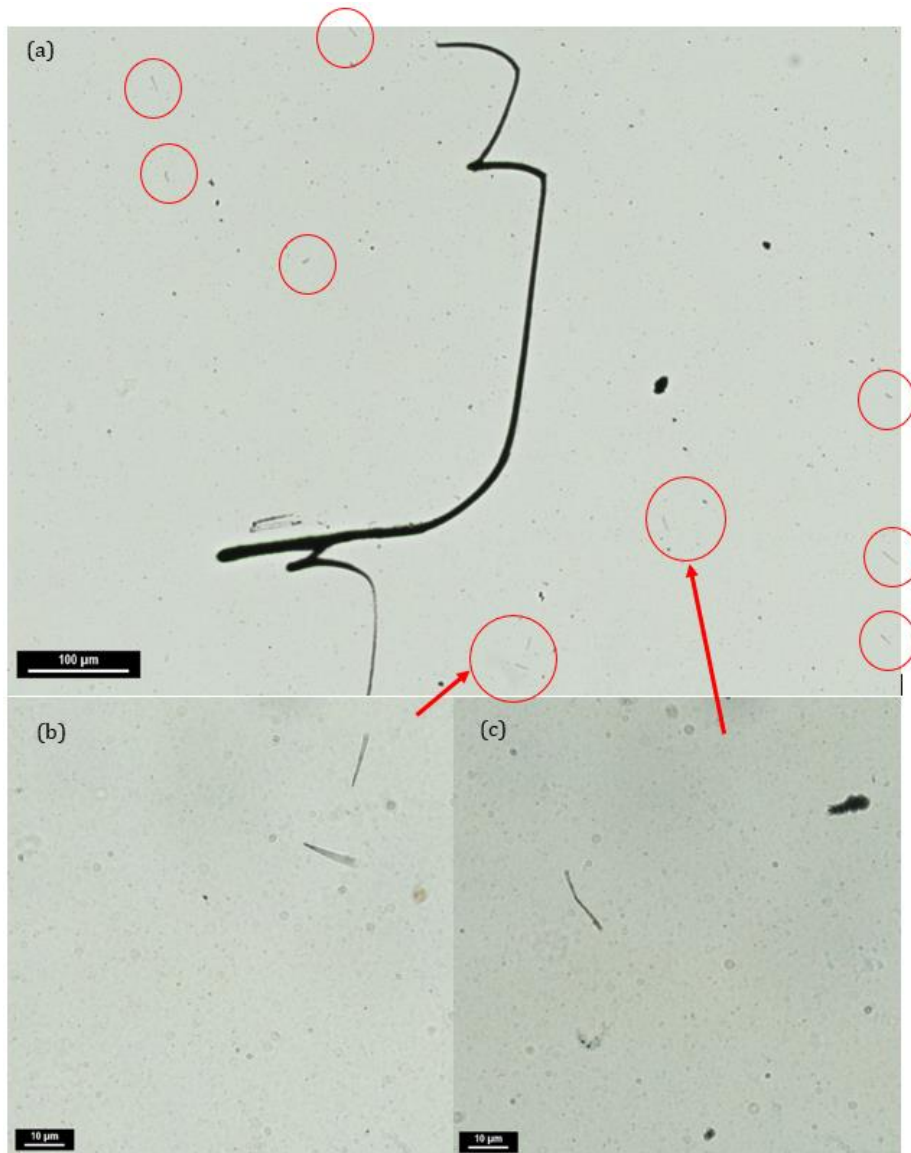tracks, the red circles highlight where the alpha tracks are located. Images (b) and (c) are sections of image a under higher magnification. The red arrows from images (b) and (c) point to the location that they were taken from image (a).

Figure 6.12 above shown the results on the alpha track emulsion from a known ^{210}Po source. The large black line is the scratch in the gel from the Po-210 source. The small lines surrounding the scratch are visible alpha tracks resulting from the Po-210. The scratch mark makes the positive control location easily identifiable.

Negative Control

The alpha track emulsion was also applied to blank microscope slides and was exposed for the same amount of time as the samples, this provides a control result that has been in the same conditions as the samples. Figure 6.13 below shows the results from the alpha track

emulsion applied to a blank microscope slide. No alpha tracks were identified in these samples.
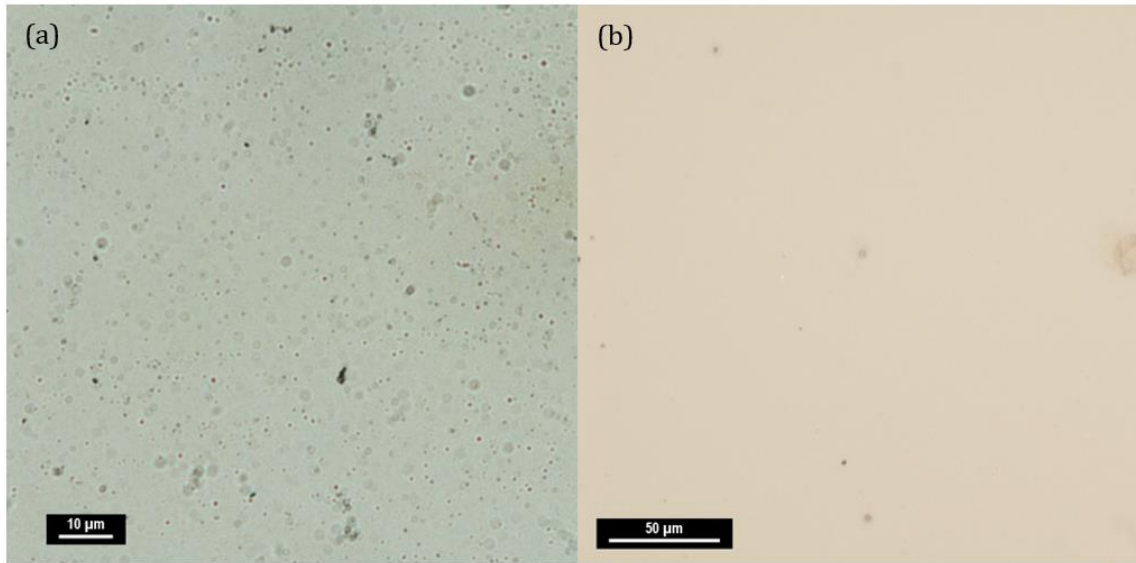
Figure 6.13. Nuclear emulsion gel over blank microscope slides only (a). Resin with emulsion gel coating, no leaf, no unwanted interaction with the gel from the resin (b). No alpha tracks are observed within these two images.

As the microtome method development involves embedding the sample within an araldite resin, samples of the araldite resin used were also coated with the alpha track emulsion. The results from this are shown below in Figure 6.14 (a), these results shows the araldite resin when cracking occurs. The results from the resin only, show no unwanted interference between the gel and the resin. This sample of resin shows some cracks, the figure below shows that cracks in the resin are easily distinguishable from the alpha tracks. Figure 6.14 (b) below shows the appearance of air bubbles within the alpha track emulsion over a blank microscope slide, this artifact is also clearly distinguishable from the alpha tracks.

There is a potential of interference from background radiation, however this was limited by placing the samples in a microscope slide box spaced apart to limit fallout from radon. Blank microscope slides were also prepared, the blank space between vegetation samples has been considered background and has been analysed for tracks. Other artifacts that may be present within the samples are the potential interferences with the gel, resin or stain, these are addressed below.
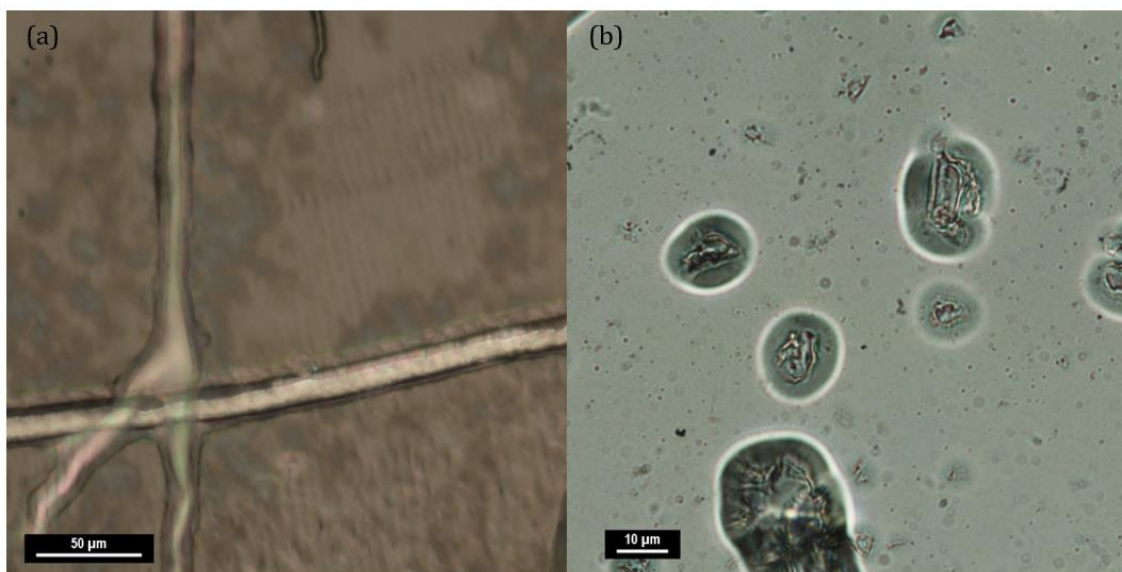
Figure 6.14. Resin with no leaf, with nuclear emulsion coating, some locations showed cracking, however no interference between the gel and the resin (left). Blank microscope slide coated with nuclear emulsion gel, air bubbles (right). No alpha tracks are observed within these two samples.

Justification

As the majority of the radionuclides of interest for this research project are alpha emitters this emulsion is appropriate for use within this research project. The application of the nuclear emulsion or 'Alpha Track' gel to a sample can indicate spatially where the alpha emitting radiation is within the sample. This technique will be the most sensitive and specific spatial technique available for this analysis.

Alpha Track Analysis Experimental Methods

The samples analysed in this section were prepared followed the alpha track analysis sample preparation procedures detailed above. After microtomy the nuclear emulsion is applied to the samples. The nuclear emulsion gels are light sensitive therefore the process need to take place within a dark room under red safety lights. The Ilford nuclear emulsion gel L4 (contains 0.162 g Ag/g emulsion and 0.042 g gelatine/g emulsion) contains AgBr crystal at a diameter of 0.11 µm and gelatine, gelatine is an important part of the nuclear emulsion gel as it provides the 3D structure to the nuclear emulsion layer. The gelatine suspends the AgBr crystals without allowing migration to occur during development. Gelatine is able to absorb water which enables the development and rinse steps to occur. The emulsion was prepared by placing in a beaker and adding deionized water as a 1:2 water to gel ratio. This was placed into a beaker on a hot plate at 36 °C, stirring lightly occasionally. After about 10 minutes of

heating the emulsion gel was a consistent paste consistency. The gel was placed onto the sample on the microscope slide by transferring it with a scoop, ensuring the entire sample is covered. The gel covered microscope slides are then covered with a box to minimize any light exposure and minimize the chance of any radon interference from the background. After the sample has been left for an appropriate length of time the slides are developed. The development process involves placing the slide in the development solution Phenisole Developer for 5 minutes (ID-19 developer formulation metol 2.2g, sodium sulphite, anhydrous 72 g, Hydroquinone 8.8 g, sodium carbonate, anhydrous 48 g, Potassium bromide 4 g, water to 1 L), this solution contains hydroquinone, which is the active chemical, this solution is also basic. This is followed by briefly dunking the slide in the ILFOSTOP PRO solution, this is an acidic solution to neutralize the first solution. The Ag nanoparticles will be stable in the gel where the alpha tracks are. The final step is a wash solution and fixer, this solution washes away any excess AgBr in the gel. The slides are left in this solution for up to an hour. The slides are then rinsed with tap water followed by rinsing with deionized water (Ilford, 2010).

After the sample has been exposed to the gel for an appropriate length of time, for the radioactivity of the sample, the gel was developed. The development process involves multiple steps. The development process reduces the Ag in the latent image centres (Ag^+) to elemental Ag^0. This process makes the Ag from the AgBr crystals to visible metallic Ag (Ilford, 2010). Using Ilford Developer which contains hydroquinone is the active component. The hydroquinone is in alkaline conditions to assist with the deprotonation of the hydroxyl groups (Figure 6.15).
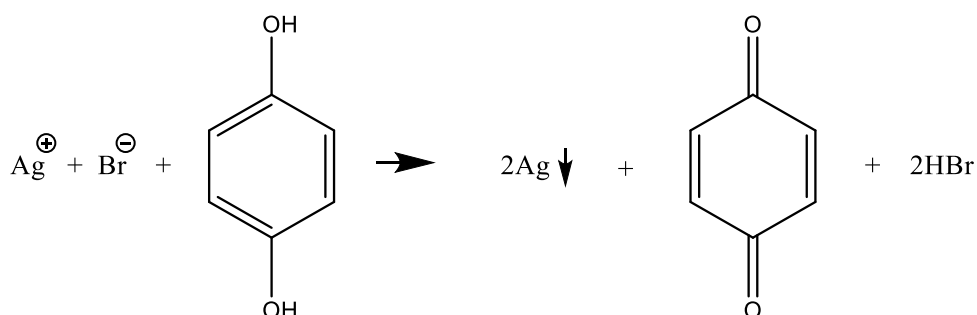

*Figure 6.15. Redox reaction between AgBr and hydroquinone, *Light exposure.*

A redox reaction occurs between the hydroquinone and the Ag^+ and the Br^-, the Ag reduces to Ag^0, 2HBr and 1,4-benzoquinone are produced (Figure 6.15). It is important that the developer does not reduce the Ag that is not in the latent image centres. The developer needs

to leave the unaffected by ionizing radiation Ag unchanged. There will be a few crystals that will be converted to elemental Ag without containing the latest image centres. These AgBr crystals are called fog or background (Ilford, 2010). At the development step, a stop is used, this is a mildly acidic chemical, citric acid is often used. This step neutralizes the pH from the alkaline development stage. When the developer is neutralized it is no longer active. The gel is only left in the Stop solution for two to three seconds. Ilford ILFOSTOP pro is used after development, this stops development to enable a precise development time (Ilford, 2010). Fixation is the step that removes all of the unreacted AgBr from the gelatine. The excess Ag is removed from the gelatine to preserve the image, if it is let the image will degrade. Ammonium thiosulphate is used to complex with the remaining AgBr. The emulsion is left in the fixer for twice the clearing time. As a colour change from white to colourless is observed after approximately 15 minutes, depending on the thickness of the emulsion layer. The sample is washed with running tap water for 5 minutes, this is followed by rinsing with distilled water. During this step the ammonium thiosulphate is washed away as it is soluble in water, removing any unreacted AgBr from the emulsion. The microscope slides are then dried and are ready for imaging, at this stage the slides can be exposed to daylight (Ilford, 2010). A Nikon Eclipse LV100 POL Optical Petrographic Microscope was used to image the slides.

6.3. Results

6.3.1. Radionuclide spatial and stratified distribution of soil

Soil autoradiography results

Autoradiography was used to determine the presence of radioactivity spatially over a 2-dimensional area of the soil samples from the Olympic Dam region. This shows the difference in activity of primarily β radiation within the samples through the soil depth. The soil fractionation and presence of radioactive particles is discussed. Figure 6.16. shows the Autoradiography results from the Olympic Dam Raise bore site. The darker coloured spots on the autoradiography results in Figures 6.16 and 6.17 indicates the presence of radioactive particles, these radioactive particles are likely representing process materials although this needs to be tested further via isotopic analysis.
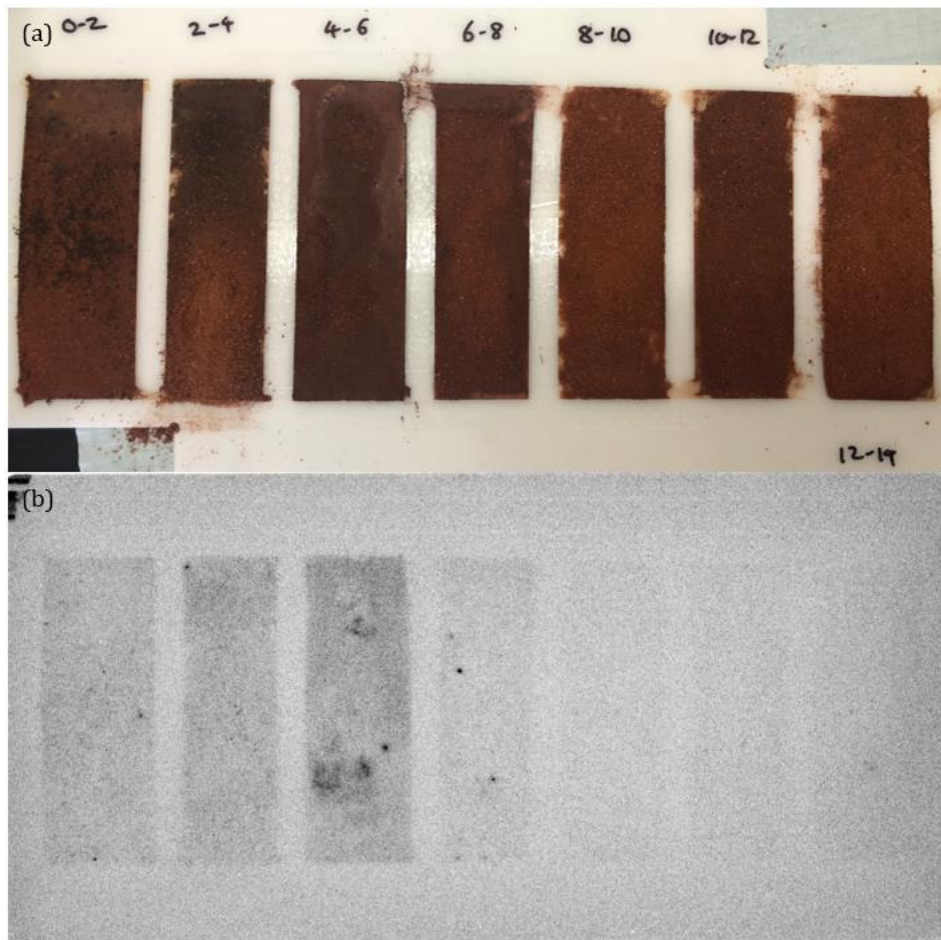
Figure 6.16. Autoradiography results of Raise Bore soils from Olympic Dam, (December 2018). The samples were exposed on the plate from 13:30 pm 20th March 2019. Soil depth left to right respectively, 0-2 cm, 2-4 cm, 4-6 cm, 6-8 cm, 8-10 cm, 10-12 cm and 12-14 cm. (a) soil samples (b) corresponding autoradiography plate results. Samples were exposed to the autoradiography plate for 7 days, the pixel size is 200 by 200 μm.

Figure 6.16 (a) shows the soil samples from the raise bore site, in 7 different depths decreasing in depth from left to right. The soil from the raise bore site is not consistent in colour across the different depths or within each interval, where the colours range from light orange to dark purple. The colours of each interval using the Munsell colour chart are 0-2 ¾ and 3/6, 2-4 is 4/6, 3/3 and ¾, 4-6 is3/3, 6-8 is ¾, 8-10 3/6, 10-12 is ¾ is 12-14 3/6 The colour difference is likely due to the sample collection location being highly mechanically disturbed. The autoradiography results from the raise bore site depth profile is shown in Figure 6.16 (b). All soil intervals were visible from the autoradiography plate; however, the 0-2 cm, 2-4 cm, 4-6 cm and 6-8 cm are easily visible and show unique features. The Intervals 8-10 cm, 10-12 cm and 12-14 cm are indistinguishable from each other.

The autoradiography results from the Pilot and Tailings site samples are shown below in Figure 6.17. Figure 6.17 (a) shows the soil samples that were analysed by autoradiography and Figure 6.17 (b) shows the autoradiography results from the samples.
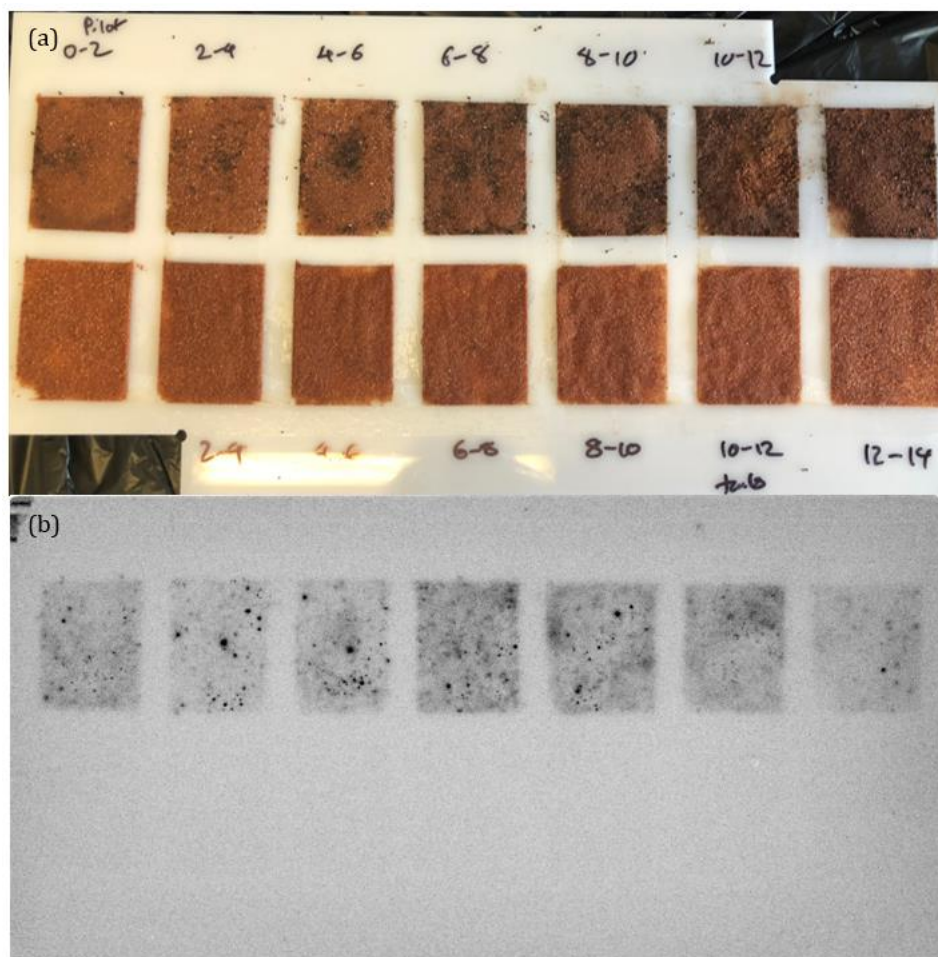
Figure 6.17. Autoradiography results of tailings and pilot site soils from Olympic Dam, (December 2018). The sample was exposed on the plate from 12:30pm 20th March 2019 sample. The pilot site samples are located at the top of the image, left to right respectively, 0-2 cm, 2-4 cm, 4-6 cm, 6-8 cm, 8-10 cm, 10-12 cm and 12-14 cm. The Tailings site samples are located at the bottom of the figure left to right respectively, 0-2 cm, 2-4 cm, 4-6 cm, 6-8 cm, 8-10 cm, 10-12 cm and 12-14 cm. (a) Soil samples (b) corresponding autoradiography results. Samples were exposed to the autoradiography plate for 7 days, the pixel size is 200 by 200 μm.

Figure 6.17 (a) shows the soil samples from the Pilot (top) and the Tailings site (bottom) site in 7 different 2 cm depth intervals decreasing in depth from left to right. The colour of the soil does not appear to be obviously different in any of the samples from either site or interval. However, the soil samples from the pilot site appear to have a fraction of organic matter within the samples as small sections of leaves and sticks were observed, this is what appears darker in colour within the pilot samples. The autoradiography results from the pilot site

depth profile are shown in Figure 6.17 (b) (top) and the Tailings site (bottom). No samples from the tailings site produced a visible signal. All soil depth interval samples from the pilot site were visible from the autoradiography plate. The pilot samples from 0-12 cm are similar in shade and content of radioactive particles, these samples are indistinguishable of each other. The 12-14 cm interval from the pilot site is lighter in signal and contains fewer radioactive particles in comparison to the 1-12 cm intervals.

Samples from the arid, Roxby Downs, south control and north control sites were analysed using autoradiography. The 0-2 cm and 12-14 cm interval was analysed from each site to provide the largest possible range of potential signal from each site. The results from this autoradiography analysis are in appendix H. No signal was detected using the autoradiography technique from any of the soil samples.

Radionuclide quantitative analysis of stratified soil by gamma spectroscopy

Samples collected from Olympic Dam during the May 2018 sampling trip have been analysed using gamma spectroscopy using the SAGe well detector. Gamma spectroscopy analysis of the soil samples from different depths will provide activity determination and identification of what radionuclides are present within each sample. The gamma spectroscopy results are in Table 6.1 below.

Table 6.1. Gamma spectroscopy of soil stratified soil samples from Olympic Dam Autumn May 2018

Site	Depth (cm)	Ra-226 Act (Bq/kg)	Uncert ± (Bq/kg)	MDA (Bq/kg)	Th-228 Act (Bq/kg)	Uncert ± (Bq/kg)	MDA (Bq/kg)	Pb-210 Act (Bq/kg)	uncert ± (Bq/kg)	MDA (Bq/kg)	Pb-212 Act (Bq/kg)	uncert ± (Bq/kg)	MDA (Bq/kg)	U-235 Act (Bq/kg)	uncert ± (Bq/kg)	MDA (Bq/kg)
North Control	0-2	4.72	0.79	2.77	6.15	0.72	3.08	-	-	-	-	-	-	-	-	-
	2-5	4.72	0.74	2.62	4.86	0.64	3.19	-	-	-	6.46	1.98	5.03	-	-	-
	5-8	4.69	0.77	2.81	4.16	0.70	3.28	-	-	-	8.27	2.14	5.56	-	-	-
	8-10	6.73	0.57	2.51	6.71	0.63	1.64	-	-	-	-	-	-	-	-	-
Arid	0-2	4.43	1.33	3.26	4.82	0.85	3.55	18.2	3.96	6.28	7.11	2.32	6.41	-	-	-
	2-4	6.03	0.85	2.82	5.88	0.69	3.61	-	-	-	7.52	2.3	5.76	-	-	-
	4-6	3.86	1.19	3.25	6.76	0.81	3.30	-	-	-	-	-	-	-	-	-
	6-8	6.58	0.89	2.98	6.71	0.72	3.27	-	-	-	6.29	2.33	6.02	-	-	-
	8-10	8.07	0.58	2.42	6.38	0.53	1.19	-	-	-	-	-	-	-	-	-
Raise Bore	0-2	58.9	2.75	4.53	8.92	1.11	4.87	89.8	17.2	9.72	12.9	3.36	8.03	9.11	0.90	4.85
	2-4	27.7	1.57	3.78	7.21	0.92	4.06	39.7	7.93	8.13	12.1	2.89	6.73	3.69	0.46	2.59
	4-6	7.67	1.44	3.5	6.61	0.87	4.15	-	-	-	8.79	2.68	6.83	-	-	-
	6-8	8.63	0.89	3.21	6.23	0.78	3.77	-	-	-	9.37	2.43	5.88	-	-	-
	8-10	6.40	1.33	3.42	8.46	0.85	3.79	-	-	-	-	-	-	-	-	-
Pilot	0-2	68.3	3.08	4.39	5.49	1.13	4.04	104	19.8	9.97	-	-	-	8.37	0.83	4.56
	2-4	20.5	1.00	2.89	7.70	0.66	1.60	-	-	-	-	-	-	2.18	0.34	1.83
	4-6	12.7	0.83	2.94	8.01	0.66	1.58	-	-	-	-	-	-	2.08	0.36	1.87
	6-8	16.1	1.10	3.18	6.22	0.79	3.27	-	-	-	6.22	2.18	5.69	2.16	0.31	1.74
	8-10	5.95	1.57	3.31	6.32	0.86	3.80	-	-	-	-	-	-	1.81	0.31	1.68
Roxby Downs	0-2	3.69	1.42	3.38	6.97	0.88	3.61	-	-	-	-	-	-	-	-	-
	2-4	-	-	-	6.93	0.49	1.50	-	-	-	-	-	-	-	-	-
	4-6	4.33	0.77	2.74	5.59	0.66	3.09	-	-	-	5.63	2.06	5.44	-	-	-
	6-8	-	-	-	7.76	0.69	1.45	-	-	-	-	-	-	-	-	-
	8-10	4.72	0.79	2.77	6.15	0.72	3.08	-	-	-	-	-	-	-	-	-
South Control	0-2	6.09	0.58	2.44	6.72	0.55	1.39	-	-	-	-	-	-	-	-	-
	2-4	-	-	-	6.96	0.58	1.68	-	-	-	-	-	-	-	-	-
	4-6	5.78	0.50	2.45	6.35	0.51	1.16	7.54	2.29	6.12	-	-	-	-	-	-
	6-8	-	-	-	5.79	0.89	3.24	-	-	-	7.60	2.52	6.79	-	-	-
	8-10	-	-	-	6.20	0.78	3.75	-	-	-	-	-	-	-	-	-

The results of soil activity from gamma spectroscopy shown in Table 6.1 details the activity of radionuclides throughout the first 10 cm of soil depth. This table provides quantification to the autoradiography images in Figure 6.16 which show the raise bore site and Figure 6.17 which shows the pilot site. The activities for the other sites were below the detection capabilities of the autoradiography plate. The activity data from Table 6.1 is also shown in Figure 6.18 below.
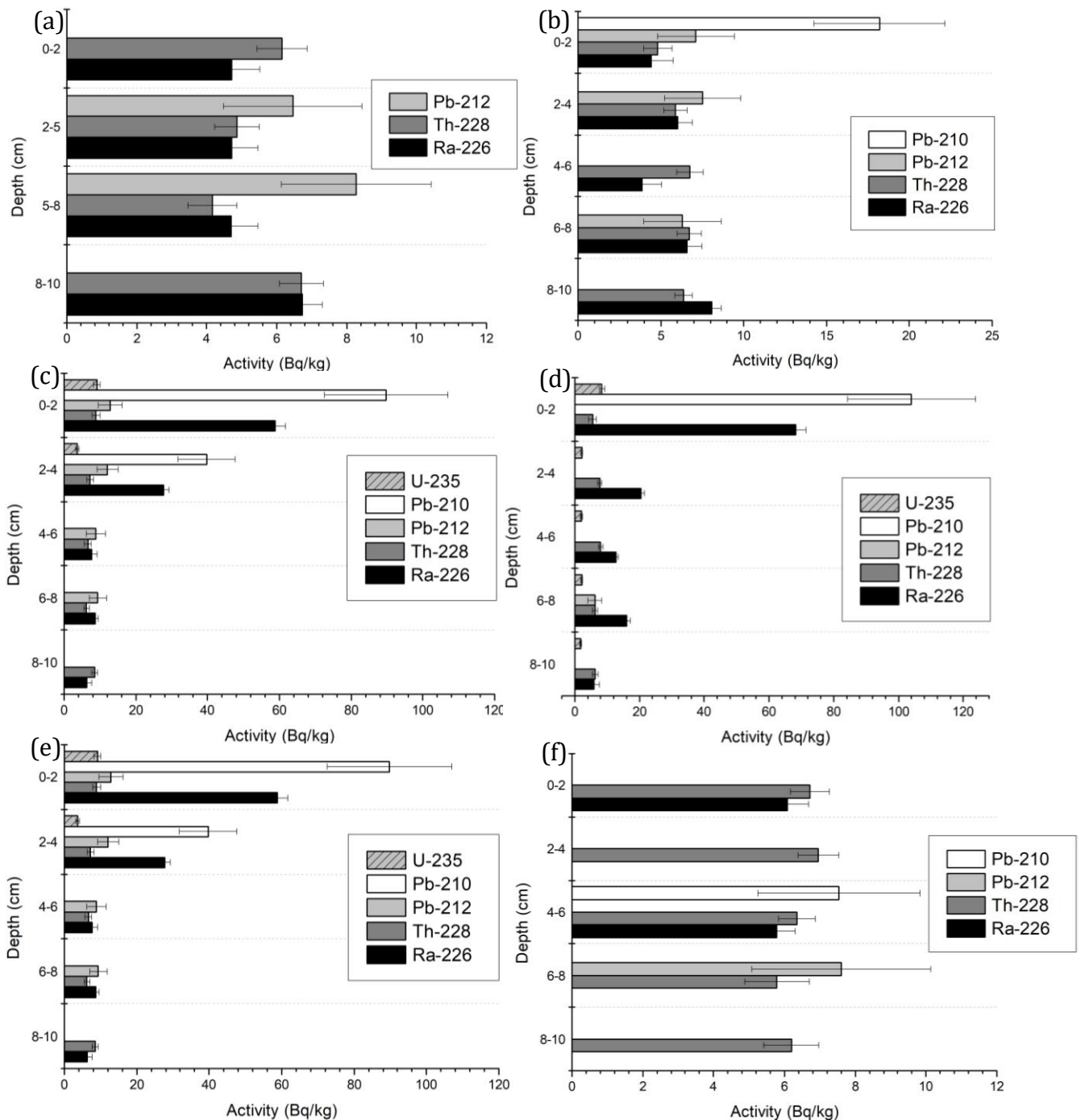
Figure 6.18. Soil depth radionuclide analysis Olympic Dam May 2018, gamma spectroscopy. (a) North Control, (b) Arid, (c) Raise Bore, (d) Pilot, (e) Roxby Downs and (f) South Control soil. (Note. there is a change in scale between the figures).

Figure 6.18 shows that the raise bore, pilot and Roxby Downs sites clearly have gradients. The activity of the radionuclides detected within the north and south control sites were very similar. However, ^{210}Pb was identified in one of the south control sites and none of the north control sites. The samples from the raise bore, pilot and Roxby Downs sites show clear differences within the activities of radionuclides within the surface soil and the rapid decrease

in activity as the depth of the soil increases. The samples from all sites don't show any variation below the depth of 4cm.

6.3.2. Radionuclide spatial distribution within vegetation

Autoradiography results

To determine whether the radionuclides within the flora samples could be spatially resolved, autoradiography was used. This technique was used to determine whether the deposition from the dust fallout could be observed using autoradiography. Flora samples were exposed to an autoradiography plate, the samples chosen were from the raise bore site at Olympic Dam. This site was chosen as it has previously shown to have higher radionuclide activity compared to the other sample sites. Both *Acacia ligulata* and *Dodonaea viscosa* were analysed. The results are shown in Figure 6.19 below.
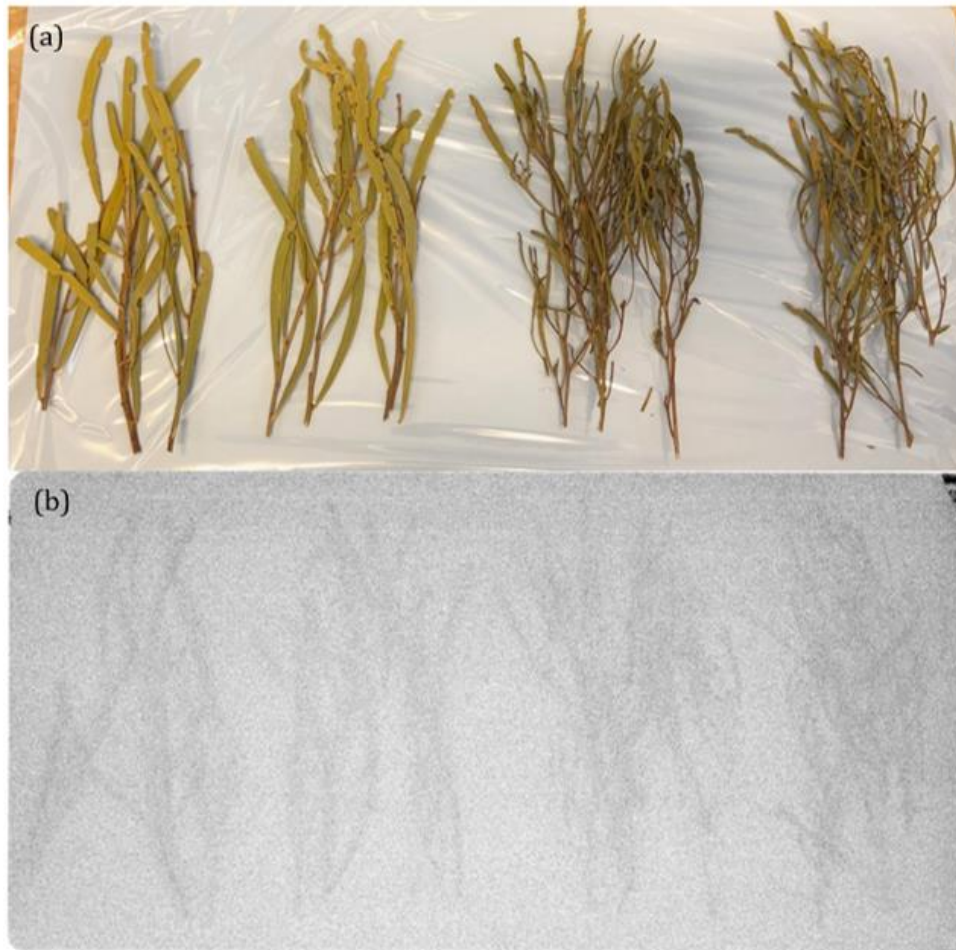
Figure 6.19. Autoradiography plate for analysis of vegetation from the raise bore site from Olympic Dam, May 2018 sampling visit, Acacia ligulata washed, Acacia ligulata unwashed, Dodonaea viscosa washed, Dodonaea viscosa unwashed, left to right respectively (a) samples and (b) corresponding autoradiography results. Samples were exposed to the autoradiography plate for 7 days, the pixel size is 200 by 200 μm.

Figure 6.19. shows the washed samples of *Acacia ligulata* and *Dodonaea viscosa* from the Autumn (May 2018). Samples from the same batch have previously been analysed quantitatively, the activity of the *Acacia ligulata* is ~60 Bq/kg and the *Dodonaea viscosa* is ~80 Bq/kg from respectively Chapter 3. The autoradiography image of the stems and leaves appeared the same. Therefore, autoradiography has showed that there is radioactivity within the samples however the technique is not sensitive enough to provide any spatial information. The results show there is no visible difference between the two different species of vegetation, when the known activities are different and *Dodonaea viscosa* is of higher activity compared to the *Acacia ligulata*. There was also no visible difference between the activity of the washed and unwashed vegetation samples of the same species. This indicates that there is less than the quantitative amount difference between washed and unwashed samples of vegetation, which was performed to capture dust deposition.

Olympic Dam alpha-particle radiography results

Samples of *Dodonaea viscosa* from Olympic Dam were prepared successfully and were coated with the alpha track emulsion. Kalnins *et al*. 2019 have previously used alpha-particle radiography to successfully spatially locate the origin of radioactive nuclei within low activity mineral samples (Kalnins et al., 2019). Therefore, the same theory has been used for a biological sample, using the alpha-particle radiography technique to determine what part of the leaf physiology the radionuclides are originating at a microscopic scale. An example of a *Dodonaea viscosa* sample with clearly visible cells and alpha tracks is shown below in Figure 6.20.

Figure 6.20. Dodonaea viscosa species from the raise bore site before 38-days, three visible alpha tracks from the name location.

The Figure 6.20 above shows the alpha tracks and the directionality determined by scrolling through the z-axis focal plane of the microscope (Kalnins et al., 2019). This Figure also shows the cells of the leaf clearly behind the tracks, allowing for clear identification of the location within the leaf of the radionuclide. The alpha tracks in Figure 6.20 originate within the palisade parenchyma near the outer surface of the leaf. This image shows that the radionuclide locations can be located within the different cells and microstructures within the leaf.

The samples from Olympic Dam that were coated before the 38 days were exposed for to the alpha track emulsion for between 100 and 106 days. The orientation of leaf was cut at both transverse and longitudinal to increase the data of the radionuclide locations within the leaves. Alpha tracks are shown in Figures 6.21 to 6.23.
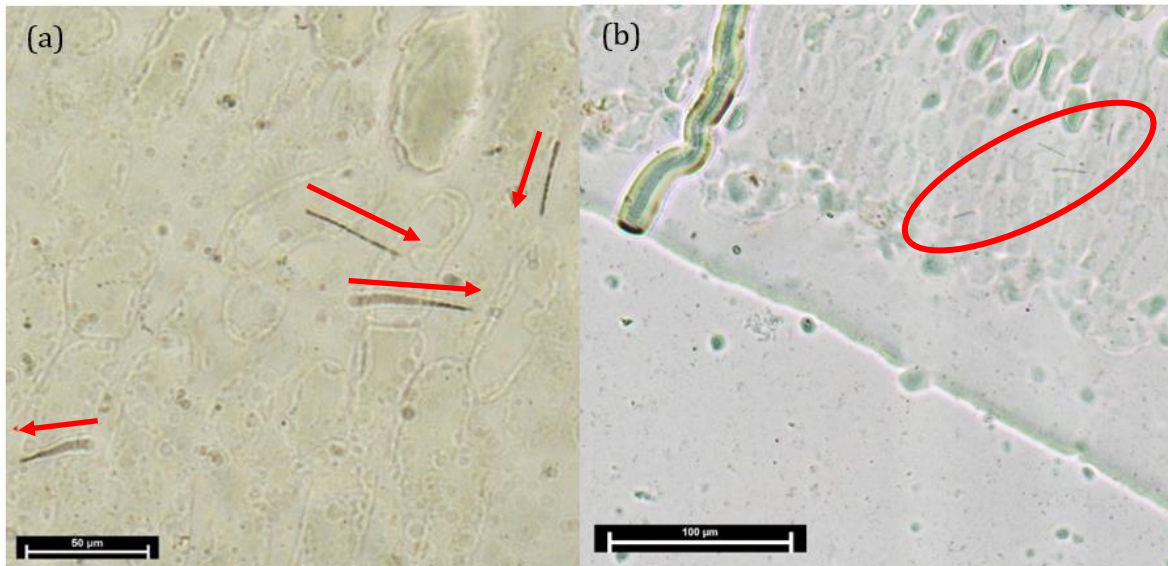

Figure 6.21. Alpha tracks clustered near the edge of a leaf, Dodonaea viscosa from the pilot plant site. Plant 2 leaf d slide d.
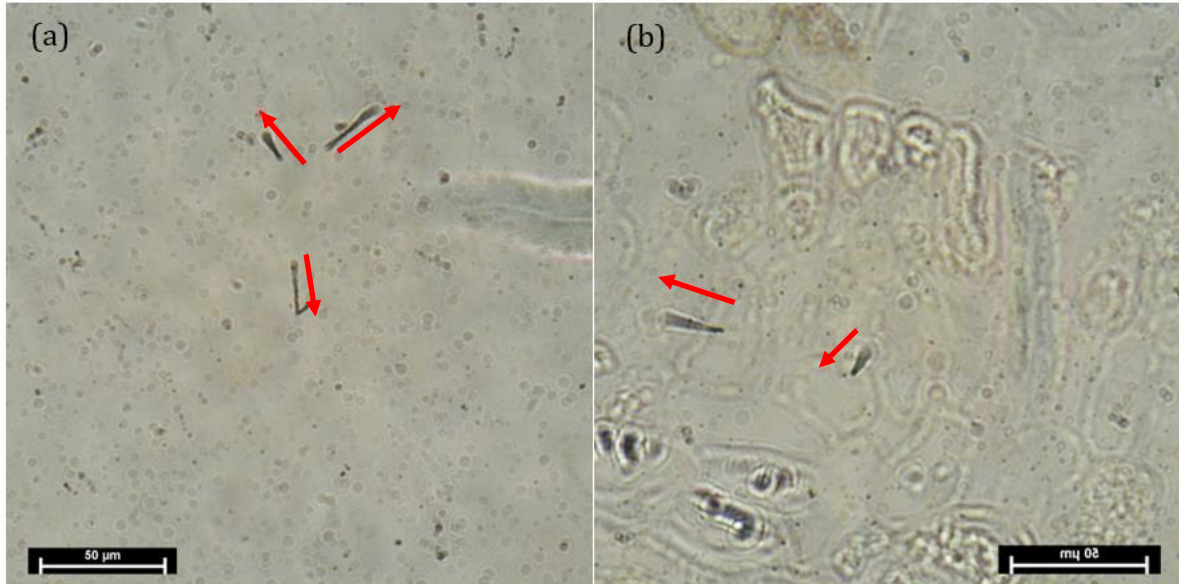

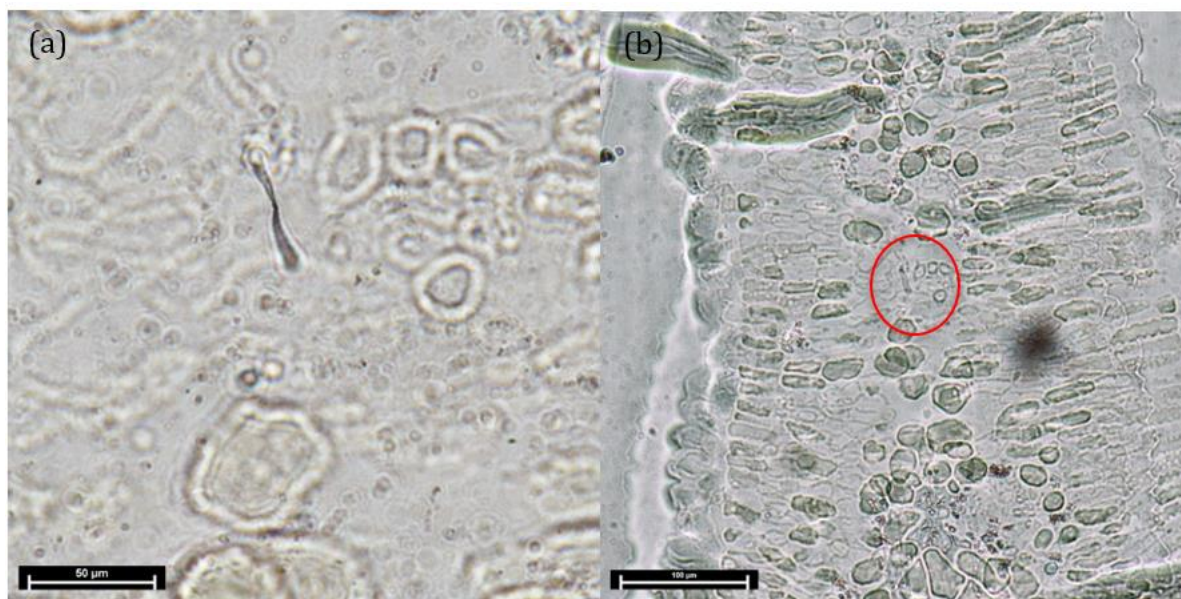*Figure 6.22. Alpha tracks clustered near the edge of a leaf, Dodonaea viscosa from the tailings site.*

Figure 6.23. Dodonaea viscosa, pilot plant 2, leaf d, section cut 2 where a is a zoomed in view of the track shown in b.

6.4. Discussion

6.4.1. Stratified soil radionuclide discussion

From the autoradiography results shown in Figure 6.16, the large colour variability at the raise bores site is likely due to the sample collection location being highly mechanically disturbed as the site is within the mining lease area near the mining operations including ore stockpiling and the raise bores. The radioactive particles in the raise bore samples were not observed in the intervals 8-10 cm, 10-12 cm and 12-14 cm indicating that the disturbance from mining activities was likely to be minimal below a depth of 8 cm. This signal greatly reduces within the 6-8 cm fraction and then reduces further within the 8-10 cm, 10-12 cm and 12-14 cm intervals. The pilot mine soil samples contained radioactive particles consistently throughout all of the soil depth analysed. There was no measurable variability throughout the 0-14 cm soil depth. This shows that the mechanical disturbance of the soil in the vicinity of the pilot plant reached depths greater than 14 cm, this is likely due to the operations of the pilot plant. Radionuclide containing dust from the mining operations was not observable from the data collected at the pilot plant site. The results from Figures 6.16 and 6.17 also show that radionuclides are present within a fine dust across the samples. This is observed as there is a defined line surrounding the sample well for each of the samples and there is a consistent signal across the samples.

213

From Figure 6.16 (b) the soil depth interval 4-6 cm showed the darkest image on the autoradiography plate compared to all other sections. This qualitatively shows that this interval is likely the most radioactive compared to the other intervals in the image. The 4-6 cm interval appeared to be the darkest purple in colour from Figure 6.16 (a). From the autoradiography results, the intervals 0-2 cm, 2-4 cm, 4-6 cm and 6-8 cm show small concentrated dark patches. These are indicative of a higher activity of radiation compared to the surrounding sample. Small, concentrated accumulations of radiation in the are due to radioactive particles. These radioactive particles were not observed in the intervals 8-10 cm, 10-12 cm and 12-14 cm indicating that the disturbance from mining activities was likely to be minimal below a depth of 8 cm.

The results from Figure 6.16 (b) show that radionuclides are present within a fine dust across the samples. This is observed as there is a defined line surrounding the sample well for each of the samples and there is a consistent signal across the samples. This signal greatly reduces within the 6-8 cm fraction and then reduces further within the 8-10 cm, 10-12 cm and 12-14 cm intervals. The results from Figure 6.17 show that the activity of radionuclides within all the depths of soil from the Tailings site are below the β activity autoradiography is capable of imaging. Were the LOD for Autoradiography of ~200 Bq/g. The results from the Pilot site showed, radioactive particles contained at each soil depth, there was also a fine dust throughout each sample, consistent with the raise bore site from Figure 6.16. The Pilot site showed consistent results from 0-12 cm, this indicates that the disturbance of the surface soil reaches 12 cm in depth at this site. The 12-14 cm interval is still visible using the autoradiography technique and contains radioactive particles. This further indicates that the mechanical disturbance reaches deeper than 14 cm however there is a decrease at the 12-14 cm interval.

To further understand the stratified soil samples, implementing a technique that is quantitative or specific to one type of radiation would be beneficial and informative. Therefore, providing activity data on the different radionuclides within the samples, gamma spectroscopy will be used to determine activities of each fraction.

No signal was detected using the autoradiography technique from any of the soil samples from the tailings, arid, Roxby Downs, south control and north control sites. Therefore, the limitation of the β activity in the soil samples were below the limit of detection capable from autoradiography. Autoradiography has been useful in showing the distribution of radioactivity within the soil samples in terms of identification of the radioactive particles and or a fine radioactive dust. Autoradiography also provided a visual representation of the variation of radioactivity throughout the depth of soil within the raise bore site.

The results from the gamma spectroscopy analysis indicate there is minimal difference in the radionuclide content throughout the 0-10 cm intervals for the sites, north control, and south control. The arid site has a very similar concentration of radionuclides compared to the north and south control sites, however, at the 0-2 cm interval ^{210}Pb was present, where it was absent at all lover intervals. The raise bore, pilot and Roxby Downs sites show some indication of surface deposition. The pilot plant had ^{210}Pb in the 0-2 cm interval and nothing below. The 0-2 cm interval of the pilot plant also showed increased concentration of ^{226}Ra in comparison to the lower soil intervals. The raise bore and pilot plants show an increase in the concentration of ^{210}Pb from 0-4 cm and ^{226}Ra to 0-4. All sites from 4cm show negligible interference from surface deposition.

The comparison of the autoradiography of soils and the radionuclide data shows that there was not a signal below the activity of ~50 Bq/kg within the soils. This agrees well with the gamma and alpha spectroscopy results when considering the magnitude of the activity. The limitation in the LOD for autoradiography is noted as it detects mostly beta radiation. This would underestimate the overall activity of NORM samples, which are primarily alpha and gamma emitters. Due to the limitation of the macroscopic view of autoradiography and the limitations of the primary emissions detectable being beta.

6.4.3. Vegetation spatial discussion

Autoradiography discussion
The sensitivity of autoradiography was inadequate to differentiate between any of the structures on the plants. The difference in the autoradiography signal between the vegetation

with dust deposition and the vegetation with no dust deposition was not observable using autoradiography. The difference between the two different species can also not be determined by autoradiography. The autoradiography technique also did not provide enough detail in the image to determine if there were sections of the sample that were of higher activity than others. A limitation of the autoradiography method is that it is primarily sensitive to beta radiation, where the majority of the radionuclides within NORM are alpha emitters. However, from the autoradiography results of vegetation samples, we can conclude that a more sensitive technique is required for analysis of spatial locations of radionuclides within vegetation. An alternative method to autoradiography is alpha-particle radiography analysis, it is on a microscopic scale compared with autoradiography. Alpha-particle radiography analysis is also specific to alpha emitters, which is the primary emission from NORM. Therefore, this technique was more appropriate for low activity NORM materials. However, extensive method development for alpha track analysis of vegetation was required. Alpha particle radiography was implemented as a more sensitive technique, the results from this are discussed below.

Alpha-particle radiography method development discussion

The results from the initial method development show that alpha tracks can be visualised from the leaf samples using the alpha-particle radiography method. A flatter surface on a microscopic scale was required, microtomy was determined to be an effective method to provide a flat surface for application of the alpha-particle emulsion. Therefore, the microtome method was continued for the remaining of the experiment on the Olympic Dam vegetation samples. Due to the *Acacia ligulata* requiring much more extensive resin embedding steps, the *Dodonaea viscosa* was the focus species of interest for this experiment.

The stain trial to enhance the cell walls was unsuccessful using toluidine blue due to the interference that occurred with the alpha particle emulsion (De Campos Vidal & Mello, 2019; O'Brien et al., 1964). However, when the alpha-particle emulsion was applied there was significant interference to the emulsion with the stain. The interference was only in the focal plane of the emulsion that is in contact with the stain. Therefore, the alpha emulsion was applied to the unstained samples, and an individual section was stained for reference.

Samples of *Acacia ligulata* were attempted to be analysed using this method however, the cells of the leaves were not penetrated by the resin resulting in brittle samples from thin sectioning. Therefore, no conclusions can be made on the *Acacia ligulata* from this study. A more extensive ethanol dehydration and propylene oxide steps may improve the resin infiltration for the cells from this species which would allow for alpha track analysis of this species.

Alpha-particle radiography on Olympic Dam samples

The alpha-particle radiography technique was successful for samples of *Dodonaea viscosa* from Olympic Dam. The radionuclide locations can be located within the different cells and microstructures within the leaf. The activity of vegetation from chapter 3 has been shown to be very low, therefore, the alpha-particle radiography method is useful as it tells us there is radioactivity present within the sample (Kalnins et al., 2019).

The alpha tracks originate within the palisade parenchyma near the outer surface of the leaf, the pongy parenchyma, sclerenchyma or within the midrib area on almost all occasions tracks were observed. The midrib of the leaf is composed of the xylem and phloem which transport water, sugars and other plant nutrients around the plant, they run from the roots to the leaves of plants. Where alpha tracks were present in these structures, this indicates the originating radioactive nucleus is likely being taken up by the roots of the plant. Where the alpha tracks are near the cuticle of the leaf, this means they are likely taking in through stomata or through adsorption through the leaf (Shahid et al., 2017).

The three alpha tracks observed appear to be originating from the same location, as the radioactive nucleus could be at any depth within the 2 μm thickness of the leaf there is the possibility that these tracks would intersect and originate from the same radioactive nucleus. In the case where three tracks originating from the same nucleus occurs, there is a strong likelihood that the resulting decay is from the ^{222}Rn and Daughters as ^{222}Rn, which is followed by the decay of ^{218}Po, ^{214}Pb, ^{214}Bi and ^{210}Tl as these radionuclides all emit alpha particles and all decay within an hour. Therefore, the cluster of three alpha tracks is likely the result of this. The sample was prepared and coated before the 38-day decay for ^{222}Rn equilibrium. The difference between tracks from samples prepared and coated before and after the 38-day

decay could be explored further due to the low activity of the Olympic Dam samples. This research aimed to begin a quantification method for alpha track analysis, by comparing to the activity of the sample. However, further data is required to begin quantification of samples, especially at low activity.

Overall, the alpha-particle radiography technique is an extensive process to go through for a qualitative result. However, this technique did provide unique insight as to where the radionuclides are located within the structures of leaves. This method provided invaluable data regarding the location being within the midrib location or on the inside of the cuticle of the leaf being the main location of alpha emitting particles.

6.5. Conclusions

Autoradiography is a complementary technique to alpha track analysis for analysis of vegetation as they are both sensitive to different types of radiation and provide different information from the results on a macroscopic and microscopic level. However, in this study the activity of ionising radiation within the vegetation was not high enough to provide spatial distribution detail. Autoradiography was useful for soil analysis to determine the distribution of radiation through the soil fractionation. As larger radioactive particles and a fine radiation containing powder were both observed. Autoradiography was not sensitive enough to provide information on the spatial distribution of radiation from the samples from the sample sites outside of the mining lease at Olympic Dam.

Autoradiography was a useful analytical technique for the analysis of environmental samples. It was very useful for determining the distribution of radiation within soil samples and across the stratified soil samples. This easily visualised the difference in higher radioactivity of the surface soil samples in comparison to sampled at lower soil depth, at sites from adjacent mining activities at Olympic Dam. The gamma and autoradiography are complimentary as they both show greater activity towards the higher surface level soil. This was clear when comparing the activity gradient from the stratified soil analysis to the background sites of the north and south control sites at the Olympic Dam region. The results also showed that within

the disturbed samples, there were clustered emissions from radioactive particles as well as more numerous finer particles with weaker emission.

Alpha-particle radiography is useful for low activity radionuclide concentrations due to the microscopic level, long exposure times (Kalnins et al., 2019). However, from this present study, the use of alpha track analysis is recommended for use on samples above the activity of 100 Bq/kg.

Chapter 7. Phase analysis of Australian uranium ore concentrates determined by variable temperature synchrotron powder X-ray diffraction

This chapter is adapted from a paper titled "Phase Analysis of Australian Uranium Ore Concentrates Determined by variable Temperature Synchrotron Powder X-ray Diffraction" by S. B. Pandelus *et al*. that has been published in the journal *Inorganic Chemistry*.

7.1. Introduction

Australia is the world's third largest producer of U, and it exports approximately 7000 tons of UOC per annum from three active, or recently active, U mines namely the Olympic Dam, Ranger, and Beverley mines. The ore at each mine varies in mineralogy and minor and trace element geochemistry, and these are further impacted by differences in mining procedures as well as ore-processing methods and by the customer needs and regulation requirements. The final step in the production of the UOC at both the Olympic Dam and Ranger mines is roasting (calcining) and this results in the formation of U_3O_8. At the Beverley mine, the product is $UO_4 \cdot 2H_2O$ precipitated by the addition of peroxide. Keegan et al. determined the concentrations of 40 minor and trace elements in UOC from these three Australian mines and was able to use this information to build characteristic elemental and isotope signatures for the samples (Keegan et al., 2008). Ditcham and co-workers, working with the same bulk samples as Keegan, demonstrated that a combination of differential thermal analysis, thermogravimetric analysis, and powder X-ray diffraction (PXRD) could be used to differentiate between the original sources; however, a number of minor phases in the UOCs could not be fully characterized (Ditcham et al., 2016; Keegan et al., 2008). An interesting observation in that work was that the temperature at which various intermediate phases formed during the thermal decomposition measurements depended on the origin of the sample. Other studies on the thermal decomposition of a number of UOC phases have been reported and although it is generally agreed that the final product of calcination is either U_3O_8 or UO_2 depending on the atmosphere, there is little consensus regarding the nature of any intermediate phases (Desfougeres et al., 2020).

The accurate identification of secondary U oxide phases can be very challenging using laboratory-based diffractometers (Su et al., 2018). In the current study, the major phases present within three UOC samples and the temperature induced phase transitions of these were determined using high energy monochromatic X-ray measurements from synchrotron radiation. The energy was selected to minimize absorption from the sample and particularly to avoid the effects of the U L-absorption edges. The extended d-range accessible using high energies allows precise and accurate structural data to be refined. In this study, we explore the change in the phase composition in UOCs brought about by the absorption of moisture

during a prolonged storage (12–14 years). From these data, we can accurately calculate the amount of structurally bound water and follow the evolution of the phases of the Australian UOC characterized by Keegan et al. (Keegan et al., 2008).

7.1.1. Chapter directions

This chapter endeavours to determine UOC signatures of samples from Olympic Dam, Beverley and Ranger for nuclear forensic applications. This will be done by assessing whether there are unique phases in the UOC's from different mines. This study will also identify the crystal structure phase transformation of three different UOC samples through heating the sample. Different gas flow conditions will be used to assess their effect on the crystal structure changes. This study used synchrotron-XRD to determine the structural phases present in UOC samples from Australian Uranium mines Olympic Dam, Ranger and Beverley. This study will determine and confirm the formation and structure of UO_3 (α- or β-) as an intermediate transition to U_3O_8 and to identify and understand the stability if any other crystalline phases. This study also characterises other intermediates not identified in the previous studies and gain a fuller understanding of morphological characteristics of U ore concentration to be used in a nuclear forensic context. The diffractometer from the Australian synchrotron will allow observations of the micro-domains and stresses within the sample as well as detection and quantification of any transient species. To determine whether the phase assemblages within each sample are affected by different conditions sealed, N_2 gas flow and air gas flow through the variable temperature analysis. Overall, to determine whether the synchrotron-XRD analysis on UOC samples could be useful for nuclear forensic analysis.

7.2. Experimental methods

7.2.1. Samples

UOC samples

The samples used in this study were from the same bulk sample lots studied by Keegan et al. and were made available by the Australian Nuclear Science and Technology Organization (ANSTO) (Keegan et al., 2008). The Ranger mine sample, NFS13-091, was received by ANSTO

in October 2004, and collected by the mine operators in the period 2003/2004. The Beverley mine sample, NFS13-088, was received by ANSTO in September 2004, and collected by the mine operators in 2003/2004. The Olympic Dam mine sample, NSF13-094, was received by ANSTO in February 2006, and was collected by the mine operators in 2005. The UOC produced at the Ranger and Olympic Dam mines is described as U_3O_8 and at the time of initial receipt by ANSTO and the current analysis, in 2017, both samples appeared dark green to black in colour. The Beverley mine UOC is nominally $UO_4 \cdot 2H_2O$ and was yellow/orange in colour on receipt at ANSTO and in 2017. Further details and the production methods for the UOC samples are given elsewhere (Ditcham et al., 2016; Keegan et al., 2008). The samples were stored in the containers in which they were collected at the respective mine sites, either plastic screw-top bottles or zip-lock bags. Each container was placed within secondary containment (another zip-lock bag) and stored in a cupboard in an air-conditioned laboratory (22 °C, relative humidity 40%), and only opened for subsampling on several occasions over the ~10 year period. All of the samples for the synchrotron experiments were loaded into capillaries in mid-September 2017 and data were collected shortly thereafter.

All UOC samples for the synchrotron experiments were loaded into capillaries in mid-September 2017 and data were collected shortly thereafter. The UOC samples for the gas flow analysis were mixed and ground with equal masses of analytical grade quartz glass to minimize absorption effects and the powders were packed tightly into the quartz capillaries for analysis. The sealed samples were undiluted and prepared in 0.2 mm quartz glass capillaries while for gas flow analysis, 0.8 mm quartz glass capillaries (Hilgenberg) were used. Above the sample the capillaries were packed with coarse analytical grade quartz glass and glass wool to allow gas flow but prevent sample movement.

7.2.3. Experimental

Instrument and Data Analysis

Preliminary X-ray diffraction patterns were collected for the three samples in 2006, shortly after they were supplied by the mining companies. Patterns were collected on a Philips PW1050 X-ray diffractometer (PANalytical Ltd., Almelo, Netherlands) with Cu Kα radiation; data were collected over the angular range 5° ≤ 2θ ≤ 100° with a step size of 0.05° and an

acquisition time of 5 s per step. The data measured in 2014 used a Bruker D8 X-ray diffractometer (Billerica, Massachusetts, USA) with a Cu X-ray tube (1.5418 Å) (40 kV, 40 mA) and a diffraction angle range of $10° \leq 2\theta \leq 150°$ with a step size of 0.02° and a counting time of 20 s per step. Samples were adhered onto double-sided carbon tape and mounted on Si single crystals in preparation for XRD analysis (Ditcham et al., 2016). Finely ground subsamples of the UOC samples were placed in 0.2 mm quartz glass capillaries that were then flame sealed. Synchrotron X-ray diffraction (S-XRD) data were measured on the powder diffraction (PD) beamline at the Australian Synchrotron operating at around 16 keV (0.728938 Å based on calibrations using a NIST LaB6 (660b) standard reference) using an array of 16 MYTHEN II microstrip detectors (Wallwork et al., 2007). Each sample was heated from 25 to 875 °C with a ramp rate of 5 °C per minute and patterns were collected at 25 °C intervals. Data collection was commenced after a 60 s thermal equilibration period. Temperature was controlled using an FMBOxford hot air blower placed below the capillary. A smaller number of datasets were collected on the cooling cycle, where a cooling rate of 10 °C per minute was employed. The structures were refined against the S-XRD data by the Rietveld method as implemented in the program GSAS with the EXPGUI frontend (Larson & Von Dreele, 1994; Toby, 2001). The peak shapes were modelled using a pseudo-Voigt function and the background was estimated using a shifted Chebyshev function. The scale factor, detector zero-point, lattice parameters, atomic coordinates, and isotropic atomic displacement parameters were refined together with the peak profile parameters.

Figure 7.1 (b) below shows a Norby-type flow cell, this attachment was used for measurements where the sample environment was controlled (Norby, 1995). During such measurements the capillary was rocked to minimize the effects of preferred orientation. A flow meter was attached to the gas inlet line to ensure constant flow. Compressed atmospheric air and nitrogen were fed through the capillaries.
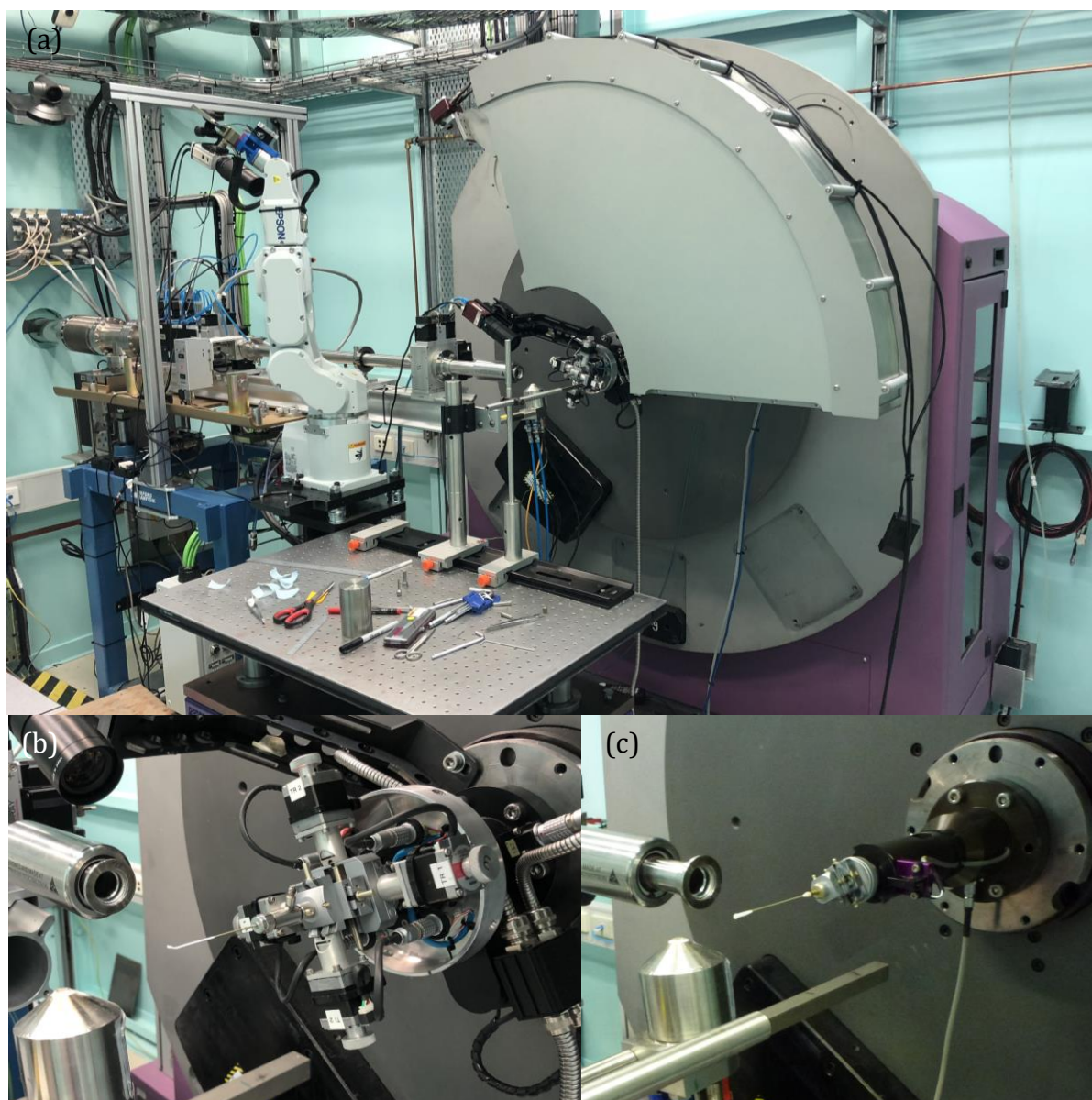
Figure 7.1. (a) Powder Diffraction beamline end station at the Australian Synchrotron. (b) (left) Norby Flow cell attached to the goniometer on the PD beamline end station setup for a gas flow experiment. (right) Goniometer and sealed capillary at the PD beamline end station at the Australian Synchrotron.

Each sample was heated room temperature to 850 °C at ramp rate of 5°C per minute and patterns were collected at 25 °C intervals. Data collection was commenced after a 60 second thermal equilibration period. Temperature was controlled using an FMB-Oxford hot air blower placed below the capillary. All sealed, Olympic Dam, N_2 and air flow samples were set up for data collection for either 400 seconds (Beverley) or 300 seconds (Olympic Dam and Ranger) at each of the two positions of the MYTHEN II microstrip detector. The 25% longer measurement time was used for Beverley samples to improve the signal to noise ratio.

7.3. Results and discussion

7.3.1. UOC results and discussion

Preliminary X-ray analysis

Analysis of the preliminary X-ray data, recorded in 2006, using the Rietveld method, revealed that the crystalline material in the samples from the Ranger and Olympic Dam mines was orthorhombic U_3O_8 and within the sensitivity of the data, both samples were single phase. There was no evidence in the data for the presence of any hydrated species. The diffraction pattern of the sample from the Beverley mine was distinctly different and could be fitted to a $UO_4 \cdot 2H_2O$ model. Rietveld analysis revealed a number of weak unfitted reflections that could be indexed to the presence of metaschoepite $(UO_2)_4O(OH)_6 \cdot 5H_2O$; sometimes described as $UO_3 \cdot 2H_2O$. The starting models used in the Rietveld refinements were taken from the literature: for metaschoepite, we used Weller et al., for orthorhombic U_3O_8 Loopstra, and for metastudtite, the orthorhombic model developed by Weck et al. was used (Loopstra, 1964; Weck et al., 2012; Weller et al., 2000). The phase composition was estimated to be $UO_4 \cdot 2H_2O$, 95.9(5) wt %, and α-$(UO_2)_4O(OH)_6 \cdot 5H_2O$ 4.1(3) wt % with $\chi2 = 2.34$. Refinements against the Beverley data with a single-phase model gave $\chi2 = 2.58$. As will be demonstrated below, during storage, these UOC samples underwent partial alteration due to interaction with atmospheric moisture.

Room-temperature structures and phases

Figure 7.2 shows Rietveld refinements for diffraction profiles measured at 25 °C for each of the three UOC samples studied. The phase compositions of these samples (Figure 7.2) are summarized in Table 7.1.
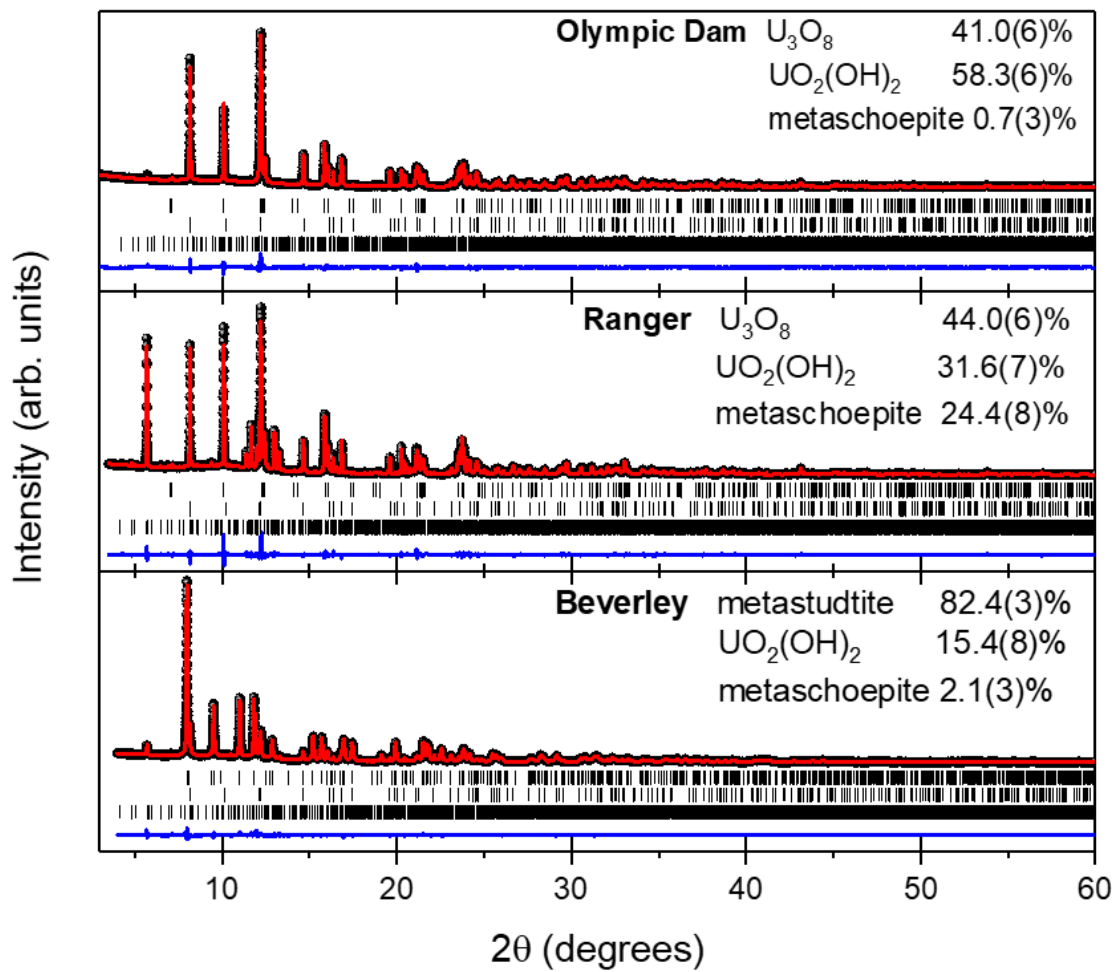
226

Figure 7.2. Room temperature S-XRD Rietveld refinement profiles for the three UOC samples studied. In each case the observed data is represented by the symbols, the continuous line through these is the fit and the lower continuous line is the difference between the observed and calculated profiles. The lower tick marks indicate the positions of the space group allowed reflections for the three phases, that are given in the same order as the compositions listed in each panel.

Sample	Phase	Wt %	SG	Lattice Parameters (Å)			Volume (Å²)
				a	*b*	*c*	
Olympic Dam	U_3O_8	40.98(6)	*C2mm*	6.7200(5)	11.9516(9)	4.1469(3)	333.06(8)
	$\alpha\text{-}UO_2(OH)_2$	58.34(6)	*Cmce*[*]	4.2801(3)	10.2346(8)	6.8802(6)	301.39(7)
	metaschoepite	0.68(3)	*Pbcn*	14.628(4)	13.961(4)	16.614(4)	3393.0(14)
Ranger	U_3O_8	44.00(6)	*C2mm*	6.7276(3)	11.9110(6)	4.1438(2)	332.05(5)
	$\alpha\text{-}UO_2(OH)_2$	31.63(7)	*Cmce*	4.2793(2)	10.2367(5)	6.8869(3)	301.69(4)
	metaschoepite	24.37(8)	*Pbcn*	14.6779(6)	13.9337(7)	16.6959(8)	3426.9(5)
Beverley	metastudtite	82.44(3)	*Pnma*	8.430(2)	8.787(2)	6.512(1)	482.4(3)
	$\alpha\text{-}UO_2(OH)_2$	15.43(8)	*Cmce*	4.2885(8)	10.252(2)	6.901(1)	303.4(2)
	metaschoepite	2.13(3)	*Pbcn*	14.625(3)	13.953(3)	16.559(3)	3379.0(19)

* Cmce is the recommended notation for Space Group 64, it replaced *Cmca* which is used in much of the literature.

Though the samples from both Ranger and Olympic Dam mines were found to be U_3O_8 in the preliminary X-ray analysis (conducted in 2006), the diffraction patterns of subsamples from the two aged (2017) samples are noticeably different. Analysis of the S-XRD patterns demonstrated that the two samples contained the same three phases, U_3O_8, $\alpha\text{-}UO_2(OH)_2$, and $\alpha\text{-}(UO_2)_4O(OH)_6 \cdot 5H_2O$ (metaschoepite); however, there are significant differences in the relative phase abundances. Interestingly, the differences are more significant than evident in the results obtained 2 years prior to using a conventional Cu source (Bruker D8 diffractometer) reported by Ditcham (Ditcham et al., 2016). These differences are shown below, Figures 7.3, shows the results for Olympic Dam, Figure 7.4 shows Ranger and Figure 7.5 shows Beverley. It appears that during a prolonged storage, U_3O_8 has reacted with the atmosphere and partially converted to $\alpha\text{-}UO2(OH)2$ and $\alpha\text{-}(UO_2)_4O(OH)_6 \cdot 5H_2O$. The presence of the latter, which is found naturally as the mineral metaschoepite, is consistent with the earlier work of Oerter et al. Brugger et al. recently described dehydrated schoepite as the mineral species paulscherrerite, with an empirical formula $UO_3 \cdot 1.02(H_2O)$ due to the presence of the metaschoepite contaminant (Table 7.2) (Brugger et al., 2011; Oerter et al., 2020; Wronkiewicz & Buck, 2018).
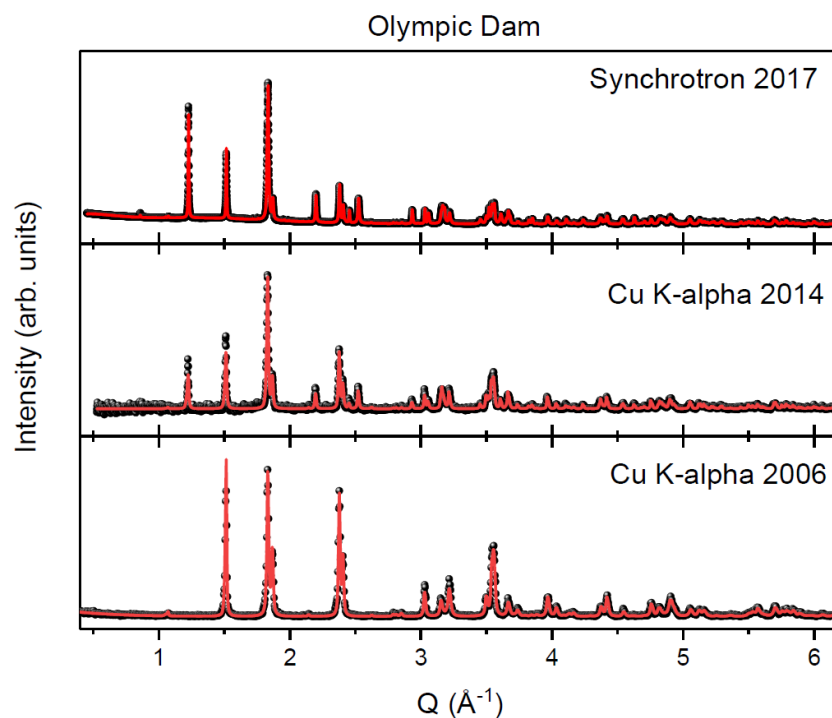
Figure 7.3. Comparison of Synchrotron and laboratory XRD profiles for UOC from Olympic Dam. The symbols represent the measured profiles and the solid line is the Rietveld fit. The full Q-range for the synchrotron profile is not shown. XRD measured in 2015 used a Bruker D8 X-ray diffractometer (Billerica, MA) with a Cu Xray tube (1.5418 Å) (40 kV, 40 mA) with a diffraction angle range of 10° > 2θ > 150°. In these measurements the samples were adhered onto double-sided carbon tape and mounted on Si single crystals
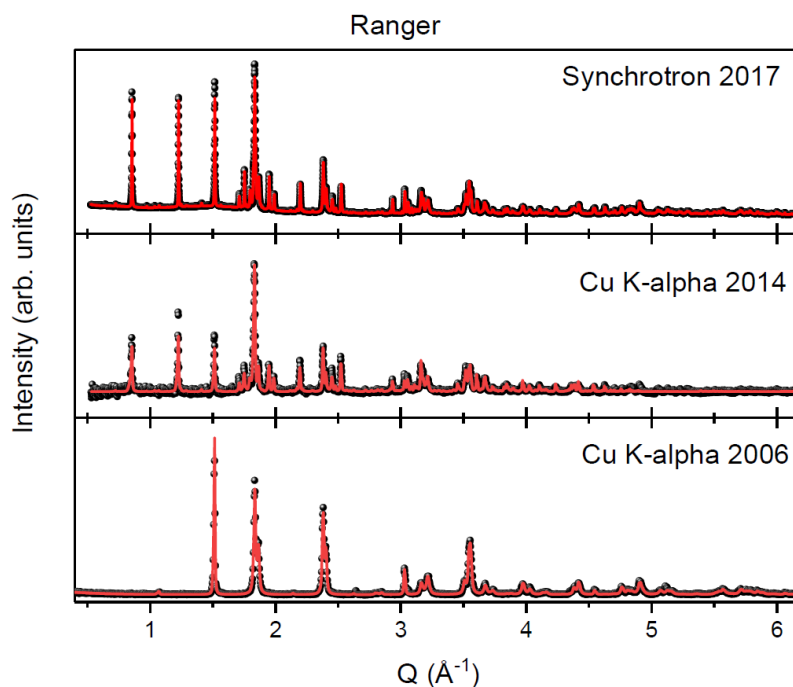

Figure 7.4. Comparison of Synchrotron and laboratory XRD profiles for UOC from Ranger. The symbols represent the measured profiles and the solid line is the Rietveld fit. The full Q-range for the synchrotron profile is not shown.
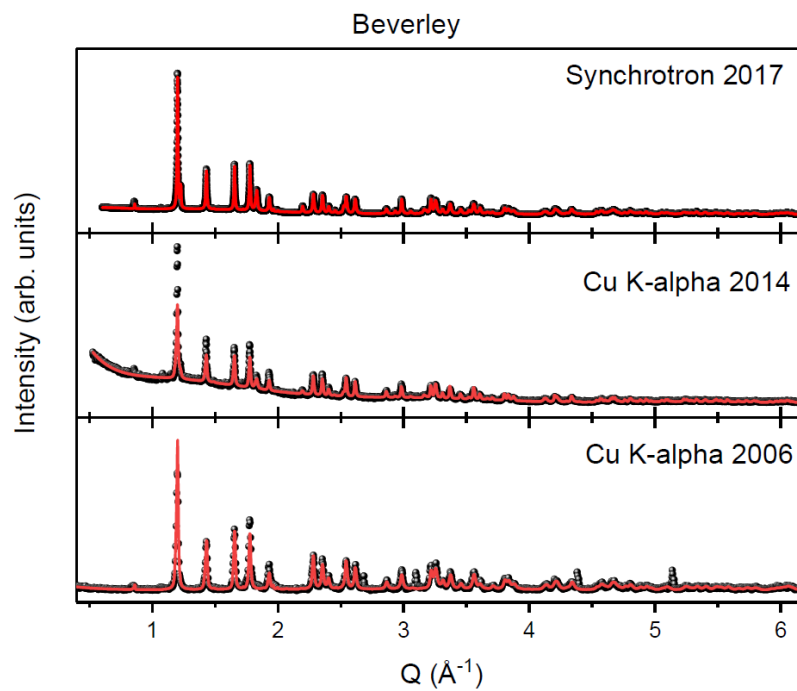
Figure 7.5. Comparison of Synchrotron and laboratory XRD profiles for UOC from Beverley. The symbols represent the measured profiles and the solid line is the Rietveld fit. The full Q-range for the synchrotron profile is not shown. Parasitic peaks from the sample holder are evident in the Cu profile.

Table 7.2. Refined Structural parameters for the crystalline phases identified in the three UOC samples. In all cases the listed lattice parameters correspond to the lowest temperature of the quoted range.

Temperature (°C)	Phase	SG	Lattice Parameters (Å)		
			a	b	c
Ranger					
	U_3O_8	*C2mm*	6.7276(3)	11.9110(6)	4.1438(2)
25-125	$UO_2(OH)_2$	*Cmce*	4.2793(2)	10.2367(5)	6.8869(3)
	metaschoepite	*Pbcn*	14.6779(6)	13.9337(7)	16.6959(8)
150-375	U_3O_8	*C2mm*	6.7484(10)	11.8851(16)	4.1449(6)
	$UO_2(OH)_2$	*Cmce*	4.2931(7)	10.2248(15)	6.9235(10)
400-525	U_3O_8	*P6̄2m*	6.8164(16)	6.8164(16)	4.1432(9)
550-750	U_3O_8	*P6̄2m*	6.8181(8)	6.8181(8)	4.1399(5)
	UO_3	*C2mm*	3.9593(5)	6.8930(10)	4.1594(5)
750-875	U_3O_8	*P6̄2m*	6.8270(6)	6.8270(6)	4.1383(3)
Olympic Dam					
	U_3O_8	*C2mm*	6.7200(5)	11.9516(9)	4.1469(3)
25-125	$UO_2(OH)_2$	*Cmce*	4.2801(3)	10.2346(8)	6.8802(6)
	metaschoepite	*Pbcn*	14.628(4)	13.961(4)	16.614(4)
150-375	U_3O_8	*C2mm*	6.7403(9)	11.916(2)	4.1463(5)
	$UO_2(OH)_2$	*Cmce*	4.2970(6)	10.204(1)	6.9239(9)
400-525	U_3O_8	*P6̄2m*	6.8106(19)	6.8106(19)	4.1416(11)
550-750	U_3O_8	*P6̄2m*	6.8174(9)	6.8174(9)	4.1402(5)
	UO_3	*C2mm*	3.9717(6)	6.8596(12)	4.1588(5)
750-875	U_3O_8	*P6̄2m*	6.8234(2)	6.8234(2)	4.1378(1)
Beverley					
25-125	metastudtite	*Pnma*	8.430(2)	8.787(2)	6.512(1)
	$UO_2(OH)_2$	*Cmce*	4.2885(8)	10.252(2)	6.901(1)
	metaschoepite	*Pbcn*	14.625(3)	13.953(3)	16.559(3)
150-175	metastudtite	*Pnma*	8.4317(17)	8.7764(18)	6.5259(14)
	$UO_2(OH)_2$	*Cmce*	4.3017(9)	10.220(2)	6.9408(15)
200-360	$UO_2(OH)_2$	*Cmce*	4.2729(6)	10.1570(4)	6.9242(9)
380-525	Amorphous				
550-700	UO_3	*C2mm*	3.9655(12)	6.863(3)	4.11557(13)
725-875	U_3O_8	*P6̄2m*	6.8578(20)	6.8578(20)	4.1664(12)

Tamasi et al. reported that ageing synthetic U_3O_8 samples resulted in partial transformation into metaschoepite ($UO_3 \cdot 2H_2O$) and schoepite ($UO_3 \cdot 2.25H_2O$) although they did not quantify the relative amounts of the constitute phases (Tamasi et al., 2015). Interestingly, these workers did not report evidence for the formation of α-$UO_2(OH)_2$, which is sometimes described as dehydrated schoepite (Finch et al., 1998). Tamasi et al. aged their samples for a shorter period, 1–3 years, than the more than 10 years of the present samples. That work, and the recent study of Hanson et al., highlighted that of the three key factors, aging time, temperature, and relative humidity, identified by Sweet, humidity appears to have the greatest impact on the transformations in U oxides (Hanson et al., 2021; Sweet et al., 2011). α-$UO_2(OH)_2$ is one of three polymorphs of uranyl dihydroxide, $UO_2(OH)_2$ (Siegel et al., 1972).

The U cation has 8-fold coordination with the hydroxyl groups forming a puckered hexagon that is capped by the uranyl groups. Representative refined structural parameters are given in Table 7.3.

Table 7.3. Atomic positions and fractional coordinates of α-UO$_2$(OH)$_2$ derived from refinement against the Ranger sample measured at 125 ^{0}C. Space group Cmce. Cmce is the recommended notation for SG 64, replacing Cmca. The values in italics are from reference 5 and correspond to values at room temperature. a = 4.2931(7) b = 10.225(2) c = 6.9235(11) Å Vol = 303.9(1) Å3 a = 4.242(1) b = 10.302(1) c = 6.868(1) Å Vol = 300.2 Å3.

Name	x	y	z	Ui/Ue*100
U	0	0	0	3.09(4)
	0	0	0	
O1	0	0.1612(9)	0.079(2)	4.2(4)
	0	0.158(5)	0.109(9)	
O2	0.5	-0.0657(9)	0.193(2)	7.3(5)
	0.5	-0.076(7)	0.154(10)	
H	0	0.351*	0.138*	2.0*
	0	0.351(10)	0.138(15)	

U-O(1) x 2 1.737(9) *1.79(5) Å*
U-O(2) x 4 2.617(7) *2.50(4) Å*
U-O(3) x 2 2.227(12) *2.51(7) Å*
O(1) – U- O(1) 180o *180 o*
* Not refined

That the metaschoepite is only a minor phase in the Olympic Dam sample and is considerably more abundant in the Ranger sample is remarkable because the two samples were prepared at around the same time (~2005) and have been stored under the same conditions (both in sealed containers in the same laboratory) until the measurements in 2017. It is worth noting that although the Rietveld refinements yield apparently very precise phase compositions, the sample volume analyzed in the S-XRD experiments is small leading to the possibility of some variation in the phase composition if the sample is not totally homogeneous. Three capillaries were studied for each UOC sample and these results, revealed relatively little inhomogeneity. The peaks from the main phases U$_3$O$_8$ and α-UO$_2$(OH)$_2$ were broader than expected from the instrumental resolution. Indeed, it was not possible to directly observe the symmetry lowering from hexagonal to orthorhombic for the U$_3$O$_8$ (Figure 7.6) phase. We will return to this point below. Despite the lack of resolved orthorhombic splitting in the profiles, the Rietveld refinements returned lattice parameters that are in excellent agreement with values reported previously by Miskowiec et al., Ackermann et al., and Loopstra, (Table 7.4) with the

small variation between the Olympic Dam and Ranger samples possibly indicating small differences in the oxygen stoichiometry (Ackermann et al., 1977; Loopstra, 1964; Miskowiec et al., 2020b).

Table 7.4. Refined Lattice Parameters for U_3O_8 at selected temperatures compared with some literature values (Ackermann et al., 1977; Loopstra, 1964; Miskowiec et al., 2020b).

T(°C)	Ref	a (Å)	b (Å)	c (Å)	Vol (Å³)
25	This work Ranger	6.7276(3)	11.9110(6)	4.1438(2)	332.05(4)
25	This Work Olympic Dam	6.7200(5)	11.9516(9)	4.1469(3)	333.06(8)
40	Mickowiec	6.721(3)	11.955(3)	4.147(3)	333.2(5)
23	Ackermann	6.726	11.961	4.149	333.785
23	Loopstra	6.717	11.968	4.148	333.453
360	This work Ranger	6.7860(10)	11.8368(18)	4.1432	332.80(15)
360	This Work Olympic Dam	6.8033(16)	11.804(2)	4.1427(8)	332.69(20)
355	Miskowiec	6.799(5)	11.817(5)	4.149(6)	332.7(1)
358	Ackermann	6.815	11.804	4.136	332.717

The presence of multiple phases in the UOC subsamples is presumably a result of the interaction of the surface of the particles with the atmosphere, resulting in a shell of the second phase coating the unreacted core of the initial phase. In such core/shell arrangements, the shell phase can be distinguished from the core region by its morphology, chemical composition, and/or crystal structure. Broadening of the diffraction peaks for either the core or shell phase can arise either due to size effects, or it may be a consequence of local strains induced by a mismatch between the core and shell lattice spacings.

As anticipated from the preliminary XRD analysis, conducted ~10 year prior to the S-XRD measurements, the sample from the Beverley mine contains metastudtite [$UO_2(\eta^2-O_2)(H_2O)_2$], ($UO_4 \cdot 2H_2O$) together with small amounts of $UO_2(OH)_2$ and metaschoepite. Studtite [$UO_2(\eta^2-O_2)(H_2O)_2$]·$2H_2O$ or $UO_4 \cdot 4H_2O$ and metastudtite [$UO_2(\eta^2-O_2)(H_2O)_2$] or $UO_4 \cdot 2H_2O$ are the only known naturally occurring uranyl peroxides and have been found on the surface of spent nuclear fuel and on depleted U munitions (Wang et al., 2016). Thomas et al. have reported that studtite transforms into the metastudtite between 75 and 175 °C and the reactivity of these peroxide species is of potential significance in the design and operation of any geological repository (Thomas et al., 2017). Mass balance calculations, based on the quantitative phase analysis and ideal stoichiometry for the phases, gave the following water

contents: Olympic Dam mine 3.6 wt % H_2O, Ranger mine 4.6 wt % H_2O, and Beverley mine 10.7 wt % H_2O. These results are in broad agreement with the thermogravimetric analyses of Ditcham et al. (Ditcham et al., 2016).

The results presented in Table 7.1 are a powerful illustration of the benefit of high-resolution S-XRD measurements. Ditcham et al. in 2016 had suggested the presence of $UO_2(OH)_2$ in the Ranger and Olympic Dam samples but had not quantified the amounts nor had they observed the presence of metaschoepite, despite this phase representing ~5 weight % of the Ranger sample. Likewise, they described the Beverley sample as containing studtite $UO_4 \cdot 4H_2O$ and metastudtite $UO_4 \cdot 2H_2O$ and did not comment on the presence of $UO_2(OH)_2$ (Figure 8.7) and metaschoepite.

Structural refinement of metastudtite

We are unaware of any previous high-resolution structural studies of metastudtite. Vitova et al. recently reported the structure from refinements against the PD data measured using a conventional (Cu Kα) X-ray source (Vitova et al., 2018). The cell volume from that work is statistically smaller than that observed here (480.88(7) versus 482.24(18) Å3), see Table 7.5. The cell volume for metastudtite refined in the present study shows weak thermal expansion on heating from RT to 125 °C to 482.98(31) Å3, suggesting there is no loss of water over this temperature range. The earlier structural refinements by Vitova et al. showed bending of the O=U=O moiety; this is not observed in the present refinements suggesting it was an artifact (Vitova et al., 2018). The U^{6+} cation in metastudtite is bonded to six oxygen atoms at the equatorial vertices of a distorted bipyramid that is capped by the two oxygens from the linear O=U=O uranyl group, see Figure 8.9. The O(1)-U-O(2) angle is 178.7(13)°. Four of the equatorial vertices are occupied by O(3) atoms, which correspond to two peroxide groups with O−O separation of 1.498(8) Å, the other two sides are occupied by the O(4) atoms of the water molecules. The two uranyl bond distances are not symmetry constrained to be equal and these are found to be statistically different 1.625(16) and 1.864(15) Å. Unequal uranyl bond distances have previously been reported for another U peroxide $Na[UO_2(O_2)_3]9H_2O$ as well as in Li_2UO_4 (Alcock, 1968; Gebert et al., 1978).

Table 7.5. Atomic positions and fractional coordinates of $[UO_2(\eta2\text{-}O_2)(H_2O)_2]$ (metastudite) obtained from refinement against the Beverley sample. The data were measured at 25 ^0C. Space group Pnma. a = 8.4297(16) b = 8.7874(17) c = 6.5118(12) Å Volume = 482.36(16) Å3

Atom	Site	x	y	z	Ui*100 Å³
U	4c	0.1263 (4)	0.25	0.7480(4)	2.138(18)
O1	4c	0.1779(20)	0.25	-0.0115(26)	1.05(13) †
O2	4c	0.0566(21)	0.25	0.4764(25)	1.05(13) †
O3	8d	0.6038(14)	0.8352(5)	0.3723(7)	1.05(13) †
O4	8d	0.1095(21)	0.9733(4)	0.7569(32)	1.05(13) †
H1	8d	0.127	0.584	0.889	2.5*
H2	8d	0.190	0.600	0.659	2.5*

* Not refined. † Constrained to be equal
U-O(1) x 1 1.625(16) Å
U-O(2) x 1 1.864(15) Å
U-O(3) x 2 2.231(10) Å
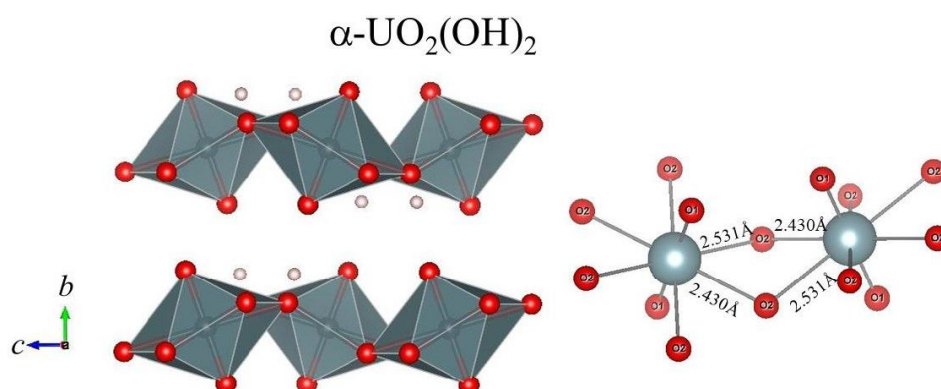U-O(4) x 2 2.520(10) Å

$\alpha\text{-}UO_2(OH)_2$

Figure 7.6. Representation of the $\alpha\text{-}UO_2(OH)_2$ structure. The U cations are at the centre of the O_8 polyhedra. The oxygen atoms are represented by the red spheres and the tans spheres in the LHS figure represent the hydrogen atoms.
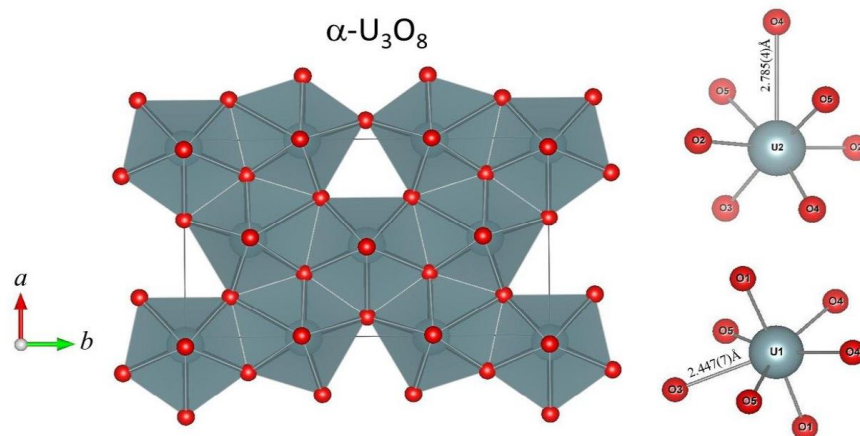
235

$\alpha\text{-}U_3O_8$

Figure 7.7. Representation of the α-U₃O₈ structure. The U cations are at the centre of the On polyhedral that are illustrated in the RHS figure. The oxygen atoms are represented by the red spheres.
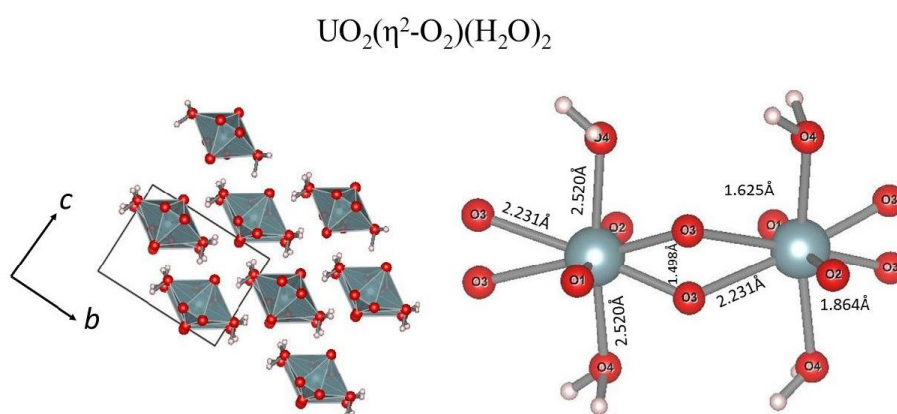
$UO_2(\eta^2\text{-}O_2)(H_2O)_2$

Figure 7.8. Representation of the [UO₂(η2-O₂)(H₂O)₂] (metastudtite). The U cations are at the centre of the O₈ polyhedra. The oxygen atoms are represented by the red spheres and the tans spheres represent the hydrogen atoms.

Temperature-dependent structures

Having established the phases present in each of the three samples at room temperature, the thermal transformations of these were then investigated using in situ S-XRD.

i.   Olympic Dam

The weak reflections indexed to the orthorhombic metaschoepite structure (space group Pbcn) observed in the sample from the Olympic Dam site were not observed in profiles measured at and above 150 °C. Finch et al. have previously reported that schoepite and metaschoepite can be distinguished by precise determination of unit cell parameters, with the partial loss of water resulting in a contraction of the b axis from ~14.2 to 14.0 Å with very little change in the a- and c-axes (Finch et al., 1998). The results presented in Table 7.1 point

236

to metaschoepite being the appropriate descriptor of the material present in this sample. Metaschoepite loses water when heated above ~100 °C, yielding a material described as "dehydrated schoepite" that appears to have the same structure as α-$UO_2(OH)_2$ (Finch et al., 1998). Examination of the profiles did not provide any evidence for the appearance of additional phases around 150 °C and so we propose that the metaschoepite has transformed into α-$UO_2(OH)_2$.

As the sample was heated to above 300 °C, the peaks from the $UO_2(OH)_2$ phase began to lose intensity, although the absolute intensity of the reflections from the U_3O_8 phase did not change, notwithstanding the coalescence of certain reflections due to the reduction in the orthorhombic splitting. This indicates that $UO_2(OH)_2$ transformed into an X-ray amorphous phase, rather than into U_3O_8. Although three broad weak unindexed peaks near 2θ = 11.95, 21.1, and 21.9° were observed in the profile measured at 400 °C, it is reasonable to conclude that between 400 and 550 °C, the only crystalline phase present is U_3O_8, and that this is accompanied by an appreciable amount of an amorphous phase.

The profile measured at 550 °C contains additional reflections that could be indexed to a second orthorhombic phase identified as α-UO_3. As this phase initially forms, there is no appreciable change in the intensity of the reflections from the U_3O_8 phase suggesting that the α-UO_3 results from the crystallization of the amorphous material formed by decomposition of $UO_2(OH)_2$. This hypothesis is supported by the observation that the weight percent of UO_3 in the sample between 600 and 700 °C is comparable to the amount of $UO_2(OH)_2$ present between 150 and 300 °C. Around 725 °C, the intensity of the reflections from the α-UO_3 phase begins to diminish and that from the U_3O_8 phase increases showing the conversion of α-UO_3 to U_3O_8 has occurred. Above 800 °C, the profiles were well produced with a single-phase hexagonal $P\bar{6}2m$ U_3O_8 model. Cooling the sample from 875 to 100 °C resulted in the transformation into the orthorhombic $C2mm$ U_3O_8 structure, confirming the $C2mm$ to $P\bar{6}2m$ transition to be reversible as noted by previous workers; no other phases were present in the profile measured at 100 °C (Figure 7.9) (Ackermann et al., 1977).
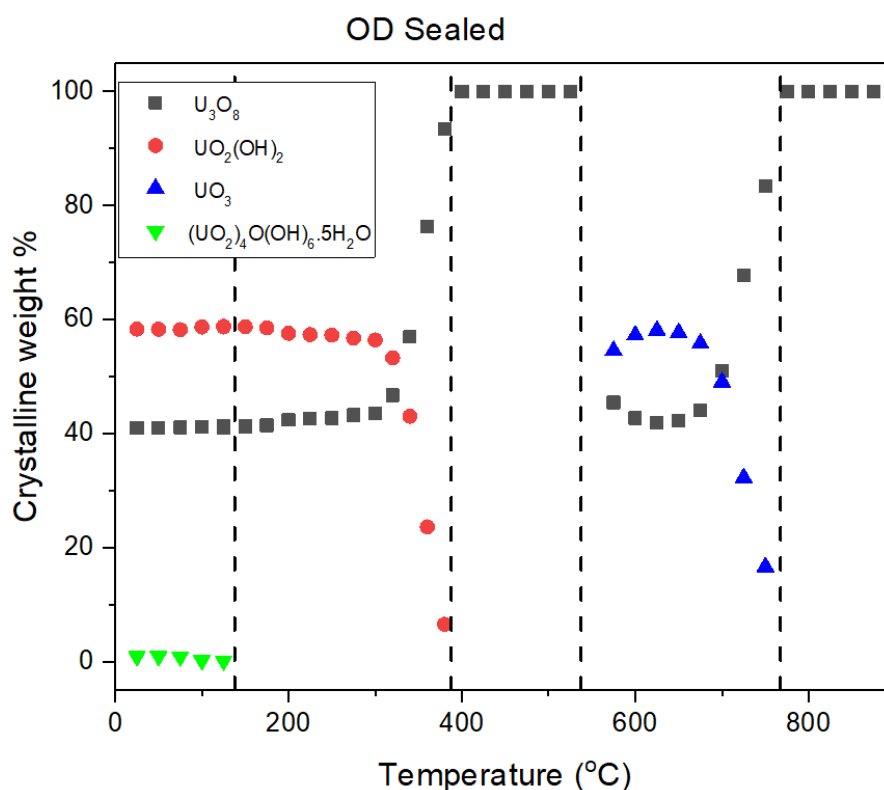
Figure 7.9. Crystalline weight fraction in Olympic Dam UOC as a function of temperature as estimated by Rietveld refinements. The ESDs from the Rietveld refinements are smaller than the symbols. The contribution of any amorphous material has been neglected in estimating the weight fractions. The dashed vertical lines indicate the temperatures were the phase components of the models used in the Rietveld refinements were altered. Below 400 ^oC the U_3O_8 structure is described by the orthorhombic space group C2mm and above this by the hexagonal space group P$\bar{6}$2m.

The peaks from the main phases U_3O_8 and $UO_2(OH)_2$ were, in the profile measured at room temperature, broader than expected from the instrumental resolution. Indeed, it was not possible to directly observe the symmetry lowering from hexagonal (PG P$\bar{6}$2m) to orthorhombic (SG C2mm) for the U_3O_8 phase (Figure 7.10). Such symmetry lowering is clear in the profile measured at 100 °C after heating the sample to 875 °C. The broadening of the peaks appears to be a consequence of water adsorption reducing the crystallinity of the material, as evidenced by the observation that a pattern measured in 2006 using a conventional (lower resolution) diffractometer showed diagnostic splitting of the hexagonal (110) reflection near d = 3.415 Å.
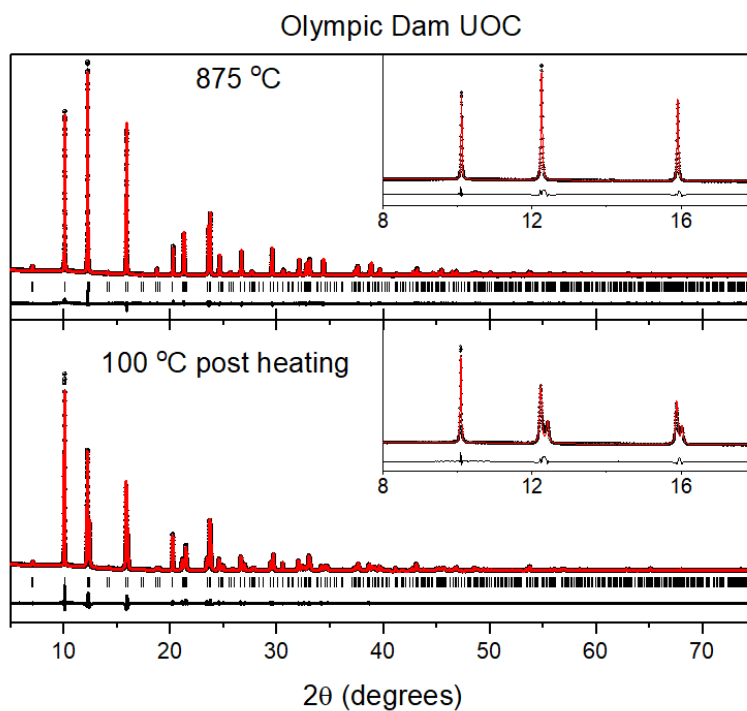
Figure 7.10. Representative examples of Rietveld refinements for Olympic Dam UOC. Data were collected on heating from RT to 875 ⁰C and then a small number of patterns were measured on cooling to 100 ⁰C. The insets highlight the splitting of reflections due to the lowering of symmetry to orthorhombic C2mm (at 100 ⁰C) from hexagonal P6̄2m (at 875 ⁰C).

The thermal expansion of the lattice parameters for the U_3O_8 phase, refined assuming orthorhombic symmetry, showed a marked change around 400 °C, see Figure 7.11. This is in good agreement with the reported temperature for the orthorhombic to hexagonal phase transition that is reported to occur around 350 °C (Miskowiec et al., 2020b).

Figure 7.11. Temperature dependence of the refined lattice parameters for the U_3O_8 phase present in the Olympic Dam UOC sample. The change in the rate of thermal expansion of the a-parameter at 400 ^0C is a consequence of the orthorhombic to hexagonal phase transition. The values shown in this figure were from refinements in SG C2mm below 400 ^0C and P6¯2m at 400 ^0C and above. Where not apparent the errors are smaller than the symbols.
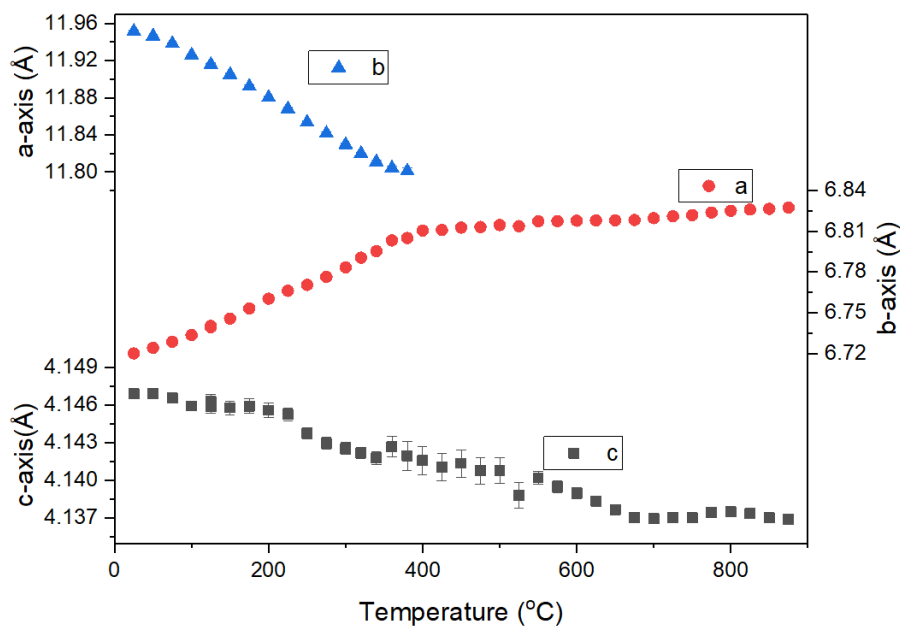
The minimum in cell volume of U_3O_8 around 325 °C was highlighted in the recent study by Miskowiec et al., as was the change around 220 °C (Miskowiec et al., 2020a). It was postulated that the latter is associated with an order–disorder transition, whereas the former is associated with the orthorhombic to hexagonal transition. The coexistence of multiple phases in the present sample and the transformations between these, which necessitates changes in the structural model, results in the greater scatter in Figure 7.12 compared to Figure 4 of Miskowiec et al. (Miskowiec et al., 2020a). There are no significant changes in the unit cell volume of the U_3O_8 phase between 25 and 875 °C, see Figure 7.12. This possibly reflects the very small absolute volume change over this temperature range (~0.3%), noting that the minimum in the unit cell volume around 350 °C mimics that seen in the work on a single-phase U_3O_8 sample by Miskowiec and coworkers (Miskowiec et al., 2020b).
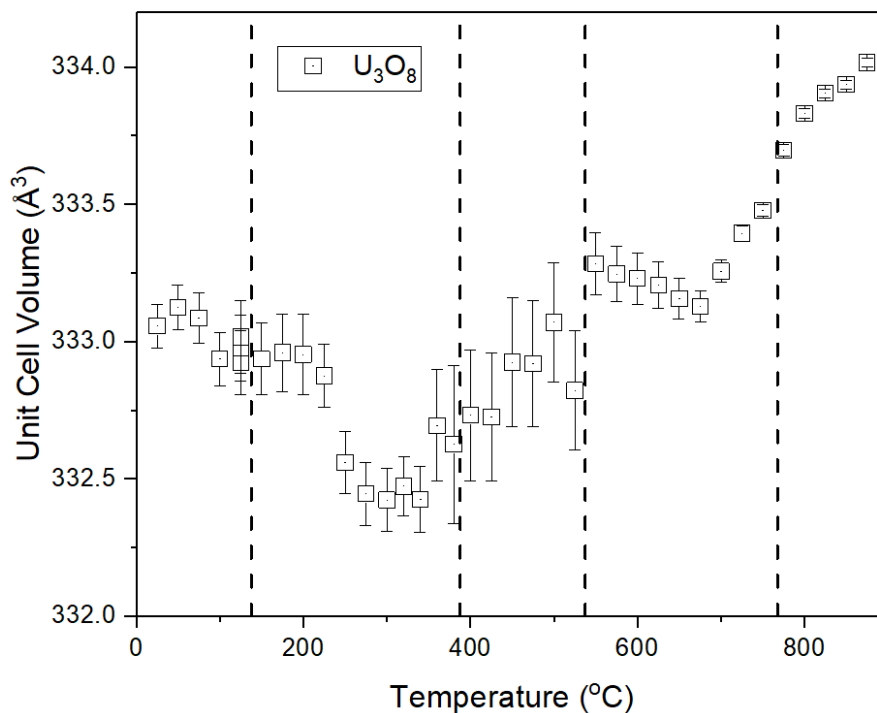
Figure 7.12. Temperature dependence of the unit cell volume for the U_3O_8 phase present in the Olympic dam UOC sample. The dashed lines indicate the temperatures where the phase composition changes.

ii.   Ranger

Although the absolute crystalline phase weight percentages observed in the Ranger sample are different to that found in the Olympic Dam sample, their thermal behavior is essentially identical. Figure 7.13 shows the loss of metaschoepite occurs at around 125 °C as was observed for the Olympic Dam sample. The loss of intensity of the reflections diagnostic of metaschoepite correlates with increased intensity of the reflections due to $UO_2(OH)_2$ validating the earlier assertion that metaschoepite transforms into $UO_2(OH)_2$ at around this temperature. Across this transition, the intensity of the reflections diagnostic of U_3O_8 remains essentially unchanged, an observation that is true for all patterns measured from room temperature to around 600 °C. At approximately 300 °C, the peaks due to $UO_2(OH)_2$ begin to lose intensity and these are no longer observed by 600 °C. Although this results in an increase in the crystalline weight percentage of the U_3O_8 phase, the peak intensities from this phase do not significantly change between 300 and 600 °C indicating that the absolute amount of U_3O_8 remains constant and that $UO_2(OH)_2$ transforms into an amorphous material. There is an increase in the intensity of the U_3O_8 peaks from around 700 °C as a consequence of the transformation from UO_3 into U_3O_8. In summary, the diffraction data reveal that

241

metaschoepite transforms into $UO_2(OH)_2$ around 125 °C. This is presumably associated with the loss of water of crystallization (Weck & Kim, 2014). At approximately 300 °C, $UO_2(OH)_2$ transforms into an amorphous phase, and this persists to about 600 °C at which point crystallization of UO_3 occurs. Finally, above approximately 750 °C, UO_4 is reduced to U_3O_8. At temperatures above 400 °C, U_3O_8 has a hexagonal structure that distorts to an orthorhombic structure when cooled below this, Figure 7.13.
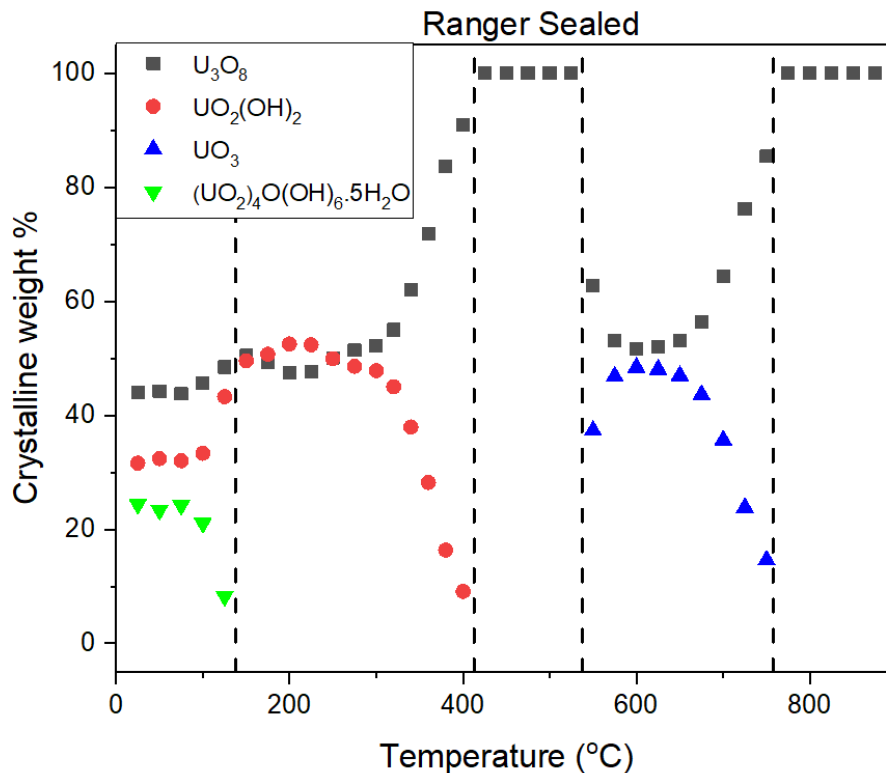
Figure 8.13. Crystalline weight fraction in Ranger Mine UOC as a function of temperature as estimated by Rietveld refinements. The ESDs from the Rietveld refinements are smaller than the symbols. The contribution of any amorphous material has been neglected in estimating the weight fractions. The dashed vertical lines indicate the temperatures were the phase components of the models used in the Rietveld refinements were altered. Below 400 ^0C the U_3O_8 structure is described by the orthorhombic space group C2mm and above this by the hexagonal space group P6̄2m.
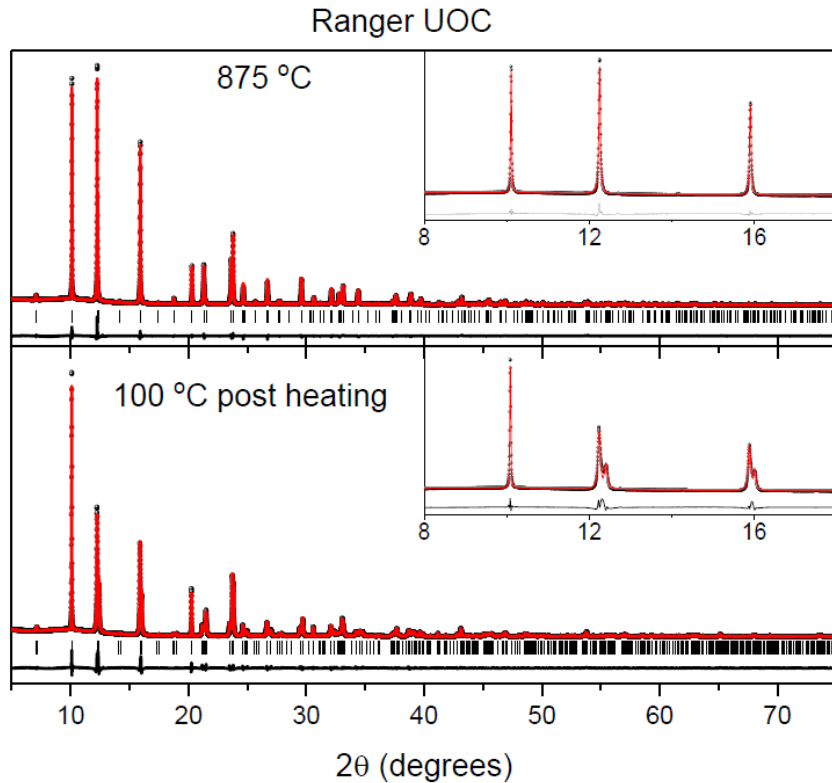
Figure 7.14. Rietveld refinements for Ranger UOC. Data was collected on heating from RT to 875 ^{0}C and on cooling to 100 ^{0}C. The insets highlight the noticeable splitting of reflections that are diagnostic of a lowering of symmetry from hexagonal P62m (at 875 ^{0}C) to orthorhombic C2mm (at 100 ^{0}C).

iii.   Beverley

As noted above, at room temperature, the sample from the Beverley mine consisted of 82.4(3) wt % metastudtite [$UO_2(\eta^2\text{-}O_2)(H_2O)_2$], or $UO_4 \cdot 2H_2O$, 15.4(8) wt % $UO_2(OH)_2$ together with trace amounts, 2.1(3) wt %, of metaschoepite. Heating the sample to around 125 °C resulted in the loss of the peak near 2θ = 5.91° (d = 7.312 Å), that is indexed as the (200) reflection of metaschoepite, which is the strongest peak for this phase (Finch et al., 1995). As seen for the Olympic Dam sample, there is no change in the intensity of the other peaks at around this temperature; however, it is believed that the metaschoepite transforms into α-$UO_2(OH)_2$. Further heating to around 200 °C results in the loss of intensity of the peaks due to the main metastudtite phase; however, this is not accompanied by any significant change in the intensity of the remaining peaks that are from α-$UO_2(OH)_2$. This indicates that metastudtite transforms into an amorphous material around 200 °C. It should be stressed that although α-$UO_2(OH)_2$ is the only crystalline phase present between around 250 and 400 °C, and therefore appears as 100% in Figure 7.15, based on the observed intensities of the persistent U_3O_8 phase, it is believed that only about 15% of the original sample remains

crystalline over this temperature range. Continued heating above 400 °C results in the loss of all resolved peaks and it is not until the sample is heated to above 550 °C that any well-resolved peaks re-emerge. That the α-UO$_2$(OH)$_2$ phase in the Beverley mine sample becomes amorphous around 400 °C is consistent with the results described above for the samples from the Ranger and Olympic Dam mines. Odoh et al. described heating metastudtite to 200 °C to form an X-ray amorphous phase, which they described as U$_2$O$_7$. Based on neutron pair distribution function analysis, it was concluded that this species retained the peroxide group of the starting phase (Odoh et al., 2016). Further heating of this U$_2$O$_7$ resulted in its decomposition with Odoh et al. concluding that UO$_3$ initially forms before ultimately transforming into U$_3$O$_8$. Our observations are consistent with this work, although we cannot comment on the nature of the amorphous species (Brincat et al., 2014; Leinders et al., 2020). Attempts to model the profiles measured around 600 °C to the hexagonal U$_3$O$_8$ model were unsuccessful, as there was no evidence for any intensity near $2\theta = 7.06°$ (d = 5.917 Å) that could be indexed to the hexagonal (100) reflection. It was concluded that at this temperature the α-UO$_3$ structure, which has the orthorhombic $C2mm$ space group, has formed. Different polymorphs of UO$_3$ can be obtained by altering the heating conditions, for example, flash heating UO$_2$(NO$_3$)·6H$_2$O in air to 450 °C, followed by prolonged annealing at the same temperature is reported to result in the formation of β-UO$_3$ that has a monoclinic structure (Manaud et al., 2020; Spano, Shields, et al., 2020). Independently, Tamasi et al. described heating UO$_2$(O$_2$)·xH$_2$O (studtite) in air to 400 °C to form amorphous UO$_3$ (A-UO$_3$) that transformed into U$_3$O$_8$ upon further heating to 800 °C (Tamasi et al., 2015). It would be interesting to establish if the two amorphous phases contain the same functional groups. Spano and co-workers have recently studied the dehydration of metastudtite and observed the co-existence of mixed-phase UOx dehydration products of metastudtite and concluded that the decomposition involved the conversion of some uranyl centers from hexagonal to pentagonal bipyramidal coordination units via peroxide liberation (Spano et al., 2020). Tamasi et al. demonstrated that heating α-UO$_3$ at 485 °C under air for 96 h converted this to α-UO$_3$; this is a comparable temperature to where the emergence of reflections reappeared in our in situ diffraction data (Tamasi et al., 2017). As the temperature is progressively increased, topotactic reduction of the α-UO$_3$ phase occurs resulting in the formation of crystalline U$_3$O$_8$ with the hexagonal structure as evident from the appearance of a peak near $2\theta = 7.06°$. The U$_3$O$_8$ phase remains the only crystalline phase present upon cooling the sample back to 100

°C. It is worth noting that the diffraction pattern measured at 100 °C for this sample does not show well-resolved orthorhombic splitting, Figure 7.16, suggesting the presence of considerable strain remains in this sample. Although the orthorhombic α-U_3O_8 polymorph is usually observed at room temperature, slow cooling has been shown to result in the formation of β-U_3O_8, the structure of which is described in SG Cmcm. β-U_3O_8 has a doubling of the c-axis, and there is no evidence for this in the S-XRD profiles. It is postulated that annealing for a longer period of time would result in the emergence of a highly crystalline sample as was observed for the other two samples studied in this work.
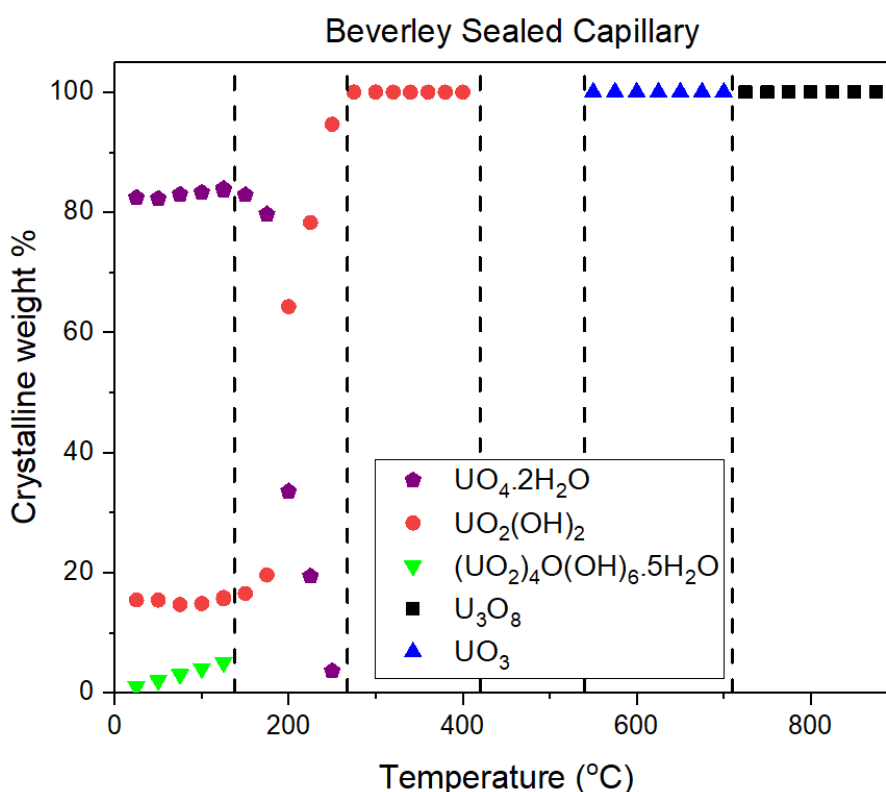
Figure 7.15. Crystalline weight fraction in Beverley UOC as a function of temperature as estimated by Rietveld refinements. The ESDs from the Rietveld refinements are smaller than the symbols. The contribution of any amorphous material has been neglected in estimating the weight fractions. The dashed vertical lines indicate the temperatures were the phase components of the models used in the Rietveld refinements were altered. Below 400 ^{0}C the U_3O_8 structure is described by the orthorhombic space group C2mm and above this by the hexagonal space group P6̄2m.
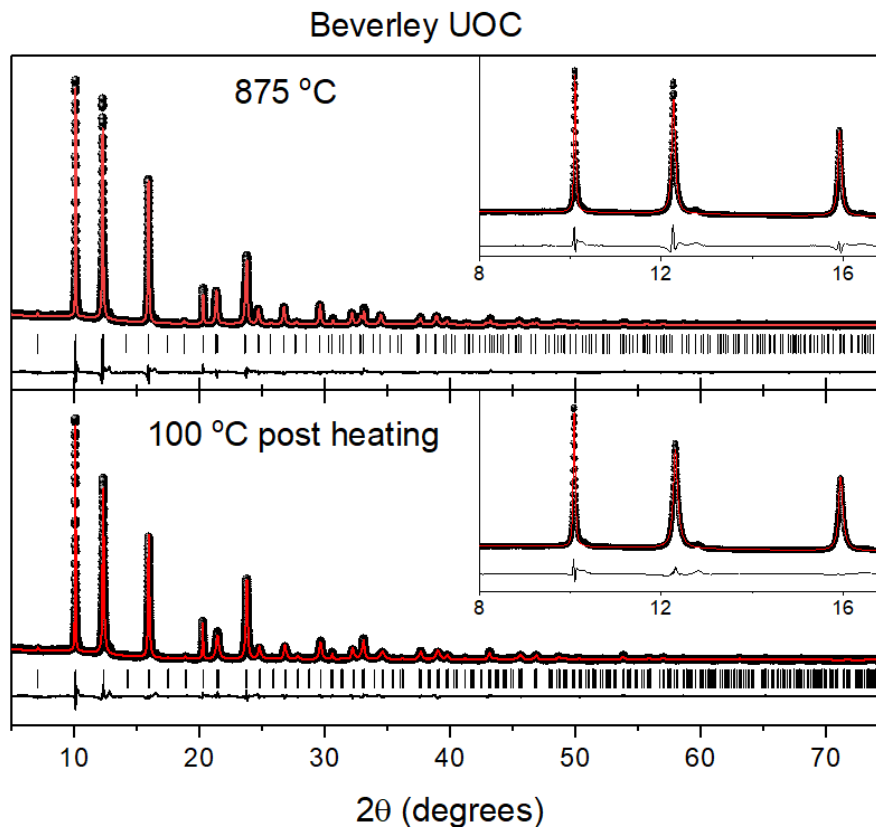
Figure 7.16. Rietveld refinements for Beverley UOC. Data was collected on heating from RT to 875 ⁰C and on cooling to 100 ⁰C. The insets highlight the absence of any noticeable splitting of reflections that are diagnostic of a lowering of symmetry from hexagonal P6⁻2m (at 875 ⁰C) to orthorhombic C2mm (at 100 ⁰C).

Experimental observations

Although thermal treatment did not result in any noticeable change in the dark green colour of the two samples obtained from the Olympic Dam and Ranger mines, the Beverley sample showed two distinct colour changes over the heating cycle to 850 °C. The initial yellow sample changed to dark orange on heating to 400 °C, which is consistent with the phase transition to the amorphous phase, and then to dark green as a result of the formation of the U_3O_8 phase. These colour changes are evident in the capillaries after analysis (Figure 7.17., a). The orange and yellow colour observed throughout the reaction was observable in the capillaries after analysis. Figure 7.17 (b) shows the Beverley sample colour prior to heating and Figure 7.17 (c) shows the Beverley sample after heating to 575 °C. When the sample of UOC (U_3O_8) was heated there was a glowing pink colour observed from the sample shown in Figure 7.17 (d).
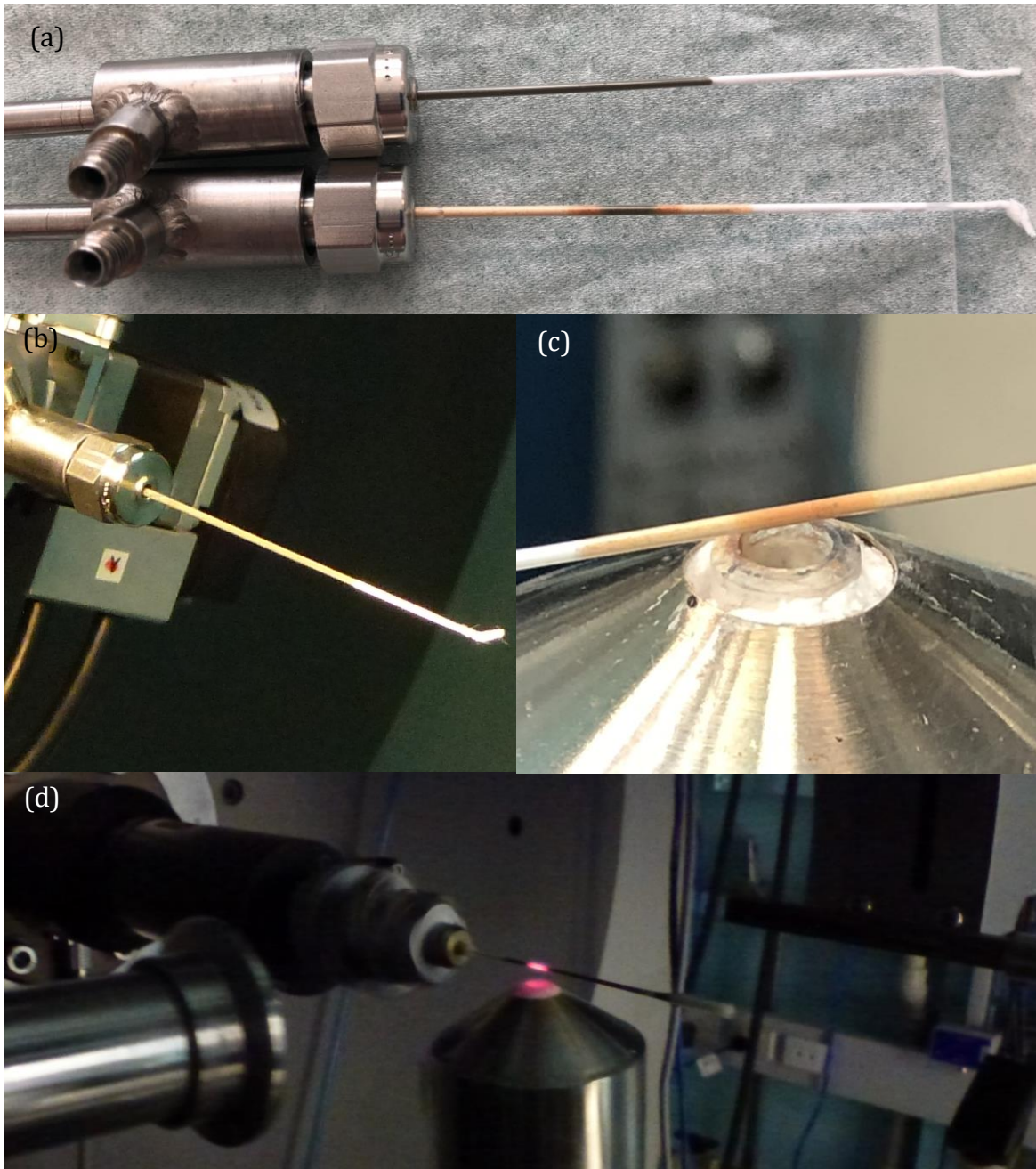
Figure 7.17. (a) UOC samples in 0.8 mm quartz capillaries, U_3O_8 sample (top), Beverley Peroxide sample after heating (bottom). (b) peroxide sample before analysis, (c) Beverley sample 0.8 mm capillary, Air flow, heated to amorphous phase. (right) (d) U_3O_8 heated to 800 °C.

7.4. Conclusions

Rietveld refinements of the S-XRD data of UOCs from three Australian uranium mines show that the UOCs have undergone alteration and hydration during over a decade of storage under laboratory conditions. The UOC from Olympic Dam and Ranger, which was U_3O_8 when

produced has altered to a mixture of U_3O_8, α-$UO_2(OH)_2$ and α-$(UO_2)_4O(OH)_6 \cdot 5H_2O$. The UOC from the Beverley Mine was metastudtite [$UO_2(\eta^2$-$O_2)(H_2O)_2$], ($UO_4 \cdot 2H_2O$) when first produced and during a prolonged storage has also altered to α-$UO_2(OH)_2$ and α-$(UO_2)_4O(OH)_6 \cdot 5H_2O$. This work has not attempted to identify the relative importance of the three key factors influencing the hydrolysis-induced transformations in uranium oxides identified by Sweet, namely aging time, temperature, and relative humidity, and we note that relative humidity reported by Tamasi et al. appears to have the greatest impact on the transformations in uranium oxides (Sweet et al., 2011; Tamasi et al., 2015).

The temperature-induced phase transitions in the three UOC samples have been established using variable temperature synchrotron X-ray PD. Two of the samples, from the Olympic Dam and Ranger mines, had been calcined as their final processing step yielding U_3O_8. The third sample from Beverley mine had been precipitated through the addition of peroxide and this produces metastudite [$UO_2(\eta^2$-$O_2)(H_2O)^2$] or $UO_4 \cdot 2H_2O$. The thermal behavior of the aged Olympic Dam and Ranger samples was very similar. At room temperature, both samples contained a mixture of three phases namely U_3O_8 (*C2mm*), α-$UO_2(OH)_2$ (*Cmce*), and metaschoepite $(UO_2)_4O(OH)_6 \cdot 5H_2O$ (*Pbcn*), although the relative abundances of these three phases were different. The Ranger sample contained much more metaschoepite than the sample sourced from the Olympic Dam mine. Through a combination of Rietveld analysis and examination of the temperature dependence of individual reflections, the sequence of transitions in both samples upon heating appears to be metaschoepite decomposes around 125 °C to an amorphous phase, and α-$UO_2(OH)_2$ also transforms into an amorphous state around 400 °C. Any similarity between the two amorphous phases formed from metaschoepite or α-$UO_2(OH)_2$ was not established. Around 575 °C, the amorphous material crystallizes, initially as α-UO_3 that converts to β-U_3O_8. The coexistence of U_3O_8 and metaschoepite has been noted previously, for example, in the work of Tamasi et al. Although α-$UO_2(OH)_2$ is described as "dehydrated schoepite" and is reported to be formed by heating metaschoepite to around 450 K (180 °C), there does not appear to be an obvious topology relationship between the two structures, and the metaschoepite structure contains layers of corner-shared pentagonal bipyramids, whereas α-$UO_2(OH)_2$ has hexagonal bipyramids (Finch et al., 1998; Hoekstra & Siegel, 1973).

We propose that metaschoepite develops by the corrosion of the U_3O_8 particles in a core−shell type model. Metaschoepite is described as being stable at room temperature and does not being stable (Finch et al., 1998). Thus, it is unlikely that the shell of metaschoepite that forms on the surface of the U_3O_8 crystallites transforms into α-$UO_2(OH)_2$, rather we speculate that it develops at the interface between U_3O_8 and metaschoepite. Irrespective of the mechanism, the core−shell model could account for the broadening of the diffraction peaks of the U_3O_8 evident in the samples.

The Beverley UOC sample was predominantly metastudtite ($UO_2 \cdot 2H_2O$ SG Pnma) together with small amounts of α-$UO_2(OH)_2$ and metaschoepite. The coexistence of the latter two phases in this sample points to metaschoepite being a precursor to the formation of α-$UO_2(OH)_2$. The in-situ diffraction data show that upon heating, $UO_2 \cdot 2H_2O$ transforms into an amorphous phase, previously described as U_2O_7, and then crystallizes as UO_3 before transforming into U_3O_8.

Chapter 8. Thesis conclusions and recommendations

This thesis expanded the knowledge on Australia's uranium in both an environmental and nuclear security context. This thesis has expanded the available dataset of radionuclide concentration ratios for Australian native vegetation in the arid environment. This thesis has also established the crystalline phases of aged UOC samples to expand our understanding of these vital samples for an Australian nuclear security context.

The transfer of radionuclides from soil to vegetation is complex and depends on many variables including the soil type; organic and clay components, which radionuclides are or interest, and the vegetation species of interest (Hegazy & Emam, 2010). Site specific concentration ratios have been proposed within this thesis (section 5.3) for the use within ERICA for radiological risk assessment for Australian native species within the arid environment. The CRs determined for the Olympic Dam region vary significantly from the default CRs within the WTD. Therefore, the CRs proposed in this thesis are recommended to be used for assessments within this region. The CRs determined from the Flinders Ranges region were in good agreement with the CRs from the WTD, therefore, the default values in ERICA are appropriate for assessments within this location. As both sites are within arid Australia and have vastly different CRs, this further emphasises the need for site specific CRs for radiological impact assessments. The Olympic Dam and Flinders Ranges regions, offer two circumstantially different opportunities for comparison within the same climate due to the difference in natural geology and surface mining operations. As the Olympic Dam region is primarily influenced by depositional radionuclides and dust, while the Flinders Ranges region has limited opportunities for radionuclide deposition. The natural background radiation at the Flinders Ranges region is elevated due to the natural geology of the region. Further research into the Flinders Ranges radionuclide samples would be useful to determine the estimated dose using the ERICA tool. This present research was unable to obtain sufficient data to perform ERICA assessments on the Flinders ranges regions.

Considering the unique environment at the Olympic Dam region, it was necessary to analyse samples using both bulk and spatial techniques, this enabled a thorough understanding of the radionuclide concentrations and distributions at the site. The bulk analysis of vegetation and soil provided the data necessary to calculate the CRs used within the internationally accepted radiological risk assessment tool ERICA. Bulk analysis also provided bulk quantitative soil and

vegetation activity concentration data for the arid Australian environment. The increase in the available CR data for the arid Australian region is of interest due to the lack of currently available data (Hirth, 2014). The majority of the measured radionuclide data from the Olympic Dam site was very low level, near the level of quantitation, this makes assessments difficult and leads to wide variations in CRs. However the activity concentrations were comparable to worldwide background concentrations (UNSCEAR, 2000). For the Olympic Dam region, the samples were also analysed further, spatial analysis of both vegetation and stratified soil was performed. This provided a more detailed analysis of where the radionuclides were accumulating within the vegetation. Spatial analysis of soil provided valuable information on the distribution of radioactivity within samples. The distribution of radioactivity throughout the depth of the soil samples at sites near surface operations shows a higher amount of radioactivity in comparison to samples t a lower depth. These data were in good agreement with the quantitative gamma spectroscopy data that show a gradient of activity. The soil samples from within the Olympic Dam mining lease area contained radioactive particles, this is likely from the ore stockpiles or slag from the ore processing stream and are unlikely to be in a bioavailable state.

The identification of the different radionuclides present within the samples has shown that there is disequilibrium within the Olympic Dam samples. Especially following radon and the radon progeny. This is likely due to radon release and fallout of the progeny. The dust deposition and radon progeny fallout are likely an increased source of radionuclides for the vegetation within the environment as the surface soil of 0-2 cm is generally higher in activity in comparison to lower depth intervals. Therefore, the 0-10 cm sampling method for soils when calculating concentration ratios is appropriate as long as the site does not have an increased likelihood of being affected by dust deposition. In the case of the sites within the Olympic Dam mining lease area, this should be considered independently to the 0-10 accepted method as it is not appropriate for the site.

Further research into understanding the fallout and dust deposition for the Olympic Dam site could be the answer to the variation in CRs. If work could be performed to produce a model to understand the dust deposition and radon emanation and resulting radioactive disequilibrium in the environment. This may be more convenient instead of individually

collecting and analysing samples to determine CRs. This would provide understanding into the mechanisms, rather than requiring extensive site specific datasets (Hirth, 2014).

This research within this thesis showed that the effect of the ^{210}Po volatility on alpha spectroscopy sample digestion is negligible when comparing the extraction from UTEVA column effluent when dealing with complex sample matrices. Further research could be undertaken in this area to further understand how the volatility is influenced when in aqueous form in comparison to a dried form in a complex matrix.

The alpha-particle radiography technique was developed for vegetation samples. Due to the low activity of the radiation in the samples of vegetation it has been shown using alpha-particle radiography that it is very unlikely that ionising radiation is causing damage to the vegetation samples analysed within this research. Alpha tracks were observed and the tracks resulting from the decay from the ^{222}Rn and daughters as ^{218}Po, ^{214}Pb and ^{214}Bi have been identified within the samples. Further research into using this technique semi-quantitatively may be possible. A further analysis of samples before and after 38-days following sample collection may provide some insight as to the radionuclide decay from radon progeny. Further work in this area could extend to exploring 3-dimensional analysis. As the samples of leaves were cut with a microtome, for samples with a higher activity, a 3-dimensional view of the radionuclide location may be possible. Spatially resolved locations of the radiation from the alpha particle analysis shows that the majority of the radiation is found near the cuticle of the leaf, this indicates that for Australian native shrubs the main intake method is from the foliar transport, either through the cuticle or stomata. This is consistent with the fact that the *Dodonaea viscosa* samples had overall higher activity in comparison to the *Acacia ligulata* species and the *Dodonaea viscosa* has more penetrable leaf cells. Further work with the alpha-particle radiography analysis could include a controlled growth experiment, where plants could be grown in a radon chamber in parallel to plants grown with U spiked soil. Where the alpha-particle radiography results of these two different conditions would likely provide great insight as to how the radionuclides enter the vegetation.

In order to increase Australia's nuclear security, characterisation of the UOC produced in Australia needs to be well established. This research has determined the crystalline phases that are present within UOC samples from Olympic Dam, Ranger and Beverley. Rietveld refinements of the S-XRD data of show that the UOCs have undergone alteration and hydration during over a decade of storage under laboratory conditions. The phase transitions at variable temperatures have also been established for each sample. This research has also proposed a core-shell model which describes the development of metaschoepite from the corrosion of the U_3O_8. We speculate that α-$UO_2(OH)_2$ develops at the interface between U_3O_8 and metaschoepite. Irrespective of the mechanism, the core–shell model could account for the broadening of the diffraction. UOC production is currently the final step in the nuclear fuel cycle that Australia is involved in. Therefore, the importance of thoroughly understanding the characteristics of Australia's UOCs is of vital importance. Future directions in this space would be to continue the ageing study over a longer period of time and to establish the crystalline profiles for future UOCs that result from future uranium mines within Australia.

References

(Canberra), M. T. (2016). Germanium Detectors. In.

Ackermann, R., Chang, A., & Sorrell, C. A. (1977). Thermal expansion and phase transformations of the U3O8– z phase in air. *Journal of Inorganic and Nuclear Chemistry*

39(1), 75-85.

Adekola, A., Colaresi, J., Douwen, J., Jäderström, H., Mueller, W., Yocum, K., & Carmichael, K. (2016). Characteristic performance evaluation of a new SAGe well detector for small and large sample geometries. *IEEE Transactions on Nuclear Science, 63*(3), 1570-1577.

Agazzi, A., & Pirola, C. (2000). Fundamentals, methods and future trends of environmental microwave sample preparation. *Microchemical Journal, 67*(1), 337-341.

Aitken, M. J. (1985). *Thermoluminescence Dating*: Academic Press.

Al-Shboul, K. F., Alali, A. E., AL-Khodire, H. Y., Batayneh, I. M., & Al-Shurafat, A. W. (2017). Assessment of secular equilibrium and determination of natural and artificial radionuclide concentrations in the zone surrounding the site of the first nuclear reactor in Jordan. *Journal of Radioanalytical and Nuclear Chemistry*

314(2), 1353-1360.

Alcock, N. W. (1968). The crystal and molecular structure of sodium uranyl triperoxide. *Journal of the Chemical Society A: Inorganic, Physical, Theoretical*(0), 1588-1594. doi:10.1039/J19680001588

Amoli, H. S., Barker, J., & Flowers, A. (2007). Closed vessels microwave digestion method for uranium analysis of soils using alpha-spectroscopy. *Journal of radioanalytical and nuclear chemistry*

273(2), 281-284.

Andersson, P., Garnier-Laplace, J., Beresford, N. A., Copplestone, D., Howard, B. J., Howe, P., . . . Whitehouse, P. (2009). Protection of the environment from ionising radiation in a regulatory context (PROTECT): proposed numerical benchmark values. *Journal of Environmental Radioactivity*

100(12), 1100-1108.

ANSTO. (2016). Neutron Activation Analysis (NAA) client information. Retrieved from http://www.ansto.gov.au/cs/groups/corporate/documents/document/mdaw/mda2/~edisp/acs014938.pdf

Arnold, J., Gianetti, T. L., & Kashtan, Y. (2014). Thorium lends a fiery hand. *Nature Chemistry, 6*(6), 554-554.

Asai, S., & Limbeck, A. (2015). LA-ICP-MS of rare earth elements concentrated in cation-exchange resin particles for origin attribution of uranium ore concentrate. *Talanta, 135*, 41-49.

Australian Government, B. o. M. (2020). Climate statistics for Australian locations *Summary Statistics Roxby Downs (Olympic Dam Aerodrome).* Retrieved from http://www.bom.gov.au/climate/averages/tables/cw_016096.shtml

Basunia, M., Morrell, J., Uddin, M., Voyles, A., Nesaraja, C., Bernstein, L., . . . Qaim, S. (2020). Resolution of a discrepancy in the γ-ray emission probability from the β decay of Ce g 137. *Physical Review C, 101*(6), 064619.

Becker, J. S. (2005). Inductively coupled plasma mass spectrometry (ICP-MS) and laser ablation ICP-MS for isotope analysis of long-lived radionuclides. *International Journal of Mass Spectrometry, 242*(2), 183-195.

Becker, J. S. (2005). Trace and ultratrace analysis in liquids by atomic spectrometry. *TrAC Trends in Analytical Chemistry, 24*(3), 243-254.

Bennett, J. (2008). Commissioning of NAA at the new OPAL reactor in Australia. *Journal of Radioanalytical and Nuclear Chemistry, 278*(3), 671-673.

Beresford, N. (2010). The transfer of radionuclides to wildlife. In: Springer.

Beresford, N., Brown, J., Copplestone, D., Garnier-Laplace, J., Howard, B., Larsson, C.-M., . . . Zinger, I. (2007). D-ERICA: An integrated approach to the assessment and management of environmental risk from ionising radiation. Description of purpose, methodology and application.

Beresford, N. A., Barnett, C. L., Howard, B. J., Scott, W. A., Brown, J., & Copplestone, D. (2008). Derivation of transfer parameters for use within the ERICA Tool and the default concentration ratios for terrestrial biota. *Journal of environmental radioactivity, 99*(9), 1393-1407.

Beresford, N. A., Horemans, N., Copplestone, D., Raines, K. E., Orizaola, G., Wood, M. D., . . . Tinsley, M. C. (2020). Towards solving a scientific controversy-The effects of ionising radiation on the environment. *Journal of environmental radioactivity 211*.

Billiton, B. (2013). *Monitoring Program - Airborne Emissions.*

Billiton, B. (2016). *Monitoring Program - Flora*. Retrieved from

Boghi, A., Roose, T., & Kirk, G. J. (2018). A model of uranium uptake by plant roots allowing for root-induced changes in the soil. *Environmental Science & Technology*.

Boisvert, J. B., Rossi, M. E., Ehrig, K., & Deutsch, C. V. (2013). Geometallurgical modeling at Olympic dam mine, South Australia. *Mathematical Geosciences, 45*(8), 901-925.

Bowell, R., Grogan, J., Hutton-Ashkenny, M., Brough, C., Penman, K., & Sapsford, D. (2011). Geometallurgy of uranium deposits. *Minerals Engineering, 24*(12), 1305-1313.

Brincat, N. A., Parker, S. C., Molinari, M., Allen, G. C., & Storr, M. T. (2014). Ab initio investigation of the UO3 polymorphs: Structural properties and thermodynamic stability. *Inorganic Chemistry, 53*(23), 12253-12264.

Britton, R., Davies, A. J. N. I., Methods in Physics Research Section A: Accelerators, S., Detectors, & Equipment, A. (2015). Characterisation of a SAGe well detector using GEANT4 and LabSOCS. *786*, 12-16.

Bronson, F. (2003). Validation of the accuracy of the LabSOCS software for mathematical efficiency calibration of Ge detectors for typical laboratory samples. *Journal of Radioanalytical and Nuclear Chemistry, 255*(1), 137-141.

Brooker, G. M., Scheding, S., Bishop, M. V., & Hennessy, R. C. (2005). Development and application of millimeter wave radar sensors for underground mining. *IEEE Sensors journal, 5*(6), 1270-1280.

Brookhaven. National Nuclear Data Center. Retrieved from https://www.nndc.bnl.gov/

Brown, J., Alfonso, B., Avila, R., Beresford, N. A., Copplestone, D., & Hosseini, A. (2016). A new version of the ERICA tool to facilitate impact assessments of radioactivity on wild plants and animals. *Journal of environmental radioactivity, 153*, 141-148.

Brown, J., Alfonso, B., Avila, R., Beresford, N. A., Copplestone, D., Pröhl, G., & Ulanovsky, A. (2008). The ERICA tool. *Journal of environmental radioactivity, 99*(9), 1371-1383.

Brugger, J., Long, N., McPhail, D., & Plimer, I. (2005). An active amagmatic hydrothermal system: the Paralana hot springs, Northern Flinders Ranges, South Australia. *Chemical Geology, 222*(1-2), 35-64.

Brugger, J., Meisser, N., Etschmann, B., Ansermet, S., & Pring, A. (2011). Paulscherrerite from the number 2 workings, Mount Painter inlier, Northern Flinders Ranges, South Australia:"dehydrated schoepite" is a mineral after all. *American Mineralogist, 96*(2-3), 229-240.

Bürger, S., Boulyga, S., Peńkin, M., Bostick, D., Jovanovic, S., Lindvall, R., . . . Riciputi, L. (2014). Quantifying multiple trace elements in uranium ore concentrates: an interlaboratory comparison. *Journal of Radioanalytical and Nuclear Chemistry, 301*(3), 711-729.

Cadieux, J., Fugate, G., & King, G. (2015). An alpha–gamma coincidence spectrometer based on the photon–electron rejecting alpha liquid scintillation (PERALS®) system. *Nuclear Instruments and Methods in Physics Research Section A: Accelerators, Spectrometers, Detectors and Associated Equipment, 783*, 22-27.

Caffrey, E. A., Johansen, M. P., & Higley, K. A. (2015). Organ Dose-Rate Calculations for Small Mammals at Maralinga, the Nevada Test Site, Hanford and Fukushima: A Comparison of Ellipsoidal and Voxelized Dosimetric Methodologies, *Radiation Research*, 184, 433-441.

Campbell, P. G., Errécalde, O., Fortin, C., Hiriart-Baer, V. P., & Vigneault, B. (2002). Metal bioavailability to phytoplankton—applicability of the biotic ligand model. *Comparative Biochemistry and Physiology Part C: Toxicology & Pharmacology, 133*(1), 189-206.

Carlsbecker, A., & Helariutta, Y. (2005). Phloem and xylem specification: pieces of the puzzle emerge. *Current opinion in plant biology, 8*(5), 512-517.

Casacuberta, N., Lehritani, M., Mantero, J., Masqué, P., Garcia-Orellana, J., & Garcia-Tenorio, R. (2012). Determination of U and Th α-emitters in NORM samples through extraction chromatography by using new and recycled UTEVA resins. *Applied Radiation and Isotopes, 70*(4), 568-573.

Cetnar, J. J. A. o. N. E. (2006). General solution of Bateman equations for nuclear transmutations. *33*(7), 640-645.

Chater, C. C., Caine, R. S., Tomek, M., Wallace, S., Kamisugi, Y., Cuming, A. C., . . . Bergmann, D. C. (2016). Origin and function of stomata in the moss Physcomitrella patens. *Nature plants, 2*(12), 1-7.

Chen, S., Zhu, Y., & Hu, Q. (2005). Soil to plant transfer of 238 U, 226 Ra and 232 Th on a uranium mining-impacted soil from southeastern China. *Journal of environmental radioactivity, 82*(2), 223-236.

Copplestone, D., Beresford, N. A., Brown, J., & Yankovich, T. (2013). An international database of radionuclide concentration ratios for wildlife: development and uses. *Journal of environmental radioactivity, 126*, 288-298.

Copplestone D, B. J., Hingston JL, Real A, Sazykina T, Sundell-Bergman S, Wood MD. (2005). *Progress on the Production of the Web-based Effects Database: FREDERICA*. (F16R-CT-2003-508847). European Commission

Copplestone, D., Hingston, J., & Real, A. (2008). The development and purpose of the FREDERICA radiation effects database. *Journal of environmental radioactivity, 99*(9), 1456-1463.

Corriveau, L. (2006). Iron oxide copper-gold (±Ag±Nb±P±REE±U) deposits: A Canadian perspective. *Mineral depos-it of Canada. Consolidation and synthesis of mineral depositknowledge. Ottawa, Ontario: Geological Survey of Canada*, 1-23.

Crean, D. E., Corkhill, C. L., Nicholls, T., Tappero, R., Collins, J. M., & Hyatt, N. C. (2015). Expanding the nuclear forensic toolkit: chemical profiling of uranium ore

concentrate particles by synchrotron X-ray microanalysis. *RSC Advances, 5*(107), 87908-87918.

Currie, L. A. (1968). Limits for qualitative detection and quantitative determination. Application to radiochemistry. *Analytical chemistry, 40*(3), 586-593.

Dai, S., Song, W., Zhao, L., Li, X., Hower, J. C., Ward, C. R., . . . Seredin, V. V. (2014). Determination of boron in coal using closed-vessel microwave digestion and inductively coupled plasma mass spectrometry (ICP-MS). *Energy Fuels, 28*(7), 4517-4522.

Dawson, T. E., & Pate, J. S. (1996). Seasonal water uptake and movement in root systems of Australian phraeatophytic plants of dimorphic root morphology: a stable isotope investigation. *Oecologia, 107*(1), 13-20.

de Campos Vidal, B., & Mello, M. L. S. (2019). Toluidine blue staining for cell and tissue biology applications. *Acta histochemica, 121*(2), 101-112.

Desfougeres, L., Welcomme, E., Ollivier, M., Martin, P. M., Hennuyer, J., Hunault, M. O., . . . Favergeon, L. (2020). Oxidation as an early stage in the multistep thermal decomposition of uranium (IV) oxalate into U3O8. *Inorganic Chemistry, 59*(12), 8589-8602.

Ditcham, T. G., Wotherspoon, A., Kirkbride, K. P., Lenehan, C. E., & Popelka-Filcoff, R. S. (2016). Thermal decomposition of Australian uranium ore concentrates: characterisation of speciation and morphological changes following thermogravimetric analysis. *Journal of Radioanalytical and Nuclear Chemistry, 310*(2), 725-732.

Doering, C., & Bollhöfer, A. (2016). A database of radionuclide activity and metal concentrations for the Alligator Rivers Region uranium province. *Journal of environmental radioactivity, 162*, 154-159.

Doering, C., Medley, P., Orr, B., & Urban, D. (2018). Whole organism to tissue concentration ratios derived from an Australian tropical dataset. *Journal of environmental radioactivity, 189*, 31-39.

Dolchinkov, N. (2019). World uranium mining production. *Machines. Technologies. Materials., 13*(3), 127-130.

Edwards, C. R., & Oliver, A. J. (2000). Uranium processing: A review of current methods and technology. *Jom-Journal of the Minerals Metals & Materials Society, 52*(9), 12-20. doi:10.1007/s11837-000-0181-2

Eikenberg, J., Jäggi, M., Beer, H., Rüthi, M., & Zumsteg, I. (2009). Separation techniques for low-level determination of actinides in soil samples. *Applied Radiation and Isotopes, 67*(5), 776-780.

Eitrheim, E. S., May, D., Forbes, T. Z., & Nelson, A. W. (2016). Disequilibrium of naturally occurring radioactive materials (NORM) in drill cuttings from a horizontal drilling operation. *Environmental Science Technology Letters, 3*(12), 425-429.

El-Daoushy, F., Olsson, K., & Garcia-Tenorio, R. (1991). Accuracies in Po-210 determination for lead-210 dating. *Hydrobiologia, 214*(1), 43-52.

El Afifi, E., Hilal, M., Khalifa, S., & Aly, H. (2006). Evaluation of U, Th, K and emanated radon in some NORM and TENORM samples. *Radiation measurements, 41*(5), 627-633.

El Afifi, E. M., Hilal, M. A., & Attallah, M. F. (2020). Performance characteristics and validation of alpha particle spectrometers for radiometric analysis of natural and anthropogenic radionuclides of environmental impacts. *Applied Radiation Isotopes*, 109548.

Eldridge D. J., Val, J. & Jamea, A. L. (2011) Abiotic effects predominate under prolonged livestock-induced disturbance. *Austral Ecology*, 36, 367-377.

Environmental Risk From Ionising Contaminants: Assessment and Management (ERICA) (2015). Retrieved from https://wiki.ceh.ac.uk/display/rpemain/ERICA

ERICA. (2015). ERICA Assessment Tool. Retrieved from http://www.erica-tool.com/

Esdale, D., Pridmore, D. F., Coggon, J., Muir, P., Williams, P., & Fritz, F. (2003). The Olympic Dam copper-iranium-gold-silver-rare earth element deposit, South Austraila: A geophysical case history. ASEG Extended Abstracts, 3, 147-168, DOI: 10.1071/ASEGSpect12_13.

Ewing, J. J. a. R. C. (1992). Structural formula of uraninite. *Journal of Nuclear Materials, 190*, 128-132.

Falciani, R., Novaro, E., Marchesini, M., & Gucciardi, M. (2000). Multi-element analysis of soil and sediment by ICP-MS after a microwave assisted digestion method. *Journal of Analytical Atomic Spectrometry, 15*(5), 561-565.

Favas, P. J., Pratas, J., Mitra, S., Sarkar, S. K., & Venkatachalam, P. (2016). Biogeochemistry of uranium in the soil-plant and water-plant systems in an old uranium mine. *Science of the Total Environment, 568*, 350-368.

Feldmann, J., Krupp, E. M., Glindemann, D., Hirner, A. V., & Cullen, W. R. (1999). Methylated bismuth in the environment. *Applied organometallic chemistry, 13*(10), 739-748.

Finch, R., Hawthorne, F., & Ewing, R. (1995). Schoepite and dehydrated schoepite. *MRS Online Proceedings Library, 412*(1), 361-368.

Finch, R. J., & Ewing, R. C. (1992). The corrosion of uraninite under oxidizing conditions. *Journal of Nuclear Materials, 190*, 133-156.

Finch, R. J., Hawthorne, F. C., & Ewing, R. C. (1998). Structural relations among schoepite, metaschoepite and "dehydrated schoepite". *Canadian Mineralogist, 36*, 831-845.

Fisher, L. A., Cleverley, J. S., Pownceby, M., & MacRae, C. (2013). 3D representation of geochemical data, the corresponding alteration and associated REE mobility at the Ranger uranium deposit, Northern Territory, Australia. *Mineralium Deposita, 48*(8), 947-966.

FREDERICA Radiation Effects Database. (2010). Retrieved from https://wiki.ceh.ac.uk/display/rpemain/FREDERICA

Gamma and X-Ray Detection. (2014).

Garnier-Laplace, J., Copplestone, D., Gilbin, R., Alonzo, F., Ciffroy, P., Gilek, M., . . . Jaworska, A. (2008). Issues and practices in the use of effects data from FREDERICA in the ERICA Integrated Approach. *Journal of environmental radioactivity, 99*(9), 1474-1483.

Gaudino, S., Galas, C., Belli, M., Barbizzi, S., de Zorzi, P., Jaćimović, R., . . . Sansone, U. (2007). The role of different soil sample digestion methods on trace elements analysis: a comparison of ICP-MS and INAA measurement results. *Accreditation and quality assurance, 12*(2), 84-93.

Gebert, E., Hoekstra, H. R., Reis, A. H., & Peterson, S. W. (1978). The crystal structure of lithium uranate. *Journal of Inorganic and Nuclear Chemistry, 40*(1), 65-68. doi:https://doi.org/10.1016/0022-1902(78)80308-X

Gilmore, G. R. (2008). Gamma Spectrometry of Naturally Occuring Radioactive Materials (NORM). In *Practical Gamma-ray Spectrometry - 2nd Edition* (pp. 315-328).

Glascock, M. D., & Neff, H. (2003). Neutron activation analysis and provenance research in archaeology. *Measurement Science Technology, 14*(9), 1516.

Glauert, A. M., & Glauert, R. (1958). Araldite as an embedding medium for electron microscopy. *The Journal of Cell Biology, 4*(2), 191-194.

Gould, I. R., Lenhard, J. R., Muenter, A. A., Godleski, S. A., & Farid, S. (2000). Two-electron sensitization: a new concept for silver halide photography. *Journal of the American Chemical Society, 122*(48), 11934-11943.

Government, A. (1991). *South Australia, Native Vegetation Act 1991*.

Government of South Australia, D. o. S. D. *The Facts About Uranium Mining in South Australia*.

Guo, P., Jia, X., Duan, T., Xu, J., & Chen, H. (2010). Influence of plant activity and phosphates on thorium bioavailability in soils from Baotou area, Inner Mongolia. *Journal of environmental radioactivity, 101*(9), 767-772.

Gurau, D., Stanga, D., & Dragusin, M. (2014). Review of the principal mechanism of radon in the environment. *Romanian Journal of Physics, 59*(9-10), 904-911.

Gut, A., Scheibe, M., Rottenberger, S., Rummel, U., Welling, M., Ammann, C., . . . Kesselmeier, J. (2002). Exchange fluxes of NO2 and O3 at soil and leaf surfaces in an Amazonian rain forest. *Journal of Geophysical Research: Atmospheres, 107*(D20).

Hall, T. D., Inman, M. E., & Taylor, E. J. J. E. S. I. (2020). Sustainable Green Processes Enabled by Pulse Electrolytic Principles.

Hanson, A. B., Lee, R. N., Vachet, C., Schwerdt, I. J., Tasdizen, T., & McDonald IV, L. W. (2019). Quantifying impurity effects on the surface morphology of α-U3O8. *Analytical chemistry, 91*(15), 10081-10087.

Hanson, A. B., Schwerdt, I. J., Nizinski, C. A., Lee, R. N., Mecham, N. J., Abbott, E. C., . . . Martinson, S. (2021). Impact of Controlled Storage Conditions on the Hydrolysis and Surface Morphology of Amorphous-UO3. *ACS omega, 6*(12), 8605-8615.

Harmsen, K., & De Haan, F. (1980). Occurance and behaviour of uranium and thorium in soil and water. *NJAS wageningen journal of life sciences, 28*(1), 40-62.

Harris, J. R., Itakura, T., McOrist, G. D., Payne, T. E., & Smiles, D. E. (2000). Radionuclide migration in arid soils. *Radioactive Tracers*, 129.

He, H., Eldridge, D. J., & Lambers, H. (2018). Mineral nutrition of plants in Australia's arid zone. In *On the Ecology of Australia's Arid Zone* (pp. 77-102): Springer.

Hegazy, A., & Emam, M. (2010). Accumulation and soil-to-plant transfer of radionuclides in the Nile Delta coastal black sand habitats. *International journal of phytoremediation, 13*(2), 140-155.

Hein, K. (2002). Geology of the Ranger Uranium Mine, Northern Territory, Australia: structural constraints on the timing of uranium emplacement. *Ore Geology Reviews, 20*(3-4), 83-108.

Hill, S. M., Hore, S. B. (2011), Key Insights into range-front mineral system expression and evolution from regolith and long-tern landscape history, NE Flinders Ranges, MESA Journal, 63, 20-31.

Hirth, G. (2014). *A review of existing Australian radoinuclide activity concentration data in non-human biota inhabliting uiranium mining environments*. (Technical Report Series No. 167).

Hirth, G. A., Johansen, M. P., Carpenter, J. G., Bollhöfer, A., & Beresford, N. A. (2017). Whole-organism concentration ratios in wildlife inhabiting Australian uranium mining environments. *Journal of environmental radioactivity, 178*, 385-393.

Hoekstra, H. R., & Siegel, S. (1973). Uranium trioxide-water system. *Journal of Inorganic & Nuclear Chemistry, 35*(3), 761-779. doi:10.1016/0022-1902(73)80444-0

Horwitz, E. P., Dietz, M. L., Chiarizia, R., Diamond, H., Maxwell III, S. L., & Nelson, M. R. (1995). Separation and preconcentration of actinides by extraction chromatography using a supported liquid anion exchanger: application to the characterization of high-level nuclear waste solutions. *Analytica Chimica Acta, 310*(1), 63-78.

Hossain, I., Sharip, N., & Viswanathan, K. (2012). Efficiency and resolution of HPGe and NaI (Tl) detectors using gamma-ray spectroscopy. *Sci. Res. Essays, 7*(1), 86-89.

Hosseini, A., Brown, J., Szymanska, M., & Ciupek, K. (2011). Application of an environmental impact assessment methodology for areas exhibiting enhanced levels of NORM in Norway and Poland. *Radioprotection, 46*(6), S759-S764.

Hou, B., Keeling, J., & Li, Z. (2017) Paleovalley-related uranium deposits in Australia and China: A review of geological and exploration models and methods. Ore Geology Reviews, 88, 201-234. http://dx.doi.org/10.1016/j.oregeorev.217.05.005.

Howard, B. J., Beresford, N. A., Copplestone, D., Telleria, D., Proehl, G., Fesenko, S., . . . Higley, K. (2013). The IAEA handbook on radionuclide transfer to wildlife. *Journal of environmental radioactivity, 121*, 55-74.

Hu, N., Ding, D.-x., Li, S.-m., Tan, X., Li, G.-y., Wang, Y.-d., & Xu, F. (2016). Bioreduction of U (VI) and stability of immobilized uranium under suboxic conditions. *Journal of environmental radioactivity, 154*, 60-67.

Hwang, H., Hotchandani, M., Gonzales, B., Myers, R., Thein, M., & Ferguson, R. (1992). *Estimating MDA for low-level radioactivity in a radiobioassay laboratory*. Retrieved from

IAEA. (2000). *Generic Procedures for Assessment and Response During a Radiological Emergency*.

IAEA. (2013). *Incidents of nuclear and other radioactive material out of regulatory control - 2013 Fact Sheet*. Retrieved from Vienna:

ICRP. (2007). *Annals of the ICRP., ICRP Publication 103, The 2007 Recommendationd of the International COmmission on Radiological Protection*.

ICRP. (2008). *Environmental Protection: the Concept and Use of Reference Animals and Plants*.

Ikeda-Ohno, A., Shahin, L. M., Howard, D. L., Collins, R. N., Payne, T. E., Johansen, M. P. (2016). Fate of Plutonium at a former Nuclear Testing Site in Australia, *Environmental Science and Technology*, 50, 9098-9104.

Ilford. (2010). Ilford Nuclear Emulsions Technical Information for particle physics applications In. Harman Technology Limited

Islam, N., Kotha, R. R., Luthria, D. L., & Natarajan, S. (2020). Enhanced separation and analysis of low abundant soy proteins by dual washing extraction process. *Analytical Biochemistry, 610*, 113931.

Janeczek, J., & Ewing, R. (1996). Phosphatian coffinite with rare earth elements and Ce-rich françoisite-(Nd) from sandstone beneath a natural fission reactor at Bangombé, Gabon. *Mineralogical Magazine, 60*(4), 665-669.

Johansen, M., Child, D., Davis, E., Doering, C., Harrison, J., Hotchkis, M., . . . Wood, M. (2014). Plutonium in wildlife and soils at the Maralinga legacy site: persistence over decadal time scales. *Journal of environmental radioactivity, 131*, 72-80.

Johansen, M., & Twining, J. (2010). Radionuclide concentration ratios in Australian terrestrial wildlife and livestock: data compilation and analysis. *Radiation environmental biophysics, 49*(4), 603-611.

Kahn, A.M., Abu Bakar, N. K., Abu Bakar, A.F. & Ashraf. M.A. (2017). Chemical speciation and bioavailability of rare earth elements (REEs) in the ecosystem: a review, Environ Sci Pollut Res, 24, 22764-22789.

Kalnins, C. A., Spooner, N. A., Clarke, M. J., & Ottaway, D. (2019). Alpha particle autoradiography for high spatial resolution mapping of radionuclides. *Journal of environmental radioactivity, 197*, 9-15.

Kalve, S., Saini, K., Vissenberg, K., Beeckman, T., & Beemster, G. (2015). Transverse sectioning of Arabidopsis thaliana leaves using resin embedding. *Bio-protocol, 5*(18).

Katz, R., & Pinkerton, F. (1975). Response of nuclear emulsions to ionizing radiations. *Nuclear Instruments and Methods, 130*(1), 105-119.

Keegan, E., Kristo, M. J., Colella, M., Robel, M., Williams, R., Lindvall, R., . . . Gaffney, A. (2014). Nuclear forensic analysis of an unknown uranium ore concentrate sample seized in a criminal investigation in Australia. *Forensic science international, 240*, 111-121.

Keegan, E., Richter, S., Kelly, I., Wong, H., Gadd, P., Kuehn, H., & Alonso-Munoz, A. (2008). The provenance of Australian uranium ore concentrates by elemental and isotopic analysis. *Applied Geochemistry, 23*(4), 765-777.

Keith, L. S., Faroon, O. M., & Fowler, B. A. (2015). Uranium. In *Handbook on the Toxicology of Metals 4E* (pp. 1307 - 1345): Elsevier.

Kim, G., Kim, T.-H., & Church, T. M. (2012). Po-210 in the environment: biogeochemical cycling and bioavailability. In *Handbook of Environmental Isotope Geochemistry* (pp. 271-284): Springer.

Kinoshita, S. (1910). The photographic action of the α-particles emitted from radio-active substances. *Proc. R. Soc. Lond. A, 83*(564), 432-453.

Kirchenbaur, M., Maas, R., Ehrig, K., Kamenetsky, V. S., Strub, E., Ballhaus, C., & Münker, C. (2016). Uranium and Sm isotope studies of the supergiant Olympic Dam Cu–Au–U–Ag deposit, South Australia. *Geochimica et Cosmochimica Acta, 180*, 15-32.

Koranda, J, J. & Robison, W, L. (1978) Accumulation of Radionuclides by Plants as a Monitor System, Environmental Health Perspectives, 27, 165-179.

Kosior, G., Frontasyeva, M., Ziembik, Z., Zincovscaia, I., Dołhańczuk-Śródka, A., Godzik, B. J. A. o. e. c., & toxicology. (2020). The Moss Biomonitoring Method and Neutron Activation Analysis in Assessing Pollution by Trace Elements in Selected Polish National Parks. *79*(3), 310-320.

Kotelnikova, A. d., Rigova, O. B., & Stolbova V. V. (2021). Lanthanides in the Soil: Routes of Entry, Content, Effect on Plants, and Genotoxicity(a Review), Eurasian Soil Science, 54(1), 117-134.

Laboratory, B. N. (2019). National Nuclear Data Center.

Laboratory, N. R. E. (2002, May 6-10). *Proceedings of the 2002 U.S. DOE Hydrogen and Fuel Cells Annual Program/Lab R&D Review*.

Landsberger, S., Tamalis, D., Leblanc, C., & Yoho, M. J. J. o. e. r. (2017). Disequilibrium in the uranium and actinium series in oil scale samples. *166*, 126-129.

Lane, D. J., Cook, N. J., Grano, S. R., & Ehrig, K. (2016). Selective leaching of penalty elements from copper concentrates: A review. *Minerals Engineering, 98*, 110-121.

Larson, A. C., & Von Dreele, R. B. (1994). Gsas. *Report lAUR*, 86-748.

Leinders, G., Bes, R., Kvashnina, K. O., & Verwerft, M. (2020). Local Structure in U (IV) and U (V) Environments: The Case of U3O7. *Inorganic Chemistry, 59*(7), 4576-4587.

León‑Sánchez, L., Nicolás, E., Prieto, I., Nortes, P., Maestre, F. T., & Querejeta, J. I. (2020). Altered leaf elemental composition with climate change is linked to reductions in photosynthesis, growth and survival in a semi‑arid shrubland. *Journal of Ecology, 108*(1), 47-60.

Li, P., Zhang, R., Gu, M., & Zheng, G. (2018). Uptake of the natural radioactive gas radon by an epiphytic plant. *Science of the Total Environment, 612*, 436-441.

Limited, T. E. (2011). *Wiluna Uranium Project, Environmental Review and Management Programme (ERMP)*. Retrieved from

Linge, K. L., & Jarvis, K. E. (2009). Quadrupole ICP‑MS: Introduction to instrumentation, measurement techniques and analytical capabilities. *Geostandards geoanalytical research, 33*(4), 445-467.

Liu, B., Peng, T., Sun, H., & Yue, H. (2017). Release behavior of uranium in uranium mill tailings under environmental conditions. *Journal of environmental radioactivity, 171*, 160-168.

Long, S., Sdraulig, S, Tate, B and Martin, P. (2012). A Survey of Naturally Occuring Radioactive Material Associated with Mining. *Technical Report series No. 161*.

Loopstra, B. O. (1964). Neutron diffraction investigation of U_3O_8. *Acta Crystallographica, 17*(6), 651-654. doi:10.1107/s0365110x6400158x

Lozano, J., Fernandez, F., & Gomez, J. (1999). Preparation of alpha-spectrometric sources by co-precipitation with Fe (OH) 3: application to uranium. *Applied Radiation Isotopes, 50*(3), 475-477.

Lozano, R., San Miguel, E., & Bolívar, J. (2011). Assessment of the influence of in situ 210Bi in the calculation of in situ 210Po in air aerosols: Implications on residence time calculations using 210Po/210Pb activity ratios. *Journal of Geophysical Research: Atmospheres, 116*(D8).

MacDonell, M. M. (1986). Uptake of radium-226 from uranium mill tailings by C-3 and C-4 Plants and implications for transport of radium-226 and radon-222 into the disposal site environment. In. Northwestern University.

Macmillan, E., Ciobanu, C. L., Ehrig, K., Cook, N. J., & Pring, A. (2016). Chemical zoning and lattice distortion in uraninite from Olympic Dam, South Australia.

Macmillan, E., Cook, N. J., Ehrig, K., Ciobanu, C. L., & Pring, A. (2016). Uraninite from the Olympic Dam IOCG-U-Ag deposit: Linking textural and compositional variation to temporal evolution. *American Mineralogist, 101*(6), 1295-1320.

Mamand, S. F., Khudhur, N. S., & Darwesh, D. A. (2020). Phytoremediation Efficiency of Some Evergreen Plant Genera for Lead Polluted Soil. *Zanco Journal of Pure Applied Sciences, 32*(5), 174-178.

Manaud, J., Maynadie, J., Mesbah, A., Hunault, M. O., Martin, P. M., Zunino, M., . . . Clavier, N. (2020). Hydrothermal conversion of uranium (IV) oxalate into oxides: a comprehensive study. *Inorganic Chemistry, 59*(5), 3260-3273.

Marshall, T. A., Morris, K., Law, G. T., Livens, F. R., Mosselmans, J. F. W., Bots, P., & Shaw, S. (2014). Incorporation of uranium into hematite during crystallization from ferrihydrite. *Environmental Science Technology, 48*(7), 3724-3731.

Märten, H. (2006). Environmental Management and Optimization of In-situ-Leaching at Beverley. In *Uranium in the Environment* (pp. 537-546): Springer.

Martin, P. Hancock, G.J., Johnston, A. and Murray A.S., (1998). Natural-series Radionuclides in Traditional North Australian Aboriginal Foods. *Journal of Environmental Radioactivity,* 40(1), 37-58.

Martin, R., Dowling, K., Pearce, D. C., Florentine, S., McKnight, S., Stelcer, E., . . . Bennett, J. W. (2017). Trace metal content in inhalable particulate matter (PM 2.5–10 and

PM 2.5) collected from historical mine waste deposits using a laboratory-based approach. *Environmental geochemistry health, 39*(3), 549-563.

Matthews, K. M., Kim, C.-K., & Martin, P. (2007). Determination of 210Po in environmental materials: a review of analytical methodology. *Applied Radiation Isotopes, 65*(3), 267-279.

Mayer, K., Wallenius, M., & Varga, Z. (2013). Nuclear Forensic Science: Correlating Measurable Material Parameters to the History of Nuclear Material. *Chemical Reviews, 113*(2), 884-900. doi:10.1021/cr300273f

Medley, P., Doering, C., Evans, F., & Bollhöfer, A. (2017). Natural radionuclides and stable elements in weaver ants (Oecophylla smaragdina) from tropical northern Australia. *Journal of environmental radioactivity, 178*, 404-410.

Melaku, S., Dams, R., & Moens, L. (2005). Determination of trace elements in agricultural soil samples by inductively coupled plasma-mass spectrometry: microwave acid digestion versus aqua regia extraction. *Analytica Chimica Acta, 543*(1), 117-123.

Meteoblue, Simulated historical climate & weather data for Olympic Dam Airport, 2022.

Metcalfe., D & Biu., E. (2016). Soil: Understanding, Australia: State of the Environment, https://soe.environment.gov.au/theme/land/topic/2016/soil-understanding

Michalik, B., de With, G., & Schroeyers, W. (2018). Measurement of radioactivity in building materials–Problems encountered caused by possible disequilibrium in natural decay series. *Construction Building Materials, 168*, 995-1002.

Miskowiec, A., Spano, T., Hunt, R., Shields, A. E., Niedziela, J., & Finkeldei, S. (2020a). Structural features of solid-solid phase transitions and lattice dynamics in U 3 O 8. *Physical Review Materials, 4*(9), 093610.

Miskowiec, A., Spano, T., Hunt, R., Shields, A. E., Niedziela, J. L., & Finkeldei, S. (2020b). Structural features of solid-solid phase transitions and lattice dynamics in U_3O_8. *Physical Review Materials, 4*(9), 093610. doi:10.1103/PhysRevMaterials.4.093610

Mitchell, N., Pérez-Sánchez, D., & Thorne, M. (2013). A review of the behaviour of U-238 series radionuclides in soils and plants. *Journal of Radiological Protection, 33*(2), R17.

Moens, L., & Dams, R. (1995). NAA and ICP-MS: A comparison between two methods for trace and ultra-trace element analysis. *Journal of radioanalytical nuclear chemistry, 192*(1), 29-38.

Mudd, G. M. (2008). Radon releases from Australian uranium mining and milling projects: assessing the UNSCEAR approach. *Journal of environmental radioactivity, 99*(2), 288-315.

Müllerová, M., Holý, K., Blahušiak, P., & Bulko, M. (2018). Study of radon exhalation from the soil. *Journal of Radioanalytical and Nuclear Chemistry, 315*(2), 237-241.

Murphy, R. D. M. a. B. L. (2005). Radioactive Compounds. In *Environmental Forensics: Contaminant Specific Guide* (pp. 111-141).

Nations, U. (2000). *Sources and Effects of Ionising Radiation* New York

NEA, N. E. A. (2006). *Comprehensive report of the task group on activity measurements at release levels.* . (JT03215685).

NIST, N. I. o. S. a. T. *Standard Reference Material 4359 Seaweed Radionuclide Standard* Retrieved from Gaithersburg, Maryland 20899:

NIST, N. I. o. S. a. T. (2018). *Standard Reference Material 2711a Montana II Soil*. Retrieved from

NIST, N. I. o. S. a. T. (2019). *Standard Reference Material 1547 Peach Leaves*. Retrieved from

Nizinski, C. A., Hanson, A. B., Fullmer, B. C., Mecham, N. J., Tasdizen, T., & McDonald IV, L. W. (2020). Effects of process history on the surface morphology of uranium ore concentrates extracted from ore. *Minerals Engineering, 156*, 106457.

Noller, B. (1991). Non-radiological contaminants from uranium mining and milling at Ranger, Jabiru, Northern Territory, Australia. *Environmental monitoring assessment, 19*(1-3), 383-400.

Norby, P. (1995). *In-situ time resolved synchrotron powder diffraction studies of synthesis and chemical reactions*. Retrieved from

Noto, T., Tomita, H., Sakai, Y., Kawarabayashi, J., Naka, T., Morishima, K., . . . Iguchi, T. (2014). Alpha track analysis using nuclear emulsions as a preselecting method for safeguards environmental sample analysis. *Radiation measurements, 71*, 533-536.

O'Brien, T., Feder, N., & McCully, M. E. (1964). Polychromatic staining of plant cell walls by toluidine blue O. *Protoplasma, 59*(2), 368-373.

Odoh, S. O., Shamblin, J., Colla, C. A., Hickam, S., Lobeck, H. L., Lopez, R. A. K., . . . Burns, P. C. (2016). Structure and Reactivity of X-ray Amorphous Uranyl Peroxide, U2O7. *Inorganic Chemistry, 55*(7), 3541-3546. doi:10.1021/acs.inorgchem.6b00017

Oerter, E. J., Singleton, M., Dai, Z., Deinhart, A., Thaw, M., & Davisson, M. L. (2020). Hydrogen and oxygen stable isotope composition of water in metaschoepite mineralization on U3O8. *Applied Geochemistry, 112*, 104469.

OPAL multi-purpose reactor. (2020). Retrieved from https://www.ansto.gov.au/research/facilities/opal-multi-purpose-reactor#content-capabilities

Ortu, F., Formanuik, A., Innes, J. R., & Mills, D. P. (2016). New vistas in the molecular chemistry of thorium: low oxidation state complexes. *Dalton Transactions, 45*(18), 7537-7549.

Osborne, O., Pring, A., Popelka-Filcoff, R., Bennett, J., Stopic, A., Glascock, M., & Lenehan, C. (2012). Comparison of the relative comparator and k 0 neutron activation analysis techniques for the determination of trace-element concentrations in pyrite. *Mineralogical Magazine, 76*(5), 1229-1245.

Outola, I., Filliben, J., Inn, K., La Rosa, J., McMahon, C., Peck, G., . . . Smedley, P. (2006). Characterization of the NIST seaweed standard reference material. *Applied Radiation Isotopes, 64*(10-11), 1242-1247.

P. Strans, N. B., D. Copplestone, J. Godoy, L. Jianguo, R.Saxen, T.Yankovich, J.Brown. (2009). *Environmental Protection: Transfer Parameters for Reference Animals and Plants*.

Pastoor, K. J., Kemp, R. S., Jensen, M. P., & Shafer, J. C. (2021). Progress in Uranium Chemistry: Driving Advances in Front-End Nuclear Fuel Cycle Forensics. *Inorganic Chemistry*. doi:10.1021/acs.inorgchem.0c03390

Peijnenburg, W. J., Teasdale, P. R., Reible, D., Mondon, J., Bennett, W. W., & Campbell, P. G. (2014). Passive sampling methods for contaminated sediments: State of the science for metals. *Integrated environmental assessment and management, 10*(2), 179-196.

Pickett, D. A., Murrell, M. T., & Williams, R. W. (1994). Determination of femtogram quantities of protactinium in geologic samples by thermal ionization mass spectrometry. *Analytical chemistry, 66*(7), 1044-1049.

Pietrzak-Flis, Z., & Skowrońska-Smolak, M. (1995). Transfer of 210Pb and 210Po to plants via root system and above-ground interception. *Science of the Total Environment, 162*(2-3), 139-147.

Popelka-Filcoff, R., Lenehan, C., Glascock, M., Bennett, J., Stopic, A., Quinton, J., . . . Walshe, K. (2012). Evaluation of relative comparator and k 0-NAA for characterization of Aboriginal Australian ochre. *Journal of Radioanalytical and Nuclear Chemistry, 291*(1), 19-24.

Prince, J. R. (1979). Comments on equilibrium, transient equilibrium, and secular equilibrium in serial radioactive decay. *Journal of nuclear medicine: official publication, Society of Nuclear Medicine, 20*(2), 162-164.

Radioecologists, I. A. e. A. a. I. U. o. Wildlife Transfer Parameter Database. Retrieved from http://www.wildlifetransferdatabase.org/

Rajaković, L. V., Marković, D. D., Rajaković-Ognjanović, V. N., & Antanasijević, D. Z. J. T. (2012). The approaches for estimation of limit of detection for ICP-MS trace analysis of arsenic. *102*, 79-87.

Rea, M. A. D., Johansen, M. P., Payne, T. E., Hirth, G., Hondros, J., Pandelus, S., . . . Green, L. (2021). Radionuclides and stable elements in vegetation in Australian arid environments: Concentration ratios and seasonal variation. *Journal of environmental radioactivity, 234*, 106627.

Read, J., & Pickering, R. (1999). Ecological and toxicological effects of exposure to an acidic, radioactive tailings storage. *Environmental monitoring assessment, 54*(1), 69-85.

Recovery, A. (2019). Arid Recovery. Retrieved from https://aridrecovery.org.au/

Reid, N., Robson, T., Radcliffe, B., & Verrall, M. (2016). Excessive sulphur accumulation and ionic storage behaviour identified in species of Acacia (Leguminosae: Mimosoideae). *Annals of Botany, 117*(4), 653-666.

Richardson, K., Jarett, L., & Finke, E. (1960). Embedding in epoxy resins for ultrathin sectioning in electron microscopy. *Stain technology, 35*(6), 313-323.

Richter, S., Alonso, A., De Bolle, W., Wellum, R., & Taylor, P. (1999). Isotopic "fingerprints" for natural uranium ore samples. *International Journal of Mass Spectrometry, 193*(1), 9-14.

Roger, K.-S. (1982). *Olympic Dam Project, Draft Environmental Impact Statement*. Retrieved from

Schmandt, D. S., Cook, N. J., Ciobanu, C. L., Ehrig, K., Wade, B. P., Gilbert, S., & Kamenetsky, V. S. (2017). Rare earth element fluorocarbonate minerals from the olympic dam Cu-U-Au-Ag deposit, South Australia. *Minerals, 7*(10), 202.

Schmidt, V., & Hamel, P. (2001). Measurements of deposition velocity of radon decay products for examination of the correlation between air activity concentration of radon and the accumulated Po-210 surface activity. *Science of the Total Environment, 272*(1-3), 189-194.

Scholz, G., & Scholz, F. (2015). First-order differential equations in chemistry. *ChemTexts, 1*(1), 1.

Sedelnikova, O. V., Hughes, T. E., & Langdale, J. A. (2018). Understanding the genetic basis of C4 Kranz anatomy with a view to engineering C3 crops. *Annual review of geneticsv, 52*, 249-270.

Seiner, B. N., Morley, S. M., Beacham, T. A., Haney, M. M., Gregory, S., & Metz, L. (2014). Effects of digestion, chemical separation, and deposition on Po-210 quantitative analysis. *Journal of Radioanalytical and Nuclear Chemistry, 302*(1), 673-678.

Sengupta, A., Sankhe, R. H., & Natarajan, V. (2015). Rapid and non-destructive determination of uranium and thorium by gamma spectrometry and a comparison with ICP-AES. *Journal of Radioanalytical and Nuclear Chemistry, 306*(2), 401-406.

Shahid, M., Dumat, C., Khalid, S., Schreck, E., Xiong, T., & Niazi, N. K. (2017). Foliar heavy metal uptake, toxicity and detoxification in plants: A comparison of foliar and root metal uptake. *Journal of hazardous materials, 325*, 36-58.

Shishkina, E. A., Pryakhin, E. A., Popova, I. Ya., Osipov, D. I., Tikhova, Yu., Andreyev, S. S., . . . Akleyev, A. V. (2016). Evaluation of distribution coeffficeints and concentration ratios of ^{90}Sr and ^{137}Cs in the Techa RIver and the Miass River. *Journal of Environmental Radioactivity, 148-163.*

Siegel, S., Hoekstra, H. R., & Gebert, E. (1972). The structure of γ-uranyl dihydroxide, $UO_2(OH)_2$. *Acta Crystallographica Section B, 28*(12), 3469-3473. doi:doi:10.1107/S0567740872008192

Simsek, A., & Aykut, O. (2007). Evaluation of the microelement profile of Turkish hazelnut (Corylus avellana L.) varieties for human nutrition and health. *International journal of food sciences nutrition, 58*(8), 677-688.

Singh, G., & Luly, J. (1991). Changes in vegetation and seasonal climate since the last full glacial at Lake Frome, South Australia. *Palaeogeography, Palaeoclimatology, Palaeoecology, 84*(1-4), 75-86.

Skirrow, R. G., Mercadier, J., Armstrong, R., Kuske, T., & Deloule, E. (2016). The Ranger uranium deposit, northern Australia: Timing constraints, regional and ore-related alteration, and genetic implications for unconformity-related mineralisation. *Ore Geology Reviews, 76*, 463-503.

Skwarzec, B., Strumińska, D., Ulatowski, J., & Golebiowski, M. (2001). Determination and distribution of 210Po in tobacco plants from Poland. *Journal of Radioanalytical and Nuclear Chemistry, 250*(2), 319-322.

Spano, T. L., Niedziela, J. L., Shields, A. E., McFarlane, J., Zirakparvar, A., Brubaker, Z., . . . Miskowiec, A. (2020). Structural, Spectroscopic, and Kinetic Insight into the Heating Rate Dependence of Studtite and Metastudtite Dehydration. *The Journal of Physical Chemistry C, 124*(49), 26699-26713.

Spano, T. L., Shields, A. E., Barth, B. S., Gruidl, J. D., Niedziela, J. L., Kapsimalis, R. J., & Miskowiec, A. (2020). Computationally Guided Investigation of the Optical Spectra of Pure β-UO3. *Inorganic Chemistry, 59*(16), 11481-11492.

Su, Y.-F., Tonkyn, R., Sweet, L., Corbey, J., Bryan, S., & Johnson, T. (2018). *Characterization of uranium ore concentrate chemical composition via Raman spectroscopy* (Vol. 10629): SPIE.

Sweet, L., Henager, C. H., Hu, S., Johnson, T., Meier, D., Peper, S. M., & Schwantes, J. M. (2011). Investigation of Uranium Polymorphs. *Pacific Northwest National Laboratory, Richland, Washington, 99352*.

Taddei, M., Silva, N., Fernandes, E., & Cipriani, M. (2001). Determination of alpha-emitting isotopes of uranium and thorium in vegetables and excreta. *Journal of Radioanalytical and Nuclear Chemistry, 248*(2), 483-486.

Tajuddin, S., Mat, N., Yunus, A. G., & AR, S. B. (2013). Anatomical study of stem, petiole, leaf, tuber, root and flower of Dioscorea hispida Dennst.(Dioscoreaceae) by using optical microscope, SEM and TEM. *Journal Of Agrobiotechnology, 4*, 33-42.

Tamasi, A. L., Boland, K. S., Czerwinski, K., Ellis, J. K., Kozimor, S. A., Martin, R. L., . . . Sutton, A. D. (2015). Oxidation and hydration of U3O8 materials following controlled exposure to temperature and humidity. *Analytical chemistry, 87*(8), 4210-4217.

Tamasi, A. L., Boland, K. S., Czerwinski, K., Ellis, J. K., Kozimor, S. A., Martin, R. L., . . . Wilkerson, M. P. (2015). Oxidation and Hydration of U_3O_8 Materials Following

Controlled Exposure to Temperature and Humidity. *Analytical Chemistry, 87*(8), 4210-4217. doi:10.1021/ac504105t

Tamasi, A. L., Cash, L. J., Mullen, W. T., Pugmire, A. L., Ross, A. R., Ruggiero, C. E., Wilkerson, M. P. (2017). Morphology of U_3O_8 materials following storage under controlled conditions of temperature and relative humidity. *Journal of Radioanalytical and Nuclear Chemistry, 311*(1), 35-42. doi:10.1007/s10967-016-4923-1

Taylor, S. R., & McLennan, S. M. (1985). The continental crust: its composition and evolution.

Technologies, M. (2016). Small Anode Germanium Well Detector (SAGe). In Canberra (Ed.).

Telahigue, F., Agoubi, B., Souid, F., & Kharroubi, A. (2018). Groundwater chemistry and radon-222 distribution in Jerba Island, Tunisia. *Journal of environmental radioactivity, 182*, 74-84.

Thakur, P., & Ward, A. (2020). 210 Po in the environment: insight into the naturally occurring polonium isotope. *Journal of Radioanalytical and Nuclear Chemistry 323*(1), 27-49.

Thibes, R., & de Oliveira, S. L. (2014). General Solution To Bateman's Differential Equations With Direct Index Notation. *International Journal of Pure and Applied Mathematics*
93(6), 879-883.

Thomas, R., Rivenet, M., Berrier, E., de Waele, I., Arab, M., Amaraggi, D., Abraham, F. (2017). Thermal decomposition of $(UO_2)O_2(H_2O)_2 \cdot 2H_2O$: Influence on structure, microstructure and hydrofluorination. *Journal of Nuclear Materials, 483*, 149-157. doi:https://doi.org/10.1016/j.jnucmat.2016.11.009

Ticianelli, R., Ribeiro, A., Figueiredo, A., & Zanh, G. (2013). U, TH and lanthanides in street soils of Sao Paulo city, Brazil.

Toby, B. H. (2001). EXPGUI, a graphical user interface for GSAS. *Journal of Applied Crystallography, 34*(2), 210-213.

Tuovinen, H., Vesterbacka, D., Pohjolainen, E., Read, D., Solatie, D., & Lehto, J. (2015). A comparison of analytical methods for determining uranium and thorium in ores and mill tailings. *Journal of Geochemical exploration, 148*, 174-180.

UC Davis Interdisciplinary Center for Inductively-Coupled Plasma Mass Spectrometry (2015). Retrieved from http://icpms.ucdavis.edu/facilities-procedures

UNSCEAR. *1996 Report, Sources and effects of ionising radiation*

UNSCEAR. (2000). *Sources and Effects of Ionising Radiation, United Nations Scientific Committee on the Effects of Atomic Radiation UNSCEAR 2000 Report to the General Assembly, with Annexes*

Van Nostrand, J. D., Wu, L., Wu, W.-M., Huang, Z., Gentry, T. J., Deng, Y., Gu, B. (2011). Dynamics of microbial community composition and function during in situ bioremediation of a uranium-contaminated aquifer. *Applied and environmental microbiology, 77*(11), 3860-3869.

Varga, Z., Ozturk, B., Meppen, M., Mayer, K., Wallenius, M., & Apostolidis, C. (2011). Characterization and classification of uranium ore concentrates (yellow cakes) using infrared spectrometry. *Radiochimica Acta, 99*(12), 807-813. doi:10.1524/ract.2011.1886

Varga, Z., Wallenius, M., Mayer, K., & Meppen, M. (2011). Analysis of uranium ore concentrates for origin assessment. *Proc Radiochim Acta, 1*, 1-4.

Venkataraman, R., Bronson, F., Atrashkevich, V., Field, M., & Young, B. (2005). Improved detector response characterization method in ISOCS and LabSOCS. *Journal of Radioanalytical and Nuclear Chemistry, 264*(1), 213-219.

Venkatesh, S., Reddy, Y. R., Ramesh, M., Swamy, M., Mahadevan, N., & Suresh, B. (2008). Pharmacognostical studies on Dodonaea viscosa leaves. *African Journal of Pharmacy and Pharmacology, 2*(4), 083-088.

Vitova, T., Pidchenko, I., Biswas, S., Beridze, G., Dunne, P. W., Schild, D., Baker, R. J. (2018). Dehydration of the Uranyl Peroxide Studtite,[UO2 (η2-O2)(H2O) 2]· 2H2O, Affords a Drastic Change in the Electronic Structure: A Combined X-ray Spectroscopic and Theoretical Analysis. *Inorganic Chemistry, 57*(4), 1735-1743.

Wallbrink, P., Walling, D., & He, Q. (2002). Radionuclide measurement using HPGe gamma spectrometry. In *Handbook for the assessment of soil erosion and sedimentation using environmental radionuclides* (pp. 67-96): Springer.

Wallwork, K. S., Kennedy, B. J., & Wang, D. (2007). *The high resolution powder diffraction beamline for the Australian Synchrotron.* Paper presented at the AIP Conference Proceedings.

Wang, F., Song, Z., Cheng, X., & Huanhuan, M. (2017). *Patterns and Features of Global Uranium Resources and Production.* Paper presented at the IOP Conference Series: Earth and Environmental Science.

Wang, H., Ma, L., Cao, K., Geng, J., Liu, J., Song, Q., . . . Li, S. (2012). Selective solid-phase extraction of uranium by salicylideneimine-functionalized hydrothermal carbon. *Journal of hazardous materials, 229*, 321-330.

Wang, Y., von Gunten, K., Bartova, B., Meisser, N., Astner, M., Burger, M., & Bernier-Latmani, R. (2016). Products of in Situ Corrosion of Depleted Uranium Ammunition in Bosnia and Herzegovina Soils. *Environmental Science & Technology, 50*(22), 12266-12274. doi:10.1021/acs.est.6b03732

Weck, P. F., & Kim, E. (2014). Layered uranium (VI) hydroxides: structural and thermodynamic properties of dehydrated schoepite α-UO 2 (OH) 2. *Dalton Transactions, 43*(45), 17191-17199.

Weck, P. F., Kim, E., Jove-Colon, C. F., & Sassani, D. C. (2012). Structures of uranyl peroxide hydrates: a first-principles study of studtite and metastudtite. *Dalton Transactions, 41*(32), 9748-9752. doi:10.1039/c2dt31242e

Weller, M. T., Light, M. E., & Gelbrich, T. (2000). Structure of uranium(VI) oxide dihydrate, $UO_3.2H_2O$; synthetic meta-schoepite $(UO_2)_4O(OH)_6.5H_2O$. *Acta Crystallographica Section B, 56*(4), 577-583. doi:doi:10.1107/S0108768199016559

Wetle, R., Bensko-Tarsitano, B., Johnson, K., Sweat, K. G., & Cahill, T. (2020). Uptake of uranium into desert plants in an abandoned uranium mine and its implications for phytostabilization strategies. *Journal of environmental radioactivity, 220*, 106293.

Wilkerson, M. P., Hernandez, S. C., Mullen, W. T., Nelson, A. T., Pugmire, A. L., Scott, B. L., . . . Walensky, J. R. (2020). Hydration of α-UO3 following storage under controlled conditions of temperature and relative humidity. *Dalton Transactions, 49*(30), 10452-10462. doi:10.1039/D0DT01852J

Wood, M. D., Beresford, N. A., Barnett, C. L., Copplestone, D., & Leah, R. T. (2009). Assessing radiation impact at a protected coastal sand dune site: an intercomparison of models for estimating the radiological exposure of non-human biota. *Journal of environmental radioactivity, 100*(12), 1034-1052.

Wood, M. D., Beresford, N. A., Howard, B. J., & Copplestone, D. (2013). Evaluating summarised radionuclide concentration ratio datasets for wildlife. *Journal of environmental radioactivity, 126*, 314-325.

Wood, M. D., Beresford, N. A., Semenov, D. V., Yankovich, T. L., & Copplestone, D. (2010). Radionuclide transfer to reptiles. *Radiation environmental biophysics, 49*(4), 509-530.

Woods, P. (2011). Sustainability aspects of the Beverley Uranium Mines. In *Heathgate Resources Pty Ltd*. Bulletin.

Wronkiewicz, D. J., Bates, J. K., Wolf, S. F., & Buck, E. C. (1996). Ten-year results from unsaturated drip tests with UO2 at 90 C: implications for the corrosion of spent nuclear fuel. *Journal of Nuclear Materials, 238*(1), 78-95.

Wronkiewicz, D. J., & Buck, E. C. (2018). 10. Uranium Mineralogy and the Geologic Disposal of Spent Nuclear Fuel. *Uranium*, 475-498.

Wülser, P.-A., Brugger, J., Foden, J., & Pfeifer, H.-R. (2011). The sandstone-hosted Beverley uranium deposit, Lake Frome Basin, South Australia: mineralogy, geochemistry, and a time-constrained model for its genesis. *Economic Geology, 106*(5), 835-867.

Xu, Z., Kawahito, K., Ye, X., Timerbaev, A. R., & Hirokawa, T. (2011). Electrokinetic supercharging with a system‐induced terminator and an optimized capillary versus electrode configuration for parts‐per‐trillion detection of rare‐earth elements in CZE. *Electrophoresis, 32*(10), 1195-1200.

Yanase, N., Payne, T. E., & Sekine, K. (1995). Groundwater geochemistry in the Koongarra ore deposit, Australia (II): activity ratios and migration mechanisms of uranium series radionuclides. *Geochemical Journal, 29*(1), 31-54.

Young, J. (2015). NexION ICPMS traning - general analysis. In F. University (Ed.). Flinders Analytical Laboratory, Training Procedure.

Yuksel, B. and Arica, E. (2018). Assessment of Toxic, Essential, and Other Metal Levels by ICP-MS in Lake Eymir and Morgan in Ankara, Turkey: An ENvironemtal Application. Atomic Spectroscopy, 39(5), 179-218.

Zahorowski, W., Chambers, S., & Henderson-Sellers, A. (2004). Ground based radon-222 observations and their application to atmospheric studies. *Journal of environmental radioactivity, 76*(1-2), 3-33.

Zarubin, P. (2016). Recent applications of nuclear track emulsion technique. *Physics of Atomic Nuclei, 79*(13), 1525-1535.

Zhu, Z., Pranolo, Y., & Cheng, C. Y. (2016). Uranium recovery from strong acidic solutions by solvent extraction with Cyanex 923 and a modifier. *Minerals Engineering, 89*, 77-83.

Zinger, I., Copplestone, D., & Howard, B. (2008). Decision-making in environmental radiation protection: using the ERICA Integrated Approach. *Journal of environmental radioactivity, 99*(9), 1510-1518.